Collinear resonance ionization spectroscopy of exotic francium and radium isotopes

A thesis submitted to the University of Manchester for the degree of Doctor of Philosophy in the Faculty of Science and Engineering

2017

Shane Wilkins

School of Physics and Astronomy

University of Manchester

Contents

List of Figures **7**

List of Tables **11**

Abstract **13**

Declaration of Authorship **15**

Copyright Statement **17**

Acknowledgements **19**

1 Introduction **21**
1.1 This work 22

2 The hyperfine structure as a probe of the atomic nucleus **23**
2.1 The hyperfine structure 23
2.2 Extraction of nuclear electromagnetic moments 25
2.2.1 Magnetic dipole moment 25
2.2.2 Spectroscopic electric quadrupole moment 27
2.3 Isotope shift 28
2.3.1 Mass shift 28
2.3.2 Field shift 29
2.4 Changes in the mean-square charge radii 30
2.4.1 King-plot method 30
2.5 Nuclear shapes and deformation 31
2.5.1 Parametrization of nuclear shape 31
2.5.2 Estimating the nature of deformation of the nucleus 32

3 Production of radioactive nuclei **35**
3.1 The ISOLDE facility 35
3.1.1 Radioactive-ion-beam production at ISOLDE 35
3.2 Other facilties and methods 39

4 Laser spectroscopy of radioactive nuclei 41
4.1 Resonance ionization spectroscopy . . . 41
4.2 Collinear laser spectroscopy . . . 44
4.2.1 Fluorescence detection . . . 45
4.2.2 Particle-detection methods . . . 47
4.3 Ion-beam cooler bunchers . . . 49
4.3.1 ISCOOL: The ISOLDE ion-beam cooler buncher . . . 50
4.4 Collinear resonance ionization spectroscopy . . . 51
4.4.1 Experimental setup . . . 52

5 Laser requirements and delivery 55
5.1 Lasers at CRIS . . . 56
5.2 Continuous-wave lasers . . . 57
5.2.1 M-Squared SolsTiS and ECD-X . . . 57
5.2.2 Matisse 2 DS and Wavetrain . . . 58
5.2.3 'Chopping' of continuous-wave light . . . 60
5.3 Pulsed lasers . . . 64
5.3.1 Lee Laser LDP-100MQ . . . 65
5.3.2 Z-cavity Ti:Sa . . . 65
5.3.3 Injection-seeded Ti:Sa . . . 66
5.3.4 Spectron Spectrolase 4000 . . . 67
5.3.5 Sirah Cobra . . . 67
5.3.6 Litron LPY 601 50-100 PIV and Nano TRLi HR 250-100 . . . 67
5.4 Wavelength measurement and referencing . . . 69
5.4.1 HighFinesse WSU2 . . . 70
5.4.2 HighFinesse WS6 . . . 71
5.5 Higher-harmonic generation of light . . . 71
5.5.1 Third-harmonic generation . . . 72

6 Developments and setup for experiments on francium and radium 79
6.1 Francium experiment . . . 79
6.1.1 Ionization scheme . . . 79
6.2 Radium experiment . . . 85
6.2.1 First experiment - July 2016 . . . 85
6.2.2 Second experiment - August 2016 . . . 94

7 Neutron-deficient francium 101
7.1 Motivation . . . 101
7.1.1 Shape coexistence around $N = 104$ and $Z = 82$ . . . 101
7.1.2 Intruder states in odd-Z trans-lead elements . . . 102
7.1.3 Laser-spectroscopy studies of the intruder state . . . 103
7.2 Results . . . 105
7.2.1 Hyperfine A and B factors and isotope shifts . . . 105
7.2.2 Extraction of nuclear observables . . . 108

7.3 Discussion . . . 110
7.3.1 Spin of ^{203}Fr . . . 110
7.3.2 Spectroscopic quadrupole moments . . . 113
7.3.3 Evolution of quadrupole deformation in trans-lead elements below $N = 126$ . . . 114
7.3.4 Estimating the static component of the nuclear deformation 118
7.4 Outlook . . . 121
7.4.1 Feasibility of measuring ^{203m}Fr . . . 121
7.4.2 Search for ^{203m}Fr . . . 126

8 Neutron-rich radium **129**
8.1 Motivation . . . 129
8.1.1 Octupole deformation . . . 129
8.1.2 Atomic-parity violation . . . 130
8.2 Results . . . 132
8.2.1 High-resolution results . . . 132
8.2.2 Low-resolution results . . . 134
8.2.3 Isotope shifts . . . 136
8.2.4 Hyperfine A and B factors . . . 136
8.3 Extraction of nuclear observables . . . 138
8.3.1 Magnetic moments . . . 138
8.3.2 Spectroscopic electric quadrupole moments . . . 139
8.3.3 Change in mean-square charge radii . . . 139
8.4 Results and discussion . . . 142
8.4.1 Quadrupole moments . . . 142
8.4.2 Changes in mean-square charge radii . . . 145
8.4.3 Odd-even staggering . . . 147

9 Conclusions **151**

A Appendix **153**

Bibliography **157**

List of Figures

2.1 Schematic hyperfine splitting of two atomic states with $J = 1/2$ from coupling to a $I = 1/2$ nucleus. 25

3.1 Layout of the ISOLDE facility. Image is from Ref. [30]. 36
3.2 Schematic of a surface ion source at ISOLDE. Image courtesy of Ref. [32]. 37

4.1 Schematic of possible resonance-ionization routes. 42
4.2 Schematic of collinear laser spectroscopy using fluorescence detection. 46
4.3 Schematic of the collinear resonance ionization spectroscopy experiment 52

5.1 Schematic of a general ionization scheme. 56
5.2 Schematic of the lasers installed at CRIS. 57
5.3 Partial tuning curve for an ECD-X LBO crystal cut for 834 nm. . 59
5.4 Schematic detailing 3 mechanisms for an excited state to decay. . 60
5.5 Schematic overview of the continuous-wave light 'chopping' method. 62
5.6 Schematic of the wavemeters installed at CRIS. 69
5.7 Schematic of the separated-beams configuration frequency-tripling unit. 73
5.8 Picture of the separated-beams configuration of frequency-tripling unit. 74
5.9 Schematic of the linear configuration of frequency-tripling unit. . . 75
5.10 Picture of the linear configuration of frequency-tripling unit. . . . 76

6.1 Ionization scheme used in the francium experiment. 80
6.2 Example pulse shapes of 422-nm light after the dual Pockels cells setup. 82
6.3 Pulse shape used during the francium experiment. 83
6.4 Saturation curves of the transitions used in the francium experiment. 84
6.5 Initial populations of states in atomic radium after neutralization in a potassium vapour at a beam energy of 30 keV. 86
6.6 Initial and final populations of states in atomic barium after neutralization in a potassium vapour at a beam energy of 30 keV. . . 87
6.7 Ionic-radium ionization scheme used in the first radium experiment. 88

6.8 Atomic-radium ionization scheme used in the first radium experiment. 91
6.9 Scan of the 615-nm transition in ^{226}Ra. 92
6.10 Scan of the 783-nm transition in ^{226}Ra. 93
6.11 Atomic-radium ionization scheme used in the second radium experiment. 94
6.12 Scan of the PDL for ^{226}Ra. 96
6.13 Scan of the PDL for ^{226}Ra. 97

7.1 Proton configurations of ground and isomeric states in odd-Z elements around $Z = 82$. 103
7.2 Low-lying levels in even-N francium isotopes. 104
7.3 Example spectrum of the $7s\ ^2S_{1/2} \rightarrow 8p\ ^2P_{3/2}$ transition in ^{219}Fr. . 105
7.4 Centroid frequencies of ^{219}Fr reference scans during the experiment. 107
7.5 Example spectrum of the $7s\ ^2S_{1/2} \rightarrow 8p\ ^2P_{3/2}$ transition in ^{203}Fr. . 108
7.6 A-factor ratio analysis for ^{203}Fr. 111
7.7 Hyperfine anomaly in even-N francium isotopes below $N = 126$. . 112
7.8 Spectroscopic quadrupole moments of even-N francium isotopes below the $N = 126$ shell closure. 114
7.9 Normalized quadrupole moments of $\pi 1h^n_{9/2}$ states below $N = 126$. 115
7.10 Changes in mean-square charge radii of neutron-deficient francium and lead isotopes. 119
7.11 Calculated static and total deformation parameters for even-N francium isotopes below $N = 126$. 120
7.12 Isomer shifts in neutron-deficient odd-Z nuclei around $Z = 82$. . . 123
7.13 Predicted high-resolution hyperfine structure of ^{203}Fr. 125
7.14 Predicted low-resolution hyperfine structure of ^{203}Fr. 126
7.15 Isomer search data from the 2015 experiment. 127

8.1 An example of a high-resolution scan of the $7s^2\ ^1S_0 \rightarrow 7s7p\ ^3P_1$ transition in ^{226}Ra. 132
8.2 Centroid frequencies of high-resolution ^{226}Ra reference scans over the course of the experiment. 133
8.3 Reference-scan corrected Isotope shifts of high-resolution ^{231}Ra scans over the course of the experiment. 134
8.4 Example high-resolution spectrum of the $7s^2\ ^1S_0 \rightarrow 7s7p\ ^3P_1$ transition in ^{231}Ra. 135
8.5 Centroid frequencies of low-resolution ^{226}Ra reference scans taken during the experiment. 136
8.6 Example low-resolution spectrum of the $7s\ ^1S_0 \rightarrow 7s7p\ ^3P_1$ transition in ^{233}Ra. 137
8.7 King-plot analysis used to determine the atomic F and M factors for the 714-nm transition. 140
8.8 Spectroscopic and intrinsic quadrupole moments of odd-A neutron-rich radium isotopes. 143

8.9 Changes in mean-square charge radii of neutron-rich radium and francium isotopes. 146
8.10 Odd-even staggering parameter for neutron-rich radium and francium isotopes. 149

A.1 $A(7s\ ^2S_{1/2})$ of ^{219}Fr during the experiment. 153
A.2 $A(8p\ ^2P_{3/2})$ of ^{219}Fr during the experiment. 154
A.3 $B(8p\ ^2P_{3/2})$ of ^{219}Fr during the experiment. 154
A.4 Example spectrum of the $7s\ ^2S_{1/2} \rightarrow 8p\ ^2P_{3/2}$ transition in ^{207}Fr. . 155
A.5 Example spectrum of the $7s\ ^2S_{1/2} \rightarrow 8p\ ^2P_{3/2}$ transition in ^{221}Fr. . 155

List of Tables

6.1 Laser setup for the francium experiment. 80
6.2 Laser setup for the ionic-radium experiment. 89
6.3 Laser setup for the atomic-radium experiment. 91
6.4 Count rates with different lasers blocked. 92
6.5 Laser setup for the second radium experiment. 95
6.6 Measured centroid frequencies of transitions in ^{226}Ra. 98
6.7 Signal, background and signal-to-background ratios for different schemes. 99

7.1 Hyperfine A and B factors and isotope shifts of ^{203,207,219,221}Fr. . . 107
7.2 Spins, magnetic dipole moments, spectroscopic electric quadrupole moments and changes in the mean-square charge radii of ^{203,207,219,221}Fr. 110
7.3 Intrinsic quadrupole moments, calculated static and total deformation parameters and the static deformation ratios of even-N francium isotopes below $N = 126$. 118
7.4 Estimated Isomer shift ranges for ^{203m}Fr. 124
7.5 Estimated $A(7s^2S_{1/2})$ for ^{203m}Fr. 124
7.6 Isomer hunt data from 2015 experiment. 127

8.1 Isotope shifts of neutron-rich radium isotopes for the $7s^2\ ^1S_0 \rightarrow 7s7p\ ^3P_1$ transition. 137
8.2 Hyperfine A and B factors of the $7s7p\ ^3P_1$ state in neutron-rich odd-A radium isotopes. 138
8.3 Electromagnetic moments of neutron-rich odd-A radium isotopes. 142
8.4 Changes in mean-square charge radii of neutron-rich radium isotopes. 146

Abstract

Two experimental campaigns were performed at the Collinear Resonance Ionization Spectroscopy (CRIS) experiment, located at the ISOLDE radioactive-beam facility.

The spectroscopic quadrupole moment of ^{203}Fr was measured. Its magnitude with respect to the other even-N francium isotopes below $N = 126$ suggests an onset of static deformation. However, calculations of the static and total deformation parameters reveal that it cannot be considered as purely statically deformed.

The neutron-rich radium isotopes were investigated. The spectroscopic quadrupole moment of ^{231}Ra was measured and the continuation of increasing quadrupole deformation with neutron number in neutron-rich radium isotopes was further established. Measurements of the changes in mean-square charge radii of ^{231,233}Ra allowed the odd-even staggering parameter to be calculated for $^{230-232}$Ra. A normal odd-even staggering which increases in magnitude with neutron number was observed in these isotopes.

Declaration of Authorship

I, Shane Wilkins, confirm that no portion of the work referred to in the thesis has been submitted in support of an application for another degree or qualification of this or any other university or other institute of learning.

Copyright Statement

i. The author of this thesis (including any appendices and/or schedules to this thesis) owns certain copyright or related rights in it (the "Copyright") and s/he has given The University of Manchester certain rights to use such Copyright, including for administrative purposes.

ii. Copies of this thesis, either in full or in extracts and whether in hard or electronic copy, may be made **only** in accordance with the Copyright, Designs and Patents Act 1988 (as amended) and regulations issued under it or, where appropriate, in accordance with licensing agreements which the University has from time to time. This page must form part of any such copies made.

iii. The ownership of certain Copyright, patents, designs, trade marks and other intellectual property (the "Intellectual Property") and any reproductions of copyright works in the thesis, for example graphs and tables ("Reproductions"), which may be described in this thesis, may not be owned by the author and may be owned by third parties. Such Intellectual Property and Reproductions cannot and must not be made available for use without the prior written permission of the owner(s) of the relevant Intellectual Property and/or Reproductions.

iv. Further information on the conditions under which disclosure, publication and commercialisation of this thesis, the Copyright and any Intellectual Property and/or Reproductions described in it may take place is available in the University IP Policy (see `http://documents.manchester.ac.uk/DocuInfo.aspx?DocID=24420`), in any relevant Thesis restriction declarations deposited in the University Library, The University Library's regulations (see `http://www.library.manchester.ac.uk/about/regulations/`) and in The University's policy on Presentation of Theses

Acknowledgements

Studying towards my PhD over the past three years has been an immensely rewarding and enjoyable experience. I have been fortunate to travel to lots of great places and work with many talented people, some of which I'd like to mention here.

First and foremost, I would like to thank my supervisor, Kieran, for giving me the opportunity to work on this project and for your continued support and guidance throughout.

Secondly, I would like to thank Kara for the unquantifiable amount of help, advice and support you have given me throughout my studies and for the many proofreads of this thesis.

I would also like to thank Adam, Agi, Cory, Greg, Ronald, Ruben, Wouter and Xiaofei for making lab work at CRIS so much fun and for making all of this possible.

To Professors Jon Billowes, Gerda Neyens and Thomas Cocolios, thank you for providing constructive feedback and physics insight for my abstracts and papers.

I would also like to thank the ISOLDE community for providing a friendly and welcoming environment to work in. In particular, thanks to the Building 508 lunch crew for the stimulating and wide-ranging lunchtime conversations.

And finally, I'd like to thank my family for your continued support and encouragement.

Chapter 1

Introduction

The field of nuclear physics centres on studying the ensemble of protons and neutrons at the heart of atoms. Each nucleus is defined by its number of protons, Z, and number of neutrons, N. To date, over 3,000 isotopes have been discovered and yet around 7,000 are predicted to exist [1]. Of these, just 253 are stable and do not radioactively decay. 33 more exist with half-lives comparable to the age of the Earth. These stable nuclei form the valley of stability on the nuclear chart. Either side of this valley lie the regions of radioactive nuclei bordered by the proton and neutron driplines.

Studying radioactive nuclei presents significant experimental and theoretical challenges. Radioactive nuclei can only be produced in minute quantities and are often short-lived, requiring ultra-sensitive techniques to study them experimentally. For all but the lightest nuclei, exact calculations of their structure cannot be performed. The description of heavier systems rapidly becomes more and more complex as the dimensionality of the nuclear many-body problem exponentiates.

Laser spectroscopy of radioactive nuclei has proven a powerful experimental tool in the study of their nuclear structure. By measuring the influence of the nucleus on the electrons that are bound to it, precise measurements of nuclear ground- and isomeric states can be obtained. The nuclear-model independence and precision

of such measurements provide stringent tests for modern state-of-the-art nuclear-structure theory.

1.1 This work

This thesis presents results from laser-spectroscopy experiments on neutron-deficient francium and neutron-rich radium isotopes. The experiments were performed at the Collinear Resonance Ionization Spectroscopy (CRIS) experiment, located at the ISOLDE radioactive-beam facility. Chapter 2 describes how the properties of the atomic nucleus can be studied by measuring the hyperfine structure, with an emphasis of how information on the size and shape of the nucleus may be obtained. Chapter 3 briefly outlines how radioactive ion-beams are produced at the ISOLDE facility. Chapter 4 describes two common laser-spectroscopy approaches used to study radioactive nuclei and how these are combined to form the technique that was used for this work. Chapter 5 details the laser requirements for performing CRIS and presents technical developments used to extend the applicability of the technique. Chapter 6 describes the setups and developments for the two experimental campaigns. Chapter 7 presents results of the experiment on neutron-deficient francium isotopes. Chapter 8 presents results of experiments on the neutron-rich radium isotopes. Chapter 9 summarizes the nuclear-structure physics results presented in this thesis.

Chapter 2

The hyperfine structure as a probe of the atomic nucleus

2.1 The hyperfine structure

The coupling of the nuclear spin, I, and atomic spin, J, leads to the quantum number, F. In absence of nuclear electromagnetic moments, these F states are degenerate. However, non-zero nuclear electromagnetic moments cause the hyperfine interaction between the nucleus and the electrons that are bound to it. This interaction causes perturbations to the electronic fine structure, resulting in the hyperfine structure.

The hyperfine interaction is precisely known through quantum electrodynamics [2, 3]. The details of the interaction depends on nuclear properties such as the spin, magnetic dipole moment, electric quadrupole moment and charge radius. Therefore, by measuring the hyperfine structure of an isotope, information about the atomic nucleus can be extracted in a nuclear model-independent way.

Hyperfine levels are identified by the quantum number, F, obtained by the vector summation of I and J,

$$\mathbf{F} = \mathbf{I} + \mathbf{J}. \tag{2.1}$$

The perturbation of each hyperfine F state is given by [4]

$$\frac{\Delta E}{h} = \frac{K}{2}A + \frac{3K(K+1) - 4I(I+1)J(J+1)}{8I(2I-1)J(2J-1)}B, \tag{2.2}$$

where $K = F(F+1) - I(I+1) - J(J+1)$. A and B are the hyperfine factors defined as

$$A = \frac{\mu_I B_e(0)}{IJ}, \tag{2.3}$$

$$B = eQ_s\langle\frac{\partial^2 V_e}{\partial z^2}\rangle. \tag{2.4}$$

The terms containing A and B in Equation 2.2 show how the nuclear magnetic dipole moment, μ_I, and electric quadrupole moment, Q_s, affect the perturbation of the hyperfine F states, respectively.

Equation 2.3 shows how nuclear magnetic dipole moments are related to the hyperfine A factor, where $B_e(0)$ is the magnetic field generated by the orbiting electrons within the nuclear volume. Equation 2.4 describes the relation between the hyperfine B factor and the nuclear spectroscopic electric quadrupole moment, where $\langle\frac{\partial^2 V_e}{\partial z^2}\rangle$ is the electric-field gradient at the nucleus produced by the orbiting electrons.

Electric dipole transitions between the initial F state, F_i, and final F state, F_f, can occur if the following condition is satisfied:

$$\Delta F = F_f - F_i = 0, \pm 1. \tag{2.5}$$

Transitions where $\Delta F = 0$ are only allowed when $F_i, F_f \neq 0$. Figure 2.1 shows an example of the hyperfine splitting of two atomic states with $J = 1/2$ from coupling to a $I = 1/2$ nucleus.

The frequency, γ, of an allowed transition between F states is given by

$$\gamma = \nu + \alpha_u A_u + \beta_u B_u - \alpha_l A_l - \beta_l B_l, \tag{2.6}$$

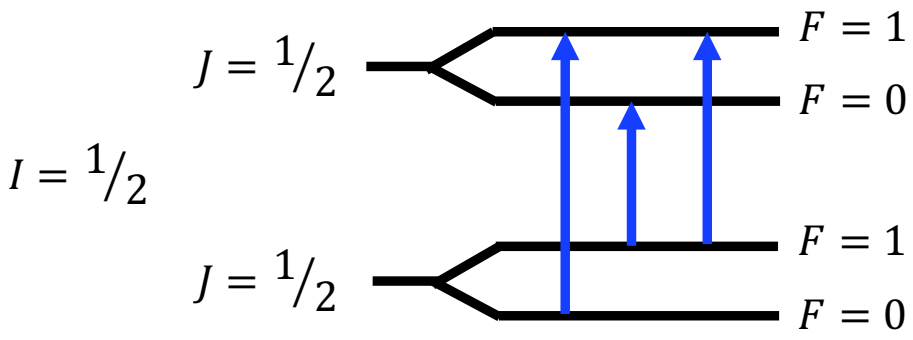

FIGURE 2.1: Schematic hyperfine splitting of two atomic states with $J = 1/2$ from coupling to a spin $I = 1/2$ nucleus.

where ν is the centroid frequency and α, β are equal to

$$\alpha = \frac{K}{2}, \tag{2.7}$$

$$\beta = \frac{3K(K+1) - 4I(I+1)J(J+1)}{8I(2I-1)J(2J-1)} \tag{2.8}$$

respectively. Hyperfine spectra can be fitted using a χ^2-minimization routine to determine the centroid frequency, ν, and the hyperfine factors, $A_{u,l}$ and $B_{u,l}$. The nuclear spin, I, can also be determined through a χ^2-hypothesis test.

2.2 Extraction of nuclear electromagnetic moments

2.2.1 Magnetic dipole moment

Isotopes with a non-zero spin will possess a magnetic dipole moment. This influences the hyperfine structure of atomic states with $J > 0$. Once the hyperfine A factor of a given isotope has been determined through fitting of its hyperfine

structure, the magnetic dipole moment can be extracted. It is possible to extract the magnetic dipole moment directly using Equation 2.3. However, doing so relies upon calculations of $B_e(0)$, introducing atomic-model dependence. By taking the ratio of Equation 2.3 for any two isotopes of the same element, the atomic dependencies, J and $B_e(0)$, disappear.

In the absence of the hyperfine anomaly (see Section 2.2.1.1), the ratio, $\frac{\mu}{IA}$, is constant for all isotopes of a given element. The magnetic moment can be determined against a reference isotope for which μ, A, and I are already known. This is done using the following equation:

$$\mu = \mu_{ref} \frac{IA}{I_{ref} A_{ref}}. \tag{2.9}$$

For elements for which a stable (or quasi-stable) isotope exists, nuclear magnetic moments can be determined very precisely via techniques such nuclear magnetic resonance spectroscopy (NMR). In such elements, the magnetic moment of the unstable isotopes can often be determined to a similar precision with the reference values dominating the overall uncertainty. In other cases, the quality of the experimental data limits the precision on the extracted magnetic moments.

2.2.1.1 Hyperfine anomaly

Equation 2.3 assumes a point nucleus. However, the hyperfine interaction is sensitive to the finite size and magnetization of the nuclear volume. The Breit-Rosenthal-Crawford-Schawlow correction accounts for the modification of electron wave functions due to the extended nuclear charge distribution [5–8]. The Bohr-Weisskopf effect accounts for the extended nuclear magnetization [9]. The hyperfine factor, A, is modified by these two effects so that Equation 2.9 can be rewritten as

$$\mu = \mu_{ref} \frac{IA}{I_{ref} A_{ref}} (1 + \Delta), \tag{2.10}$$

where $\Delta \approx \epsilon - \epsilon_{ref}$. The effect is largest for electrons occupying states with the highest spatial overlap with the nucleus ($s_{1/2}$ and relativistic-$p_{1/2}$ electrons).

However, other electron states may contain contributions to their wavefunction from like s or p states due to the electron-electron interaction [10].

The hyperfine anomaly is a negligible effect in most nuclei. However, it is of relevance for weak-interaction studies using heavy atoms/ions, for example atomic-parity violation measurements. These studies require precise knowledge of both the nuclear and atomic wavefunctions. The nuclear magnetic dipole moment is an important property for describing the nucleus (see Section 8.1.2). As the hyperfine anomaly alters the extraction of the magnetic moment, it must be understood and accounted for to reach the precision required for weak-interaction studies [11].

2.2.2 Spectroscopic electric quadrupole moment

Isotopes with $I > 1/2$ will have a non-zero electric quadrupole moment that will influence the hyperfine structure of atomic states possessing $J > 1/2$. The spectroscopic electric quadrupole moment can be determined directly using Equation 2.4. This requires calculation of the electric-field gradient, $\langle \frac{\partial^2 V_e}{\partial z^2} \rangle$. To avoid this, the spectroscopic electric quadrupole moment is extracted in a similar fashion to the magnetic dipole moment. The ratio, B/Q_s, is the same for all isotopes of a given element. If there exists an isotope of a given element where the spectroscopic quadrupole moment is known, the spectroscopic quadrupole moment of the element's other isotopes can be determined by

$$Q_s = Q_{s,ref} \frac{B}{B_{ref}}. \tag{2.11}$$

The quadrupole moment is a measure of how the nuclear charge distribution deviates from sphericity, which allows the static deformation of nuclei to be directly studied [12]. A positive quadrupole moment indicates a prolate-deformed spheroid (elongated along its symmetry axis). A negative quadrupole moment indicates an oblate-deformed spheroid (compressed along its symmetry axis).

2.3 Isotope shift

The isotope shift, $\delta\nu^{A,A'}$, is the difference between the hyperfine-structure centroids of two isotopes, A and A', and is defined as

$$\delta\nu^{A,A'} = \nu^{A'} - \nu^{A}, \tag{2.12}$$

where ν^{A} and $\nu^{A'}$ are the centroid frequencies for isotopes A and A', respectively. The isotope shift can be decomposed into two terms: the mass shift and the field shift

$$\delta\nu^{A,A'} = \nu_{MS}^{A,A'} + \nu_{FS}^{A,A'}. \tag{2.13}$$

2.3.1 Mass shift

The mass-shift term, $\nu_{MS}^{A,A'}$, in Equation 2.13 is caused by the recoil of a nucleus with a finite mass. This can be written as

$$\nu_{MS}^{A,A'} = M\frac{A' - A}{AA'}, \tag{2.14}$$

where M is the mass-shift factor for a given atomic transition. The mass-shift factor can be written as

$$M = k^{NMS} + k^{SMS} \tag{2.15}$$

where k^{NMS} and k^{SMS} are the normal mass-shift and specific mass-shift constants, respectively. The normal mass-shift constant is given as

$$k^{NMS} = \nu_0 m_e \tag{2.16}$$

where ν_0 is the transition frequency and m_e is the mass of the electron (in amu). The specific mass-shift constant is defined as the expectation value of the

$$\sum_{i<j} \frac{\mathbf{p}_i \cdot \mathbf{p}_j}{M_0} \tag{2.17}$$

operator where M_0 is the mass of the nucleus. This is challenging to determine as it involves calculating two-body interactions between electron momenta [13]. In Equation 2.14, the mass-shift constant is multiplied by $\frac{A'-A}{AA'}$ and therefore the contribution of the mass shift to the total isotope shift decreases for heavier systems.

2.3.2 Field shift

The field shift, $\nu_{FS}^{A,A'}$, is caused by the modification of the charge distribution within the nucleus. This change affects the Coulomb interaction between the nucleus and electrons. By assuming the electron density remains constant over the nuclear volume, the change in electron energy levels can be shown to equal the nuclear mean-square charge radius, $\langle r^2 \rangle$. This is defined as

$$\langle r^2 \rangle = \frac{\int_0^\infty \rho(\mathbf{r}) r^2 dV}{\int_0^\infty \rho(\mathbf{r}) dV}. \tag{2.18}$$

The field shift has been shown to be solely dependent on changes in the mean-square charge radius [14] and can be given by

$$\nu_{FS}^{A,A'} = \frac{Ze^2}{6h\epsilon_0} \Delta|\psi(0)|^2 \delta\langle r^2 \rangle^{A,A'}, \tag{2.19}$$

where $\Delta|\psi(0)|^2$ is the change in the probability density function of electrons. A consequence of the $\Delta|\psi(0)|^2$ term in Equation 2.19 is that transitions involving s-state electrons have a higher sensitivity to changes in the mean-square charge radius, $\delta\langle r^2 \rangle^{A,A'}$. This is due to their increased spatial overlap within the nuclear volume.

2.4 Changes in the mean-square charge radii

The isotope shift can be written as

$$\delta\nu^{A,A'} = M\frac{A'-A}{AA'} + F\delta\langle r^2\rangle^{A,A'}, \tag{2.20}$$

allowing the nuclear ($\frac{A'-A}{AA'}$ and $\delta\langle r^2\rangle^{A,A'}$) and atomic ($M$ and F) dependencies of the quantity to be separated. Rearranging Equation 2.20 allows the change in the mean-square charge radii between isotopes A and A' to be determined using

$$\delta\langle r^2\rangle^{A,A'} = \frac{1}{F}\left(\delta\nu^{A,A'} - \frac{A'-A}{AA'}M\right), \tag{2.21}$$

if the atomic F and M factors are known. For elements with more than 2 stable isotopes, the atomic F and M factors can be determined using charge radii measurements from muonic x-ray or electron-scattering experiments. Otherwise, calculations utilizing atomic theory must be used, introducing atomic-model dependence to the extraction of the changes in mean-square charge radii.

2.4.1 King-plot method

If the atomic F and M factors are known for a transition in a given element, the atomic factors for other transitions in that element can be obtained using the King-plot method [15]. This method can be used if at least 3 different isotopes have been measured using both transitions. By multiplying Equation 2.21 for both transitions, (denoted by subscripts 1 and 2) by the mass-modification factor,

$$\mu^{A,A'} = \frac{AA'}{A'-A}, \tag{2.22}$$

the following is obtained,

$$\mu^{A,A'}\delta\nu_1^{A,A'} = M_1 + \mu^{A,A'}F_1\delta\langle r^2\rangle^{A,A'}, \tag{2.23}$$

$$\mu^{A,A'}\delta\nu_2^{A,A'} = M_2 + \mu^{A,A'}F_2\delta\langle r^2\rangle^{A,A'}. \tag{2.24}$$

The common factor of $\mu^{A,A'}\delta\langle r^2\rangle^{A,A'}$ can be eliminated and rearranged to give a linear relationship between $\mu^{A,A'}\delta\nu_2^{A,A'}$ and $\mu^{A,A'}\delta\nu_1^{A,A'}$,

$$\mu^{A,A'}\delta\nu_2^{A,A'} = \frac{F_2}{F_1}\mu^{A,A'}\delta\nu_1^{A,A'} + M_2 - \frac{F_2}{F_1}M_1. \tag{2.25}$$

Plotting $\mu^{A,A'}\delta\nu_2^{A,A'}$ against $\mu^{A,A'}\delta\nu_1^{A,A'}$ gives a straight line with a gradient of F_2/F_1 and intercept of $M_2 - (F_2/F_1)M_1$. This allows the atomic factors, F_2 and M_2, to be evaluated from the known factors, F_1 and M_1. This therefore enables the changes in mean-square charge radii to be extracted from isotope-shift measurements from a different transition.

2.5 Nuclear shapes and deformation

2.5.1 Parametrization of nuclear shape

The nuclear shape is commonly parametrized in terms of a spherical-harmonic (multipole) expansion [16, 17]

$$R(\theta,\phi) = c(\alpha_{\lambda\mu})R_0\left(1 + \sum_{\lambda=0}^{\infty}\sum_{\mu=-\lambda}^{\lambda}\alpha_{\lambda\mu}Y_{\lambda\mu}(\theta,\phi)\right), \tag{2.26}$$

The factor, $c(\alpha_{\lambda\mu})$, ensures volume conservation and $R_0 = r_0A^{1/3}$. The standard deformation parameters are given by $\alpha_{\lambda\mu}$. By fixing the centre-of-mass to be the same as the origin of the body-fixed frame, the parameters with $\lambda = 0, 1$ become zero, leaving only terms with $\lambda \geq 2$. These can be reduced further assuming the deformation is axially symmetric so that of these, only the parameters with $\mu = 0$ remain. This gives

$$R(\theta) = c(\beta_\lambda)R_0\left(1 + \sum_{\lambda=2}^{\infty}\sqrt{\frac{2\lambda+1}{4\pi}}\beta_\lambda P_{\lambda 0}(\cos(\theta))\right), \tag{2.27}$$

where

$$\beta_\lambda = \alpha_{\lambda 0}, \lambda \geq 2. \tag{2.28}$$

The nuclear distribution can be approximated to an expansion in terms of β_λ. The nuclear multipole moments, Q_λ, measured through different experimental techniques, can be related to the deformation parameters β_λ allowing information on the nuclear size and shape to be obtained.

2.5.2 Estimating the nature of deformation of the nucleus

2.5.2.1 Static deformation

The spectroscopic quadrupole moment, Q_s, provides a measure of the time-averaged static nuclear deformation. This can be related to the intrinsic quadrupole moment, Q_0, by

$$Q_0 = \frac{(I+1)(2I+3)}{3\Omega^2 - I(I+1)} Q_s, \tag{2.29}$$

where Ω is the projection of the nuclear spin on the axis of deformation. In the strong-coupling limit, the projection is set so that $\Omega = I$, giving

$$Q_0 = \frac{(I+1)(2I+3)}{I(2I-1)} Q_s. \tag{2.30}$$

This assumption is considered valid for strongly-deformed nuclei. The Coriolis interaction modifies the projection, Ω, by admixing different Ω values. The magnitude of this interaction decreases with increasing deformation and increasing I [18].

The intrinsic quadrupole moment is related to the static deformation parameter, $\langle\beta_2\rangle$, by

$$Q_0 \approx \frac{5Z\langle r^2\rangle_{sph}}{\sqrt{5\pi}} \langle\beta_2\rangle(1 + 0.36\langle\beta_2\rangle), \tag{2.31}$$

where $\langle r^2\rangle_{sph}$ is the radius of a spherical nucleus calculated by the liquid-droplet model [19, 20]. Alternatively, $\langle r^2\rangle_{sph}$ can be given as $\frac{3}{5}R^2$ with $R = r_0 A^{1/3}$ to give

$$Q_0 \approx \frac{3ZR^2}{\sqrt{5\pi}} \langle\beta_2\rangle(1 + 0.36\langle\beta_2\rangle). \tag{2.32}$$

2.5.2.2 Total deformation

The total deformation, $\langle\beta_2^2\rangle^{1/2}$, of the nucleus can be broken down into static and dynamic components,

$$\langle\beta_2^2\rangle = \langle\beta_2\rangle^2 + (\langle\beta_2^2\rangle - \langle\beta_2\rangle^2) = \langle\beta_2\rangle^2 + \beta_{dyn}^2, \tag{2.33}$$

where $\langle\beta_2\rangle^2$ is the square of the static deformation parameter described previously and β_{dyn}^2 is the dynamic contribution to the total deformation.

The mean-square charge radius can be related to the total nuclear deformation by

$$\langle r^2\rangle = \langle r^2\rangle_{sph}\left(1 + \frac{5}{4\pi}\sum_{\lambda=2}^{\infty}\langle\beta_\lambda^2\rangle\right). \tag{2.34}$$

In most cases, the quadrupole deformation term ($\lambda = 2$ term) dominates. By only taking this term, the expression in Equation 2.34 becomes

$$\langle r^2\rangle = \langle r^2\rangle_{sph}\left(1 + \frac{5}{4\pi}\langle\beta_2^2\rangle\right) \tag{2.35}$$

As the total deformation in Equation 2.35 is squared, information on the sign of the deformation is lost. This means only the magnitude of the total deformation can be calculated and not whether it is prolate or oblate in nature. The total deformation parameter will now be defined as $\langle\beta_2^2\rangle^{1/2} \equiv \beta_2^{rms}$ for the remainder of the discussion and throughout this thesis.

The total deformation, β_2^{rms}, can be calculated by comparing changes in the mean-square charge radii to predictions from theoretical models. The most commonly used is the liquid-droplet model [21]. To perform this, the liquid-droplet model is commonly used to calculate lines of different deformation parameters for an isotope chain. The relative positions of these 'iso-deformation' lines are fixed to an isotope for which the total deformation, β_2^{rms}, is known. This can be calculated from energies of first-excited 2^+ states and $B(\mathrm{E2})\uparrow$ transition probabilities of even-even nuclei [22]. This approach allows the total deformation of nuclei to be

quantified, albeit with some nuclear-model dependence. Generally, a nucleus is considered deformed once its total deformation parameter, β_2^{rms}, exceeds 0.1.

Applying this approach to measurements of the changes in mean-square charge radii across an isotope chain allows the often dramatic evolution of nuclear deformation across major shells to be charted [23, 24].

2.5.2.3 Ratio of deformation parameters

Once the static and total deformation parameters have been calculated for a nucleus, the ratio of their magnitudes may be taken to give insight to the nature of nuclear deformation. For purely statically-deformed nuclei, the static deformation ratio, defined as

$$R_{stat} = \frac{|\langle\beta_2\rangle|}{\beta_2^{rms}} \tag{2.36}$$

approaches unity.

Chapter 3

Production of radioactive nuclei

3.1 The ISOLDE facility

The Isotope Separation On-Line Device (ISOLDE) facility [25–27] is located at CERN, Geneva. The first beams at this facility were delivered in 1967 allowing measurements on the decay of short-lived isotopes of a variety of elements [28]. Today, beams of over 1300 isotopes [29] of 75 elements can be produced with production yields ranging from 10^{-1} s^{-1} to 10^{11} s^{-1}. The layout of the facility is shown in Figure 3.1.

The facility serves a large community of users working in many fields, encompassing many areas of nuclear, solid-state and medical physics. A recent overview of the facility with selected research highlights can be found in Ref. [25].

3.1.1 Radioactive-ion-beam production at ISOLDE

Radioactive-ion beams at ISOLDE are produced using the isotope-separation on-line (ISOL) method. In this approach, thick targets are bombarded by light ions. In the case of ISOLDE, protons are used. The reaction products are stopped within the target material before being extracted, mass separated and delivered to experiments.

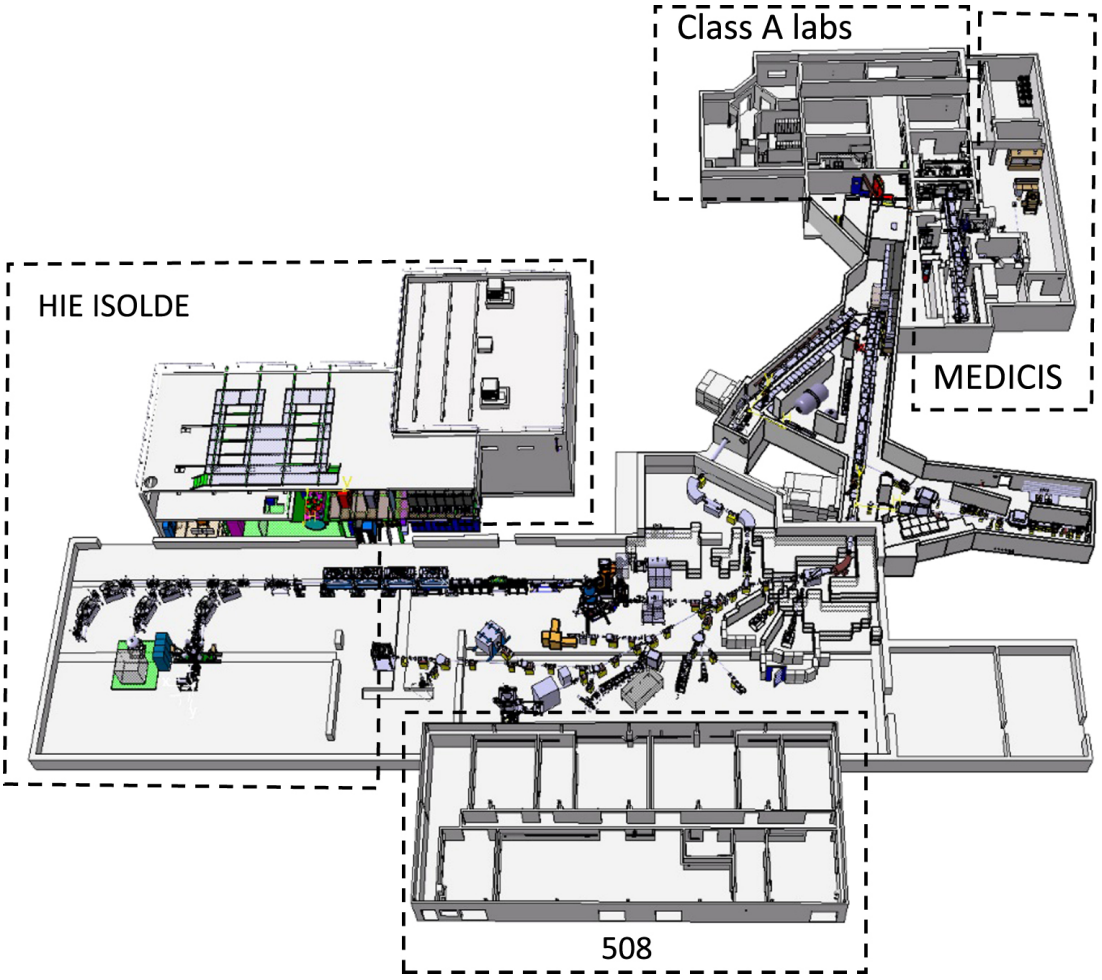

FIGURE 3.1: Layout of the ISOLDE facility. Image is from Ref. [30].

At ISOLDE, pulses of 1.4-GeV protons with average intensities of up to 2 μA are impinged upon a thick target. Each pulse contains around 10^{13} protons and is produced by the Proton Synchrotron Booster (PSB). Each pulse is separated in time by 1.2 s and forms part of the proton super cycle. The ISOLDE facility uses over 50% of the protons produced by the CERN accelerator complex.

Radioactive isotopes are produced via spallation, fission and fragmentation reactions within the target material. The reaction products are stopped within the target material where they effuse and diffuse out of the target. The target is usually heated to temperatures in excess of 2000 K to reduce the release time of species produced within it. The reaction products enter a metal transfer line, 34 mm in length with an inner diameter of 3 mm [31], where they are ionized. The chemical properties of the elements being studied dictates the ionization

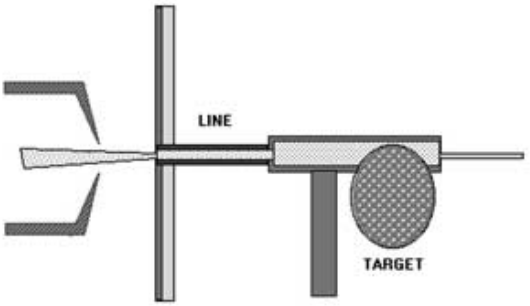

FIGURE 3.2: Schematic of a surface ion source at ISOLDE. Image courtesy of Ref. [32].

mechanism used to extract them.

The use of thick targets has both advantages and disadvantages for the production of radioactive nuclei using the ISOL method. The thickness of the target greatly improves the number of interactions between it and the incident light-ion beam. Stopped reaction products within the target must effuse and diffuse out before they can be ionized and extracted. This means that only isotopes with half-lives greater than a few ms may be produced. Furthermore, certain species produced within the target react with the target material before they escape. This introduces a chemical dependence to the process, rendering the production of certain elements with the ISOL technique extremely difficult.

3.1.1.1 Methods of ionization

Elements with a low ionization potential, for example the alkali metals, can surface ionize through collisions with the transfer line. Figure 3.2 shows a schematic of the surface ion source. To achieve a high surface-ionization efficiency, the transfer line is constructed from a material possessing a high work function and heated to >2000 K. The high operating temperatures necessitate the material also has a high melting point. Surface-ionizable elements are often the main sources of contamination in delivered beams.

Elements with a high ionization potential, such as the noble gas elements, are extracted through plasma ionization.

The most commonly used method of ionization involves the process of resonance ionization (see Section 4.1). In this process, isotopes of a particular element are selectively ionized through stepwise excitation and subsequent ionization using lasers. The lasers are tuned to excite specific transitions that constitute the atomic 'fingerprint' of a given element. Due to its high degree of selectivity and efficiency (see Section 4.1.0.3), the Resonance Ionization Laser Ion Source (RILIS) is the most requested target ion-source by users, providing more than 70 % of delivered beam time in recent years [33–35]. The transfer line of the laser ion source is constructed from a material with a low work function to suppress surface-ionized contamination.

In certain mass regions, surface-ionized contamination can overwhelm laser-ionized beams. New ion-source types have been developed to address this and suppress the surface-ionized contamination, for example the Laser Ion Source and Trap (LIST) [36, 37] and the Versatile Arc Discharge and Laser Ion Source (VADLIS) [31, 38].

3.1.1.2 Mass separation

There are two target stations at the ISOLDE facility, each with its own mass separator. Once ionized, the isotopes of interest are accelerated to energy of between 30-60 keV and mass separated. The general-purpose separator (GPS), consists of a single magnet with a bending radius and angle of 1.5 m and 70^o. Its mass-resolving power, $m/\delta m$, is approximately 800 [30]. In addition to delivering a primary beam, the GPS has two beam lines that are able to simultaneously extract secondary beams with a mass of up to $\pm 13\%$ of the primary beam mass [30].

The high-resolution separator (HRS), consists of 2 magnets both possessing a bending radius of 1 m. The beam is first steered by a magnet with a bending angle of 90^o and then steered through 60^o by the second magnet. The resolution of each magnet of the HRS has been measured at approximately 6000 [30]. A

radio-frequency quadrupole cooler-buncher, ISCOOL [39], is located after HRS for cooling and bunching of the ion beam (see Section 4.3.1).

3.2 Other facilties and methods

There are numerous radioactive ion-beam facilities currently in operation around the world. Many next-generation facilities are under construction, designed to eventually provide intense beams of exotic nuclei that are currently inaccessible to today's user communities.

Some of these facilities utilise the ISOL method, for example, the TRIUMF-ISAC facility [40, 41], Canada and the SPIRAL facility [42], located at GANIL [43], France. Future facilities such as SPIRAL2 at GANIL, SPES at INFN, Italy [44], ARIEL at TRIUMF and EURISOL [45] will also utilize the ISOL method.

A variation on the ISOL method, employed at the IGISOL facility, Finland (and previously LISOL, Belgium) impacts an ion beam onto a thin target situated in a gas cell [46]. The reaction products are caught in the buffer gas and thermalize through collisions with it. The products are carried out of the cell by the continuous flow of the buffer gas. Ions leaving the cell are caught by an ion guide and delivered to experiments. Atoms leaving the cell must be ionized to be guided to experiments. The use of a thin target in this approach provides advantages when compared to the thick-target ISOL method. The first is that shorter-lived isotopes can be produced for study. Furthermore, there is a much smaller variation in the extraction efficiency of different elements. This allows many elements that cannot be extracted at thick-target ISOL facilities to be delivered to experiments.

Another well-established method used in producing radioactive ion-beams is the in-flight separation technique. In this approach, a high-energy heavy-ion beam is impacted upon a thin target. The kinematics of the reaction produces fragments that are emitted in the forward direction with a similar kinetic energy to the incident beam. The use of a thin target also ensures the momentum distribution

of the produced fragments is narrow. A momentum-selective spectrometer can be used to select fragments with the desired momentum before delivering to experiments.

The in-flight separation technique allows beams of nuclei with shorter half-lives to be produced when compared to the ISOL technique. The high beam energies also allow nuclear reaction experiments without the need of post-acceleration. The major limitation of this method is that the poor quality of produced beams, making them unsuitable for precision experiments. However, advances in beam cooling have allowed precision experiments to be performed at facilities utilizing the in-flight separation technique. For example, the SHIPTRAP facility [47, 48] at GSI, Germany and the BECOLA facility [49, 50] at NSCL, USA.

The in-flight separation method is used at the FRS at GSI, Germany, LISE-3 facility at GANIL, NSCL in the USA and RIBF at RIKEN [51], Japan. Future facilities that will utilise the method include the FAIR facility at GSI [52], Germany and FRIB at NSCL [53, 54], USA.

Chapter 4

Laser spectroscopy of radioactive nuclei

Collinear resonance ionization spectroscopy (CRIS) combines two well-established laser spectroscopy techniques: collinear laser spectroscopy and resonance ionization spectroscopy. These two techniques will be described here.

4.1 Resonance ionization spectroscopy

Resonance ionization involves stepwise exciting an atomic system and subsequently ionizing it using laser light. In this approach, atoms from the ground state or a thermally-populated metastable state are resonantly excited to a higher-lying excited state. They are then either non-resonantly ionized via a single photon (denoted by Scenario 1 in Figure 4.1) or further excited to a high-lying Rydberg state (for field or collisional ionization) (Scenario 2) or to an auto-ionizing state (Scenario 3).

To saturate the ionization process, the photon flux, F, exciting the atom from the excited state must be larger than the depopulation rate to dark states, β_{dark}, such that

$$\sigma_i F \gg \beta_{dark} \tag{4.1}$$

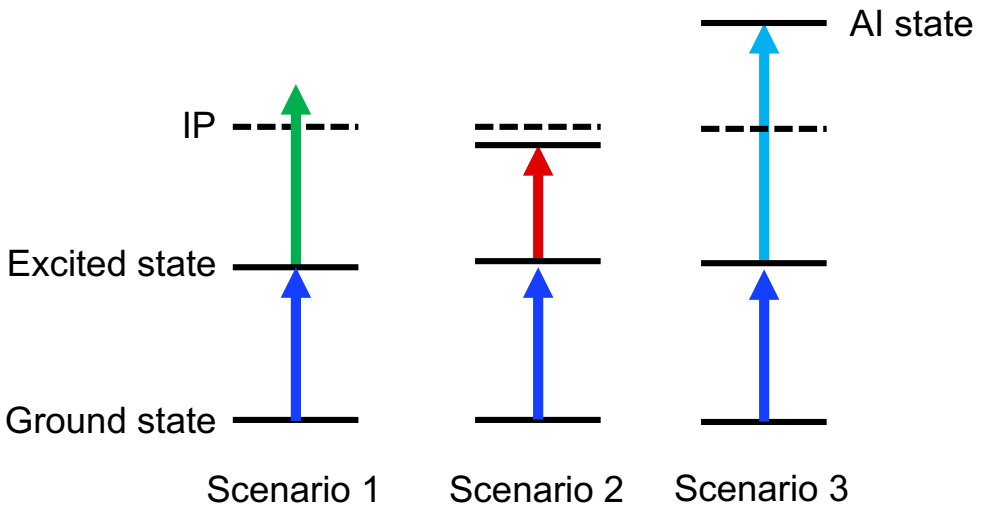

FIGURE 4.1: Schematic of possible resonance-ionization routes.

where σ_i is cross-section for the ionization process from the excited state. This is known as the flux condition. The fluence condition is defined as

$$\frac{\sigma_I \psi g_2}{g_1 + g_2} \gg 1, \tag{4.2}$$

where ψ is the photon fluence and g_1, g_2 are the statistical weights of the ground- and excited state. If the flux and fluence conditions are satisfied, the process is saturated and the entire atomic ensemble interacting with the laser light will be resonantly ionized. These two conditions determine the required photon densities and therefore the type of laser system required to saturate the ionization process. Using typical values of $\sigma_I = 10^{-17}$ cm^2 for a non-resonant final step and $\beta = 10^6 - 10^7$ s^{-1} gives $F \gg 10^{23}$ cm^{-2}s^{-1}. This photon flux is difficult to achieve with a continuous-wave laser, even when tightly focused. Pulsed laser systems with pulse durations of tens of ns, can achieve this with a modest pulse energy.

A key feature of the resonance ionization process is its high selectivity. Elemental, isotopic and even isomeric selectivity can be achieved through multi-step resonance ionization. The selectivity, S, of a single resonant excitation is defined as [23]

$$S \approx 4(\Delta/\Gamma)^2 \text{ for } \Delta \gg \Gamma \tag{4.3}$$

where Δ is the difference in frequency between adjacent elements, isotopes or isomers and Γ is the linewidth of the interaction (combined natural linewidth and laser linewidth). The overall selectivity resulting from multiple resonant excitations is the product of the selectivities of each resonant excitation.

The resonantly-ionized species are then detected as a function of laser frequency, allowing the hyperfine structure to be measured. Ion detectors typically provide a high quantum efficiency and large solid-angle coverage (> 70 %).

4.1.0.3 Resonance ionization laser ion sources

The high efficiency and selectivity of resonance ionization stimulated work on its application at ISOL facilities. The application was first realized at the IRIS facility, Gatchina, where the ionization efficiency of ytterbium was improved by over two orders of magnitude [55]. Shortly after, it was implemented at the ISOLDE facility where laser ionization of tin, thulium, ytterbium and lithium was performed in a hot cavity [56]. Since then, the resonance ionization laser ion source (RILIS) has been used to produce numerous new beams for users of the ISOLDE facility [34, 35]. It is now the mostly commonly used ion-source type, accounting for $> 70\%$ of the delivered beams in recent years [33]. The increasing demand for laser-ionized beams has necessitated numerous technical developments, some of which are detailed in Refs. [57–59].

4.1.0.4 In-source laser spectroscopy

In-source laser spectroscopy uses resonance ionization to measure the hyperfine structure of atoms within a hot-cavity ion source [60]. Combining resonance ionization with detection of radioactive decays (e.g α-particle decay) allows ultra-sensitive measurements to be performed on isotopes produced with yields as low as 0.1 s^{-1} (e.g. ^{191}Po [61]).

The main limitation of this approach is the Doppler broadening of the atomic ensemble within the hot cavity. Typical temperatures in these cavities exceed

2000 K resulting in a mass-dependent 1-10 GHz broadening of the hyperfine structure with heavier elements experiencing a smaller degree of Doppler broadening. This broadening completely obscures the hyperfine structure of isotopes of light- and medium-mass elements. In heavy elements, the reduced Doppler broadening and large hyperfine structures and field shifts present mean that the technique can often measure hyperfine A factors and isotope shifts. This allows a sufficient precision to be obtained on the extracted spins, magnetic dipole moments and changes in mean-square charge radii. In most cases, the hyperfine B factors can not be measured as they are too small. However, in some cases quadrupole moments have been extracted albeit with a very limited precision.

4.2 Collinear laser spectroscopy

Collinear laser spectroscopy exploits the reduction in velocity spread along the axis of motion that an accelerated beam experiences according to,

$$\Delta E = \delta \left(\frac{1}{2} m v^2 \right) = m v \delta v = k \tag{4.4}$$

where ΔE is the energy spread, m is the mass, v is the velocity and δv is the velocity spread of the beam and k is a constant. Therefore, increasing the velocity, v, will decrease the velocity spread, δv, of the beam.

The typical energy spread of beams produced at on-line facilities are of the order 0.1 eV. When an acceleration voltage of $30-40$ kV is applied, the velocity spread is compressed by approximately 3 orders of magnitude. The resulting Doppler width (4-10 MHz) is comparable to the natural linewidth of a hyperfine transition. When light from a laser with a sufficiently narrow linewidth is overlapped with the accelerated beam either collinearly or anti-collinearly, high-resolution laser spectroscopy can be performed.

The lab-frame laser frequency, ν_{lab}, will be Doppler shifted according to

$$\nu = \nu_{lab}\frac{\sqrt{1-\beta^2}}{1 \pm \beta} \tag{4.5}$$

where ν is the frequency in the rest frame of the accelerated beam, and

$$\beta = \sqrt{1 + \frac{m^2c^4}{(eV + mc^2)^2}} \approx \sqrt{\frac{2eV}{mc^2}}, \tag{4.6}$$

where m is the mass of the isotope being studied and V is the acceleration voltage. The $\pm$ before β in the denominator of Equation 4.5 indicates the propagation direction of the laser relative to the beam. $+\beta$ corresponds to the collinear direction and $-\beta$ corresponds to the anti-collinear direction. A Taylor expansion of the expression in Equation 4.5 yields

$$\nu = \nu_{lab}(1 \mp \beta + \frac{1}{2}\beta^2 + ...) \tag{4.7}$$

where $-\beta$ corresponds to the collinear direction and $+\beta$ corresponds to the anti-collinear direction.

4.2.1 Fluorescence detection

The most common variant of collinear laser spectroscopy involves fluorescence detection. In this approach, a high-resolution continuous-wave laser is scanned across the hyperfine structure of a given isotope. This can be done by directly scanning the laser or by varying the energy of the beam according to Equation 4.5.

When the laser frequency is on resonance, atoms are excited from the ground (or metastable) state to an excited state. Atoms in the excited state then decay, emitting a photon. The fluorescent photons are detected by a photo-multiplier tube (PMT). By measuring the detected fluorescent photon rate as a function of laser frequency (or scanning voltage), the hyperfine structure of an isotope can be measured. This technique is applied to both atomic and ionic systems.

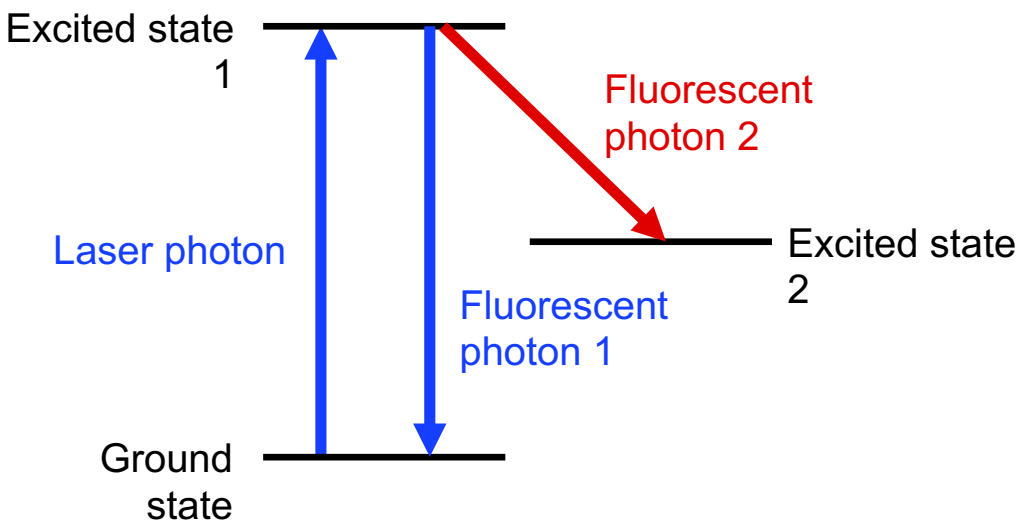

FIGURE 4.2: Schematic of collinear laser spectroscopy using fluorescence detection.

A schematic of the process is shown in Figure 4.2. To ensure the fluorescent photon has the highest probability of being detected, it must be emitted in the interaction region where the PMTs are most sensitive. This means that strong transitions, with an Einstein A coefficient of the order 10^8 s^{-1}, are required to maximize the detection efficiency. If an atom in the excited state decays to the same hyperfine level it was excited from, it can be re-excited and emit another fluorescent photon. The stronger the transition, the more likely that the atom interacts multiple times with the laser and emits multiple fluorescent photons, enhancing the chance of the detection.

The most common approach detects photons of the same energy as the laser frequency as illustrated by the blue lines in Figure 4.2. This means that the PMT detects both the fluorescence photons and scattered laser light. In some cases, the excited state possesses a larger branching ratio when decaying to a different state entirely. It can sometimes be more sensitive to detect the photons resulting from the decay to the different state as the laser-related background can be reduced . If the wavelengths of fluorescent photon 2 and the laser photon are significantly different, a filter can be chosen that maximizes the detection of fluorescent photon 2 but suppresses the laser-related background.

The high resolution of continuous-wave lasers combined with the velocity-spread compression associated with an accelerated beam allows most hyperfine structures to be fully resolved. The techniques routinely achieves linewidths between 10-100 MHz allowing precise measurements of hyperfine A and B factors and isotope shifts.

The main disadvantages of the technique stem from using photon detection as a means of measuring the hyperfine structure. The quantum efficiency (1-20 %) and typical solid angle coverage (1-5 %) of PMTs are poor when compared to ion detection. Scattered laser light will also be detected by the PMTs often resulting in large background rates. Ions/atoms will scatter light as they collide with gas molecules in the interaction region resulting in background beam light. Beam contaminants can also cause a large background after being neutralized into a state that decays by emitting a photon with a similar wavelength to the desired fluorescent photons. The advent of cooler bunchers at on-line facilities greatly improved the signal-to-background and therefore sensitivity of the technique (see Section 4.3). There are various techniques to reduce the background and improve the sensitivity of collinear laser spectroscopy [23].

The technique is routinely able to measure isotopes down to yields of around 10^3 s^{-1} to 10^4 s^{-1} [23]. In some cases, isotopes with much smaller yields have been measured. ^{52}Ca was measured using bunched-beam fluorescence spectroscopy by the COLLAPS collaboration with a yield of 150 s^{-1} [62].

4.2.2 Particle-detection methods

Some atomic/ionic systems allow bespoke techniques that are highly sensitive but not universally applicable. These approaches combine collinear laser spectroscopy with particle detection to access exotic isotopes with yields that render them inaccessible to fluorescence detection.

4.2.2.1 Collisional reionization

This technique was developed to study exotic isotopes of the noble gas elements [63–68]. In this approach, a high-lying metastable state is efficiently populated in the charge-exchange cell. Atoms in this metastable state are excited by a laser to a short-lived higher-lying state which decays to the ground state. The atom beam is selectively ionized through collisional ionization with a gas. The ionized portion of this are deflected and counted. The residual atoms can also be detected and used to normalize any variations in the ion beam intensity entering the setup. The cross section for collisional re-ionization for excited atoms in the high-lying metastable state is much higher than those in the ground state. This is because the excitation energy of the first excited state in the noble gas elements is very high. When the laser is on resonance, the population of the high-lying metastable state is transferred to the ground state and a 'dip' is seen in the collisional ion rate. Therefore, by recording the collisional re-ionization rate as a function of laser frequency, the hyperfine structure of the transition from the metastable state to high-lying excited state can be measured. For short-lived species, the sensitivity of the approach can be further enhanced by detection of β-particles emitted after implantation of the ions into a tape.

4.2.2.2 State-selective neutralization

This technique was developed to measure the ground-state properties of calcium isotopes [69]. The first realization of the technique measured up to ^{50}Ca [70]. Later, the sensitivity limit of bunched-beam fluorescence detection was reached when ^{52}Ca was measured [62], prompting a new experimental setup utilizing state-selective neutralization to be developed.

In this approach, calcium ions are optically pumped from the $4s^2\ S_{1/2}$ ground state to the metastable $3d\ ^2D_J$ states via the $4p^2\ P_{3/2}$ state. Ions in the $3d\ ^2D_J$ states have a greater neutralization cross section in a sodium vapour than ions in the $4s^2\ S_{1/2}$ state for a range of kinetic energies. The difference between the

neutralization cross sections is highest for energies of approximately 4 keV so the beam is decelerated to this energy. After the ions interact with the laser, they are passed through a charge-exchange cell filled with a sodium vapour. Ions which were optically pumped to the $3d\ ^2D_J$ states have a greater chance of being neutralized and detected by an atom detector. The non-neutralized ions are deflected towards an ion detector. When the laser is scanned across a resonance in the hyperfine structure of the $4s\ ^2S_{1/2} \rightarrow 4p\ ^2P_{3/2}$ transition, ions are optically pumped to the $3d\ ^2D_J$ states and a 'dip' is observed in the detected ion rate and a peak is observed in the detected atom rate [71].

Whilst its application has so far been limited to the calcium isotopes, the technique could also be applied for other alkaline-earth metals e.g. strontium, barium and radium.

4.3 Ion-beam cooler bunchers

Collinear laser spectroscopy using fluorescence detection has benefited significantly from the implementation of ion traps and coolers at radioactive-beam facilities. Ion traps are extensively used in low-energy nuclear-physics research. Some devices can directly measure nuclear properties, e.g. Penning traps which allow high-precision measurements of nuclear ground- and isomeric-state masses [72]. Other types of traps are used in the preparation of an ion beam before delivery to an experimental setup [73].

Radioactive ion beams often possess poor ion-optical properties with a large energy spread and emittance. Radio-frequency cooler bunchers were developed to improve the ion-optical properties of ion beams. Many of these devices are operational at facilities worldwide [39, 74–79]. Improving the energy spread and emittance of delivered ion beams has numerous benefits for collinear laser spectroscopy. The reduction in energy spread decreases Doppler broadening, improving the overall linewidth and the peak intensity of observed resonances. The improved emittance reduces the waist of the ion/atom beam in the interaction

region allowing a smaller laser beam to be used. The required photon density needed to saturate a transition can be obtained with less laser power, decreasing the laser-related background [80].

The most dramatic improvement for collinear laser spectroscopy results from bunching of the ion beam. The ions are slowed and subsequently trapped within the cooler buncher. These are allowed to accumulate and released in bunches to experiments. For laser-spectroscopy setups, longer ion-bunch widths of around 1-5 μs are used to give a small energy spread of $\leq$1 eV. The bunching of the ion beam reduces the laser-related background by multiple orders of magnitude. The use of an radio-frequency cooler buncher was pioneered at the IGISOL facility, Jyväskylä [74].

4.3.1 ISCOOL: The ISOLDE ion-beam cooler buncher

ISCOOL is the ion-beam cooler buncher installed at the ISOLDE facility [39, 81, 82]. ISCOOL is a gas-filled radio-frequency quadrupole Paul trap. Mass-separated ions produced at the high-resolution separator (HRS) target station are injected into ISCOOL. The velocity and velocity distribution of injected ions decrease through collisions with a buffer gas (0.1 mbar of helium is typically used). Radial confinement during this process is provided by the oscillating quadrupole field. An array of electrostatic elements produces the necessary electric-field gradient to inject the ions into the trapping volume. A small potential of 50-60 V confines the ions while they accumulate. The trapping potential is then switched to 0 V, allowing the cooled ions to be released in bunches. Typical bunch widths of released ions are between 1-5 μs. The cooled ion bunches are then re-accelerated and delivered to experimental setups.

Laser spectroscopy at the ISOLDE facility greatly benefited from the installation of an ion-beam cooler buncher. The background due to scattered laser light was reduced by up to a factor of 4×10^4 [39], allowing the sensitivity of fluorescence detection to be significantly improved.

4.4 Collinear resonance ionization spectroscopy

Collinear resonance ionization spectroscopy is a natural extension to the family of collinear-beam techniques. It combines aspects of both resonance ionization spectroscopy and collinear laser spectroscopy. The combination of the two allows the strengths of each technique to compensate for the the weaknesses of the other.

In collinear resonance ionization spectroscopy, resonance ionization is performed on an accelerated beam in the collinear geometry. The velocity compression along the axis of motion in the collinear geometry allows a high resolution to be obtained. This is combined with the sensitivity and efficiency of resonance ionization.

The idea was first proposed in 1982 [83]. Results from the first on-line experimental realization of the technique came in 1991 [84] where Schulz *et al.* performed resonance ionization spectroscopy on a fast atomic ytterbium beam. A two-step scheme excited ytterbium atoms from the metastable $6s6p\ ^3P_0$ to a Rydberg state where field ionization occurred, allowing an experimental efficiency of $1 : 10^5$ to be achieved. A limitation was the duty cycle losses associated with using a pulsed laser on a continuous atom beam.

The idea was not explored further at on-line facilities until the development of ion-beam cooler bunchers. By accumulating ions and releasing them in well-defined bunches, temporal overlap between the bunches and the pulsed lasers can be ensured, removing duty-cycle losses. Work constructing a dedicated CRIS setup at the ISOLDE facility began in 2008 [85]. The first experiments on francium isotopes demonstrated a two orders of magnitude improvement in sensitivity compared to bunched-beam fluorescence detection [86–88]. The hyperfine structures of ^{202g,m}Fr, produced at a rate of around 100 s^{-1}, were measured. The limited resolution (1.5 GHz) of this initial work was due to the laser system used. Developments in producing high-resolution laser pulses allowed a two orders of magnitude improvement in resolution (20 MHz) in later experiments on francium isotopes [89, 90].

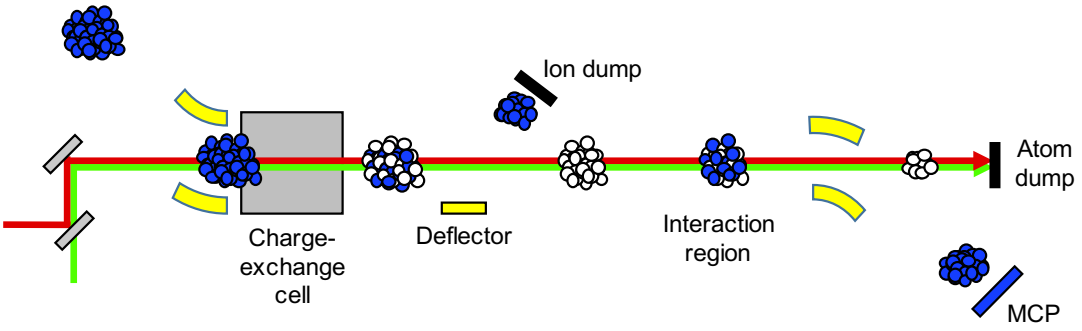

FIGURE 4.3: Schematic of the collinear resonance ionization spectroscopy experiment

4.4.1 Experimental setup

Figure 4.3 shows a schematic diagram of the CRIS beamline [86, 91–94]. A bunched-ion beam with an energy of 30 or 40 keV from the HRS separator at ISOLDE is deflected into the setup. The beam is focused by a quadrupole triplet and bent through 34^o. The ion beam enters the charge-exchange cell where it is neutralized by a potassium vapour. Typical neutralization efficiencies between $50-70$ % are achieved, however this is element dependent. Any non-neutralized component of the beam is electrostatically deflected away in the differential-pumping region.

The atom bunches enter the ultra-high vacuum interaction region, typically operating at a pressure of 2×10^{-8} mbar for the measurements reported in this thesis. When the charge-exchange cell is at operating temperature, the pressure in the cell exceeds 1×10^{-6} mbar. To maintain the interaction region at ultra-high vacuum, a differential-pumping region exists between the interaction region and the charge-exchange cell. Two 10-mm diameter apertures are installed at either end of the differential-pumping region.

The atom bunches in the interaction region are then collinearly overlapped with 2 or more laser pulses. When the lasers are on resonance, the atom bunches are resonantly ionized and deflected through 20^o towards a multichannel-plate (MCP) ion detector. By recording the detected-ion rate as a function of scanning-laser frequency, the hyperfine structure of an isotope can be measured. The timing

of the laser pulses and ion-bunch release from ISCOOL is controlled by two Quantum Composers QC9258 digital delay pulse generators. This is to ensure the atom bunch is temporally overlapped with the laser pulses when it is in the interaction region.

There are two MCP ion-detection sites. The first, named MCP4 (due to its proximity to Fardaday cup 4 (or FC4)), is a positive-ion detector placed directly in the beam path after the 20^o bend. The second, named MCP5, is a negative-ion detector located further downstream in the decay-spectroscopy station chamber. Ions are implanted onto a copper plate adjacent to MCP5 and the secondary electrons created by the impact process are detected. Ion detection using MCP5 is less efficient compared to MCP4 due to transport losses. Therefore, MCP5 is preferred for offline testing and ionization scheme development.

Alternatively, the resonantly-ionized beam can be implanted into the decay-spectroscopy station for decay studies [93, 95]. The excellent selectivity of CRIS enables production of pure nuclear-state beams allowing laser-assisted nuclear-decay spectroscopy to be performed [87, 90].

The lasers used to produce the light required for resonance ionization are situated in two areas. The first area is directly adjacent to the CRIS beam line and the second is the dedicated laser laboratory situated in Building 508, located adjacent to the ISOLDE hall. Further details on the lasers installed can be found in Chapter 5.

Chapter 5

Laser requirements and delivery

As CRIS combines aspects of both collinear laser spectroscopy and resonance ionization spectroscopy, it must utilize laser technology routinely used in both approaches. Continuous-wave lasers offer the high spectral resolution required to fully resolve the hyperfine structure but have a limited peak power. Pulsed lasers offer much higher peak powers that are required to saturate transitions but have a lower resolution. Achieving sensitive, high-resolution CRIS necessitates using both and the required technical complexity varies largely from one element to another.

Figure 5.1 shows a general schematic of a resonance ionization scheme. Many factors contribute to the development of an ionization scheme. This section will focus on the technical challenges of producing the laser light for a given scheme.

Step 1 in Figure 5.1 is the resonant transition, which will be probed to measure the hyperfine structure of the isotope under investigation. To fully resolve the hyperfine structure, high-resolution laser light is required. In all but the heaviest elements, a continuous-wave laser is required to either directly probe the hyperfine structure, or 'seed' a high-resolution pulsed-laser setup [96].

The high-resolution step is often the first step in an ionization scheme however this does not necessarily need to be the case. A higher-lying transition may offer better sensitivity to the nuclear observables that will be investigated in an

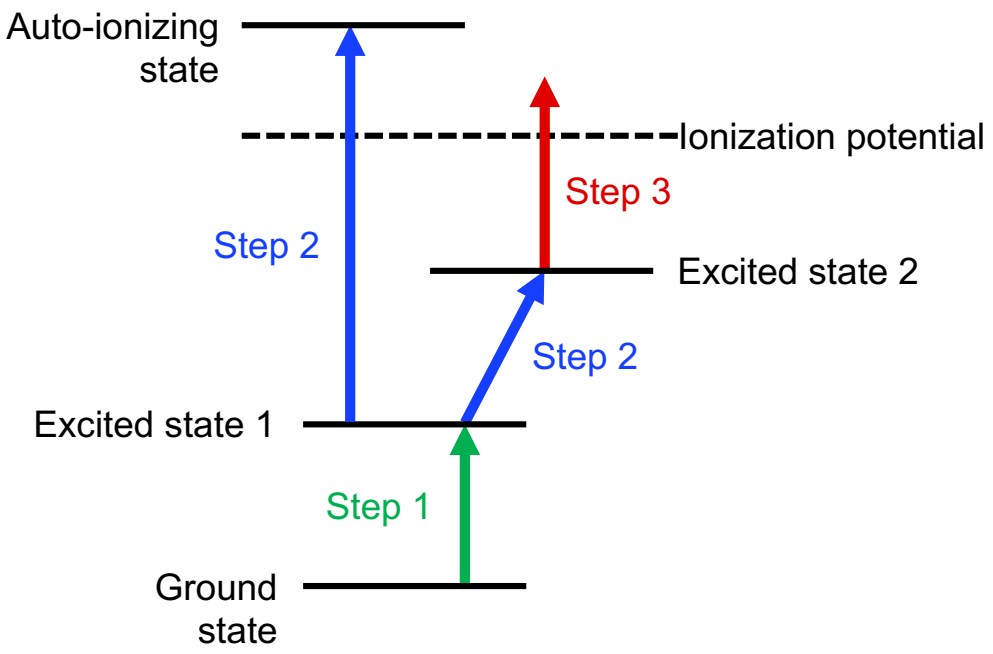

FIGURE 5.1: Schematic of a general ionization scheme.

experiment. However, for this discussion, Step 1 will be assumed to be the high-resolution transition which will be used to probe the hyperfine structure of the isotopes being studied.

5.1 Lasers at CRIS

Figure 5.2 shows a schematic of the lasers installed at CRIS. There are continuous-wave and pulsed lasers offering high-resolution and lower-resolution (broadband) options of both titanium-sapphire (Ti:Sa) and dye lasers. Lasers within the lilac-shaded area are situated in the laser laboratory in Building 508. Lasers within the peach-shaded area are situated on the optical table adjacent to the beamline. Each laser has the option to produce higher harmonics, extending its tunable range to include blue and UV wavelengths. The variety of lasers installed provides as much flexibility in developing ionization schemes as possible.

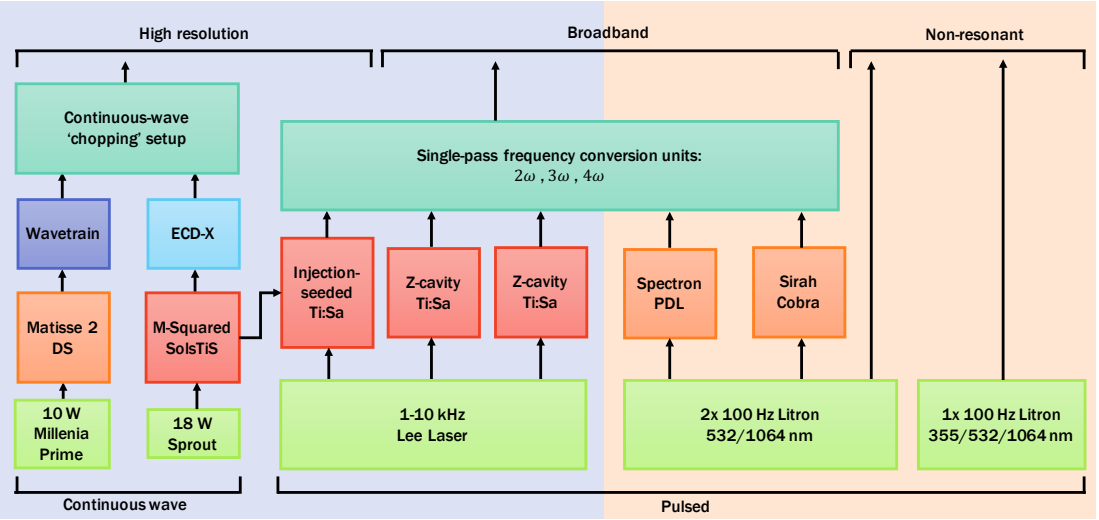

FIGURE 5.2: Schematic of the lasers installed at CRIS. Lasers within the lilac-shaded area are situated in the laser laboratory in Building 508. Lasers within the peach-shaded area are situated on the optical table adjacent to the beamline.

5.2 Continuous-wave lasers

Continuous-wave lasers are characterized by a constant output power. They can achieve single-mode operation allowing a high spectral resolution ($\leq$ 1 MHz). This high resolution makes them ideal for measuring the hyperfine structure of a given isotope. These lasers form the core of any spectroscopy experiment where a high resolution is required. By scanning the laser frequency, a certain atomic transition can be probed. Performing this on an accelerated beam (30-60 keV) in the collinear geometry allows the hyperfine structure to be measured in most cases (see Chapter 4 for more details).

5.2.1 M-Squared SolsTiS and ECD-X

The M-Squared SolsTiS is a continuous-wave titanium-sapphire (Ti:Sa) laser. It produces 6 W at 780 nm, the peak of its tuning range, and can produce light from 720-970 nm. It achieves this using a single mirror set allowing any wavelength within this range to be reached within seconds. The laser is pumped by 18 W of 532-nm light produced by a Sprout G-18W continuous-wave frequency-doubled

Nd:YAG DPSS laser, manufactured by Lighthouse Photonics. The Sprout has a pick-off module which allows it to pump a second laser system.

Fundamental light from the SolsTiS laser can then be frequency doubled using the M-Squared ECD-X external-cavity frequency doubler. This extends the tunable wavelength range of the system by allowing the production of 360-485-nm light. However, multiple crystals are required to cover this range and a specific crystal is installed into the cavity based on the desired wavelength. The cavity has a bow-tie layout built around a non-linear lithium triborate (LiB_3O_5 or LBO) crystal. High initial second-harmonic generation efficiencies of up to 40 % can be achieved with a 6-W input beam however the performance of these crystals quickly degrades in humid conditions. The LBO crystals used in the cavity have a fundamental tuning range of approximately $\pm$25 nm. Figure 5.3 shows a partial tuning curve for an LBO crystal cut for 834 nm in the ECD-X. Crystals cut for 765 nm and 940 nm are also available to be used in the cavity.

5.2.2 Matisse 2 DS and Wavetrain

The Matisse 2 DS is a continuous-wave dye laser manufactured by Sirah. It is pumped with 10 W of 532-nm light produced by a Millenia eV frequency-doubled Nd:YAG laser, manufactured by Spectra Physics. The Matisse laser produces light through pumping a compressed jet of dye with 532-nm light allowing a tunable range of 550-750 nm to be achieved, depending on the dye being used. However, to cover this range, different dyes must be used. At any one time, this limits the scanning range of the dye laser to a few 10s of nm. Around 1 W of light can be produced when using the Rhodamine-6G and DCM dyes. Unless a catastrophic failure occurs, the crystals that act as the gain medium in Ti:Sa lasers do not suffer from efficiency losses over time. In dye lasers, continual pumping of the gain medium causes photo-degradation of the dye resulting in a decreased lasing efficiency. Dye changes are sometimes necessary to maintain the optimal lasing efficiency throughout the duration of an experiment. This can be reduced by using larger quantities of dye solution however a larger pump reservoir

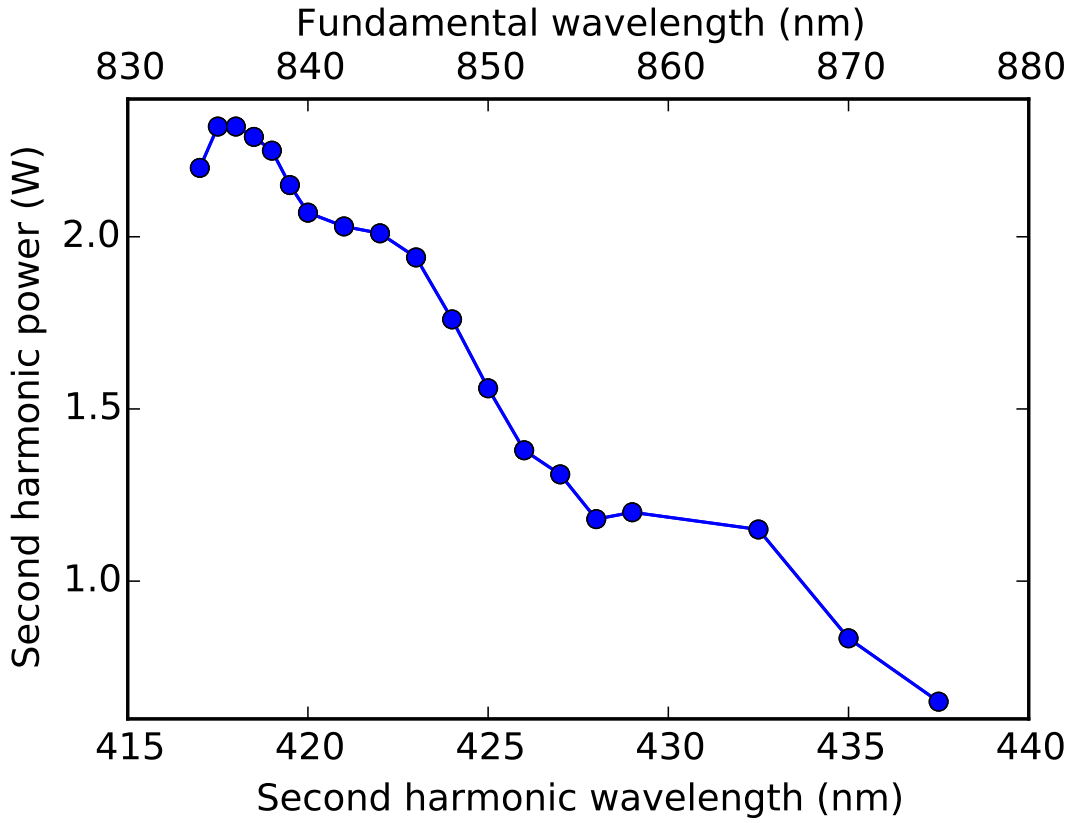

FIGURE 5.3: Partial tuning curve for an ECD-X LBO crystal cut for 834 nm. No data was taken for wavelengths below 834 nm.

is required. In general, the efficiency of a dye decreases when distance between the pumping wavelength and peak-emission wavelength of a dye increases. Because of this, this laser is only routinely used to produce wavelengths between 550-650 nm (Rhodamine-6G and DCM).

The fundamental output of the Matisse 2 dye laser can be frequency doubled using the Wavetrain external-cavity frequency doubler. This utilises a delta-shaped cavity around a non-linear crystal (BBO or LBO) to allow 275-325-nm light to be produced. Doubling efficiencies of about 10% can be achieved resulting in around 100 mW of frequency-doubled light.

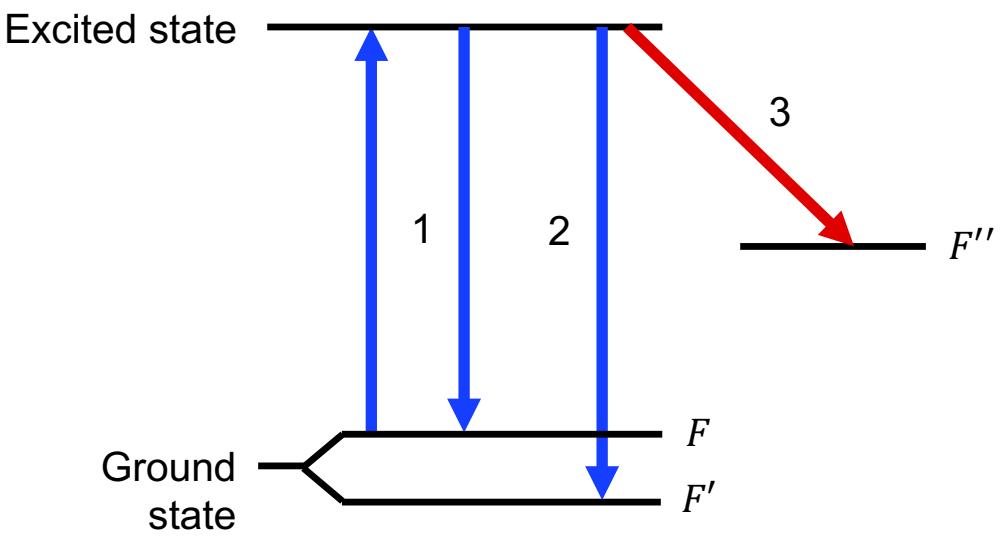

FIGURE 5.4: Schematic detailing 3 mechanisms for an excited state to decay.

5.2.3 'Chopping' of continuous-wave light

As there is a 0.93-m distance between the charge-exchange cell and the centre of the interaction region, a continuous-wave laser would continuously interact with the atom bunches before they reach the interaction region to be resonantly ionized. If the continuous-wave laser is on resonance, the atoms would be excited to an excited state before being ionized by the pulsed lasers in the interaction region.

Figure 5.4 shows a schematic of 3 different mechanisms in which an excited state can decay. In this case, the atomic ground state has an orbital angular momentum of 1/2, resulting in two hyperfine states, F and F'. In scenario 1, the excited state decays back to the same sub-level of the ground-state splitting as it was excited from, F. From here, it can then be excited again to the excited state. In scenario 2, atoms in the excited state decay to the other sub-level of the ground-state splitting, F'. In general, a high-resolution laser will not have sufficiently large linewidth that the atoms can be re-excited to the excited state. This is then called a 'dark state' as the high-resolution laser can no longer interact atoms in this state. This cannot occur for isotopes possessing a nuclear spin of 0 and/or

transitions where the lower atomic state orbital angular momentum is 0 as there is no lower-state hyperfine splitting.

In scenario 3, atoms in the excited state decay to a different state entirely, F''. The probabilities of decaying to either the ground state or F'' from the excited state are determined by the Einstein A coefficients of the transitions from the two states.

For a beam with a mass of 200 amu and an energy of 40 keV, it takes 5 μs to travel from the charge-exchange cell to the centre of the interaction region. A typical excited-state lifetime of 50-100 ns means that atoms undergo many laser-atom interactions in the 5 μs flight time before they arrive in the interaction region. This means that, in most cases, a large fraction of the population is optically pumped to 'dark states', resulting in a large loss of efficiency. Furthermore, the relative intensities of different hyperfine structure peaks will be altered, artificially lowering some. This hinders making sensitive measurements and may cause non-identification of certain components of an isotope's hyperfine structure. It also can make spin determination using relative peak intensities more difficult.

To prevent this, the continuous-wave light must be 'switched off' when the atoms are in flight between the charge-exchange cell and interaction region. The light must then be 'switched on' when they enter the region to allow resonance ionization to occur. This can be achieved through fast switching of a Pockels cell with polarization-selective optics [89].

Figure 5.5 shows a schematic of the process. Continuous-wave laser light passes through a Pockels cell. When the Pockels cell is off, the polarization of light passing through it is unaffected. The light then is transmitted by a polarizing beam-splitter cube into a beam dump. When a sufficiently high voltage is applied to the Pockels cell, light passing through it has its polarization rotated by $\lambda/2$. This light is then reflected by the polarizing beam-splitter cube and is deflected to the interaction region. Thus, by supplying high-voltage (2-3 kV) pulses to the Pockels cell, the continuous-wave light can be 'chopped' into pulses.

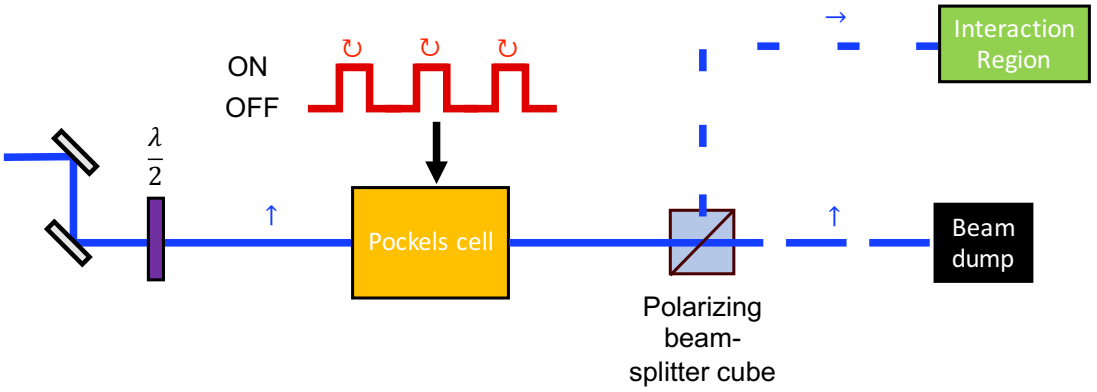

FIGURE 5.5: Schematic overview of the continuous-wave light 'chopping' method. The arrows above the beams indicate the polarization orientation of the laser light.

The efficacy of a Pockels cell setup is characterised by two factors:

1) The peak transmission through the setup

$$T = \frac{P_f}{P_i}, \tag{5.1}$$

where P_i and P_f are the peak powers entering and exiting the setup, respectively.

2) The extinction ratio

$$R = \frac{P_{\text{off}}}{P_{\text{on}}}, \tag{5.2}$$

where P_{on} and P_{off} are the laser-beam powers exiting the setup when the Pockels cell is on and off respectively. The following procedure is routinely used to set-up and optimize the Pockels cell setup:

- Adjust the two mirrors before the Pockels cell to maximize transmission through it.
- With the Pockels cell off, adjust a half-wave plate placed before it to maximize the power transmitted by the polarizing beam-splitter cube placed after the Pockels cell.
- Slowly bias the Pockels cell until the power reflected by the polarizing beam-splitter cube is maximized. This will determine the switching voltage required to induce the necessary polarization change.

- Switch off the Pockels cell. Adjust the two mirrors before the cell to minimize the power reflected by the polarizing beam-splitter cube.
- Instead of switching on the Pockels cell, rotate the half-wave plate to maximize the power reflected by the polarizing beam-splitter cube. Adjust the two mirrors before the cell to maximize the power reflected by the polarizing beam-splitter cube. Biasing the Pockels cell for extended periods of time can deteriorate performance and cause permanent damage.
- Rotate the half-wave plate to minimize the power reflected by the polarizing beam-splitter cube. Adjust the two mirrors before the cell to minimize the power reflected by the polarizing beam-splitter cube.
- Iterate the previous two steps until the extinction ratio is maximized.

The realization of such a setup allowed a two orders of magnitude improvement in resolution without a loss of efficiency [89]. The 'chopping' setup detailed in Ref. [89] achieved extinction ratios up to 1:2000. This extinction ratio was later improved upon by operating two fast-switching setups in series. Details of this are given in Chapter 6.

5.2.3.1 Lineshape distortions and broadening

The high electric fields induced by pulsed lasers can cause lineshape distortions and/or broadening [89, 97]. This is especially true if a non-resonant step is used to complete the ionization process due to the higher required photon densities for saturation. If the high-resolution laser exciting atoms to the first excited state is separated in time from the later high-power pulse(s), these effects can be removed. If the high-resolution laser is continuous wave, there will always be overlap with the pulsed lasers. 'Chopping' is therefore necessary to remove lineshape distortions and/or broadening whether or not optical pumping can occur or not.

The lineshape distortions/broadening form the main reason of why the CRIS technique targets transitions to longer-lived excited states compared to fluorescence detection. In fluorescence detection, transitions to short-lived excited states ($t_{1/2} < 10$ ns, $A > 10^8$ s^{-1}) are required to ensure that the emitted fluorescent photons have the greatest chance of being detected. For CRIS, excitation to a short-lived state would require the ionization laser pulse(s) to be overlapped with the high-resolution laser pulse, to maximize efficiency. This would induce lineshape distortions and/or broadening, sacrificing the resolution. Delaying the ionization laser pulse(s) would cause much of the excited-state population to decay, resulting in a loss of efficiency.

By targeting transitions to excited states with long lifetimes ($>$ 100 ns), the ionization laser pulse(s) can be delayed so that there is no temporal overlap between them and the high-resolution laser pulse. This removes any lineshape distortions and/or broadening, maximizing the experimental resolution without sacrificing the laser-ionization efficiency. See Refs. [89, 97–99] for more details.

5.3 Pulsed lasers

Step 2 in Figure 5.1 is another resonant transition. This transition differs from Step 1 in that it is not used to measure the hyperfine structure of the isotope under investigation. A laser used for this transition should efficiently drive atoms from excited state 1 to excited state 2 or to an auto-ionizing state. To achieve this, pulsed lasers are used due to their superior photon densities and generally larger linewidths.

In contrast to continuous-wave lasers, pulsed lasers are only on for a fraction of their duty cycle. While the average powers of pulsed and continuous-wave lasers may in some cases be comparable, the peak powers of pulsed lasers are orders of magnitudes higher. The fundamental pulse energy of a Z-cavity Ti:Sa laser is around 200 μJ spread over a pulse length of approximately 100 ns. The peak power of this laser is 2 kW, assuming a simple square pulse shape. This figure is

roughly 3 orders of magnitude larger than the peak fundamental power output of the M-Squared SolsTiS laser. This power is however spread over 1-10 GHz and not $\leq$1 MHz. The spectral density (photon density per unit frequency) of the two systems is comparable.

Pulsed lasers generally have a much larger linewidth (1-10 GHz) than continuous-wave lasers. For broadband resonant excitations, their larger linewidth is advantageous as it allows the entire hyperfine splitting of excited state 1 to be excited to either excited state 2 or an auto-ionizing state.

An exception to this is the injection-seeded Ti:Sa laser which will be described in Section 5.3.3. This system combines the high spectral resolution of continuous-wave lasers with the high peak power of pulsed lasers.

Pulse energies (rather than powers) will be used for characterization of the pulsed lasers at CRIS. This is because a range of repetition rates are routinely used. Describing the performance of the different pulsed lasers with pulse energies therefore allows a direct comparison.

5.3.1 Lee Laser LDP-100MQ

The pulsed Ti:Sa lasers are pumped by a single Lee Laser LDP-100MQ frequency-doubled Nd:YAG laser. This system can produce up to 13 mJ or 5 mJ of 532-nm light at repetition rates of 1 kHz and 10 kHz respectively. It can also run at any repetition rate which is a integer multiple of 1 kHz between 1 and 10 kHz. By using a combination of half-wave plates and polarizing beam-splitter cubes, a percentage of the Lee Laser's output can be reflected to pump each Ti:Sa cavity.

5.3.2 Z-cavity Ti:Sa

The Z-cavity lasers are pulsed Ti:Sa lasers designed by the LARISSA group at Johannes Gutenberg-Universität Mainz [59, 100, 101]. These lasers can produce wavelengths between 700-920 nm depending on the mirror set being used. At

CRIS, two of these cavities are pumped by a pulse energy of 1.2 mJ to produce 200-250 μJ of tunable broadband light. This value decreases as deeper-infrared wavelengths (>850 nm) are produced due to the decreasing lasing efficiency of the Ti:Sa gain medium at these wavelengths.

The wavelength of these systems can be changed by tuning the different frequency-selective elements within the cavity. The birefringent filter is used for coarse tuning whilst the etalon allows finer tuning of the wavelength. Presently, tuning these cavities is done manually. In the future, piezo-actuated etalon mounts will be implemented to allow wavelength stabilization and remote scanning of these cavities. The combination of a birefringent filter with a thin etalon (0.2 mm) will yield a linewidth of around 10 GHz. Using a 0.3-mm etalon will reduce this to around 6 GHz. Further reduction of the linewidth to around 1 GHz is possible by using a dual-etalon setup where one is a thick etalon (6-mm etalon) [102, 103]. In the future, a dual-etalon setup will be implemented in one of the Z-cavity Ti:Sa laser currently installed at CRIS. The 1-GHz linewidth of such a system is convenient for searching for hyperfine-structure peaks in heavier elements.

5.3.3 Injection-seeded Ti:Sa

The injection-seeded Ti:Sa laser combines the high-resolution of continuous-wave lasers with the high-peak powers of pulsed lasers. Details of the first implementation of injection-seeding can be found in Refs. [104–106]. A continuous-wave single-mode laser is overlapped with the pulsed light within the bow-tie cavity. By dithering the cavity with a piezo-mounted mirror, the cavity can be locked to single-mode laser for amplification. The injection-seeded Ti:Sa laser is pumped by up to 1.2 mJ of 532-nm light and is seeded by the M-Squared SolTiS laser. The system can produce 200-250 μJ of light in the wavelength range of 750-850 nm. It can produce light beyond this range albeit with a decreased efficiency. This limited wavelength range is a consequence of the mirrors used in the cavity. Details of a similar cavity with a wavelength range of 710-920 nm utilising a single broadband mirror set can be found in Ref. [103]. The system produces

light with a linewidth of 20 MHz. The high-photon density means that efficient single-pass higher-harmonic generation becomes feasible allowing the production of high-intensity, high-resolution deep-UV light (see Section 5.5 for more details). Details on the design and characterization of the system can be found in Ref. [107].

5.3.4 Spectron Spectrolase 4000

The Spectron Spectrolase 4000 is a pulsed-dye laser. It is pumped by up to 50 mJ of 532-nm light at 100 Hz by either head of the Litron LPY 601 50-100 PIV laser. The output pulse energy of this varies between 500 μJ and 4 mJ, depending on the dye being used. The linewidth of the system is approximately 10 GHz. If the required wavelength sits within the range of the dye currently in the dye circulators, the wavelength is tuned by simply moving a motorized grating. For large wavelength changes (5 nm near the peak wavelength of dye), re-optimization is typically required.

5.3.5 Sirah Cobra

The Sirah Cobra is a pulsed-dye laser. It is pumped by up to 50 mJ of 532-nm light at 100 Hz by either head of the Litron LPY 601 50-100 PIV laser. A 12% efficiency is quoted for producing 570-nm light with the Rhodamine 6G dye. The linewidth of the system is approximately 1.8 GHz at 570 nm.

5.3.6 Litron LPY 601 50-100 PIV and Nano TRLi HR 250-100

The Litron LPY 601 50-100 PIV is a pulsed Nd:YAG laser capable of producing either 50 mJ of 532-nm light or 80 mJ of 1064-nm light at 100 Hz from each of its two laser heads. Each laser head can be operated independently and provide

either 532-nm or 1064-nm light. Switching from 1064-nm production to 532-nm production requires the installation of a half-wave plate before the second-harmonic generation crystal.

The Litron Nano TRLi HR 250-100 is a pulsed Nd:YAG laser capable of producing 250 mJ, 130 mJ and 45 mJ of 1064-nm, 532-nm and 355-nm light respectively. It is a single-head system operating at a repetition rate of 100 Hz. Higher harmonics are generated by installing higher-harmonic generation modules onto the front of the laser head.

In Figure 5.1, Step 3 is a non-resonant transition which transfers the population of a high-lying state into the continuum. Achieving efficient ionization utilising a brute-force final non-resonant step requires very high-photon densities.

The choice of non-resonant step wavelength depends on a number of factors. A shorter non-resonant wavelength can reduce the number of resonant steps required in an ionization scheme. This can reduce setup time and make re-optimization of the laser(s)/atom overlap easier due to the reduced number of lasers. Furthermore, the use of a non-resonant final step in a two-step scheme offers advantages for offline testing. It can allow the sensitivity of different first-step transitions to be tested for an ionization scheme by changing just the first step laser.

However, there are factors to consider before using a shorter wavelength non-resonant step. The first is the composition of the beam being studied. The non-resonant wavelength should be chosen such that the element being studied, or any contaminant present in the beam, cannot be ionized through a 2-photon process. In cases where the ionization potential of any isobaric contaminant is greater than 2 times the photon energy of the non-resonant photon, any higher-lying metastable states that are strongly populated through charge exchange must also be considered as these could contribute to the background.

The efficiency of the non-resonant step depends, as with all transitions, on the photon density in the interaction region. The efficiency also depends on the density of states in the region of the continuum which the excited atoms are

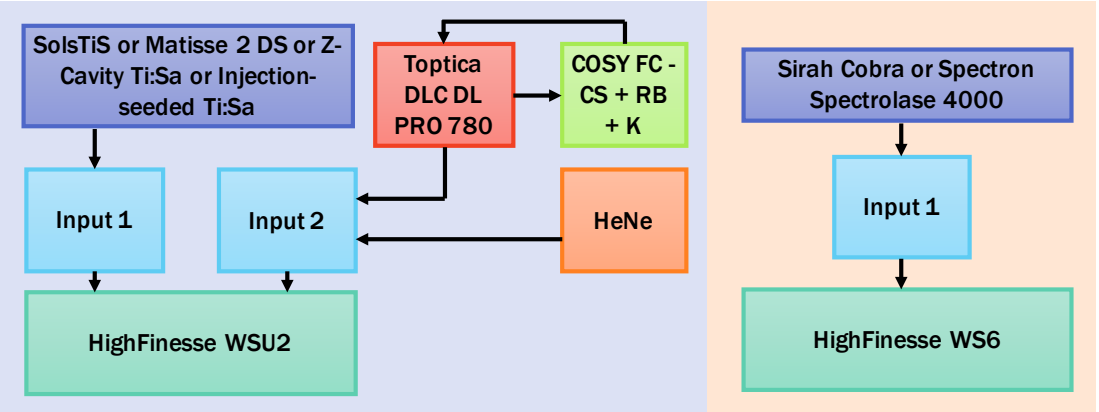

FIGURE 5.6: Schematic of the wavemeters installed at CRIS. Equipment within the lilac-shaded area are situated in the laser laboratory in Building 508. Equipment within the peach-shaded area are situated on the optical table adjacent to the beamline.

being forced to. The photon density decreases quickly as higher harmonics of Nd:YAG are used. For the Litron LPY 601 50-100 PIV, 50 mJ of 532-nm light can be produced compared to 80 mJ at 1064 nm. Each 532-nm photon has twice the energy of a 1064-nm photon. Therefore, if the spatial profiles of the two beams are the same, the photon density of the 532-nm beam will be around 30 % of the 1064-nm beam.

5.4 Wavelength measurement and referencing

To perform high-resolution collinear laser spectroscopy, both the lab-frame laser frequency and acceleration voltage of the beam must be measured precisely. Reference scans should also be taken regularly (every 3-4 hours). The frequencies of the lasers at CRIS can be measured using one of two wavelength meters (referred to as wavemeters from here on in).

Two Fabry-Pérot interferometers (FPI) can be used to analyze light from the continuous-wave lasers. One is a Toptica FPI 100-075-3VO FPI with a free-spectral range (FSR) of 1 GHz. The other is a Burleigh CFT500 has an FSR of 150 MHz. A schematic of the wavemeters and reference sources installed at CRIS is shown in Figure 5.6.

5.4.1 HighFinesse WSU2

The HighFinesse WSU2 is the most precise wavemeter installed at CRIS with a claimed absolute accuracy of 2 MHz. It is situated in the laser laboratory in Building 508. It can be used in combination with a fiber switchbox to read 2 channels simultaneously.

Drifts in the observed resonant frequencies during an experiment can be caused by a change in the acceleration voltage of the beam and/or a drift in the wavemeter itself. Simultaneous measurement of a reference light source is essential to be able to determine between the two. In the case of a change in acceleration voltage drift, only the lab-frame resonant laser frequency will drift. In the case of a wavemeter drift, both the lab-frame resonant laser frequency and reference light source frequency will drift in the same manner.

In some cases, the wavemeter can drift by a large amount (between 50-100 MHz) over the course of an experiment. In these instances, simply correcting the isotope shifts of measured isotopes using the closest-in-time reference scan may not be sufficient. Simultaneous measurement of a reference light source can be used to apply a point-by-point correction of the frequency data.

5.4.1.1 Toptica DLC DL PRO 780 and COSY FC-CS+RB+K

The Toptica DLC DL PRO 780 is a tunable diode-laser system which can produce 100 mW of light for wavelengths between 767-807 nm. It can be used in combination with the COSY FC-CS+RB+K module. This is a saturation spectroscopy module that allows the tunable-diode laser to be locked to an absorption line in atomic caesium, rubidium or potassium. Locking to an absorption line provides a robust reference light source that should not drift (so long as it remains locked).

5.4.1.2 HeNe laser

Alternatively, a stabilized helium-neon (HeNe) laser can be used as the reference light source for the wavemeter. This laser produces 1 mW of 632.8-nm light.

5.4.2 HighFinesse WS6

The HighFinesse WS6 is installed near the optical table adjacent to the beamline. It offers an absolute accuracy of 600 MHz and is used to measure the wavelength of the Spectron and Sirah pulsed-dye lasers.

5.5 Higher-harmonic generation of light

The majority of tunable lasers are pumped by 532-nm lasers. At CRIS, the dye lasers are used to produce wavelengths between 550-700 nm. The Ti:Sa lasers can produce wavelengths between 700-1000 nm. To extend the range of accessible wavelengths, higher-harmonic generation of the fundamental-laser light is required. This can be achieved using non-linear optical manipulation as laser light passes through an optically-dense medium. This section will give an experimental perspective of achieving higher-harmonic generation of pulsed lasers and will not describe the physical processes that govern it in detail. More details can be found in Refs. [108, 109].

To achieve an adequate frequency-mixing efficiency, a high-photon density within the non-linear medium is required. For continuous-wave lasers, this necessitates a multi-pass cavity that must be locked to a given mode. Such cavities are expensive and require meticulous setting up to give a high output power that is stable over the course of an experiment (typically 5-7 days). To frequency quadruple continuous-wave light, two such cavities must be operated in series. Frequency tripling requires an even more complex setup. Despite this complexity, fourth-harmonic generation has been used for experiments using fluorescence detection.

A fourth-harmonic generation efficiency of up to 2 % was achieved by the COLLAPS collaboration to produce continuous-wave 214.4-nm light for the study of cadmium isotopes [110]. As fluorescence detection requires the use of strong transitions, only around 1 mW of light is typically needed to saturate the transitions of interest.

As the CRIS technique targets weaker transitions, it requires higher peak powers than typically required for fluorescence detection. It is therefore impractical to use harmonics higher than the second for continuous-wave lasers. For pulsed lasers, the typical photon densities are sufficient such that a single-pass higher harmonic generation setup yields a respectable efficiency. This allows routine second, third- and fourth-harmonic generation to be achieved rather inexpensively.

5.5.1 Third-harmonic generation

To create a photon of frequency $3f$ (where f is the fundamental frequency), photons of frequencies f and $2f$ can be frequency summed. The optimal ratio of fundamental and second-harmonic frequency photons is 1:1. Therefore, a 66 % doubling efficiency will allow for the highest frequency-tripling efficiency. As photons of frequency $2f$ possess a polarization that is rotated by $\lambda/2$ after Type 1 frequency doubling [1], the polarization of either the fundamental or second-harmonic beams must be rotated so that efficient frequency tripling can occur. This can be achieved in two different ways, representing two configurations of the frequency-tripling unit.

5.5.1.1 Separated-beams configuration

In this configuration, the fundamental and second-harmonic beams are separated to allow the polarization of one of them to be rotated. Figure 5.7 shows the layout of this configuration of tripling-unit. Figure 5.8 shows a picture of this

[1] In type I frequency doubling, two photons with an ordinary polarization with respect to the second-harmonic generation crystal are combined to produce a single photon with double the frequency and an extraordinary polarization.

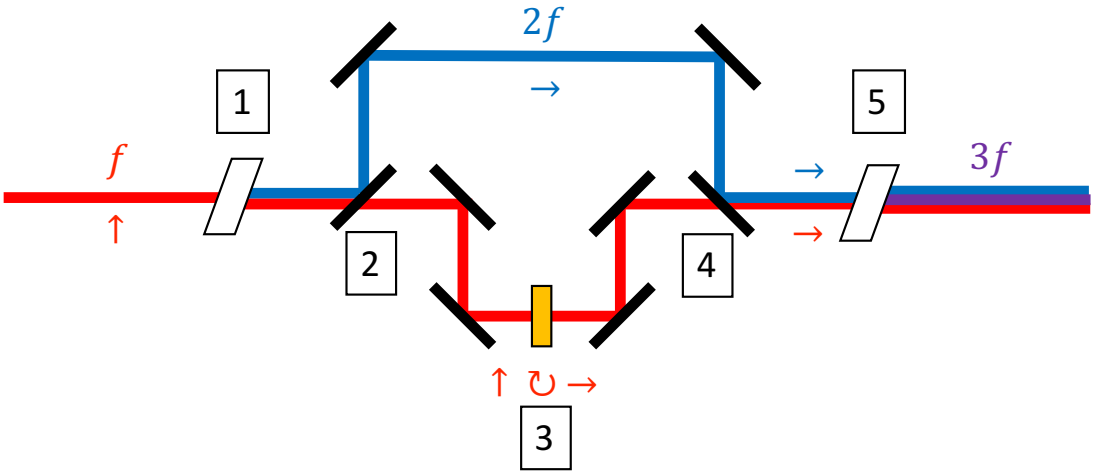

FIGURE 5.7: Schematic of the separated-beams frequency-tripling unit. The arrows denote the polarization orientation of the different wavelengths of light.

tripling unit. A laser beam of frequency f is focused into a BBO/BiBO (denoted by 1 in Figure 5.7) crystal to undergo Type I second-harmonic generation. The fundamental and second-harmonic beams are separated by a dichroic long-pass mirror (2 in Figure 5.7) (Part no: F38-661 from AHF Analysentechnik). These mirrors reflect the second-harmonic beam and allow the fundamental frequency to be transmitted through them. Long-pass mirrors are preferred to short-pass mirrors as they are more widely commercially available and generally possess better reflection and transmission properties. A tunable half-wave plate (3 in Figure 5.7) (Part no: PO-TWP-L2-25-UVIR from ALPHALAS) can then be used to rotate the polarization of either beam and compensate for any phase difference between the two. They are then recombined using a second dichroic mirror (4 in Figure 5.7) before being focused into a sum-mixing crystal (5 in Figure 5.7) allowing frequency-tripled photons to be produced.

External frequency doubling of the tunable-pulsed lasers installed at CRIS yields a typical efficiency of 20-30 %. A doubling efficiency of 33 % would result in a fundamental to second-harmonic photon ratio of 4:1. Because of this, the photon density of the frequency-doubled beam acts as one of the main limitations to the efficiency of the frequency-tripling unit. As rotating the polarization of either beam will incur some losses due to reflection on the surfaces of the tunable half-wave plate, the polarization of the fundamental beam is rotated. As frequency

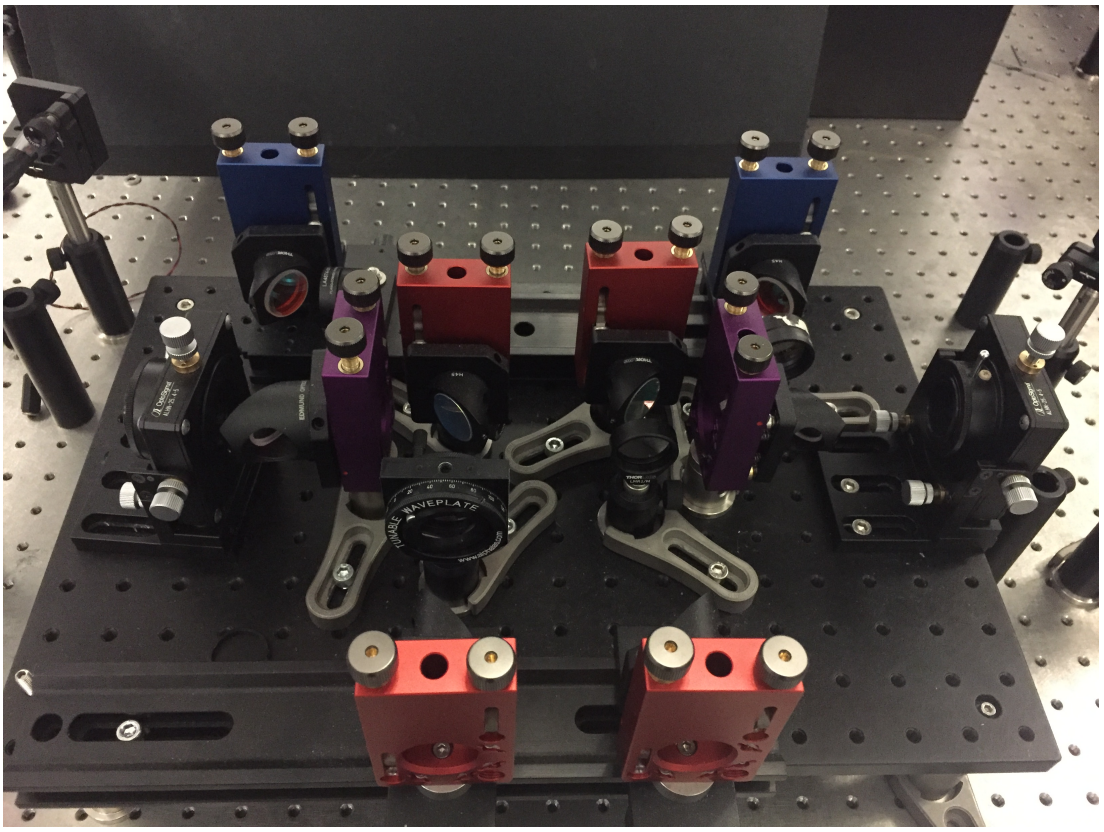

FIGURE 5.8: Picture of the separated-beams frequency-tripling unit. Fundamental Ti:Sa laser light enters the right-hand side of the unit. Frequency-tripled light exits through the left-hand side.

tripling requires the spatial overlap of both the fundamental and second-harmonic beams within the tripling crystal, variations in the fundamental beam path into the unit will affect the power output of the unit. One way to prevent this would be to not focus both beams as sharply within the tripling crystal. The resulting larger spatial profile of the beams would reduce the impact of any input-beam hysteresis. This would improve the stability of the power output albeit with the penalty of a reduced tripling efficiency.

An alternative approach involves using a BiBO crystal as the frequency-doubling crystal medium. BiBO crystals possess a higher effective non-linear coefficient than BBO crystals. This means a similar frequency-doubling efficiency can be achieved with a smaller photon density within the crystal. A longer focal length lens can be used to focus into the doubling crystal. This reduces the effect of variations in the path of the input fundamental laser beam into the tripling-unit without sacrificing the overall efficiency. The transparency range of BiBO extends

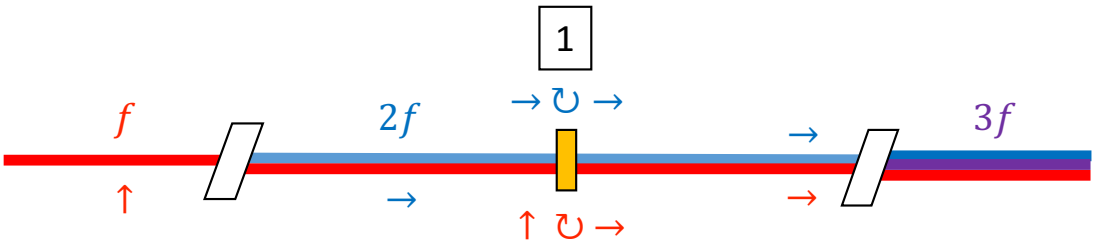

FIGURE 5.9: Schematic of the linear frequency-tripling unit. The arrows denote the polarization orientation of the different wavelengths of light.

down to 286 nm so they are usually only used for frequency doubling of Ti:Sa light.

This configuration of tripling unit uses spherical lenses to focus the second-harmonic beam into the tripling crystal. The use of cylindrical lenses would produce a higher second-harmonic photon density within the tripling crystal due to the non-spherical profile of the second-harmonic beam. This would result in a higher tripling efficiency at the the cost of a slightly more complex setup.

The beam shape of frequency-tripled light typically requires correction using cylindrical lenses. Two cylindrical and two spherical lenses are usually sufficient to reshape and refocus the beam.

5.5.1.2 Linear configuration

In this configuration, the polarization of the fundamental beam is rotated by $\lambda/2$ without separating the fundamental and second-harmonic beams. Figure 5.9 shows the layout of this frequency-tripling unit configuration. Figure 5.10 is a picture of this tripling unit. This kind of configuration is commonly used for high-photon density applications (e.g femtosecond lasers). This is achieved using a tunable dual-wavelength zero-order phase retardation plate (denoted by 1 in Figure 5.9) (Part no: PO-TWP-DW-2/1-25-UV from ALPHALAS). This waveplate is engineered so that for any frequency, f, within its tunable range,

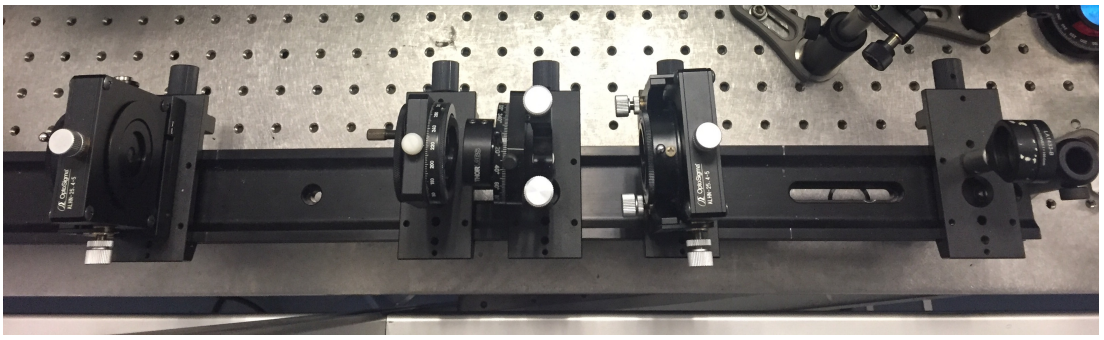

FIGURE 5.10: Picture of the linear frequency-tripling unit. Fundamental Ti:Sa laser light enters the right-hand side of the unit. Frequency-tripled light exits through the left-hand side.

the polarization is rotated by $\lambda/2$ whilst photons of frequency $2f$ are rotated by λ.

There are some advantages to this configuration of frequency-tripling unit:

1. Removing the need to separate the fundamental and second-harmonic beams reduces the cost of the unit significantly. This is because there is no need for the following:
    - 8 top-adjustable mirror mounts
    - 2 fundamental wavelength mirrors
    - 4 second-harmonic wavelength mirrors
    - 2 dichroic long-pass mirrors
2. As there are no laser-specific mirrors in this configuration, it can be used for both the pulsed-Ti:Sa and -dye lasers (only the lenses and non-linear crystals need to be exchanged).
3. The setup and optimization process is simpler compared to the traditional style.

There are some disadvantages to this configuration of frequency-tripling unit:

1. Both the fundamental and second-harmonic beams are subject to losses induced by surface reflections from optical components in the unit (tunable waveplate and lens).

2. The spatial overlap of the two beams within the tripling crystal is inferior to the traditional style. This is due to:

    - The fundamental and second-harmonic beams are emitted in slightly different directions after frequency-doubling (called walk-off).
    - The focal length of most lenses are wavelength dependent.
    - Most lenses are only anti-reflective coated for either the fundamental or second-harmonic beam.

Some of these disadvantages can be overcome. An achromatic doublet lens could be used to reduce the wavelength dependence of the lens in the unit. However, there are no commercially available achromatic doublet lenses that are achromatic over both the fundamental and second-harmonic ranges of Ti:Sa or dye lasers. It would ideally also be anti-reflective coated for both the fundamental and second-harmonic ranges of Ti:Sa or dye lasers. In this unit, a UV lens is chosen to focus the beams into the tripling crystal. This is because, as described earlier, the second-harmonic photon density is the main limitation for third-harmonic generation of the pulsed lasers at CRIS. The lens can be tilted to improve the spatial overlap of the two beams within the frequency-tripling crystal. However, the anti-reflective coating on most lenses is optimized for an angle of incidence of 0°. Tilting the lens significantly away from will cause reflections. Alternatively, a walk-off compensator can be placed after the tunable waveplate. In Refs. [111, 112], a walk-off compensator improved the third-harmonic generation efficiency by up to 3 times. The improvement was larger for smaller beam spots within the third-harmonic generation crystal.

The above factors lead to a lower efficiency when compared to the traditional configuration of frequency-tripling unit. Despite this, the linear configuration is still useful for frequency tripling of either the pulsed-Ti:Sa or -dye lasers. It is also suited for frequency tripling of high-resolution light as less power is needed to achieve the same spectral density as a broadband system. The configuration was used to produce high-resolution light that was able to saturate two weak

transitions in indium ($5p\ ^2P_{1/2} \rightarrow 8s\ ^2S_{1/2}$ (246.0 nm) and $5p\ ^2P_{3/2} \rightarrow 9s\ ^2S_{1/2}$ (246.8 nm)) isotopes during experiments in 2017. The simplified setup process means that it is ideal for quick off-line testing of ionization schemes.

Chapter 6

Developments and setup for experiments on francium and radium

6.1 Francium experiment

6.1.1 Ionization scheme

The ionization scheme used in the francium experiment is shown in Figure 6.1. Francium atoms were excited from the $7s\ ^2S_{1/2}$ ground state to the $8p\ ^2P_{3/2}$ excited state using 422-nm light. The hyperfine structure of this transition was measured during the experiment. The ionization process was completed using a non-resonant 1064-nm step transferring excited atoms in the $8p\ ^2P_{3/2}$ state into the continuum.

Table 6.1 summarises the laser setup for the francium experiment.

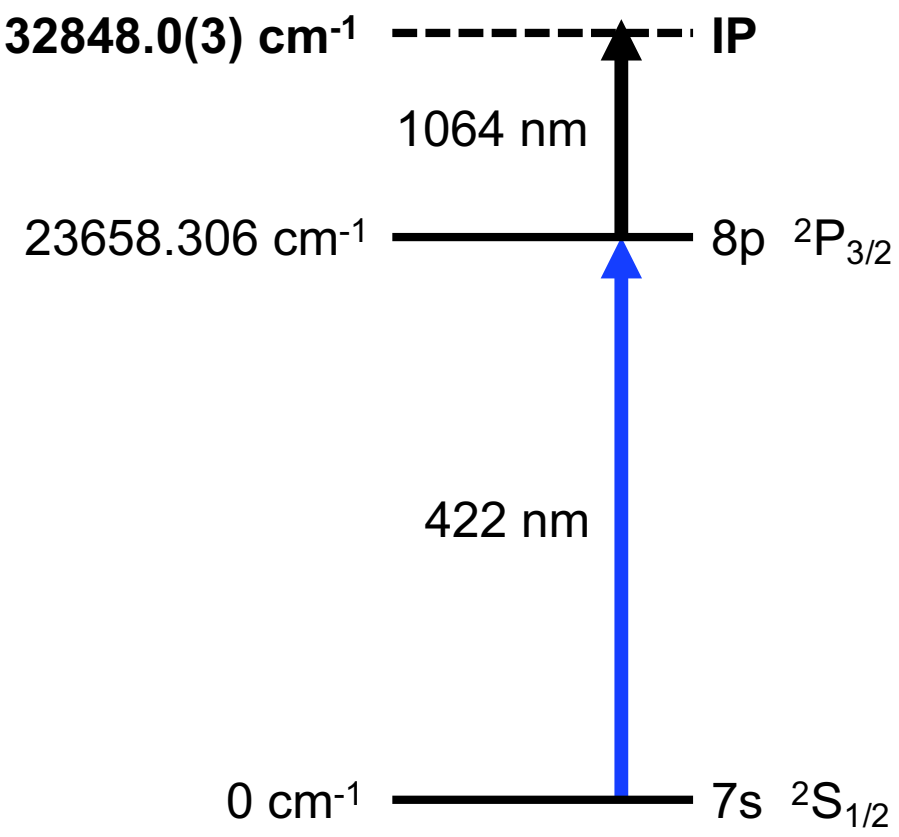

FIGURE 6.1: Ionization scheme used in the francium experiment.

TABLE 6.1: Laser setup for the francium experiment.

Wavelength (nm)	Laser	Wavemeter	Harmonic	Power/ pulse energy	Coupling
422	SolsTiS+ ECD-X	WSU2	2	1.1 W	Fibre
1064	Litron LPY 601 50-100 PIV	-	1	80 mJ	Mirror

6.1.1.1 Dual Pockels-cell setup

To prevent optically pumping to dark states, the 422-nm light was 'chopped' by using fast switching of two Pockels cells and polarization-selective optics, described earlier in Section 5.2.3. In this experiment, two fast-switching setups were operated in series.

The advantages of using two Pockels-cells setups instead of one is that it allows

greater control over the resulting pulse shape. Each Pockels cell has a different rise and fall time in response to an applied voltage. When using two Pockels cells in series, the peak transmission becomes

$$T = T_1 T_2, \tag{6.1}$$

where T_1 and T_2 are the peak transmission through the first and second Pockels cell setups. The extinction ratio becomes

$$R = R_1 R_2 \tag{6.2}$$

where R_1 and R_2 are the extinction ratios of the first and second Pockels cell setups, respectively.

Figure 6.2 shows the effect of adjusting the relative delay between the switching signals. The shapes of the light pulses, shown by the green lines, were measured by placing a photodiode after the dual Pockels cell setup. Each horizontal division is equivalent to a time interval of 50 ns. The blue and orange lines show the 100-ns wide signals supplied to the two Belkhe switches. The relative delays between the two signals in examples are (a) 0 ns, (b) 40 ns and (c) 80 ns. As the relative delay increases between the two switching signals, the peak intensity of the signal decreases. The pulse shape also varies significantly.

By tuning the pulse widths and relative delay between the two switching signals, it is possible to optimise the pulse shape. The 'chopping' process does introduce spectral broadening. The amount of broadening can be determined by taking a Fourier transform of the time profile of the 'chopped' pulse. However, the main contributing factor to the overall linewidth of the spectra taken was the Doppler broadening of the atom beam. Figure 6.3 shows the pulse shape used for the experiment. The widths of the two switching signals were 100 ns and 170 ns with a relative delay of 0 ns.

The peak transmission through the dual Pockels cell setup was 60%. The largest limitation to this was that one of the Pockels cells used was anti-reflective coated

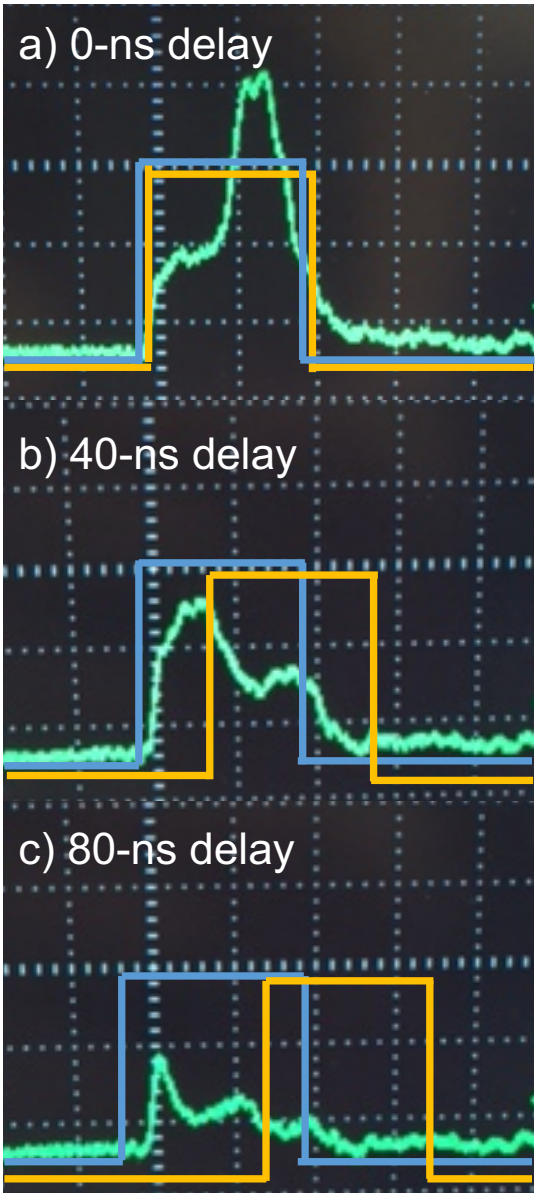

FIGURE 6.2: Example pulse shapes of 422-nm light after the dual Pockels cells setup. The green lines are the signals read on a photodiode placed after the setup. The blue and orange lines are the signals being supplied to the two Belkhe switches. Each Belkhe switch signal is 100 ns wide. The relative delays between the two switching signals are (a) 0 ns, (b) 40 ns and (c) 80 ns. Each horizontal division is equivalent to 50 ns.

FIGURE 6.3: Pulse shape used during the francium experiment. The green line is the signal read on a photodiode placed after the setup. The blue and orange lines are the signals being supplied to the two Belkhe switches. The pulse widths of the switching signals were 100 ns and 170 ns. Each horizontal division is equivalent to 100 ns.

for 1064 nm. Therefore a significant percentage of the 422-nm light was reflected from the surfaces of the 1064-nm anti-reflective coated Pockels cell. The extinction ratio of the setup exceeded 1:10^5, approximately two orders of magnitude greater than the single Pockels cell setup in Ref. [89].

6.1.1.2 Saturation curves

Figure 6.4 shows saturation curves for the 422-nm transition and the 1064-nm non-resonant step. The pulse energy of the 1064-nm light was measured after the exit window at the end of the interaction region. The peak power of the 422-nm light was measured directly after the output coupler of the fibre. The saturation function is defined as

$$I(P) = A\frac{P/P_0}{1+P/P_0}, \tag{6.3}$$

where P_0 is the saturation power or energy [113]. Fitting the 1064-nm data with a saturation curve function yields a saturation energy of 0.8 ± 0.4 mJ, showing that it was very well saturated. The saturation power of the 422-nm curve could not

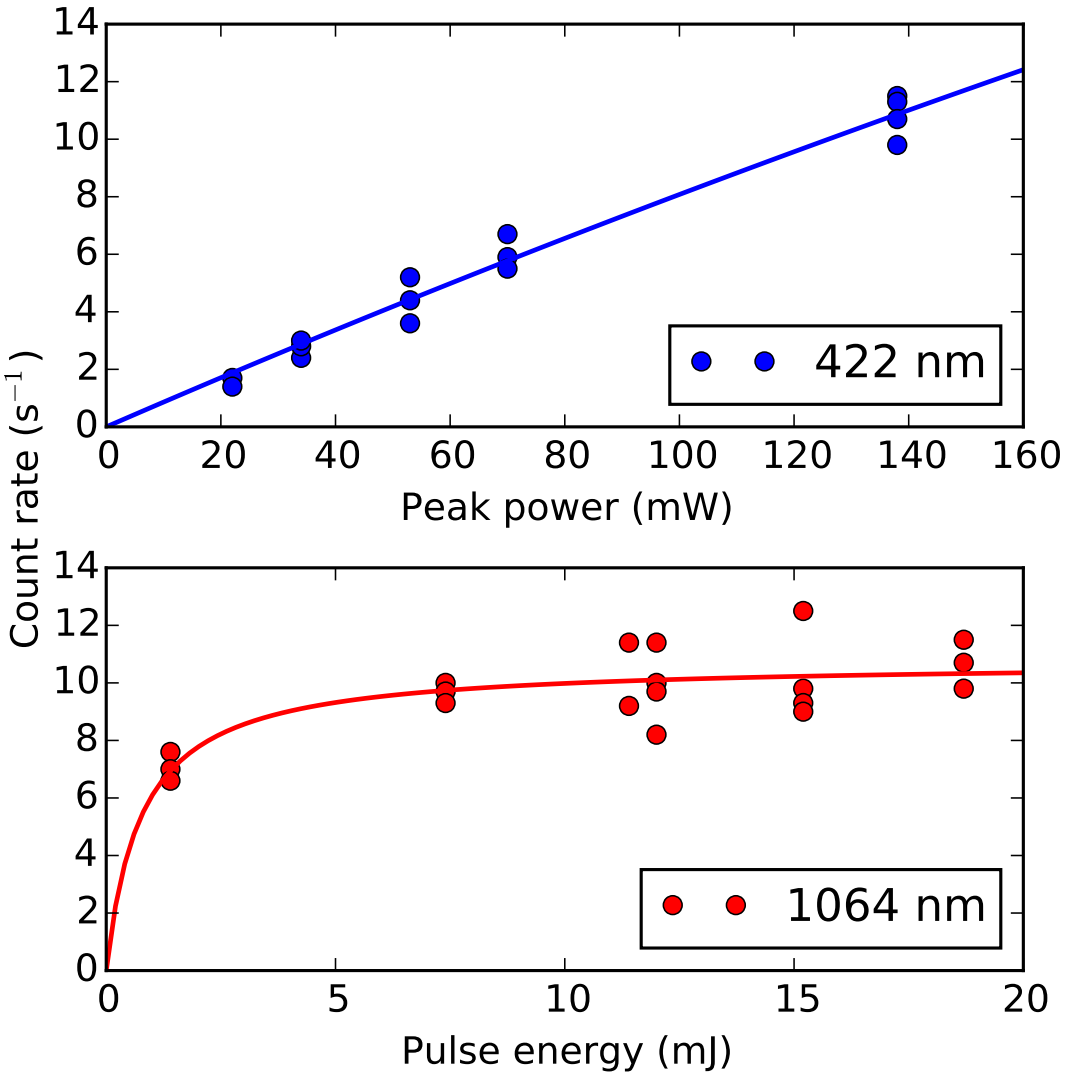

FIGURE 6.4: Saturation curves of the 422-nm transition (blue circles) and the 1064-nm non-resonant step (red circles) used in the francium experiment.

be determined as there was no 'flattening' of the saturation curve at the highest available powers, indicating that the transition was far from being saturated.

Previous experiments saturated the same transition with 25 mW of light [89, 90] indicating that the power density of the 422-nm light was the main limitation. The previous high-resolution experiment used frequency-doubled light from a Matisse 2 TS Ti:Sa laser situated on the optical table adjacent to the beamline, giving a Gaussian beam profile. This experiment used a multi-mode optical fibre to transport light from the laser laboratory to the optical table adjacent to the beamline. Collimation of light exiting the multi-mode fibre was performed using

a 12-mm reflective collimator. The resulting beam was 12 mm in diameter and with a homogenous power-density. The homogenous profile of the beam after the collimator gave a much lower maximum power density than the Gaussian profile the previous year. A telescope was used to reduce the diameter of the laser beam however the resulting power density was not sufficient to saturate the transition.

Efficiency measurements taken earlier in the run showed that the main physics aims of the experiment could be met with this setup. This combined with the very short length of the run (6 shifts) meant that no intervention was performed to change the focussing of the beam after the collimator, as the laser-ionization efficiency was deemed sufficient.

6.2 Radium experiment

6.2.1 First experiment - July 2016

An experiment performing spectroscopy on the radium ion, instead of the atom, by resonantly second ionizing Ra^+ to create Ra^{2+} was initially proposed [114]. This was due to three main factors. Firstly, the large amounts of francium contamination expected in this mass range would cause a significant non-resonant background. The cross section for collisional ionization of francium ions is expected to be lower as the second ionization potential is larger than the first (there is no experimental measurement of the second ionization potential of francium to date however it was calculated to be 22.4 eV [115]). By tuning the deflection plates after the interaction, only 2^+ ions would be steered onto the MCP to be detected.

The second factor was that radium is expected to neutralize into many metastable states during the charge-exchange process with a potassium vapour. The estimated state populations were calculated by A. R. Vernon using Rapp and Francis's semi-classical time-dependent perturbation theory [116]. More details on

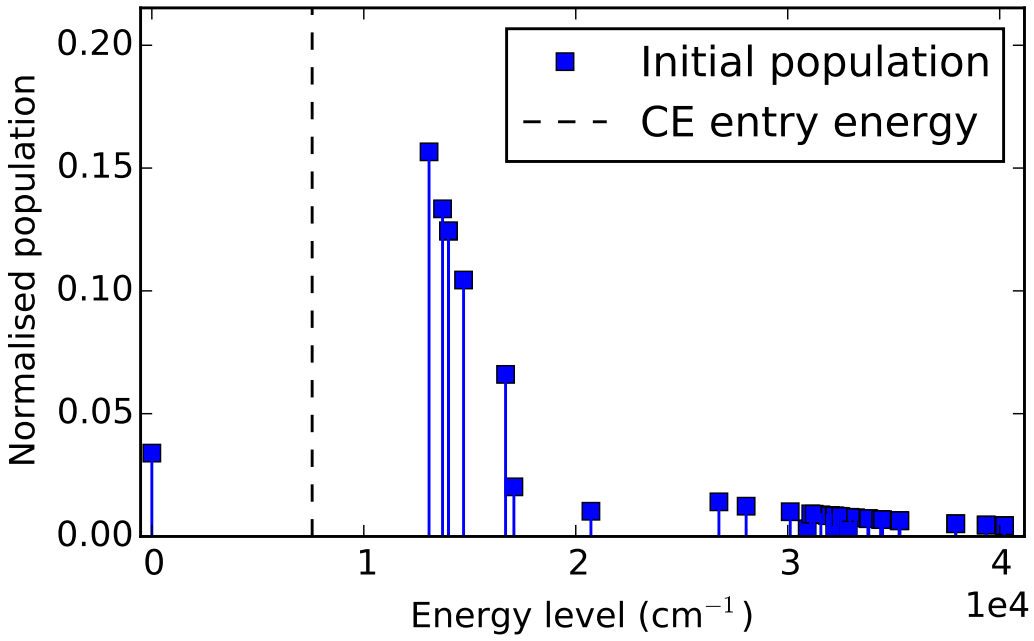

FIGURE 6.5: Initial populations of states in atomic radium after neutralization in a potassium vapour at a beam energy of 30 keV. Figure provided by A. R. Vernon.

the calculations can be found in Ref. [117]. Figure 6.5 shows the initial populations of states in atomic radium after neutralization in a potassium vapour at a beam energy of 30 keV. The initial state populations are spread over many states with the highest population being around 15 % for the $7s7p\ ^3P_0$ state. The final state populations could not be calculated as the majority of branching ratios are unknown in radium.

An estimate of the final state populations in radium can be obtained by comparing the difference in initial and final state populations in its closest chemical homologue, barium. Figure 6.6 shows the initial and final populations of states in atomic barium after neutralization in a potassium vapour at a beam energy of 30 keV. The initial state population distribution shows a similar behaviour to radium. The highest initial single state population is around 8 % in barium, compared to the 15 % in radium. This is due to there being more atomic information available for barium where 356 states are known (compared to 82 in radium) [118]. This can be seen as the higher density of states towards higher

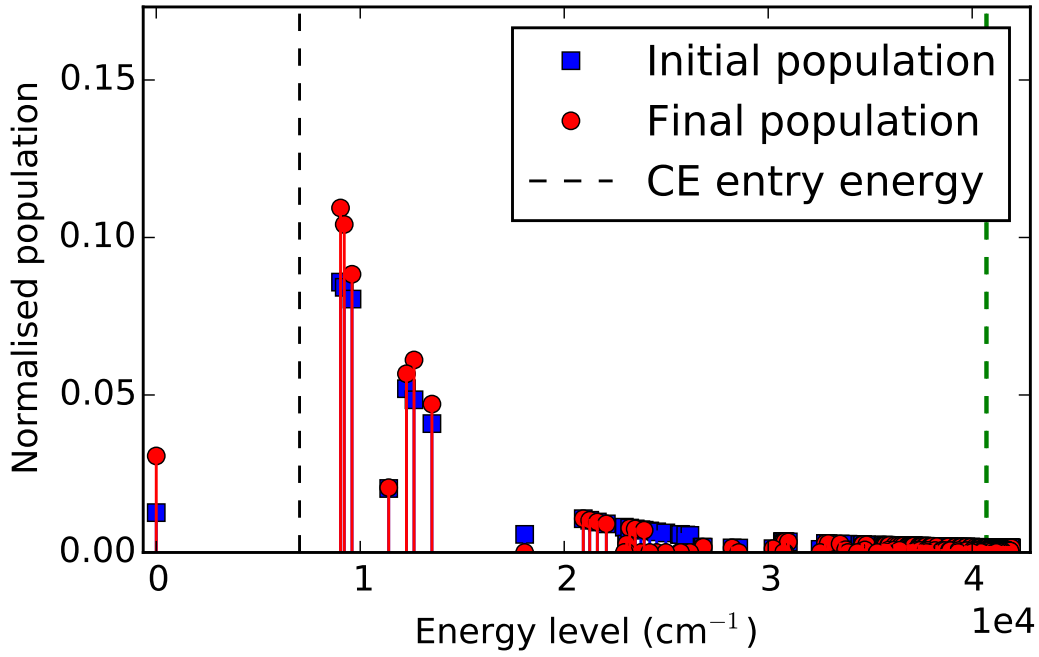

FIGURE 6.6: Initial (blue squares) and final (red circles) populations of states in atomic barium after neutralization in a potassium vapour at a beam energy of 30 keV. The vertical green dashed line is the ionization potential of barium. Figure provided by A. R. Vernon.

energies in Figure 6.6 compared to Figure 6.5.

In both radium and barium, the most strongly populated states are only populated by approximately 10 % of the neutralized atoms. By performing spectroscopy on the ion, this efficiency loss can be avoided as only the ionic ground state will be strongly populated. This would mean the charge-exchange cell and small apertures surrounding it could be removed, also resulting in an increased transmission efficiency of the radium ions entering the interaction region to be laser ionized.

The third factor was that the $7s\ ^2S_{1/2} \rightarrow 7p\ ^2P_{3/2}$ transition in ionic radium provides the necessary sensitivity to the desired nuclear observables, providing the ability to measure both hyperfine A and B factors.

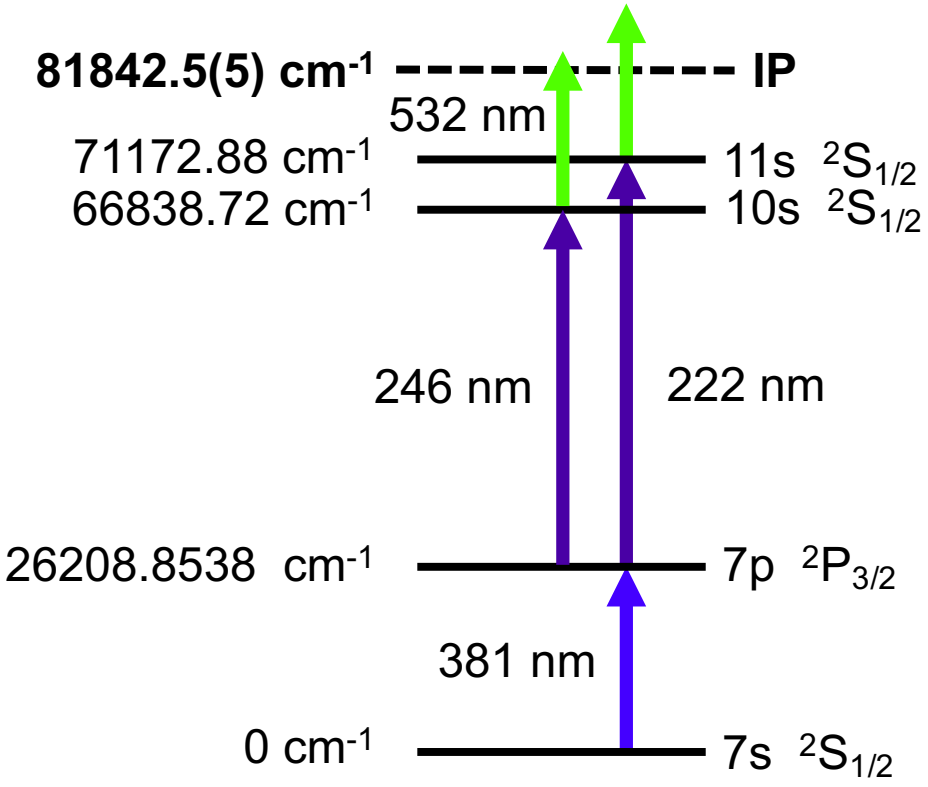

FIGURE 6.7: Ionic-radium ionization scheme used in the first radium experiment.

6.2.1.1 Ionic-radium ionization scheme

The radium-ion ionization scheme is shown in Figure 6.7. The first step excited the ion from the $7s\ ^2S_{1/2}$ ground state to the $7p\ ^2P_{3/2}$ excited state using 381-nm light. The hyperfine structure of this transition was measured during the experiment. The second step further excited the ion from the $7p\ ^2P_{3/2}$ to the $11s\ ^2S_{1/2}$ state using 222-nm light. An alternative second step excited the ion from the $7p\ ^2P_{3/2}$ to the $10s\ ^2S_{1/2}$ state using 246-nm light. The second-ionization process was completed using a non-resonant 532-nm step forcing excited ions in the $10s\ ^2S_{1/2}$ and $11s\ ^2S_{1/2}$ states beyond the second-ionization potential.

Table 6.2 summarises the laser setup for the ionic radium experiment.

TABLE 6.2: Laser setup for the ionic-radium experiment.

Wavelength (nm)	Laser	Wavemeter	Harmonic	Power/ pulse energy	Coupling
381	Injection-seeded Ti:Sa	WSU2	2	40 μJ	Fibre
222	Spectron Spectrolase 4000	WS6	3	1-2 μJ	Mirror
246	Z-cavity Ti:Sa	WSU2	3	8 μJ	Mirror
532	Litron LPY 601 50-100 PIV	-	2	50 mJ	Mirror

6.2.1.2 Non-resonant $1^+ \rightarrow 2^+$ ionization rate

The main difficulty encountered during the experiment on the radium ion was an unanticipated high non-resonant $1^+ \rightarrow 2^+$ ionization rate. The efficiency of this process was measured to be 0.5%. The cause of this was the higher pressure regions (in particular the charge-exchange cell region) of the CRIS beamline that do not usually directly contribute to the background when performing spectroscopy on an atomic system.

Due to the high pressure in the charge-exchange cell ($> 1 \times 10^{-6}$ mbar), a significant amount of 2^+ ions are produced non-resonantly through collisions with residual gas in the region. When CRIS is performed on an atomic system, any non-neutral component of the beam is deflected away before the interaction region. This includes both the non-neutralized 1^+ ions and non-resonant 2^+ ions which then cannot directly affect the background rate [1].

When performing CRIS on an ionic system, the deflector after the charge-exchange cell region must be set to 0 V to allow 1^+ ions to enter the interaction region to be resonantly second-ionized. Doing this also allows the non-resonant 2^+ ions created in the charge-exchange cell region to enter. These non-resonant 2^+ ions

[1]For an atomic beam, the main contributing factor to the non-resonant collisional background is the pressure in the interaction region. The higher-pressure regions further upstream like the charge-exchange cell and quadrupole-triplet region only indirectly contribute to the background through acting as a bottleneck on the interaction region pressure. However, this bottleneck is reduced through the use of a differential-pumping region.

are then deflected towards the MCP to be detected. This means that the higher pressure regions of the setup after the 34° bend contribute directly to the background rate when attempting spectroscopy on an ionic system. As the pressure in the charge-exchange cell region is typically two orders of magnitude greater than that in the interaction region, this creates a significant non-resonant 2^+ ion background.

The large amount of non-resonant 2^+ ions prevented a first resonant 2^+ signal to be identified. The first signals observed in experiments are typically small. Once a signal has been identified, laser/atom overlap optimization on resonance can be performed to improve the experimental efficiency. To first observe a signal on top of the non-resonant 2^+ background would require an exceptional initial experimental efficiency. Even if a 1% efficiency was achieved, a 0.5% background rate would obscure all signals.

6.2.1.3 Atomic-data deficiencies

Despite the increased experimental effort to study the atomic structure of radium in recent years, a lot remains unknown. A compilation of all existing data on transitions in atomic and singly-ionized radium is presented in Ref. [119]. Whilst the first step in the ionic-radium ionization scheme is known to a sufficient precision, the second steps used in the scheme are not. As both steps must be on resonance for resonance ionization to occur, both tunable lasers needed to be scanned to establish a first resonance. A low-resolution first step laser would have aided this process, as it would have negated the need to scan the first laser. However, only 1 Z-cavity Ti:Sa laser was available and that was used to produce light for the 246-nm transition.

6.2.1.4 Atomic-radium ionization scheme

Due to the large unanticipated background, a switch to performing spectroscopy on atomic radium was carried out towards the end of the experiment. The choice

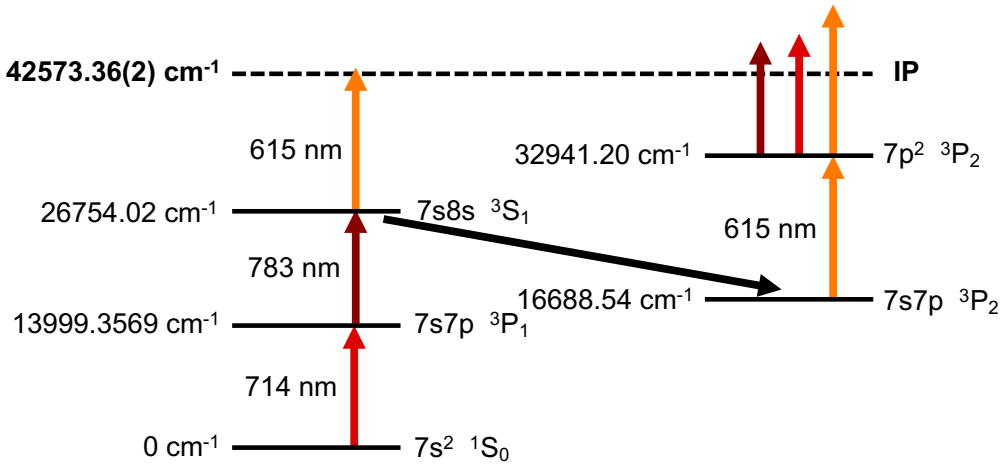

FIGURE 6.8: Atomic-radium ionization scheme used in the first radium experiment.

TABLE 6.3: Laser setup for the atomic-radium experiment.

Wavelength (nm)	Laser	Wavemeter	Harmonic	Power/ pulse energy	Coupling
714	Z-cavity Ti:Sa	WSU2	1	200 μJ	Mirror
783	Injection-seeded Ti:Sa	WSU2	1	200 μJ	Fibre
615	Spectron Spectrolase 4000	WS6	1	1.3 mJ	Mirror

of scheme was greatly aided by the scheme development carried out by RILIS prior to the run [120].

The left-hand side of Figure 6.8 shows the atomic-radium ionization scheme used in the first experiment. Atoms in the $7s^2\ ^1S_0$ ground-state were excited to the $7p\ ^3P_1$ state using 714-nm light. The second transition involved further excitation to the $8s\ ^3S_1$ state using 783-nm light. The hyperfine structure of this (second) transition was measured during the experiment. The ionization process was completed by excited atoms in the $8s\ ^3S_1$ state to an auto-ionizing state using 615-nm light.

Table 6.3 shows the laser setup used for the atomic-radium ionization scheme used in the first experiment.

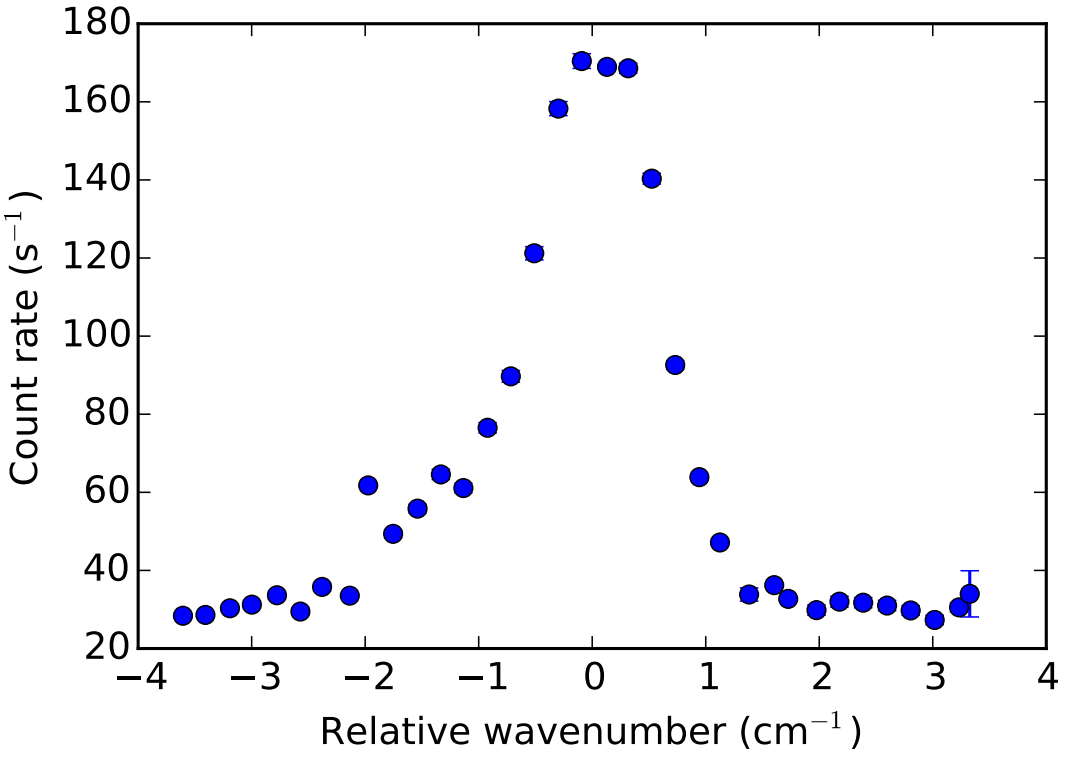

FIGURE 6.9: Scan of the 615-nm transition in ^{226}Ra. The wavenumber is given relative to the offset value of 16252.51 cm^{-1}. The error bars are smaller than the data points.

Laser blocked	Count rate (s^{-1})	
	615-nm step on resonance	615-nm step off resonance
None	170	30
714	140	30
783	140	30
615	30	30

TABLE 6.4: Observed count rates with different lasers blocked when the 615-nm laser was on and off resonance.

6.2.1.5 Realization of the scheme at CRIS

Figure 6.9 shows a scan of the 615-nm transition. A fit of this data gives the centroid frequency as 16252.51(4) cm^{-1} with a width of 1.4 cm^{-1}. Table 6.4 shows the observed count rates with different lasers blocked.

When the 615-nm laser was off resonance, a 30 s^{-1} rate was observed for when any laser was blocked. This is the non-resonant collisional background rate. When

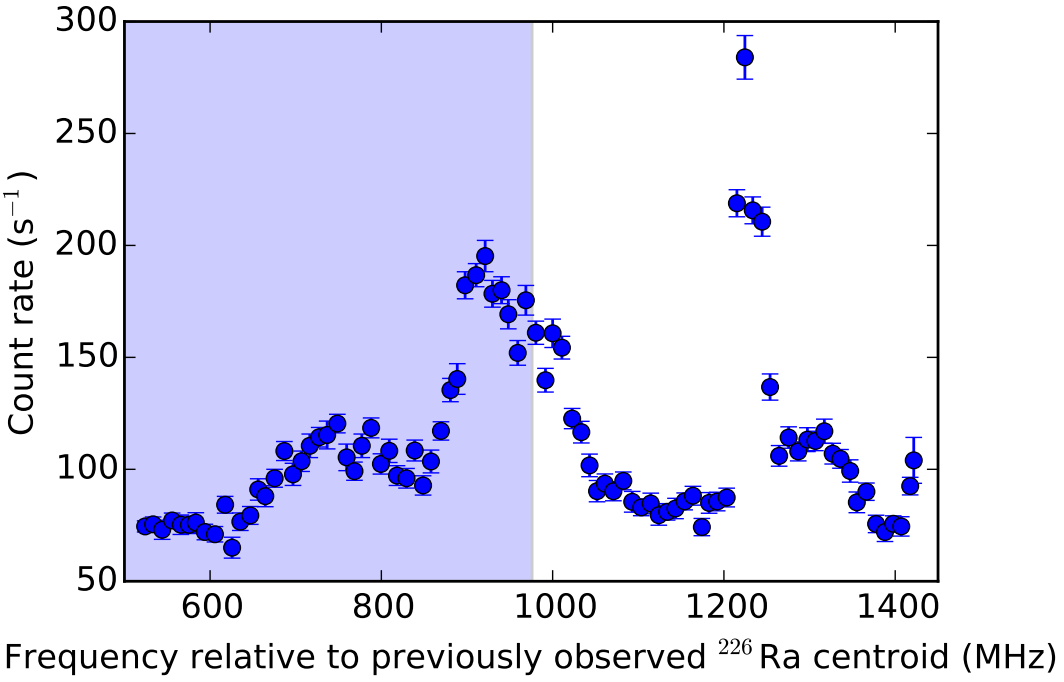

FIGURE 6.10: Scan of the 783-nm transition in ^{226}Ra plotted relative to the previously observed value. The blue-shaded area represents the 1σ boundary around the previously observed centroid.

the 615-nm laser was on resonance, a large 140 s^{-1} rate was observed when the either 714-nm and 783-nm lasers were blocked. This shows that the 615-nm laser was producing a large background from ionizing atoms which did not originate from the ground state.

Figure 6.10 shows an example scan of the 783-nm transition in ^{226}Ra. The frequency is given relative to the previously observed value of 12754.65(3) cm^{-1}. The blue-shaded area represents the 1 σ boundary around the previously observed centroid.

Due to its 0^+ spin, the hyperfine structure of ^{226}Ra should possess only 1 peak. Multiple structures can be seen in Figure 6.10. A possible explanation relates to the mode structure of light produced by the Z-cavity Ti:Sa lasers. In these cavities, resonator modes are created that are equally spaced in frequency. The frequency spacing is the free spectral range and is equal to 300 MHz for resonators of a length of 0.5 m length (a similar length to the Z-cavity Ti:Sa lasers used) [101]. Frequency-selective elements within the cavities then reduce the number

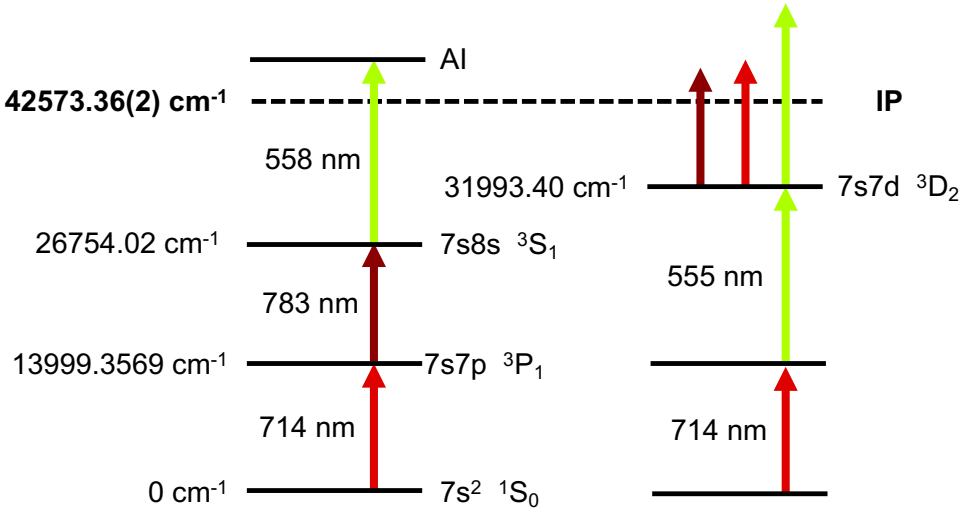

FIGURE 6.11: Atomic-radium ionization schemes used in the second radium experiment. The scheme on the left is the initial scheme and the scheme on the right is the scheme used for the experiment after scheme development.

of modes propagating within the cavity, decreasing the linewidth of the light produced. The structures observed in Figure 6.10 are separated by approximately 300 MHz, consistent with a multimode structure of the Z-cavity Ti:Sa lasers.

6.2.2 Second experiment - August 2016

6.2.2.1 Initial atomic-radium ionization scheme

A number of factors influenced the initial scheme chosen for performing CRIS on the radium atom for the second experiment. The initial scheme is shown on the left-hand side of Figure 6.11. Atoms in the $7s^2\ ^1S_0$ ground state were excited to the $7p\ ^3P_1$ state using 714-nm light. The second transition further excited atoms from the $7p\ ^3P_1$ state to the $8s\ ^3S_1$ state using 783-nm light. The ionization process was completed by exciting atoms from the $8s\ ^3S_1$ state to an auto-ionizing state using 558-nm light [38].

Performing spectroscopy on the 783-nm transition between the $7p\ ^3P_1$ and $8s\ ^3S_1$ states was preferred as it provides sensitivity to spins greater than 1/2. However,

TABLE 6.5: Laser setup for the second radium experiment.

Wavelength (nm)	Laser	Wavemeter	Harmonic	Power/ pulse energy	Coupling
714	Matisse 2 TS	WSU2	1	1 W	Mirror
714	Z-cavity Ti:Sa	WSU2	1	200 μJ	Mirror
783	Z-cavity Ti:Sa	WSU2	1	200 μJ	Mirror
555-558	Spectron Spectrolase 4000	WS6	1	3.5 mJ	Mirror

a suitable setup could not be achieved. The limited time between the two experiments meant that there was no opportunity to further understand the cause of the additional peaks observed in the ^{226}Ra spectra recorded during the previous experiment. As a result, this meant that the Z-cavity Ti:Sa lasers could not be used to provide broadband light for the first 714-nm step. It is possible to produce 714-nm light using the Pyradine 2 dye in the Spectron pulsed-dye laser but this laser was needed to produce light for the 555-nm transition to an auto-ionizing state. Ionization from the $8s\ ^3S_1$ state could be driven using a non-resonant 532-nm step. For this to be efficient, the required high-photon density would two-photon ionize a significant portion of the expected large amounts of francium contamination (all wavelengths below 610-nm can two-photon ionize francium). It was decided that spectroscopy would be performed using the 714-nm transition knowing that it would offer no spin sensitivity for spins greater than 1/2.

Table 6.5 summarises the laser setup used for the second radium experiment.

6.2.2.2 Online scheme development

During the initial setup period of the experiment, online scheme development was performed. Figure 6.12 (a) shows a scan of the pulsed-dye laser (PDL) for ^{226}Ra with all 3 lasers entering the beamline (shown by blue circles). Figure 6.12 (b) shows a scan of the PDL for ^{226}Ra with just the PDL light entering the beamline (shown by red circles). The wavenumber is given relative to the offset value of 17971 cm^{-1}.

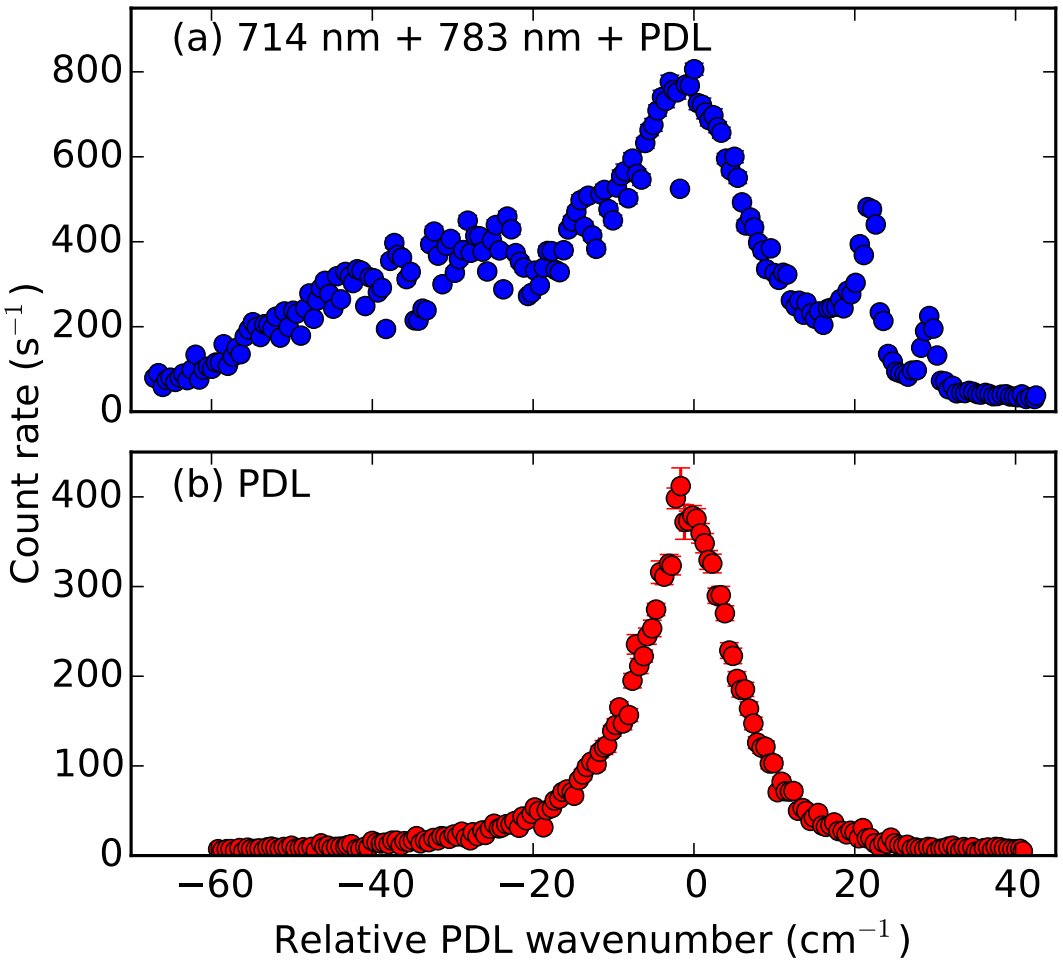

FIGURE 6.12: Scan of the PDL for ^{226}Ra with (a) 714-, 783- and PDL light (blue circles) entering the beamline and (b) only the PDL light (red circles) entering the beamline. The wavenumber is given relative to the offset value of 17971 cm^{-1}.

The highest observed count rate (800 s^{-1}) in Figure 6.12 (a) is seen at around 17971 cm^{-1}. Similarly, the highest observed count rate (400 s^{-1}) in Figure 6.12 (b) is seen at around 17971 cm^{-1}. This means that half of the observed peak count rate in Figure 6.12 (a) is due to resonant, non-selective background resulting from the PDL light ionizing atoms from higher-lying states. The linewidth of the peak seen in Figure 6.12 (b) is much greater than the linewidth of the pulsed-dye laser (0.3 cm^{-1}). This suggests that the resonance observed at 17971 cm^{-1} is an excitation to an auto-ionizing state. However, this does not correspond to the much wider 558-nm auto-ionizing state previously observed by RILIS with a centroid of 17932 cm^{-1} [38]. This auto-ionizing state can be seen as the wide

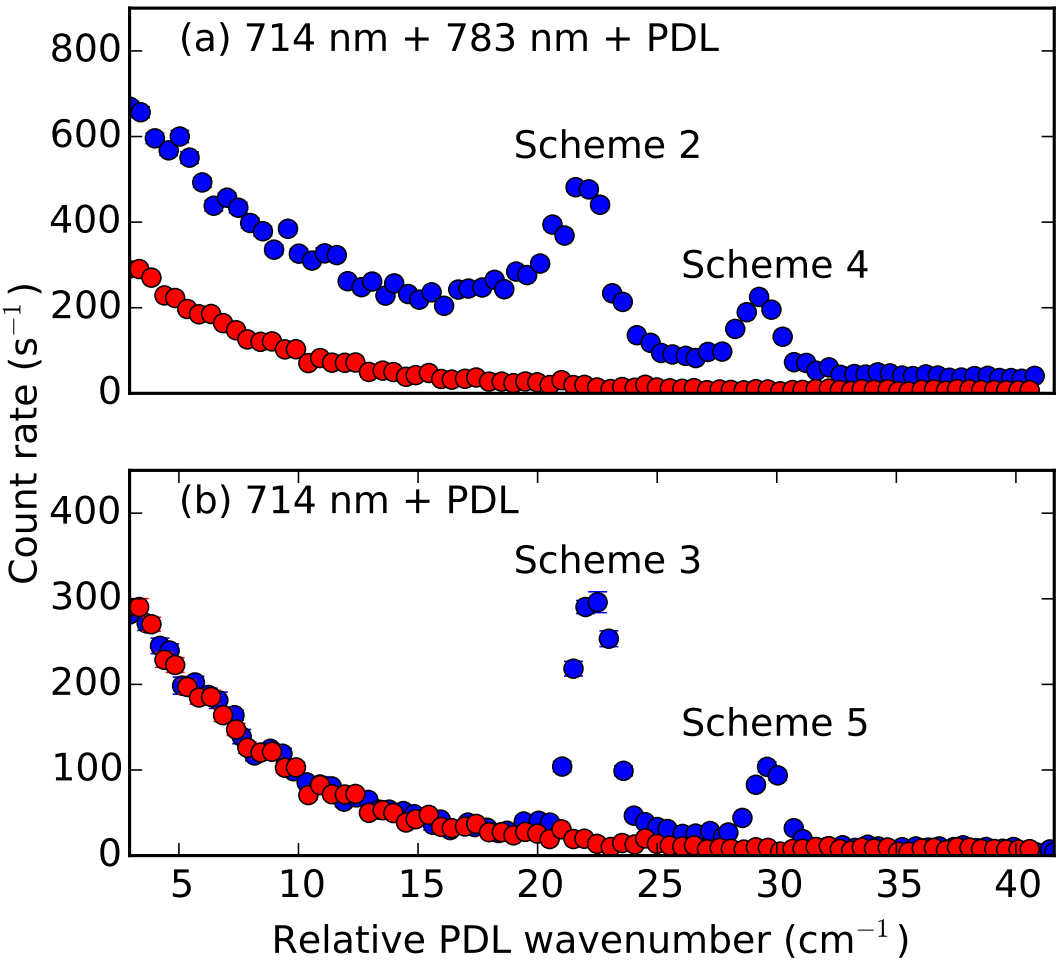

FIGURE 6.13: (a) Scan of the PDL transition in ^{226}Ra with 714-, 783- and PDL light entering the beamline (blue circles) and just the PDL light entering the beamline (red circles). (b) Scan of the PDL transition with the 714- and PDL light entering the beamline (blue circles) and just the PDL light entering the beamline (red circles). The different schemes listed in Table 6.7 are annotated. The wavenumber is given relative to the offset value of 17971 cm^{-1}.

structure to the left of the 17971-cm^{-1} resonance in Figure 6.12 (a)). This means that a high-lying long-lived state is strongly populated through charge-exchange with potassium at a beam energy of 30 keV. By considering the ionization potential of radium, this state must lie above 24601.36 cm^{-1}. However, it cannot be the $7s8s\ ^3S_1$ state lying at an energy of 26754.02 cm^{-1}. This is because it is short-lived (an upper limit on its lifetime of 19 ns can be calculated from the Einstein A coefficients of transitions to this state [118]). Furthermore, the RILIS ionization scheme populated this state and did not observe the 17971 cm^{-1} transition so it cannot be from this state.

Transition		Wavenumber (cm^{-1})	Literature (cm^{-1})
Initial state	Final state		
$7p\ ^3P_1^0$	$7d\ ^3D_1$	18001.57(6)	18001.44(7)
$7p\ ^3P_1^0$	$7d\ ^3D_2$	17994.29(4)	17994.05(7)
Unknown	Auto-ionizing state	17970.7(3)	-

TABLE 6.6: Fitted centroid frequencies of observed transitions in ^{226}Ra. Literature values are from Ref. [119].

Two additional smaller peaks were observed to the right of the largest one. Figure 6.13 (a) shows a scan of the PDL for ^{226}Ra with all 3 laser beams entering the beamline (blue circles) but cropped to only show the region to the right-hand side of the largest resonance. The red circles correspond to when just the PDL light was entering the beamline. Figure 6.13 (b) shows a scan of the PDL for ^{226}Ra with just the 714- and PDL light entering the beamline (blue circles) and with the PDL light only (red circles). The wavenumber is given relative to the offset value of 17971 cm^{-1}. The linewidth of these peaks is much narrower than the auto-ionizing states. They are also only observed when both 714- and PDL light is entering the beamline. This can be understood in terms of resonant transitions from the first excited $7p\ ^3P_1$ state to higher-lying excited states. Indeed, they correspond to the previously observed transitions from the $7p\ ^3P_1$ state to the $7d\ ^3D_1$ and $7d\ ^3D_2$ states. Excited radium atoms in the $7d\ ^3D_1$ and $7d\ ^3D_2$ states require a photon with a wavelength of 945 nm or less to be non-resonantly ionized. In this case, it is most likely that a photon produced by the PDL completes the ionization process as the photon density for this step in the interaction region is much higher than the other laser beams.

The signal-to-background ratio of the transitions to the $7d\ ^3D_1$ and $7d\ ^3D_2$ states is lower in Figure 6.13 (a) when compared to Figure 6.13 (b). The observed difference between the two must be a result to the 783-nm light. Resonantly ionized counts that do not originate from the ground state are considered as background.

Table 6.7 shows the signal, background and signal-to-background ratio for the

TABLE 6.7: Signal, background and signal-to-background ratios for the different schemes tested during the development period.

Scheme number	Scheme	PDL step wavenumber (cm^{-1})	Signal rate (s^{-1})	Background Rate (s^{-1})	Signal-to-background
1	714+783 +556	17971	780	380	2.1
2	714+783 $+555_{non-res}$	17994	460	220	2.1
3	714+555 $+555_{non-res}$	17994	290	20	15
4	714+783 $+555_{non-res}$	18001	200	20	10
5	714+555 $+555_{non-res}$	18001	90	10	9

different resonance ionization schemes discussed previously. Schemes 2, 3, 4 and 5 are annotated on Figure 6.13. Schemes 3,4 and 5 offer the best signal-to-background ratios. Schemes 3 (714+555+$555_{non-res}$, PDL wavenumber: 17994 cm^{-1}) and 5 (714+555+$555_{non-res}$, PDL wavenumber: 18001 cm^{-1}) have the advantage that they only require two lasers, making optimising the laser-atom overlap easier. Scheme 3 was chosen as it offered best signal rate and signal-to-background ratio of the two-laser schemes.

6.2.2.3 Ionization scheme used in the experiment

The ionization scheme used in the experiment is shown on the right-hand side of Figure 6.11. Atoms in the $7s^2\ ^1S_0$ ground state were excited to the $7p\ ^3P_1$ state using 714-nm light. The second transition further excited atoms from the $7p\ ^3P_1$ state to the $7s7d\ ^3D_2$ state using 555-nm light. The ionization process was completed by non-resonantly ionizing atoms from the $7s7d\ ^3D_2$ state using 555-nm light. The lasers used for each step are shown in Table 6.5.

The continuous-wave 714-nm light was 'chopped' into 200-ns pulses using a fast-switching setup, described earlier. This was done, despite the long lifetime (422 ± 20 ns [121]) of the $7s7p\ ^3P_1$ state and the spin of the $7s^2\ 1S_0$ ground state, to prevent pumping to magnetic sub-states. Only one fast-switching setup was used

due to the longer lifetime of the upper state. The 555-nm pulse followed after the 200-ns 714-nm pulse so that they did not overlap in time.

Chapter 7

Neutron-deficient francium

7.1 Motivation

7.1.1 Shape coexistence around $N = 104$ and $Z = 82$

Isotopes below $N = 126$ around the $Z = 82$ shell closure have been the subject of continued experimental and theoretical interest. In this region, low-lying excited states often possess different shape configurations to the ground state. This phenomenon is called shape coexistence [122–124].

The excitation of protons across the $Z = 82$ shell gap can lead to deformed nuclear states. Particle-hole ($p - h$) interactions between neutron holes below $N = 126$ and the excited proton(s) cause the deformed nuclear states to lower in energy. As the number of neutron holes increases and the associated proton to neutron-hole interactions increase, the excitation energy of these deformed states is lowered. This is exhibited in the excited 0^+ states of ^{196,198,200,202}Po whose excitation energy decreases with neutron number [125].

Towards the mid-shell region ($N = 104$), these states lower in energy and in some cases they become the ground state. The extremely large inverted odd-even staggering observed in the charge radii of neutron-deficient mercury ($Z = 80$)

isotopes is a famous example of this [126]. This results from a highly-deformed intruder configuration that becomes the ground state in ^{181,183,185}Hg. Another striking example involves the nucleus ^{186}Pb, lying exactly at the $N = 104$ mid-shell. Configurations involving no, $2p-2h$ and $4p-4h$ excitations across $Z = 82$ lead to a spherical ground state and two low-lying 0^+ states, one of which is oblate deformed and the other is prolate deformed [127]. These 3 states lie within 650 keV of each other and provide a textbook example of shape coexistence.

7.1.2 Intruder states in odd-Z trans-lead elements

Above $Z = 82$, less data in the vicinity of the $N = 104$ mid-shell is available. The addition of protons quickly shifts the proton dripline to higher neutron numbers resulting in rapidly decreasing yields as the mid-shell is approached. In odd-Z, even-N nuclei above $Z = 82$, a competition between the spherical $\pi 1h_{9/2}$ state and oblate-deformed $\pi 3s_{1/2}$ state occurs.

The $\pi 3s_{1/2}$ state is an intruder configuration where 1 proton from the $\pi 3s_{1/2}$ orbital beneath $Z = 82$ is excited across the shell gap to pair with the odd proton in the $\pi 1h_{9/2}$ orbital. This is shown for different odd-Z elements around $Z = 82$ in Figure 7.1. Below $Z = 82$, the spin-parities of the ground state and isomeric state are inverted compared to nuclei above $Z = 82$. The ground state configuration has a single proton in the $\pi 3s_{1/2}$ orbital which is excited across the $Z = 82$ shell gap to give a $9/2^-$ isomeric intruder state.

The excitation energy of the $\pi 3s_{1/2}$ intruder state decreases as the neutron orbitals beneath $N = 126$ are depleted. This intruder state becomes the ground state in ^{185}Bi ($N = 102$) [128–132] which is the heaviest known proton emitter [133]. In astatine ($Z = 85$), the intruder state [130, 134–139] becomes the ground state in ^{195}At ($N = 110$). In francium, the intruder state has been the subject of many studies and is thought to become the ground state in ^{199}Fr ($N = 112$) [140–145]. Two scenarios were suggested to explain the observed decay data in ^{199}Fr ($N = 112$) with the ground-state spin-parity suggested to be either

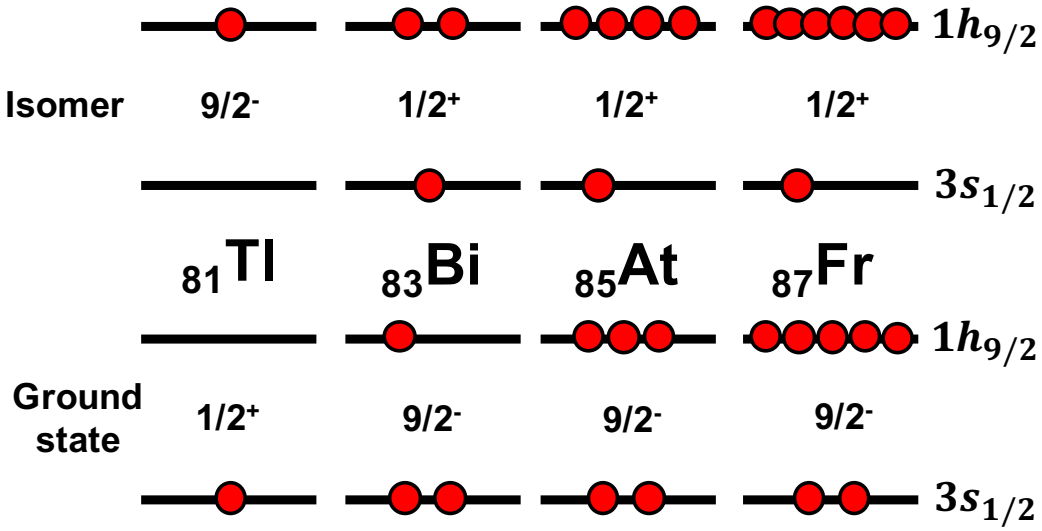

FIGURE 7.1: Schematic illustrating the occupation of the $\pi 3s_{1/2}$ and $\pi 1h_{9/2}$ orbitals for the ground (bottom) and isomeric intruder (top) states in odd-Z nuclei around $Z = 82$.

the $1/2^+$ intruder state or $7/2^-$ [144]. The near-degeneracy of the $1/2^+$ and $7/2^-$ states (47(7) keV) and limited statistics prevent the authors of Ref. [144] making firm conclusions about the ground-state spin-parity of ^{199}Fr. In another study, an onset of deformation was inferred from analysis of the decay properties of ^{199}Fr suggesting a ground-state spin-parity of $1/2^+$ from the intruder state configuration [143].

7.1.3 Laser-spectroscopy studies of the intruder state

In the bismuth isotope chain, the intruder state was studied with in-source laser spectroscopy [146]. The $\pi 1h_{9/2}$ ground states and $\pi 3s_{1/2}$ isomeric intruder states were measured in ^{193,195,197}Bi. The changes in mean-square charge radii of the ground states agreed with that of their isotones in the neighbouring proton-magic lead chain, which are spherical in shape. A large isomer shift is observed which is constant in magnitude for each of the 3 isotopes studied. This points to a significant degree of deformation in these isomeric states [146]. The isomeric states lie within 0.5 MeV of the ground state [147] which would support previous suggestions of shape coexistence in these isotopes.

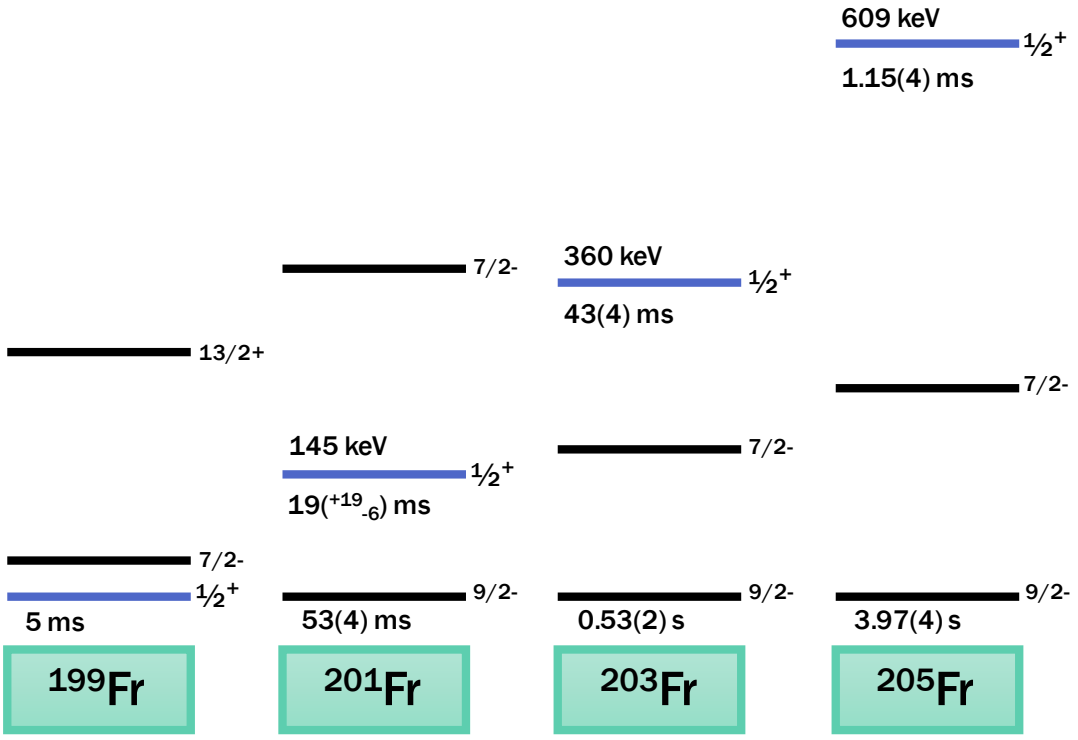

FIGURE 7.2: Energies, half-lives, spin-parities of selected low-lying levels in neutron-deficient even-N francium isotopes. Data is taken from Refs. [140–143].

The $\pi 1h_{9/2}$ intruder state was also studied with in-source laser spectroscopy in the thallium isotopes [148, 149]. Large isomer shifts were observed which were found to increase in magnitude as N decreases. In astatine, the isomer shifts in ^{197,199}At were measured with a smaller isomer shift observed in ^{197}At [150]. The isomer shift data for thallium, bismuth and astatine isotopes are shown in Figure 7.12 and will be discussed in detail later.

Laser spectroscopy has not yet been performed on the $\pi 3s_{1/2}$ intruder state in francium. The ground and low-lying excited states of the neutron-deficient even-N francium isotopes are shown in Figure 7.2 [140, 141]. The $\pi 3s_{1/2}$ intruder state is thought to become the ground state in ^{199}Fr [143] (a $7/2^-$ state is also suggested [144]). The short half-life of 1.15(4) ms in ^{205}Fr means that it would decay before reaching an experimental setup. In ^{203}Fr, the intruder state lies at excitation energy of 360 keV and has a half-life of 43(4) ms [140]. This makes ^{203}Fr an ideal nucleus to study potential shape coexistence in francium (if the yields of the ground and isomeric states are sufficient).

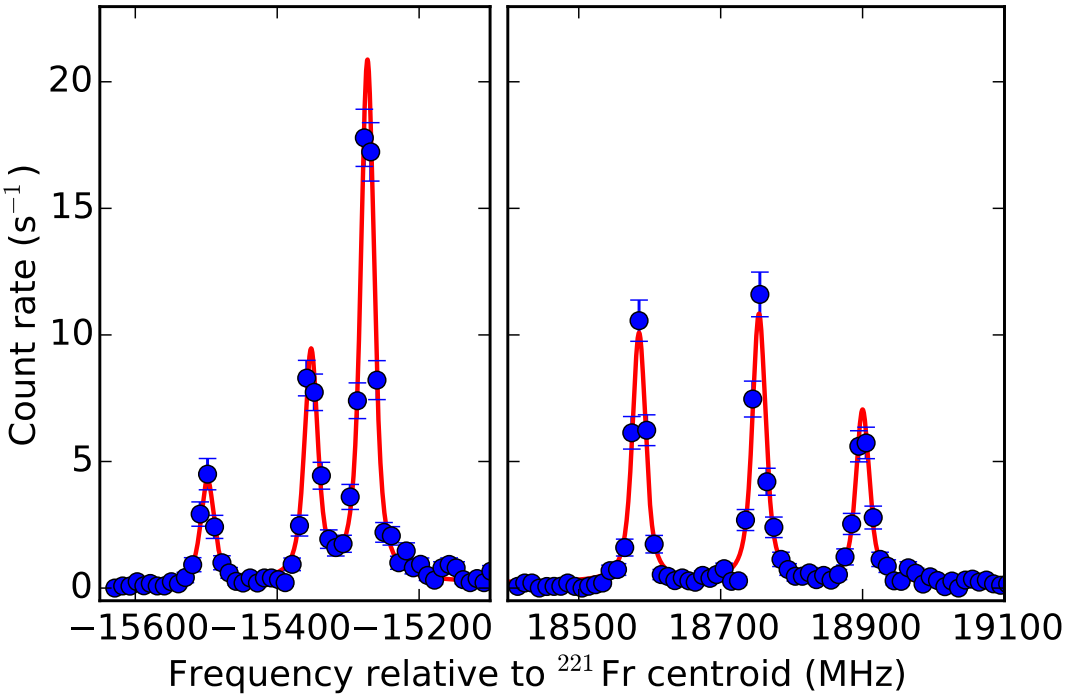

FIGURE 7.3: Example spectrum of the $7s\ ^2S_{1/2} \rightarrow 8p\ ^2P_{3/2}$ transition in ^{219}Fr. The FWHM is 25 MHz.

7.2 Results

7.2.1 Hyperfine A and B factors and isotope shifts

The isotope ^{219}Fr was used as the reference isotope throughout the experiment. However, all spectra and isotope shifts are given relative to ^{221}Fr to be consistent with earlier work [86–88, 151]. ^{219}Fr was chosen as the reference isotope due to its shorter half-life (20(2) ms) and shorter-lived progeny when compared to ^{221}Fr (286.1(10) s). The isotopes ^{213}Bi and ^{209}Pb lie in the decay chain of ^{221}Fr. Their half-lives of 45.6 m and 3.25 h, respectively, would implant long-lived activity onto the MCP for the duration of the experiment. The additional background would hinder searches for the isomer in ^{203}Fr. For ^{219}Fr, the longest half-life in its decay chain is 4.77 m for the isotope ^{207}Tl, making ^{219}Fr a better-suited reference isotope.

An example spectrum of ^{219}Fr is shown in Figure 7.3. The change in the centroid frequencies of the ^{219}Fr reference scans is shown in Figure 7.4. The uncorrected

centroid-frequency data are shown as blue circles. To account for the drift in centroid frequencies over the course of the experiment, a function was fitted to them. This was a sinusoidal function and is displayed by the red line in Figure 7.4. Each frequency data point was then corrected by an amount equal to the fitted function evaluated at the time of the frequency data point. This point-by-point correction was applied to the data and the analysis was performed again. The resulting centroid frequencies are plotted as white markers in Figure 7.4. The black dashed line shows the weighted average of the point-by-point corrected centroid frequencies.

The point-by-point correction was used in the initial processing of the data for the other isotopes measured during the experiment. This approach was preferred over simply correcting by using the centroid frequency of the closest-in-time reference scan. This is due to the long duration of some of the scans taken during the experiment. There were therefore periods of up to 6 hours in which a reference scan was not taken. An additional 5 MHz error was included to the weighted-average isotope shifts to account for this. This value was chosen as it is half of the total drift in the uncorrected ^{219}Fr centroid frequencies which was around 10 MHz.

The measured hyperfine A factors for the $7s\ ^2S_{1/2}$ and $8p\ ^2P_{3/2}$ states and hyperfine B factor for the $8p\ ^2P_{3/2}$ state in ^{219}Fr are shown in Figures A.1, A.2, A.3 respectively. Table 7.1 shows the measured hyperfine A and B factors and isotope shifts of ^{203,207,219,221}Fr.

Example spectra of ^{207}Fr and ^{221}Fr are shown in Figures A.4 and A.5. An example spectrum of ^{203}Fr is shown in Figure 7.5. The FWHM of the the data is 25 MHz.

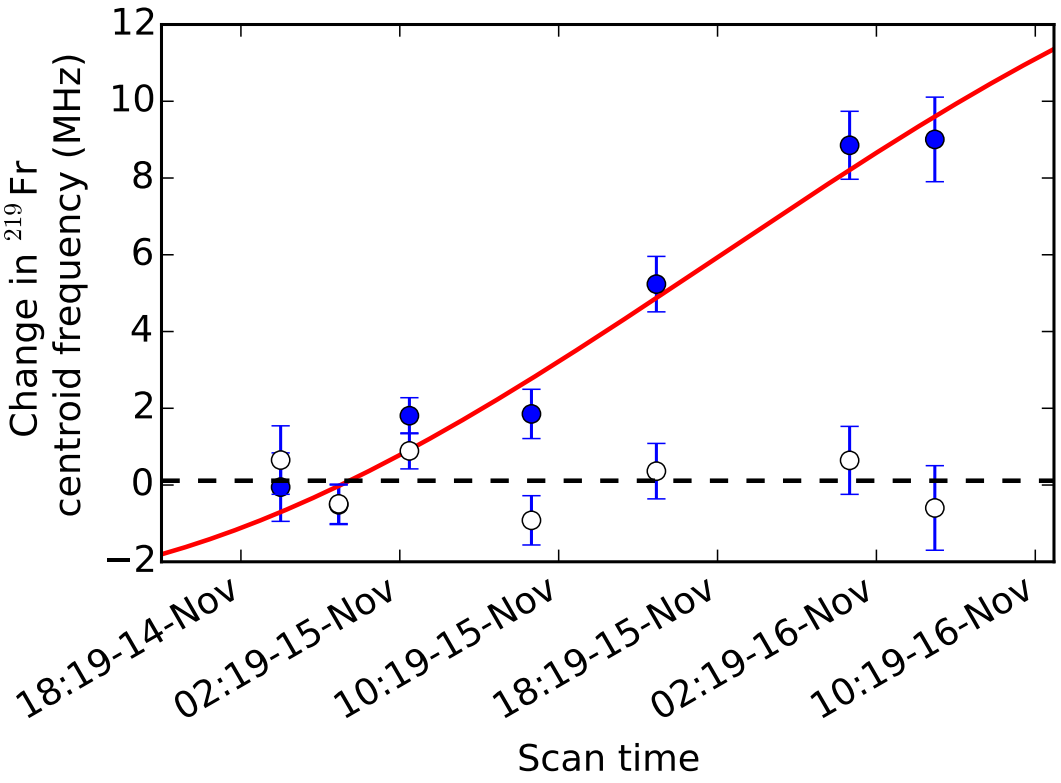

FIGURE 7.4: Centroid frequencies of ^{219}Fr reference scans during the experiment. The uncorrected centroids are shown as blue circles. The point-by-point corrected centroids are shown as white circles. The red line is the centroid-frequency correction function. The blacked dashed line is the weighted average of the point-by-point corrected centroids.

TABLE 7.1: Hyperfine A and B factors and isotope shifts measured during the experiment. All values are given in MHz. Literature values are also presented where they exist.

A	I^π		$A(7s\ ^2S_{1/2})$	$A(8p\ ^2P_{3/2})$	$B(8p\ ^2P_{3/2})$	$\delta\nu^{221,A}$	Ref.
203	$9/2^-$	This work	+8187(2)	+29.5(2)	-39.1(20)	+31327(7)	-
		Literature	+8180(30)	-	-	+31320(100)	[86]
207	$9/2^-$	This work	+8482(2)	+30.4(2)	-20.0(16)	+28495(7)	-
		Literature	+8484(1)	-	-	+28420(100)	[152]
219	$9/2^-$	This work	+6850(2)	+24.7(2)	-105(2)	+5475(5)	-
		Literature	+6851(1)	+24.7(5)	-104(1)	+5590(100)	[88, 89]
221	$5/2^-$	This work	+6211(2)	+22.6(2)	-84(2)	0	-
		Literature	+6210(1)	+22.4(1)	-85.7(8)	0	[153]

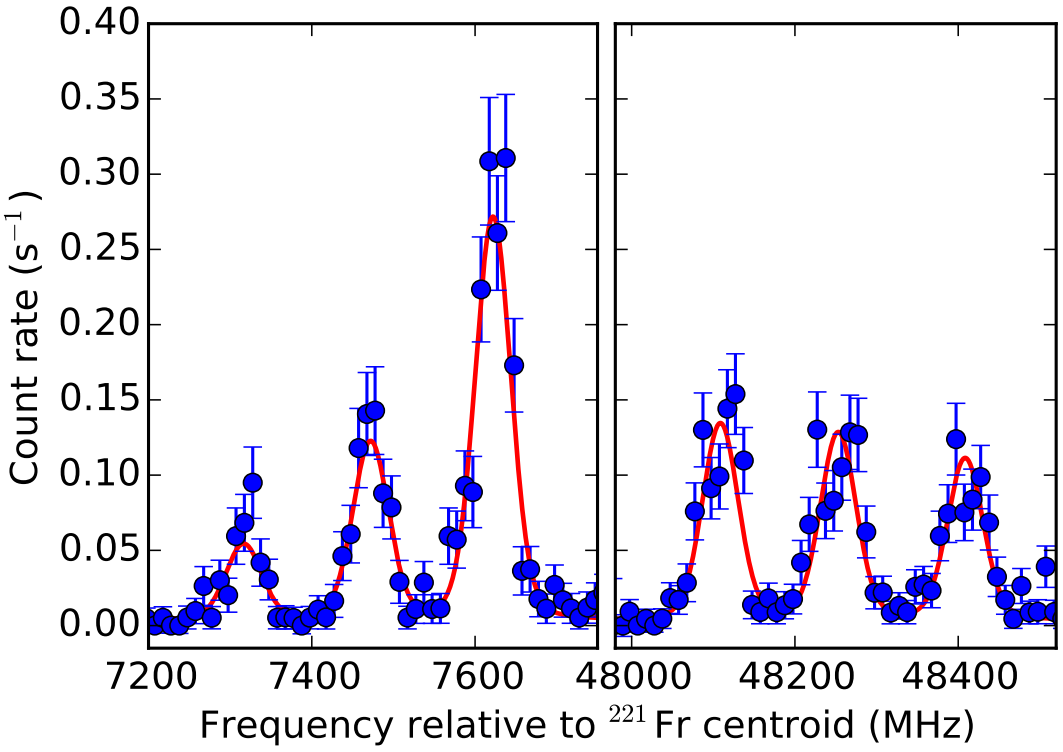

FIGURE 7.5: Example spectrum of the $7s\ ^2S_{1/2} \rightarrow 8p\ ^2P_{3/2}$ transition in ^{203}Fr. The FWHM of the data is 25 MHz.

7.2.2 Extraction of nuclear observables

7.2.2.1 Magnetic dipole moments

The magnetic dipole moments were calculated using Equation 2.9. The isotope ^{210}Fr was used as a reference [152, 154]: $I_{\text{ref}} = 6^+$, $\mu_{\text{ref}} = +4.38(5)\ \mu_N$, $A(7s\ ^2S_{1/2})_{\text{ref}} = +7195.9(9)$ MHz.

In Ref. [154], the hyperfine splitting of the $9s\ ^2S_{1/2}$ level in ^{210}Fr was precisely measured. This was combined with accurate *ab initio* calculations of the electronic wavefunctions in francium to extract the magnetic moment of ^{210}Fr. Only the A factor for the lower-state ($7s\ ^2S_{1/2}$) splitting was used to calculate the magnetic moment, due to its smaller relative uncertainty.

7.2.2.2 Spectroscopic electric quadrupole moments

No absolute spectroscopic quadrupole moment measurements have been made in the francium isotope chain. Consequently, theoretical calculations of the electric field gradient is required to relate $B(8p\ ^2P_{3/2})$ and Q_s.

In Ref. [155], Sahoo *et al.* calculated magnetic dipole and electric quadrupole hyperfine-structure constants for ^{210,212}Fr using the Dirac-Fock approximation, second-order many-body perturbation theory and the coupled-cluster method (CC). They calculate singles and doubles excitations for the CC approach. They extend this by also considering important triple excitations ($\mathrm{CCSD_{t3}}$) to improve the accuracy of the calculations. This results in the electric quadrupole hyperfine-structure constant for the $8p\ ^2P_{3/2}$ state as

$$\frac{B(8p\ ^2P_{3/2})}{Q_s} = +84.01\ \text{MHz/b}. \tag{7.1}$$

No error is given for this quantity.

7.2.2.3 Change in mean-square charge radii

The changes in mean-square charge radii were calculated using Equation 2.21. The mass- and field-shift constants were taken as:

$$M_{422} = +750(330)\ \text{GHz amu} \tag{7.2}$$

and

$$F_{422} = -20.67(21)\ \text{GHz fm}^{-2}, \tag{7.3}$$

from previous work [87] where a King-plot analysis was performed to extract atomic F and M factors from the calculated atomic factors for the 718-nm transition [156].

TABLE 7.2: Spins, magnetic dipole moments, spectroscopic electric quadrupole moments and changes in the mean-square charge radii measured in the experiment. Literature values are also presented where they exist.

A	I^π		μ (μ_N)	Q_s (b)	$\delta\langle r^2\rangle^{221,A}$	Ref.
203	$9/2^-$	This work	+3.74(4)	-0.47(2)	-1.5302(2)(168)	-
		Literature	+3.73(4)	-	-1.530(18)	[86]
207	$9/2^-$	This work	+3.87(4)	-0.24(2)	-1.3897(2)(149)	-
		Literature	+3.87(4)	-0.16(5)	-1.386(16)	[152]
219	$9/2^-$	This work	+3.13(4)	-1.25(2)	-0.2664(2)(28)	-
		Literature	+3.13(4)	-1.24(1)	-0.272(5)(6)	[88, 89]
221	$5/2^-$	This work	+1.58(2)	-1.00(2)	0	-
		Literature	+1.57(2)	-1.00(1)	0	[89, 152]

7.3 Discussion

The spins, magnetic moments, spectroscopic quadrupole moments and changes in the mean-square charge radii are shown in Table 7.2.

The measured hyperfine A and B factors and isotope shifts in Table 7.1 show good agreement with literature. The errors on A($7s\ ^2S_{1/2}$) and the isotope shift of ^{203}Fr have been reduced by more than an order of magnitude. Despite this reduction, the precision of the magnetic moment of ^{203}Fr has not improved as the uncertainty is dominated by the reference value. As expected, the statistical uncertainty on the relative charge radii of ^{203}Fr has reduced, with the systematic error from the atomic F and M factors still dominating the overall uncertainty.

7.3.1 Spin of ^{203}Fr

Due to the linewidth (1.5 GHz) of the laser used in the previous CRIS measurements of ^{203}Fr [86], no direct assignment of the spin could be made as the upper-state ($8p\ ^2P_{3/2}$) splitting was not resolved. The reported magnetic moments and charge radii used spins assigned by recoil-decay tagging studies [140]. The new measurements have a FWHM of 25 MHz which allows an A-factor ratio analysis to be performed.

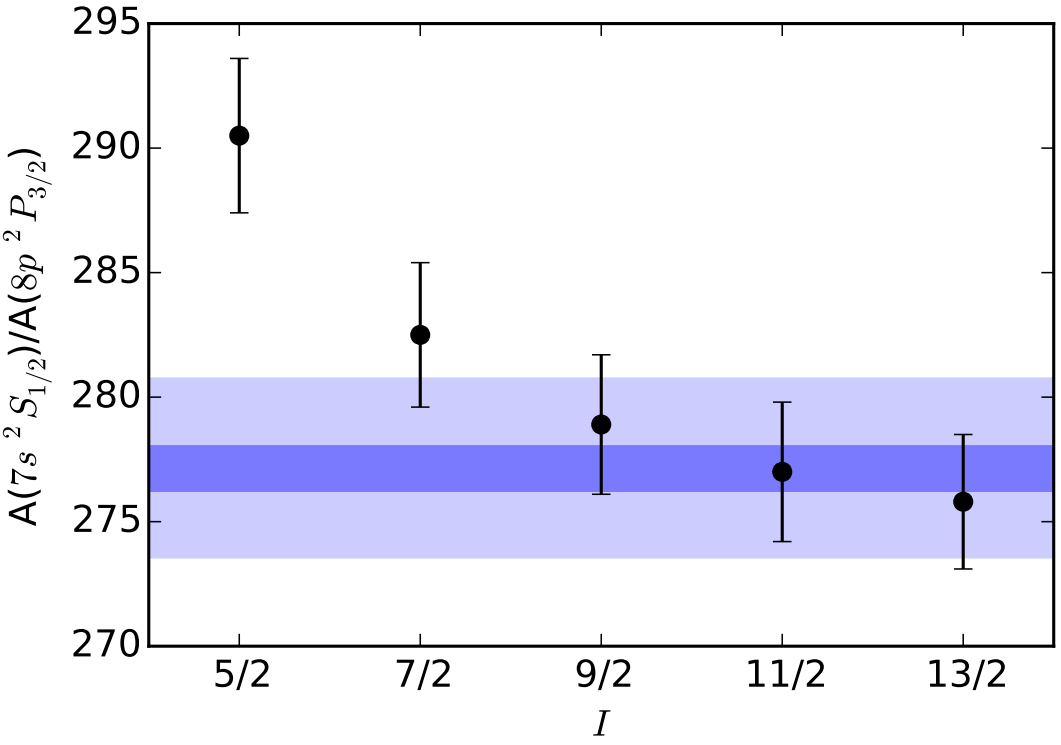

FIGURE 7.6: The ratio of hyperfine A factors of the $7s\ ^2S_{1/2}$ and $8p\ ^2P_{3/2}$ states in ^{203}Fr for different spins.

In the absence of a hyperfine anomaly, the ratio of the A factors for any two atomic states in an element is constant. To perform an A-factor ratio analysis, an isotope of a given element is fitted assuming different spins. The A-factor ratio, $A(7s\ ^2S_{1/2})/A(8p\ ^2P_{3/2})$ in this case, is calculated for each spin and compared to the isotope of the same element for which it is known to the highest precision. In the case of francium, this is the isotope ^{221}Fr however for reasons that will be discussed later, the isotope ^{213}Fr will be used despite a marginally worse precision.

By taking the ratio of the A factors of the $7s\ ^2S_{1/2}$ and $8p\ ^2P_{3/2}$ states in francium, the spin can be determined in a model-independent way, given a sufficient experimental precision on the A factors. This method was used in combination with a g-factor analysis to determine the spin of the 10^- isomer in ^{206}Fr [90, 157]. It was also used to unambiguously determine the spins of ^{76,77}Cu [158]. The A-factor ratio begins to converge at higher spins, making a firm assignment more difficult.

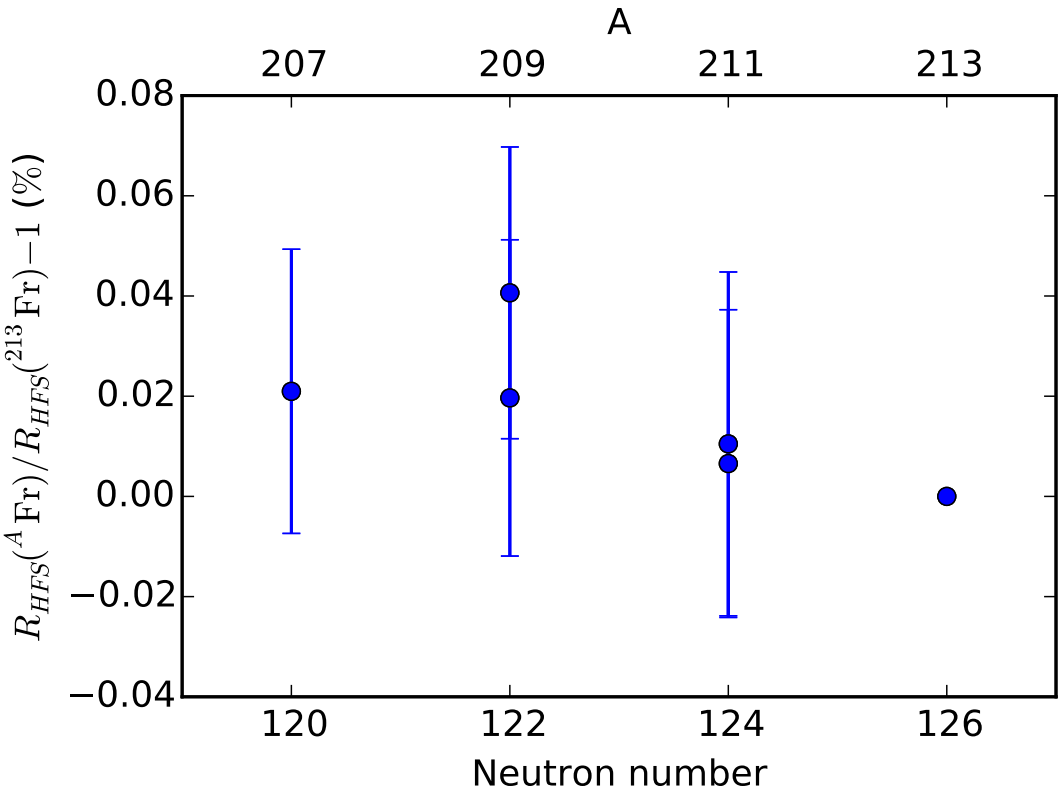

FIGURE 7.7: The percentage change in the ratio of hyperfine A factors of the $7s\ ^2S_{1/2}$ and $7p\ ^2P_{1/2}$ states for even-N francium isotopes. The data is taken from Refs. [160, 161].

Figure 7.6 shows the ratio of the A factors of the $7s\ ^2S_{1/2}$ and $8p\ ^2P_{3/2}$ states. The dark-blue shaded area is the A-factor ratio of ^{213}Fr [153]. The light-blue shaded area is a ± 1 % limit arising from the hyperfine anomaly in francium isotopes (including odd-odd isotopes ^{206,208,210}Fr) [159, 160]. If the upto 1 % hyperfine anomaly is taken into account, a firm spin assignment is not possible as the A-factor ratio for spins 7/2, 9/2, 11/2 and 13/2 all overlap with the light-blue shaded area.

The hyperfine anomaly has been studied in francium [160, 161]. In Ref. [160], Zhang *et al.* performed high-precision measurements of the $7p\ ^2P_{1/2}$ splitting on ultra-cold francium atoms in a magneto-optical trap. They showed that the hyperfine anomaly in the even-N ^{207,209,211,213}Fr isotopes was near constant (compared to the up to 1% anomaly observed in the odd-odd ^{206,208,210}Fr isotopes), suggesting these isotopes as being particularly suitable for atomic-parity violation

measurements. Figure 7.7 shows the percentage change in the ratio of hyperfine A factors for the $7s\ ^2S_{1/2}$ and $7p\ ^2P_{1/2}$ states compared to the ratio for ^{213}Fr. From this, the hyperfine anomaly can be concluded to be less than 0.1 % for even-N isotopes below $N = 126$. This reduces the width of the lighter-shaded area by a factor of at least 10. Even with this reduction, the A-factor ratio resulting from spins 9/2, 11/2 and 13/2 all overlap with the dark-blue shaded area, making a firm spin assignment impossible with the current data.

7.3.2 Spectroscopic quadrupole moments

The spectroscopic quadrupole moments of even-N francium isotopes below the $N = 126$ shell closure are shown in Fig. 7.8. As the literature values of quadrupole moments in Refs. [152, 157] were published before the publication of B/Q_s values in Ref. [13], they were re-evaluated using

$$\frac{B(7p\ ^2P_{3/2})}{Q_s} = +259.73 \text{ MHz/b}. \tag{7.4}$$

This was done to ensure consistency when comparing the spectroscopic quadrupole moments obtained from measurements on different atomic states. This increases the Q_s values of ^{205,207,209,211,213}Fr measured through the $7p\ ^2P_{3/2}$ state by approximately 1%. However, this is much smaller than the statistical uncertainty.

The data between $N = 118 - 126$ is fitted with a linear trend, shown by the dashed line, to guide the eye. A departure from this trend is observed at ^{203}Fr ($N = 116$) suggesting an onset of static deformation. A small deviation from the literature value of ^{207}Fr ($N = 120$) can be seen in the new measurement. The uncertainty of the new measurement is reduced and it agrees better with the trend seen between $^{205-213}$Fr. The literature value for ^{207}Fr comes from Ref. [152] published in 1985. In that work, ^{207}Fr was the most exotic isotope investigated.

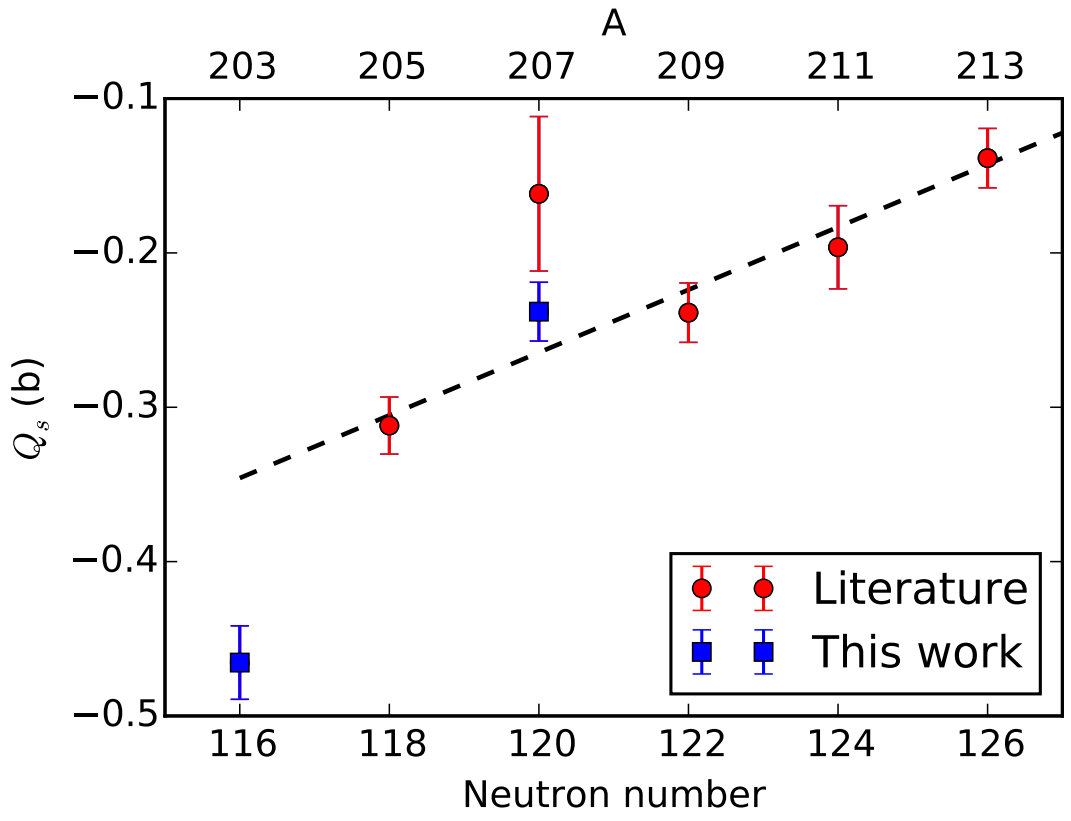

FIGURE 7.8: Spectroscopic quadrupole moments of even-N francium isotopes below the $N = 126$ shell closure. This work is shown as blue squares, literature values are shown as red circles [152, 157]. A linear fit of the data between $N = 118 - 126$ is shown as a dashed line, to guide the eye.

7.3.3 Evolution of quadrupole deformation in trans-lead elements below $N = 126$

In Ref. [12], the quadrupole moments of different nuclear states involving $\pi 1h_{9/2}$ configurations below $N = 126$ in the trans-lead elements were compared. The magnitude of the quadrupole moments of the trans-lead elements at a given neutron number vary due to the differing amount of $\pi 1h_{9/2}$ protons (and holes). To allow the evolution of quadrupole deformation of these different states to be compared, the spectroscopic moments of a given state are divided by their value at $N = 126$. These normalized quadrupole moments allow the relative evolution of static deformation in different nuclear states to be directly compared.

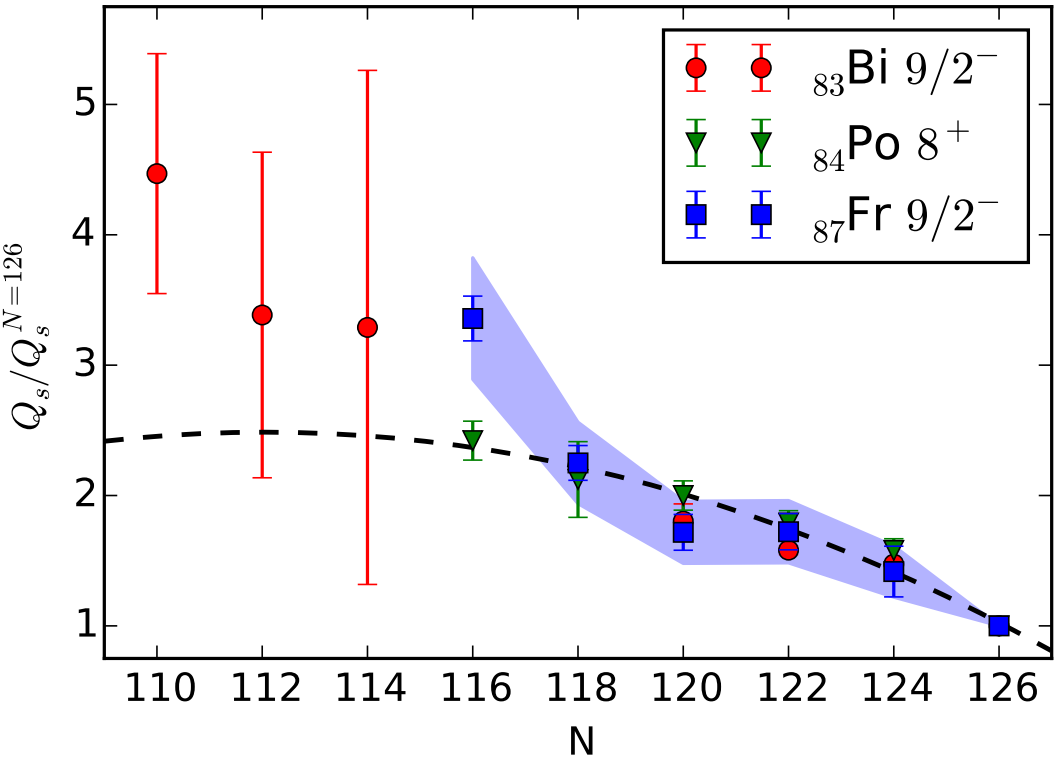

FIGURE 7.9: Ratio of quadrupole moments below $N = 126$ to the quadrupole moment at $N = 126$ for the $9/2^-$ ground states in bismuth (red circles) [162], francium (blue squares) [152, 157] and 8^+ states in polonium (green triangles) [163]. The shaded area indicates the contribution of the uncertainty on Q_s of $^{213}_{87}\mathrm{Fr}_{126}$ on the normalized quadrupole moments of the francium isotopes. The dashed line results from a quadratic fit of selected data (see text).

An increase in the normalized quadrupole moments of $\pi h^n_{9/2}$ configurations between $Z = 83 - 87$ was observed as the number of neutron holes in the N=126 shell increases in the following states [12]:

- $9/2^-$ states in bismuth from $\pi h_{9/2}$
- 8^+ states in polonium from $\pi h^2_{9/2}$
- $21/2^-$ states in astatine from $\pi h^3_{9/2}$
- $29/2^-$ states in astatine from $\pi h^2_{9/2} i_{13/2}$
- 8^+ states in radon from $\pi h^4_{9/2}$
- $29/2^-$ states in francium from $\pi h^4_{9/2} i_{13/2}$.

The normalized quadrupole moments were observed to saturate with decreasing neutron number, reaching an apparent maximum at $N = 114$. In Ref. [12], a parabolic trend was fitted to the normalized quadrupole moments of the above states. This allowed the effective proton charge at $N = 114$ to be extracted as $e_\pi^{\rm emp}(N = 114)/e_\pi^{\rm emp}(N = 126) = 2.42$. This value was used in calculations of the neutron-dependent quadrupole core polarization. This is usually estimated from experimental $B(E2)$ transition probabilities however data only existed down to $N = 116$ at the time [163].

The proposed behaviour of increasing quadrupole deformation which saturates with decreasing neutron number can be tested further by including data for the $9/2^-$ ground states in francium [152, 157] and the 8^+ isomeric states in radium [164]. Figure 7.9 shows the normalized quadrupole moments of the 8^+ isomeric states in polonium (green triangles), and the $9/2^-$ ground states in bismuth (red circles) and francium (blue squares). For clarity, these states are the only ones displayed in Figure 7.9, as they have the largest datasets of measured quadrupole moments. As the bismuth and francium quadrupole moment measurements were obtained through laser spectroscopy, the ratio of spectroscopic quadrupole moments is equal to the ratio of hyperfine B factors,

$$\frac{Q_s^N}{Q_s^{N=126}} = \frac{B_N \frac{B_{\rm ref}}{Q_{s,{\rm ref}}}}{B_{N=126} \frac{B_{\rm ref}}{Q_{s,{\rm ref}}}} = \frac{B_N}{B_{N=126}}, \tag{7.5}$$

and thus independent of any electric-field gradient calibration. For the francium data, the quadrupole moments measurements were obtained from different atomic states. To relate the hyperfine B factors from different atomic states, the theoretical $B(7p\ ^2P_{3/2})/B(8p\ ^2P_{3/2}) = 3.09$ scaling factor was used to determine the normalized quadrupole moments [155]. This theoretical scaling factor agrees perfectly with the scaling factor $B(7p\ ^2P_{3/2})/B(8p\ ^2P_{3/2}) = 3.08(6)$ determined through experimental measurements [90, 152, 153, 157]. The shaded-blue area on the francium data in Figure 7.9 is the contribution of the $Q_s^{N=126}(^{213}{\rm Fr})$ uncertainty to the overall uncertainty on the normalized quadrupole moments. The contribution of the $Q_s^{N=126}$ uncertainty is not shown for the bismuth and

polonium data as it is negligible compared to the overall uncertainty on the normalized quadrupole moments. The dashed line in Figure 7.9 is a quadratic fit of the states originally fitted in Ref. [12] in addition to the $9/2^-$ states in francium (down to ^{205}Fr at $N = 118$ [152, 157]) and the 8^+ states in radium [164]. The ^{203}Fr moment is not included in the fit due to its deviation. The bismuth data for $N = 110 - 114$ is not included due to its low precision. The effective proton charge at $N = 114$ is derived here using the fit displayed in Figure 7.9. The value of $e_\pi^{\mathrm{emp}}(N = 114)/e_\pi^{\mathrm{emp}}(N = 126) = 2.46(14)$ is in good agreement with the value of 2.42 derived in Ref. [12].

The normalized quadrupole moments of $\pi 1h^n_{9/2}$ states in bismuth, francium and polonium follow a very similar trend in Figure 7.9. The increase in quadrupole deformation of these states follow this trend as the number of neutron holes below $N = 126$ increases. This agreement continues down to $N = 118$. This increase is due to the enhancement of quadrupole collectivity resulting from increased proton-neutron correlations as more neutron holes appear [12]. This behaviour appears to be independent of the proton configuration for a given state. This steady increase of core polarization begins to saturate as the number of neutron holes increases, reaching an apparent maximum at $N = 112$, as seen in Figure 7.9.

The francium chain shows the earliest deviation from this trend at $N = 116$ (^{203}Fr), suggesting a sudden onset of static deformation. This contrasts the continued steady increase observed in the polonium data due to the gradual onset of core polarization. Another possible deviation may occur in the bismuth chain at $N = 110$, requiring 6 additional neutrons to be removed compared to francium. High-resolution measurements of bismuth isotopes are required below $N = 120$ to confirm where a deviation from the trend occurs. The in-source measurements suggest it occurs at $N = 110$. However, this is currently a 2σ effect, preventing firm conclusions.

TABLE 7.3: Intrinsic quadrupole moments, calculated static and total deformation parameters and the static deformation ratios of even-N francium isotopes below $N = 126$.

A	N	Q_0 (b)	$\langle\beta_2\rangle$	β_2^{rms}	Static ratio (%)
203	116	-0.85(4)	-0.026(1)	0.111(2)	24(1)
205	118	-0.57(3)	-0.017(1)	0.085(2)	20(1)
207	120	-0.44(3)	-0.013(1)	0.066(3)	20(2)
209	122	-0.44(4)	-0.013(1)	0.059(2)	22(2)
211	124	-0.36(5)	-0.11(1)	0.060(4)	19(3)
213	126	-0.25(4)	-0.008(1)	0.062(3)	12(2)

7.3.4 Estimating the static component of the nuclear deformation

Table 7.3 shows the calculated intrinsic quadrupole moments, static and total deformation parameters and static deformation ratios for even-N francium isotopes below $N = 126$.

The intrinsic quadrupole moments, Q_0, were calculated in the strong-coupling limit in Equation 2.30. The static deformation parameters, $\langle\beta_2\rangle$, were calculated from the intrinsic quadrupole moments using Equation 2.31 using the second parametrization of the liquid-droplet model presented in Ref. [20] to calculate $\langle r^2\rangle_{sph}$. The total deformation parameters, β_2^{rms}, were determined by comparing changes in the mean-square charge radius with droplet-model calculations. Figure 7.10 (top) shows changes in the mean-square charge radii of neutron-deficient francium and lead isotopes below the $N = 126$ shell closure. Iso-deformation lines corresponding to $\beta_2^{rms} = 0, 0.1, 0.15, 0.2$ are plotted as dashed-dotted lines. The second parametrization of the liquid-droplet model in Ref. [20] is used. As francium is an odd-Z isotope chain, no estimation of β_2^{rms} through experimental B(E2) or $E(2^+)$ values is possible. Therefore $\beta_2^{rms}(^{213}\mathrm{Fr})$ is assumed to be equal to $\beta_2^{rms}(^{212}\mathrm{Rn}) = 0.062$. This was estimated through the energy of the first 2^+ state in ^{212}Rn using [22, 165]:

$$\beta_2^{rms} = \frac{466(41)}{A\sqrt{E(2^+)}}, \tag{7.6}$$

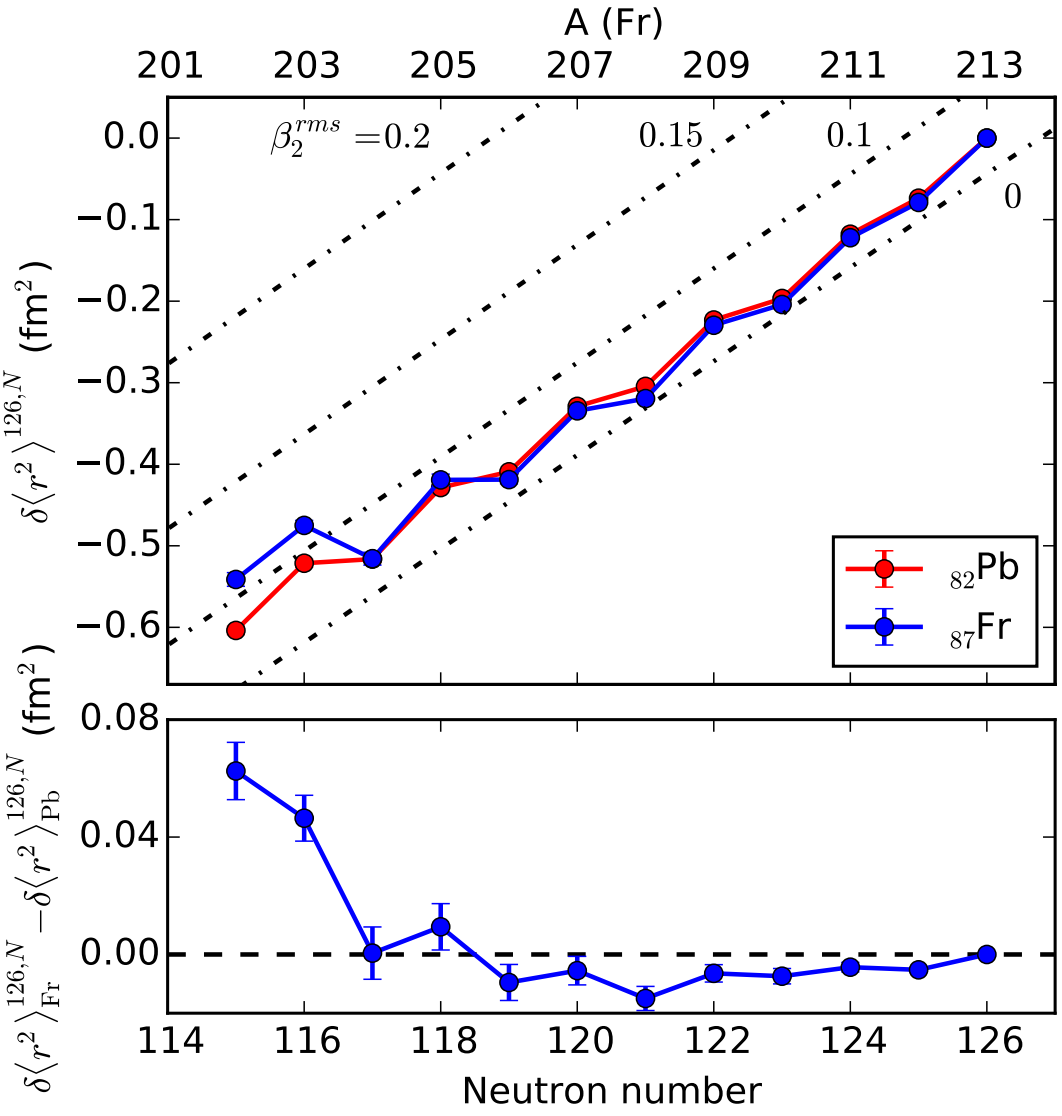

FIGURE 7.10: Changes in mean-square charge radii of neutron-deficient francium (blue circles) and lead (red circles) isotopes below the $N = 126$ shell closure (top). Iso-deformation lines corresponding to $\beta_2^{rms} = 0, 0.1, 0.15, 0.2$ are plotted as dashed-dotted lines. The difference in the changes in mean-square charge radii of neutron-deficient francium and lead isotopes (bottom).

where $E(2^+)(^{212}\text{Rn}) = 1273.8$ keV. Figure 7.10 (bottom) shows the difference in behaviour of changes in the mean-square charge radii of francium and lead isotopes [166–169]. The sudden increase observed in ^{203}Fr at $N = 116$ suggests an onset of deformation [86].

The evolution of the static and total deformation parameters for even-N francium isotopes is shown in Figure 7.11. The magnitude of the static deformation parameters, $|\langle\beta_2\rangle|$, increases as N decreases as is expected from the behaviour of

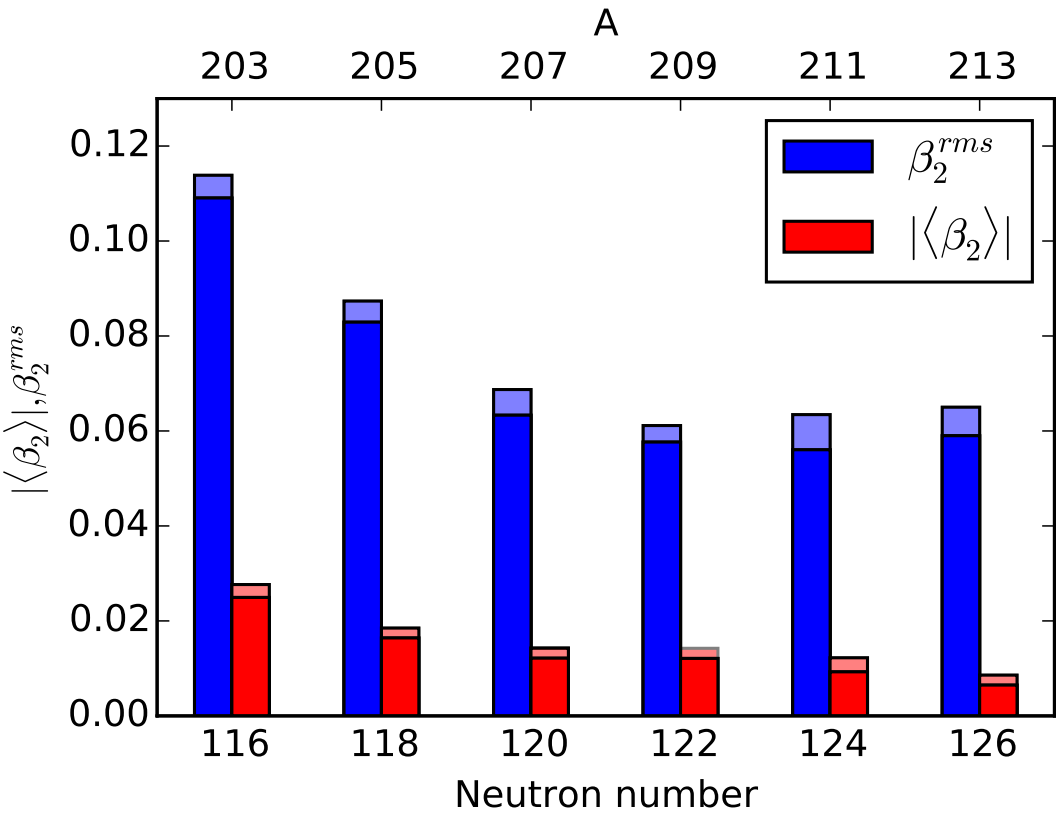

FIGURE 7.11: Calculated static and total deformation parameters for even-N francium isotopes below $N = 126$. The magnitude of the static deformation parameters $\langle\beta_2\rangle$ are shown as red bars. The total deformation parameters β_2^{rms} are shown as blue bars. The lighter-shaded areas at the top of the bars are the $\pm 1\sigma$ boundary around the calculated value.

the spectroscopic quadrupole moments seen in Figure 7.8. Despite the significant increase in static deformation observed in ^{203}Fr, the static deformation parameter comprises only 24(1)% of the total deformation. Therefore, ^{203}Fr cannot be be considered as purely statically deformed. The increase in static deformation cannot fully account for the departure of its relative charge radius from the proton-magic lead chain seen in Figure 7.10 [86], indicating the presence of other effects. In the polonium isotope chain, the observed onset of ground-state deformation, occurring at $N = 114$, was interpreted to be due to an increased admixture of deformed configurations [170], in the beyond mean-field picture. Theoretical input is needed to investigate the causes of the onset of deformation in neutron-deficient francium isotopes.

7.4 Outlook

The remaining cases that can be measured in neutron-deficient francium are challenging. The next experiment could either focus on measuring the intruder state in ^{203m}Fr or the ground state of ^{201}Fr. This section will discuss the feasibility of performing measurements on ^{203m}Fr.

7.4.1 Feasibility of measuring ^{203m}Fr

The isomer in ^{203}Fr presents a challenging case for laser spectroscopy. Production yields of 500 s^{-1} (ground state) and 1 s^{-1} (isomer) were extrapolated from α-particle decay rates at the WINDMILL experiment at ISOLDE [171]. When the alpha-decay branching ratio of 20(4)% [140] is accounted for, the total yield of ^{203}Fr is estimated as 5 s^{-1}. This low production rate is compounded by the large (10-100 GHz) hyperfine structures present in heavy elements which require a large frequency space to be scanned in order to first identify each multiplet of the isomer.

7.4.1.1 Choice of laser system

Due to the $1/2^+$ spin of the isomer, no quadrupole splitting will be present in its hyperfine structure. As francium isotopes possess large ground-state splittings (30-50 GHz) and field shifts, measurements of the magnetic dipole moments and change in mean-square charge radii using a lower-resolution laser (1-GHz linewidth) can achieve a similar precision to measurements using a high-resolution laser. This could be produced by a Z-cavity Ti:Sa laser using both a thin and thick etalon in the cavity [101]. The lack of a stable or long-lived isotope in francium means that the precision on the magnetic moment measurements is limited by the uncertainty on the reference value used to calculate them. The uncertainty on changes in the mean-square charge radii in francium is dominated by the systematic uncertainty from the atomic factors. Using a lower-resolution laser,

such as a Z-cavity Ti:Sa, will reduce the number of steps needed to scan a given frequency range, without significantly sacrificing precision on the measured observables. However, this is only possible if the hyperfine structures of the ground and isomeric state are well separated. A measurement using a high-resolution laser is required to confirm the spin of any observed isomeric state.

7.4.1.2 Contamination and background

The main contaminant in the beam will be the ^{203}Fr ground state which is produced with a yield of approximately 500 s^{-1}. Assuming a total experimental efficiency of 1%, as achieved in previous CRIS experiments [86, 89], the detected resonantly-ionized ^{203m}Fr rates for each of the 3 peaks would be approximately $0.006s^{-1}$, $0.03s^{-1}$ and $0.01s^{-1}$. A non-resonant collisional ionization rate of $1 : 10^5$, as seen in previous experiments on francium [86], would result in a background rate of $0.01s^{-1}$. However, the fitted background rate from the ^{203}Fr data presented earlier is 0.004(1) s^{-1}, a factor of 2.5 smaller than the initial experiments. Since this francium experiment, a new charge-exchange cell chamber and vacuum pumps were installed, improving the interaction-region pressure by over an order of magnitude.

7.4.1.3 Estimation of hyperfine structure

Figure 7.12 shows the isomer shifts for neutron-deficient thallium (blue squares) and bismuth (red circles) isotopes. Barzakh *et al.* showed that the large isomer shift, $\delta\langle r^2\rangle^{g,m}$, was constant for ^{193,195,197}Bi [146]. They also noted that this was similar to the isomer shifts observed in thallium [148, 172]. In a later publication, the isomer shifts for the more neutron-deficient thallium isotopes were measured [149] with larger shifts observed for the very neutron-deficient thallium isotopes. The isomer shifts were also measured in ^{197,199}At [150] with a smaller isomer shift observed in ^{197}At, compared to ^{199}At.

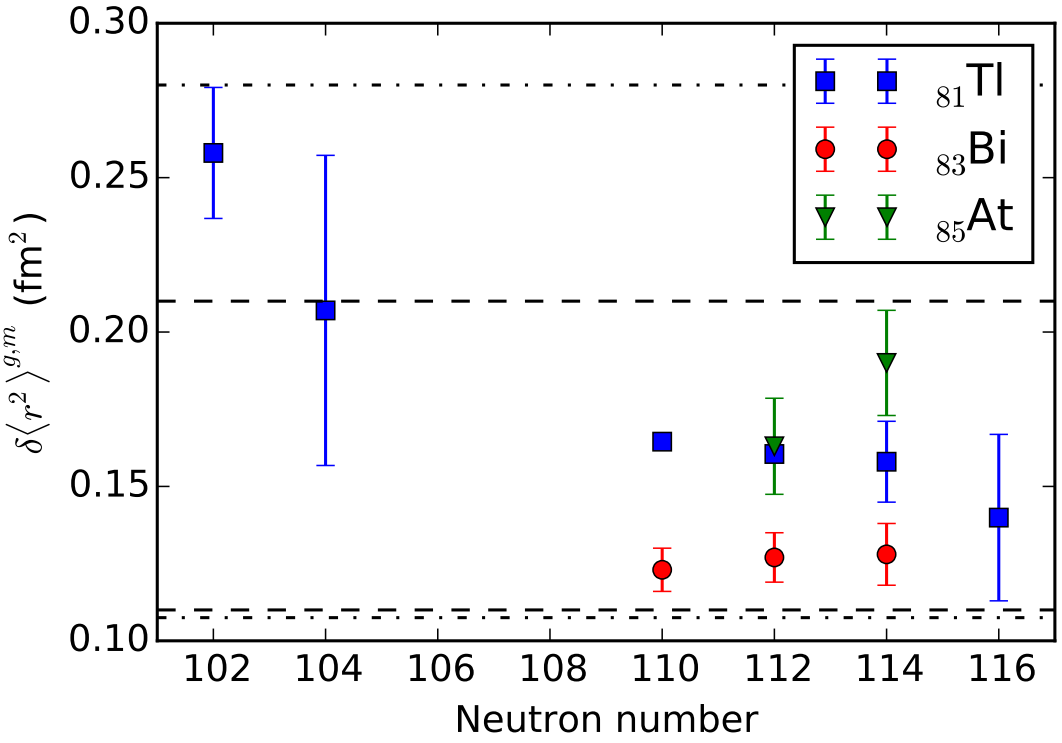

FIGURE 7.12: Isomer shifts in neutron-deficient thallium (blue squares), bismuth (red circles) and astatine (green triangles) isotopes. The dashed and dashed-dotted lines represent the two ranges used to estimate the isomer shift in ^{203}Fr. The data is taken from Refs. [146, 148–150, 172]

If one assumes the isomer shift in francium is similar to thallium and bismuth, this can be used to estimate the centroid of the isomer relative to the ground state in ^{203}Fr. Two ranges for the isomer shift in ^{203}Fr are displayed by the dashed and dashed-dotted lines. Range 1 (indicated by dashed lines in Figure 7.12) uses only the isomer shifts close to the same neutron number as ^{203}Fr ($N = 116$) in its estimation. Range 2 (indicated by dashed-dotted lines in Figure 7.12) is a more conservative range using all available isomer shift data. The ranges are presented in Table 7.4. Range 1 and Range 2 are +0.11 to +0.21 fm^2 and +0.11 to +0.28 fm^2, respectively.

The A factors can be assumed to be similar to other states of the same spin-parity in francium: ^{229,231}Fr [88]. Estimates can also be made using the magnetic moments of the $1/2^+$ states in thallium, bismuth, francium. Table 7.5 shows the magnetic moment range for the $1/2^+$ states in thallium, bismuth and francium isotopes and the corresponding range in MHz for $A(7s^2S_{1/2})$.

TABLE 7.4: Two ranges for the estimation of the isomer shift in ^{203}Fr. Range 1 uses only the isomer shifts close to $N = 116$. Range 2 uses all available isomer shifts down to $N = 102$.

Range	Linestyle	Isomer shift (fm^2)		Isomer shift (MHz)	
		Lower	Upper	Lower	Upper
1	Dashed	+0.11	+0.21	-4300	-2200
2	Dashed-and-dotted	+ 0.11	+0.28	-5800	-2200

TABLE 7.5: Estimated range of $A(7s^2S_{1/2})$ for ^{203m}Fr. The magnetic moment range uses data from Refs. [88, 146, 148, 149, 152, 172]

Magnetic moment (μ_N)		$A(7s^2S_{1/2})$ (MHz)	
Lower	Upper	Lower	Upper
+1.5	+1.7	+28900	+ 32800

Figure 7.13 shows the predicted hyperfine structure of ^{203m}Fr relative to the ground state measured in high resolution. The central values of the estimations of $A(7s\ ^2S_{1/2})$ and $\delta\nu^{203g,m}$ (Range 1) were used. The lineshape was assumed to be a Voigt profile with Gaussian and Lorentzian contributions of 20 MHz and 35 MHz respectively. The Gaussian and Lorentzian contributions from the previous experiment were 20 MHz and 15 MHz respectively. The Gaussian contribution was increased by 5 MHz and the Lorentzian contribution was further increased to 35 MHz to account for the linewidth of the frequency-doubled injection-seeded Ti:Sa that would be used for a high-resolution search of the isomer. The two resonances in the left-hand component of the hyperfine structure are separated by 220 MHz. A high-resolution laser is required to resolve these.

Both components of the hyperfine structure of the isomer are predicted to be separated from the ground state. The left-hand component is better separated from the ground state and has the most intense resonance of the hyperfine structure. This makes it the easier component to first identify.

Figure 7.14 shows the predicted hyperfine structure of ^{203m}Fr measured in low resolution. The lineshape was assumed to be a Voigt profile with Gaussian and Lorentzian contributions of 1000 MHz and 2 MHz, respectively. The lineshape

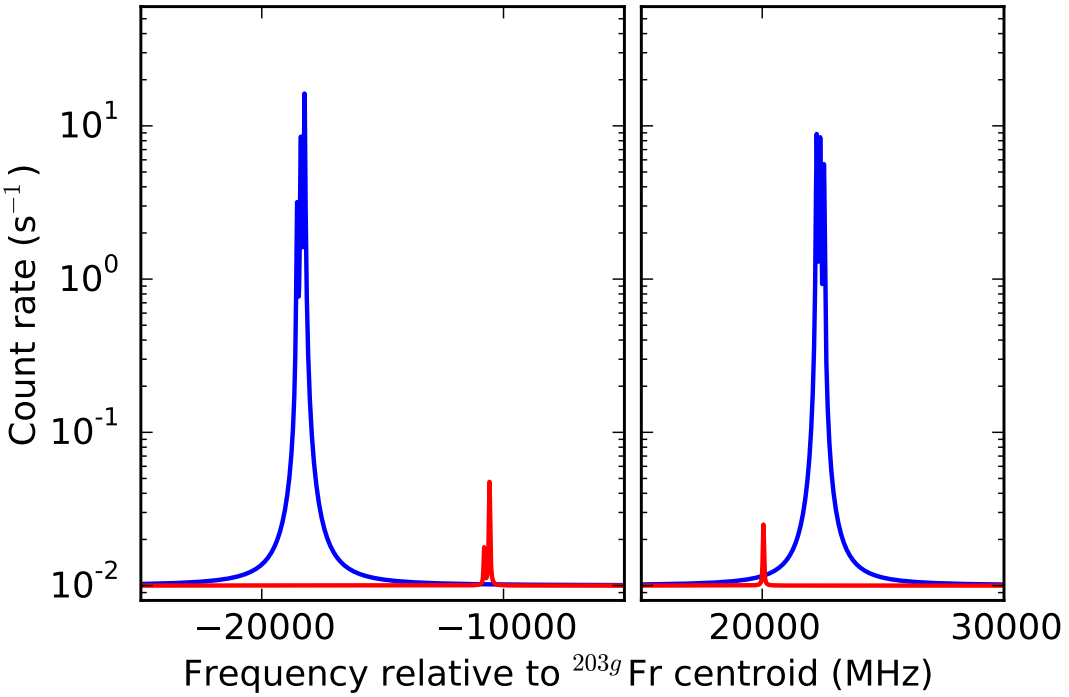

FIGURE 7.13: Predicted ^{203m}Fr hyperfine structure if measured using the high-resolution laser system (Voigt profile with Gaussian and Lorenztian contributions of 25 MHz and 35 MHz, respectively)

is dominated by the 1000-MHz linewidth of the dual-etalon Z-cavity Ti:Sa that would be used as the low-resolution laser. The 2-MHz Lorentzian contribution stems purely from the natural linewidth of the transition. The left-hand component of the hyperfine structure of the isomer is still well-separated from the ground state however the two resonances that contribute cannot be resolved. The right-hand component is not well separated from the ground state. Any unanticipated increase in the Lorentzian contribution to the lineshape would further obscure the right-hand component of the isomer.

The suggested strategy for measuring the isomer is as follows:

1. Search for the left-hand component of the isomer with the low-resolution setup.

2. Once identified, measure the left-hand component with the high-resolution setup.

3. Perform online analysis to estimate where the right-hand component lies.

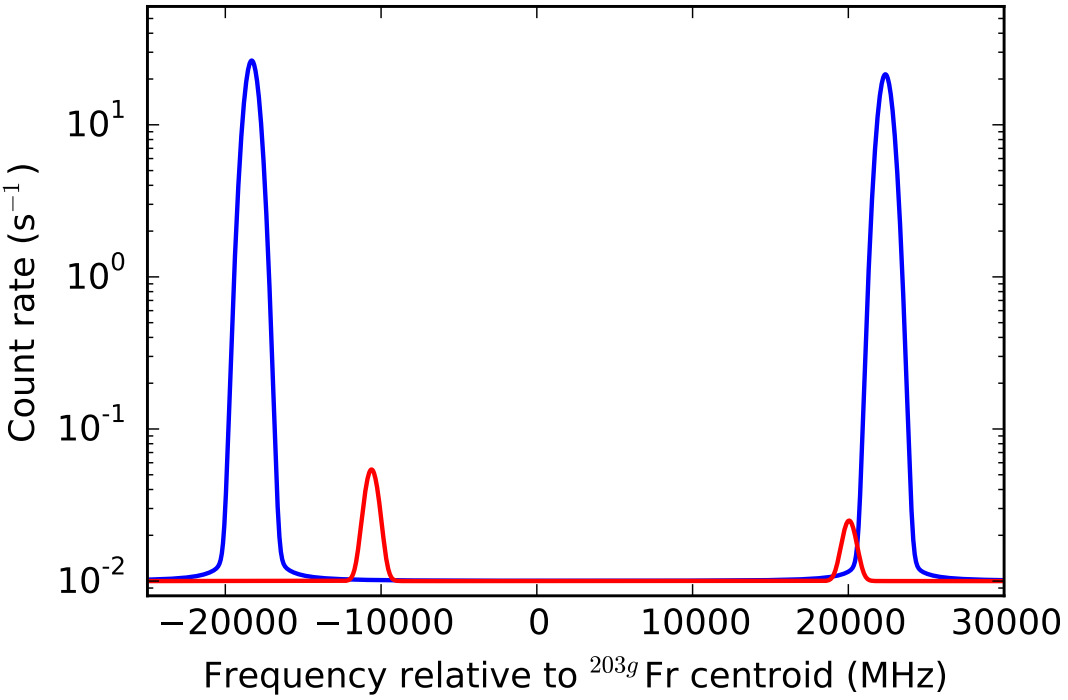

FIGURE 7.14: Predicted ^{203m}Fr hyperfine structure if measured using the low-resolution (Voigt profile with Gaussian and Lorentzian contributions of 1000 MHz and 2 MHz respectively)

4. Search for the right-hand component with the high-resolution setup.

7.4.2 Search for ^{203m}Fr

Table 7.6 shows information about the scans searching for the isomer during the 2015 experiment. A high-resolution laser was used to search for the isomer. The count rate in scans 61, 64 and 65 is of the order 10^{-4} s^{-1}. This is 1 order of magnitude less than the fitted background rate the ^{203g}Fr data. Scans 66 and 67 show a count rate that is around 10 times higher than that seen in the other scans.

Figure 7.15 shows the isomer search data from Table 7.6. The red line shows the prediction of the left-hand component of the hyperfine structure of the isomer. As the left-hand component of the isomer is predicted to be 8 GHz away in frequency space than the left-hand component of the ground state, the simulated

TABLE 7.6: Frequency ranges and count rates for different isomer-hunt scans during the 2015 experiment.

Scan	Frequency range (MHz)		Time (s)	Counts	Count rate (s^{-1})
	Lower	Upper			
61	-32650	-31050	5280	2	4×10^{-4}
64	-12330	-10350	6810	2	3×10^{-4}
65	-10350	-10300	300	0	0
66	-10350	-9310	1120	4	3.6×10^{-3}
67	-10350	-8250	2620	11	4.2×10^{-3}

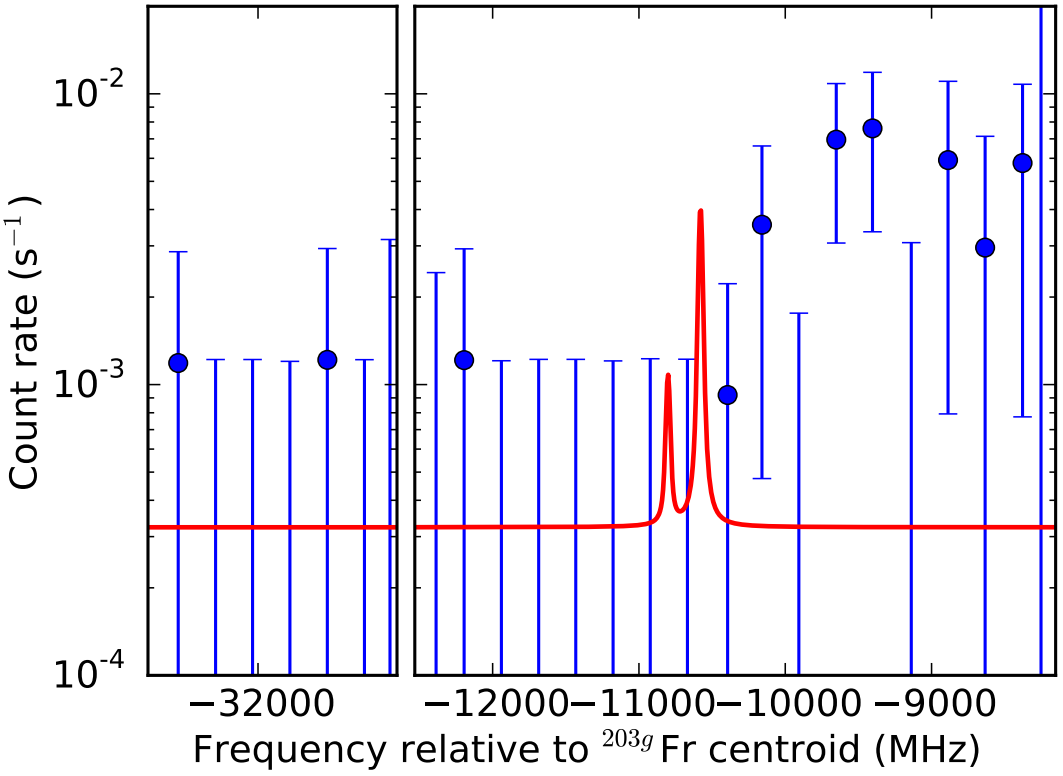

FIGURE 7.15: Isomer search data from the 2015 experiment. The red line shows the left-hand component of the predicted hyperfine structure of the isomer.

background rate is taken as the average count rate of scans 61, 64 and 65 instead of the fitted background rate of the ground-state data. This is because the Lorentzian component of the linewidth extends far away from the ground-state resonances. As such, a 'true' measurement of the background must be performed far away from the ground-state resonances. This is the case for scans 61, 64 and 65 where 4 counts were observed in 12390 s, giving a background rate of 3×10^{-4} s^{-1}.

15 counts were observed in 3740 s in scans 66 and 67 combined resulting in a count rate of 4×10^{-3} s^{-1}, an order of magnitude higher than the 'true' background rate. The frequency ranges of Scans 66 and 67 also mostly overlap with the majority of the counts observed around 1 GHz away from the prediction.

Although far from conclusive, this region offers a suitable starting point to search for the isomer in a future experiment. The consistent and increased count rate observed in scans 66 and 67 lie close to the prediction of the isomer's hyperfine structure.

This region represents the most promising area to continue the search for the isomer in ^{203}Fr. Since the last francium experiment, a new charge-exchange cell chamber was installed, improving the interaction-region pressure by over an order of magnitude. This will reduce the non-resonant collisional background rate and make searching for the isomer easier. Furthermore, using the injection-seeded Ti:Sa laser to produce high-resolution light for the 422-nm transition will ensure saturation, due to its superior peak power. The combination of these factors will greatly improve the chances of measuring the hyperfine structure of the isomer.

Chapter 8

Neutron-rich radium

8.1 Motivation

8.1.1 Octupole deformation

Octupole deformation in atomic nuclei has been a topic of interest for many decades [173, 174]. The observation of low-lying $K^{\pi} = 0^{-}$ bands in even-even radium isotopes [175, 176] was the first experimental evidence for reflection asymmetry in nuclei. These isotopes attracted further attention and many indirect signatures of octupole deformation were found e.g. the inverted odd-even staggering observed in their changes in mean-square charge radii [177], for example (see Section 8.4.3). More recently, measurement of E3 matrix elements via Coulomb excitation provided direct evidence of stable ground-state octupole deformation in ^{224}Ra [178]. Octupole deformation has also been measured directly in ^{144}Ba [179].

The properties of octupole-deformed nuclei may provide profound implications beyond the realm of nuclear physics. Atoms of such nuclei are very important in searches for a permanent atomic electric dipole moment. Measurement of a non-zero electric dipole moment could indicate P- and T- or CP-violating processes that are not present in the standard model. Atoms of octupole-deformed nuclei

could provide a 100-1000 times improvement in sensitivity [180] over atoms of nuclei which are not, for example ^{199}Hg. This atom currently provides one of the most stringent limits on an atomic electric dipole moment [181]. Recently, the isotope ^{225}Ra was used to provide a limit on an atomic electric dipole moment [182, 183].

Isotopes in the region of reflection asymmetry have been studied extensively [173]. However, there is conflicting evidence about the extent of this region and how nuclear structure evolves beyond its borders. A significant degree of octupole correlations was measured in ^{227,229}Ra [184, 185]. These correlations were found to persist in ^{231}Ra, albeit to a lesser degree [186, 187]. Studying beyond the upper border of the region of reflection asymmetry is important to investigate the interplay between quadrupole and octupole collectivity. This could shed light on the mechanism which causes the transition from octupole- to quadrupole-deformation with increasing neutron number.

8.1.2 Atomic-parity violation

More recently, radium has been the subject of interest in atomic physics, both experimentally and theoretically. Radium is a promising candidate for high-precision measurements of atomic-parity violation (also referred to as atomic-parity non-conservation). Atomic-parity violation arises from the exchange of a Z_0 boson between electrons and quarks in the atomic nucleus. The process acts as a sensitive measure of the electroweak interaction at low energies and places constraints on new physics beyond the standard model [188]. The most precise atomic-parity violation measurement to date was performed on atomic ^{133}Cs [189–192]. In Ref. [191], the weak charge of the ^{133}Cs nucleus was determined to be $Q_W = -73.16(29)_{\mathrm{exp}}(20)_{\mathrm{th}}$. This value perfectly agrees with the standard model prediction of $Q_W^{SM} = -73.16(3)$. Despite the agreement, the measurement places the most stringent lower limit on the mass of an additional heavy Z' boson at 1.3 TeV/c^2. Atomic-parity violation is also sensitive to further light,

very weakly-coupled, neutral gauge bosons (U boson) which can decay into dark-matter candidates [193].

Atomic-parity violation is measured through exciting suppressed $M1$ and $E2$ transitions [194]. The process scales strongly with Z. It is therefore enhanced in heavier atoms [195] and is predicted to be 50 times stronger in radium ($Z = 88$) than in caesium ($Z = 55$). Single-trapped atomic ions were shown to be suitable systems to measuring atomic-parity violation [196]. Because of this, plans to perform atomic-parity violation measurements on a single-trapped radium ion are underway at Kernfysisch Versneller Instituut (KVI), University of Groningen. To date, laser spectroscopy has not yet been performed on trapped radium ions, as much of the necessary spectroscopic information is lacking. Recently, experiments have taken place to address this lack of atomic data [197–201].

Atomic-structure theory is required to be accurate to a sub-1% level to interpret atomic-parity violation measurements on a single isotope of an element. In radium, the accuracy of theory is estimated to be 3% [197, 202–204]. In single-isotope atomic-parity measurements, nuclear-structure effects are neglected as the uncertainty from the atomic-structure theory dominates.

By performing atomic-parity violation measurements on two or more isotopes, taking the ratio of the measurements cancels out atomic-structure effects [205]. This makes nuclear-structure effects relating to the size and shape of the nucleus become the dominant error. In particular, knowledge of the differences in size and shape of isotopes measured are extremely important. Radium has many isotopes with suitable lifetimes for single-trapped ion atomic-parity violation experiments.

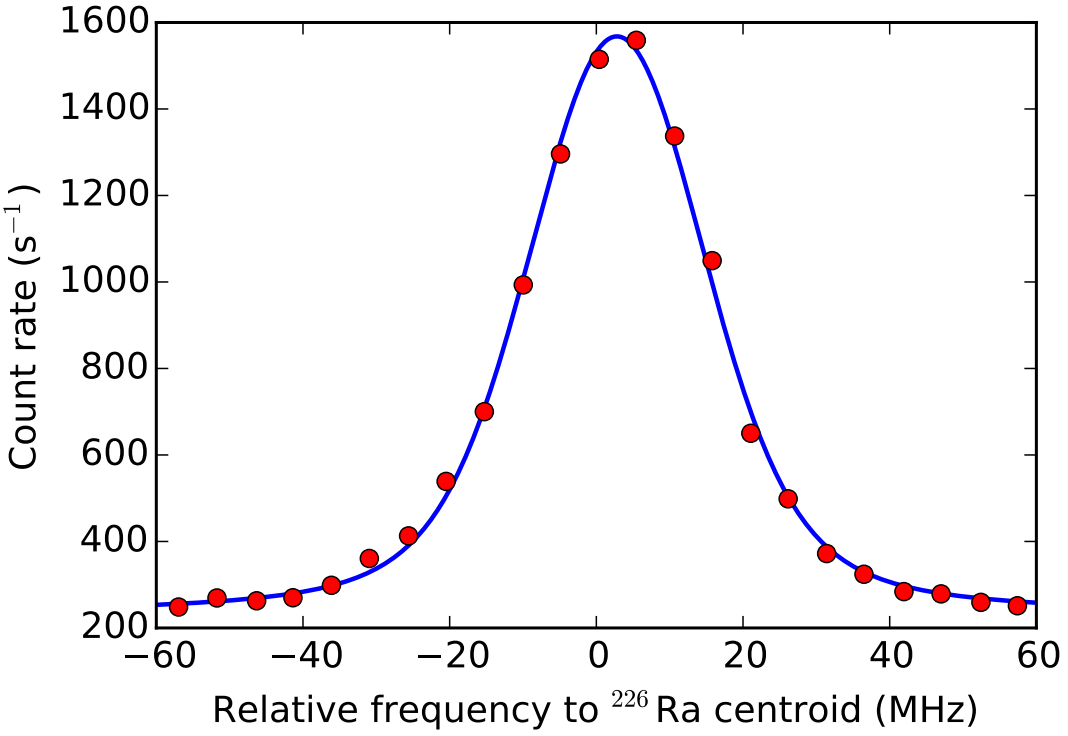

FIGURE 8.1: An example of a high-resolution ^{226}Ra scan. The error bars are smaller than the data points. The red line shows a fit of the data with a linewidth of 30 MHz.

8.2 Results

8.2.1 High-resolution results

The isotope ^{226}Ra was used as a reference when taking high-resolution data throughout the experiment. The isotope was chosen as it is the longest-lived radium isotope with a half life of 1600 years. Its 0^+ spin means that its hyperfine structure has a single peak, giving a quick scan time. An example of a high-resolution ^{226}Ra scan is shown in Figure 8.1. The fitted linewidth of the spectrum is 30 MHz.

The centroid frequencies of the ^{226}Ra scans measured over the course of the experiment are shown in Figure 8.2. The centroid frequencies scatter around a linear trend in the first 2.5 days. After this, there are large drifts for the remainder of the experiment. To account for the drift in reference-scan centroid frequencies,

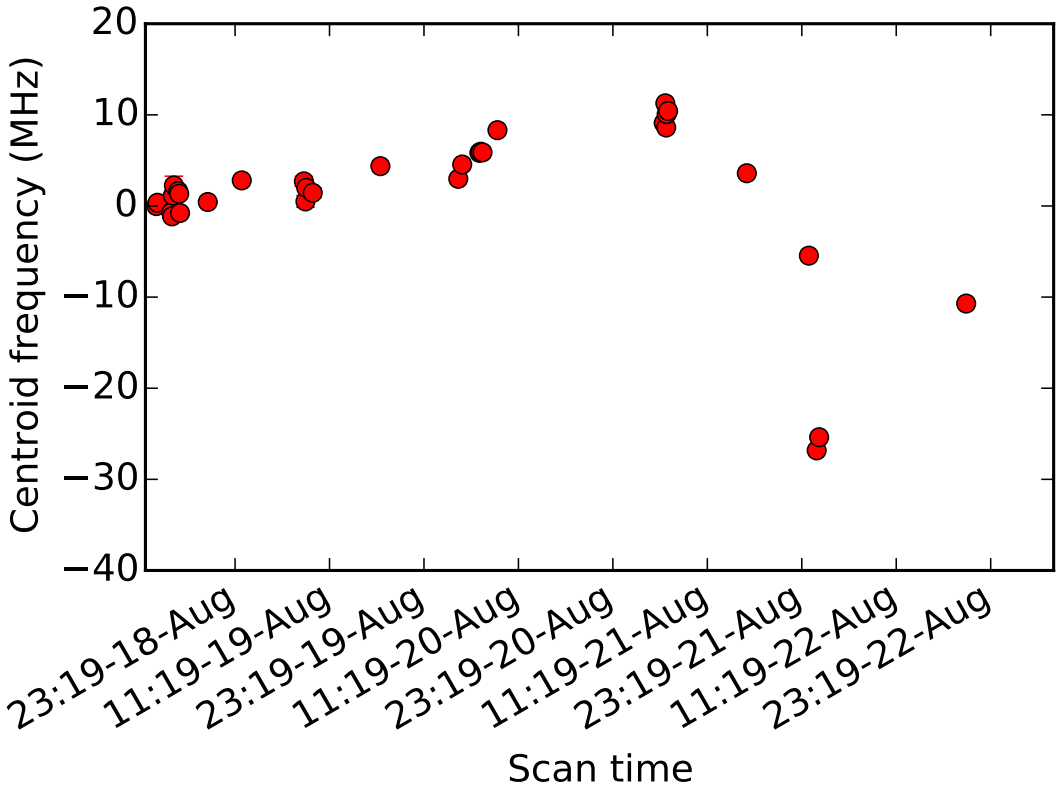

FIGURE 8.2: Centroid frequencies of high-resolution ^{226}Ra reference scans over the course of the experiment. The errors are smaller than the data points.

the isotope shifts are corrected by the centroid frequency of the closest-in-time ^{226}Ra reference scan. To account for the scatter around the drifts in reference-scan isotope shifts, an additional uncertainty is added to the statistical error of the reference-scan corrected isotope shifts. To calculate this scatter, the isotope shifts of the largest data set (^{231}Ra) taken over the course of the experiment are used. Figure 8.3 shows the reference-scan corrected isotope shifts of ^{231}Ra. The additional error to account for the scatter in the isotope shifts was taken as the standard deviation of ^{231}Ra isotope shifts. This was calculated to be $\pm$ 3 MHz which was added as a systematic error to the isotope shifts of all isotopes measured.

An example high-resolution scan of ^{231}Ra is shown in Figure 8.4. The blue line shows a fit of the data with a linewidth of 30 MHz. The relative intensity of the smaller peaks in the measured hyperfine structure of ^{231}Ra are smaller than what is expected when angular-momentum coupling is taken into consideration. This

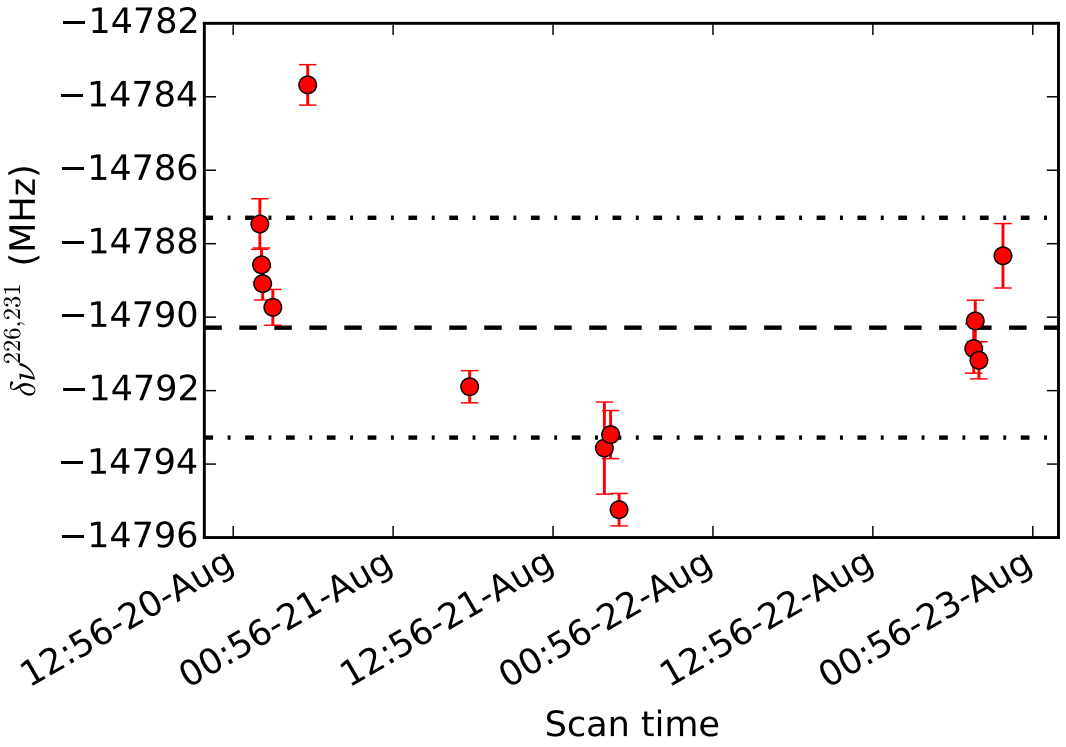

FIGURE 8.3: Isotope shifts of high-resolution ^{231}Ra scans over the course of the experiment.

is, despite 'chopping' of the continuous-wave light, due to the linearly-polarized light pumping atoms to 'dark' $7s^2\ {}^1S_0$ sub-states.

8.2.2 Low-resolution results

The isotope ^{226}Ra was also used as a reference when taking low-resolution data throughout the experiment. The centroid frequencies of the low-resolution ^{226}Ra scans are shown over the course of the experiment in Figure 8.5, which scatter around an increasing linear trend over the course of the experiment. To account for the drift in reference-scan centroid frequencies, the isotope shifts are corrected by the centroid frequency of the closest-in-time ^{226}Ra reference scan. To account for the scatter around the drift in reference-scan centroid frequencies, an additional uncertainty is added to the statistical error of the reference-scan corrected isotope shifts. Because there was not a sufficiently large low-resolution data set, a similar procedure to the high-resolution could not be performed. Consequently,

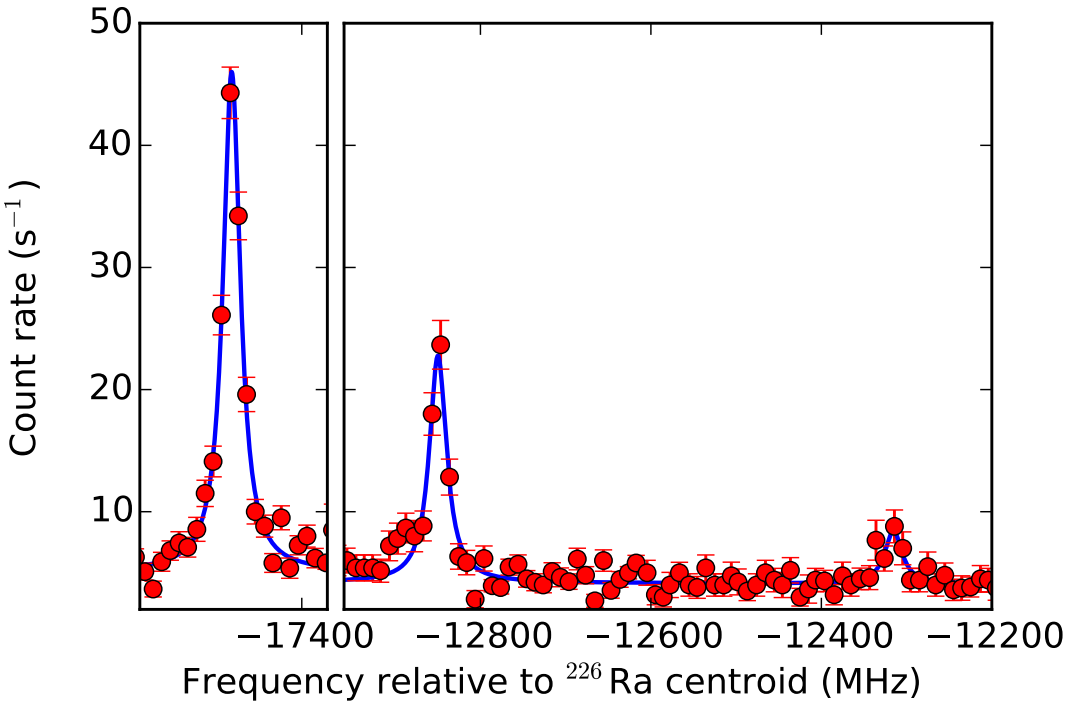

FIGURE 8.4: Example high-resolution spectrum of the $7s^2\ ^1S_0 \rightarrow 7s7p\ ^3P_1$ transition in ^{231}Ra. The blue line shows a fit of the data with a linewidth of 30 MHz.

the additional scatter was taken as the standard deviation of the ^{226}Ra centroid frequencies, calculated to be 500 MHz.

An example low-resolution spectrum of ^{233}Ra is shown in Figure 8.6. Due to its neutron-rich nature, very little is known about ^{233}Ra. A measured half-life of 30(5) s was reported when the nuclide was discovered [206]. A ground-state spin-parity of $(1/2^+)$ was suggested from nuclear data evaluations [207, 208]

Two fits fits using a spin of 1/2 are displayed in Figure 8.6 with black and blue lines, respectively. Fit 1/2 a) sets the hyperfine A and B parameters The peak intensities were fixed to their expected relative intensities from angular-momentum coupling considerations. The asymmetry present in the data is better fitted using a spin of 1/2 with free A and B parameters giving a reduced-χ^2 of 1.06 (compared to 1.31 when A and B are set to zero). As the hyperfine structure is not fully resolved, it is difficult to say whether that the asymmetry is due to the underlying structure or a lineshape-distortion effect. It was also possible to fit the ^{233}Ra data using spins 3/2 and 5/2 resulting in a reduced-χ^2 of 1.19 and

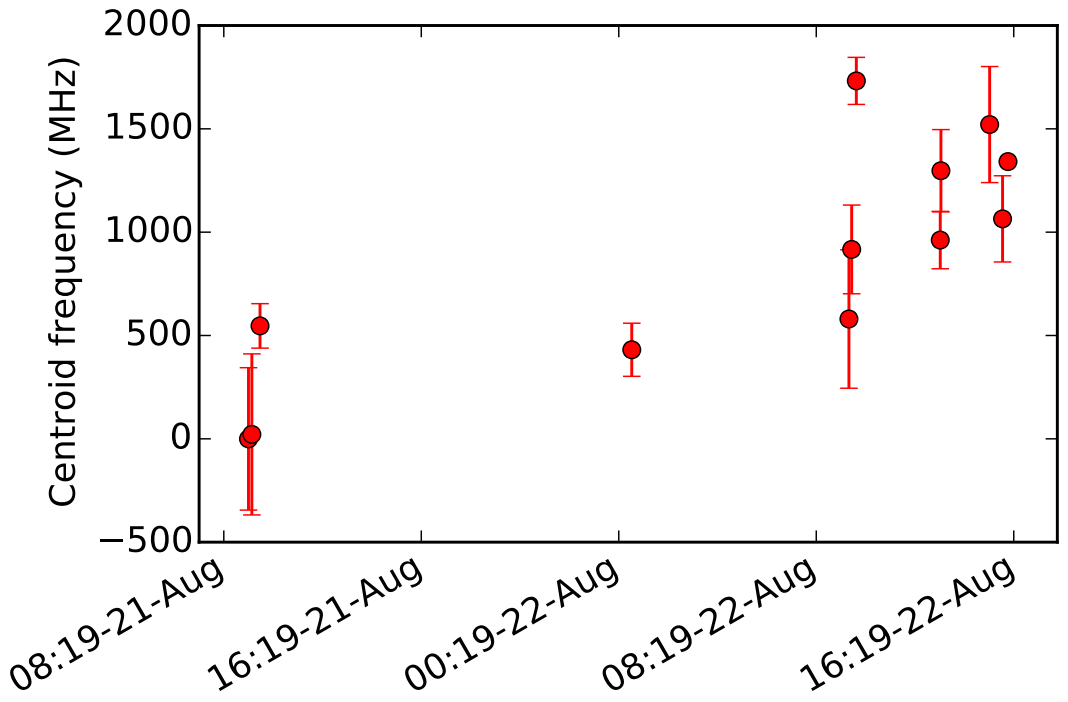

FIGURE 8.5: Centroid frequencies of low-resolution ^{226}Ra reference scans taken during the experiment.

1.07, respectively. The resulting isotope shifts were all consistent. Because of this, the isotope shift was extracted using the spin 1/2 fit with the hyperfine A and B factors set to zero.

8.2.3 Isotope shifts

Table 8.1 shows the measured isotope shifts of neutron-rich radium isotopes, relative to the reference isotope ^{226}Ra. They are also given relative to ^{214}Ra, to allow direct comparison with literature. The results reported here are consistent with literature values where they exist.

8.2.4 Hyperfine A and B factors

The measured hyperfine A and B factors of the $7s7p\ ^3P_1$ state in odd-A radium isotopes are presented in Table 8.2. The $A(^3P_1)$ values agree within 1 σ and $B(^3P_1)(^{223}\text{Ra})$ values agree within 2 σ. Only 2 of the 3 hyperfine-structure

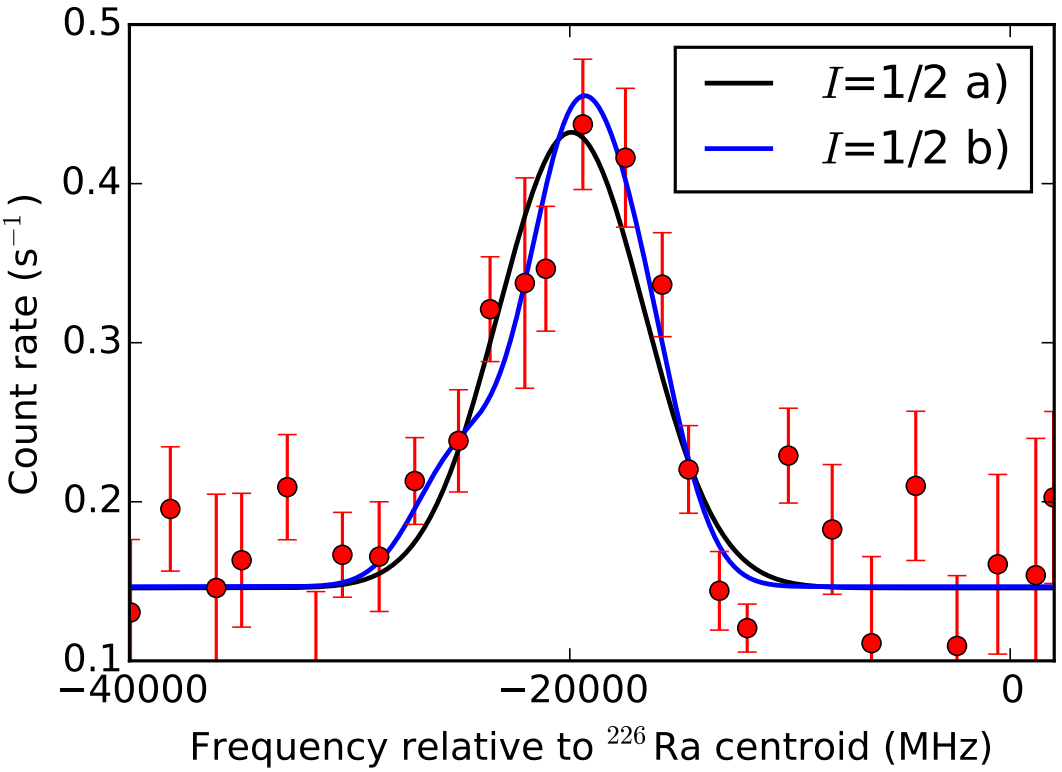

FIGURE 8.6: Example low-resolution spectrum of the $7s\ ^1S_0 \rightarrow 7s7p\ ^3P_1$ transition in ^{233}Ra. The black and blue lines are fits of the data assuming spins of $I = 1/2$. Fit $I = 1/2$ a) sets the hyperfine A and B parameters to zero and fit $I = 1/2$ b) allows non-zero values of A and B.

TABLE 8.1: Measured isotope shifts of neutron-rich radium isotopes, relative to the reference isotope ^{226}Ra and also ^{214}Ra, to allow comparison with literature. Literature values are from Ref. [209].

A	I^π	$\delta\nu^{226,A}$ (MHz)	$\delta\nu^{214,A}$ (MHz)	
			This work	Literature
222	0^+	+12483(3)	-29260(4)	-29253(9)
223	$3/2^+$	+8798(3)	-32946(4)	-32934(10)
224	0^+	+6092(3)	-35652(4)	-35644(11)
225	$1/2^+$	+2269(3)	-39475(4)	-39465(12)
226	0^+	0	-41744(4)	-41733(12)
227	$3/2^+$	-2848(3)	-44592(4)	-
228	0^+	-5921(3)	-47665(4)	-
229	$5/2^+$	-9070(3)	-50814(4)	-
230	0^+	-12700(3)	-54444(4)	-
231	$(5/2^+)$	-14790(3)	-56534(4)	-
232	0^+	-18739(3)	-60483(4)	-
233	-	-20600(500)	-62300(500)	-

TABLE 8.2: Hyperfine A and B factors of the $7s7p\ ^3P_1$ state in neutron-rich odd-A radium isotopes. The $B(^3P_1)(^{227}\mathrm{Ra})$ value was fixed using the experimentally-determined $B(^1P_1)/B(^3P_1)$ ratio (marked by an asterisks). Literature values are from Refs. [177, 210]

A	I	$A(^3P_1)$ (MHz)		$B(^3P_1)$ (MHz)	
		This work	Literature	This work	Literature
223	$3/2^+$	+1202.5(3)	+1202.1(6)	-472.1(2)	-470.2(12)
225	$1/2^+$	-9795.1(3)	-9793.9(43)	-	-
227	$3/2^+$	-1792.8(4)	-	-593(3)*	-
229	$5/2^+$	+1339.3(7)	-	-1160(3)	-
231	$(5/2^+)$	-953.5(2)	-	-1230.7(5)	-

peaks were measured for the isotope ^{227}Ra. To allow the ^{227}Ra spectra to be fitted, the $B(^3P_1)$ factor was fixed to $-593(3)$ MHz (marked by the asterisks in Table 8.2). This was calculated using the experimentally-determined ratio $B(^1P_1)/B(^3P_1) = -0.896(5)$ MHz [209]. As the $7s^2\ ^1S_0 \rightarrow 7s7p\ ^3P_1$ transition used offers no sensitivity to spins greater than 1/2, a $5/2^+$ spin was assumed for ^{231}Ra, tentatively assigned from beta-decay studies [186].

8.3 Extraction of nuclear observables

8.3.1 Magnetic moments

The magnetic dipole moments were calculated using Equation 2.9. The isotope ^{225}Ra was used as a reference [209, 211]:

$I_{\mathrm{ref}} = 1/2^+$,

$\mu_{\mathrm{ref}} = -0.7338(15)\ \mu_N$,

$A(7s7p\ ^3P_1)_{\mathrm{ref}} = -9793.9(43)$ MHz.

Direct measurement of the magnetic dipole moments of ^{213,225}Ra are presented in Ref. [211]. These measurements were made by observing the Larmor precession of optically-pumped radium atoms as a function of magnetic-field strength. ^{225}Ra

was used as the magnetic dipole moment reference in this work due to its smaller relative uncertainty compared to ^{213}Ra.

8.3.2 Spectroscopic electric quadrupole moments

The spectroscopic quadrupole moments were calculated using Equation 2.11. The isotope ^{223}Ra was used as a reference [209, 210]:

$Q_{s,\mathrm{ref}} = +1.254(3)[66]$ b,

$B(7s7p\ ^3P_1)_{\mathrm{ref}} = -470.2(12)$ MHz.

As there are no direct measurements of the spectroscopic electric quadrupole moments of radium isotopes, calculations of the electric field gradient must be used. The alkali-like nature of the radium ion means the electric field gradient can be calculated more reliably compared to the radium atom. The semi-empirical analysis in Ref. [210] accounted for some electron-correlation effects to yield spectroscopic quadrupole moments for ^{209,211,221,223,227,229}Ra. ^{223}Ra was chosen due to its smallest relative statistical uncertainty. They estimate a $\pm 5\%$ calibration error for their approach.

8.3.3 Change in mean-square charge radii

The changes in mean-square charge radii were calculated using Equation 2.21. The mass- and field-shift constants for the 714-nm transition were determined using the King-plot method (see Chapter 2). *Ab initio* calculations of field- and specific mass-shift constants for low-lying levels in the radium ion were published in Ref. [198]. The simpler alkali-like structure of the radium ion make relativistic coupled-cluster calculations for the mass- and field-shift constants feasible. Wansbeek *et al*. performed calculations of the mass- and field-shift constants for the $7s\ ^2S_{1/2}, 7p\ ^2P_{1/2}, 7p\ ^2P_{3/2}, 6d\ ^2D_{3/2}$ states in ^{214}Ra$^+$. This isotope was chosen due to its semi-magic nature with $N = 126$ and expected to be spherical. The calculations approximated the nucleus as a sphere with a constant density. The

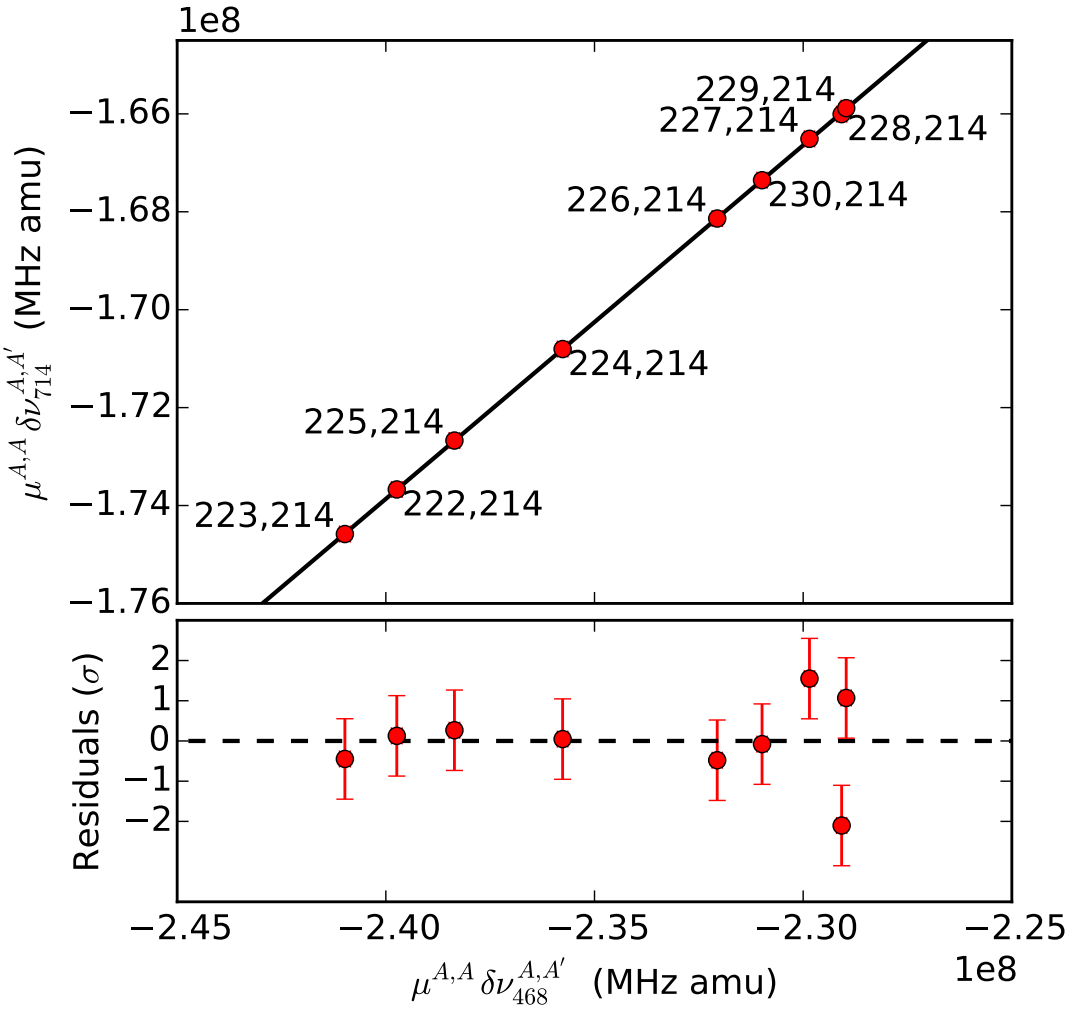

FIGURE 8.7: King-plot analysis used to determine the atomic F and M factors for the 714-nm transition. Literature values for the 468-nm transition are taken from Ref. [209].

resulting mass- and field-shift constants have uncertainties of 10% and 5% respectively. For the 468-nm $7s\ ^2S_{1/2} \rightarrow 7p\ ^2P_{1/2}$ transition in Ra II, they calculate

$$K_{\mathrm{SMS},468} = -990(99)\ \mathrm{GHz\ amu} \tag{8.1}$$

and

$$F_{468} = -39.813(1990)\ \mathrm{GHz\ fm^{-2}}. \tag{8.2}$$

The analysis in Ref. [198] used isotope shifts for the 468-nm transition for their analysis. This is because this transition has the largest number of measured

isotope shifts of all the transitions measured in atomic/ionic radium.

Figure 8.7 shows the King plot of $\mu^{A,A'}\delta\nu_{468}^{A,A'}$ against $\mu^{A,A'}\delta\nu_{714}^{A,A'}$. The field- and mass-shift constants for the 714-nm transition were determined to be

$$F_{714} = -28.75(144) \text{ GHz fm}^{-2}. \tag{8.3}$$

and

$$M_{714} = -305(117) \text{ GHz amu} \tag{8.4}$$

The resulting specific mass-shift constant for the 714-nm transition of $K_{\text{SMS},714} = -540(120)$ GHz amu agrees well with the experimentally-determined value of $K_{\text{SMS},714} = -570(260)$ GHz amu [198]. The obtained ratio of the field-shift constants $F_{714}/F_{468} = +0.7222(4)$ agrees with the value of $+0.7218(12)$ presented in Ref. [198]. The smaller errors on the mass- and field-shift constants for the 714-nm transition presented here are due to the smaller statistical errors on the measured isotope shifts as well as an extended set of isotope-shift pairs.

The changes in mean-square charge radii were multiplied by a scaling factor, Δ, to account for the nuclear deformation known to be present in the neutron-rich radium isotopes with $A \geq 220$. In Ref. [198], the nucleus is modeled as a spherical two-parameter Fermi charge distribution. Such a distribution is parametrized by the half-density radius, c, and the surface diffuseness parameter, a. The authors calculate the shift in energy due to the field shift using this model. The field-shift constants are then calculated using a Dirac-Fock numerical calculation for the Fermi and constant-density distributions. By assuming the nuclear deformation is static and axially symmetric, it can be projected onto the θ axis. This results in a modified Fermi distribution with different effective c_{eff} and a_{eff} parameters. These are varied until the experimental 468-nm transition isotope shifts are reproduced. The changes in the mean-square charge radii are calculated assuming this modified Fermi distribution. The scaling factor, Δ, is defined as the difference between this and the Dirac-Fock calculations assuming a spherical nucleus of constant density. The final values for changes in mean-square

TABLE 8.3: Magnetic dipole and spectroscopic electric quadrupole moments of neutron-rich odd-A radium isotopes. Literature values are from Ref. [177, 210].

A	I	$\mu(\mu_N)$		Q_s (b)	
		This work	Literature	This work	Literature
223	$3/2^+$	+0.2703(6)	+0.2705(19)	+1.259(1)[66]	+1.254(3)[66]
225	$1/2^+$	-0.7339(15)	-0.7338(15)	-	-
227	$3/2^+$	-0.4030(8)	-0.4038(24)	+1.581(9)[80]	+1.58(3)[11]
229	$5/2^+$	+0.5017(11)	+0.5025(27)	+3.094(8)[160]	+3.09(4)[19]
231	$(5/2^+)$	-0.3572(8)	-	+3.282(1)[170]	-

charge radii are obtained by multiplying the values calculated using the mass- and field-shift constants presented above by the scaling factor, Δ.

8.4 Results and discussion

8.4.1 Quadrupole moments

The electromagnetic moments obtained from the experiment are presented in Table 8.3, alongside literature values where they exist.

The spectroscopic (top) and intrinsic (bottom) electric quadrupole moments of neutron-rich odd-A radium isotopes are shown in Figure 8.8. The red circles are literature values. The blue square is the new quadrupole moment of ^{231}Ra. The magnitude of the spectroscopic quadrupole moments illustrate the deformed nature of neutron-rich radium isotopes. However, the spectroscopic quadrupole moments exhibit no obvious trend against neutron number.

The intrinsic quadrupole moments were calculated assuming the strong-coupling limit using Equation 2.30. This limit is valid for the strongly-deformed neutron-rich radium nuclei ($\beta_2 \approx 0.2$) [210]. In the initial laser-spectroscopy work on radium isotopes, this limit was used to derive spectroscopic quadrupole moments from the hyperfine B factors. The intrinsic quadrupole moments of even-A radium isotopes were known from $B(E2\uparrow)$ values and from this, the spectroscopic

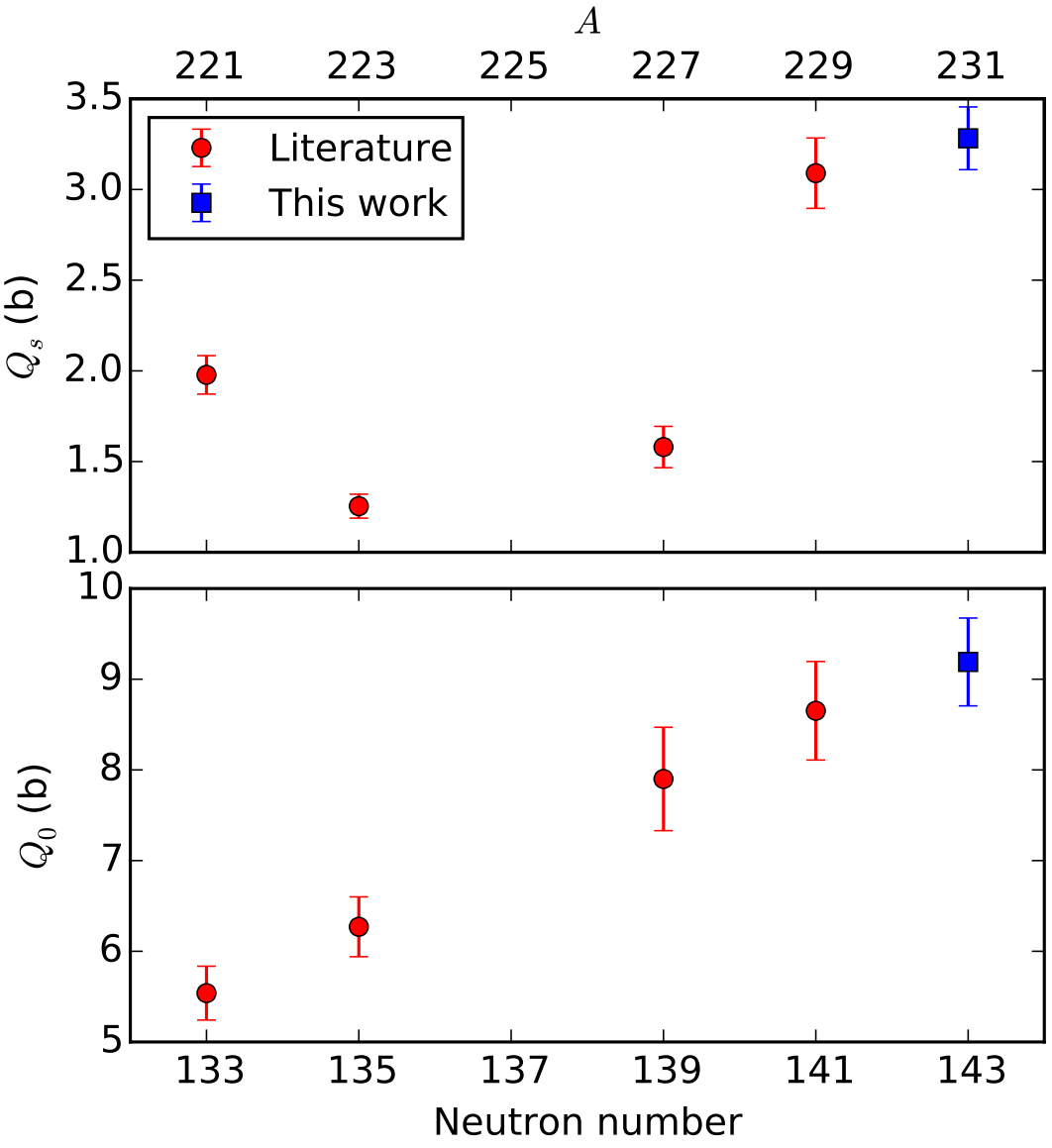

FIGURE 8.8: Spectroscopic (top) and intrinsic (bottom) electric quadrupole moments of odd-A neutron-rich radium isotopes. Literature values are shown as red circles. The quadrupole moment of ^{231}Ra is shown as a blue square.

quadrupole moment of ^{229}Ra was calibrated to 2.9(4) b [212]. Later work using the first semi-empirical evaluation of the electric field gradient of $7s7p\ ^3P_J$ states in atomic radium yielded 2.96(30) b, agreeing with the previous value [209]. More accurate calculations in ionic radium yielded 3.09(4)[19] b [210]. This confirmed the validity of the strong-coupling limit for the strong-deformed nucleus ^{229}Ra.

The Coriolis interaction affects the projection of the spin on the axis of deformation. The effect is similar to the classical Coriolis force which acts on all rotating

macroscopic bodies. The interaction modifies the coupling between a single particle and deformed rotor. This causes the projection, Ω, on the symmetry axis to be modified through admixing different Ω values. The effect of the Coriolis interaction decreases with increasing deformation [18]. The Coriolis interaction is proportional to $\hbar^2/I$ and is therefore enhanced for nuclei with $I = 1/2$, for example ^{225}Ra. As spectroscopic quadrupole moments can only be measured for nuclei with $I > 1/2$, the enhanced Coriolis interaction in these nuclei does not affect this discussion.

A linear trend, which is proportional to neutron number is observed in Figure 8.8 (bottom). The quadrupole moment of ^{231}Ra presented here establishes the continuation of this trend. The odd-A radium isotopes continue to become more deformed towards high neutron numbers.

The static deformation parameter, $\langle\beta_2\rangle$, was calculated using Equation 2.31 for ^{231}Ra. Two calculations for $\langle r^2\rangle_{sph}$ were used. The first used $\langle r^2\rangle_{sph} = \frac{3}{5}r_0^2A^{2/3}$ where $r_0 = 1.18$ fm. The second used the second parametrization of the liquid-droplet model presented in Ref. [20]. In both cases, $\langle\beta_2\rangle(^{231}\text{Ra})$ was calculated to be 0.24(1). Calculations generally underestimate changes in the mean-square charge radius for neutron-rich radium isotopes with $N > 126$ [198]. Spherical Skyrme energy density functional calculations [213] show the largest underestimation (estimated to be approximately 2 fm^2 for ^{231}Ra) as deformation effects are not taken into account in this approach. This discrepancy is reduced when a quadrupole-deformation degree of freedom is included [214] or where a more generalized liquid-droplet model is used [215]. This means the calculation of $\langle\beta_2\rangle$ is likely an overestimate. Increasing $\langle r^2\rangle_{sph}$ by 2 fm^2 reduces its value to 0.22(1).

The shortcomings of simple liquid-droplet model calculations mean a reliable calculation of the total deformation parameter of ^{231}Ra from its changes in mean-square charge radii is currently not possible. Ground-state deformations calculated using the finite-range droplet model [216] give $\langle\beta_2\rangle = 0.205$ [217]. The static deformation parameter calculated from the intrinsic quadrupole moment is larger than this. This gives an unsatisfactory static ratio of greater than 1.

Despite this, it can be concluded that the majority of the deformation is static in origin in ^{231}Ra.

8.4.2 Changes in mean-square charge radii

The changes in mean-square charge radii of neutron-rich radium isotopes, relative to ^{214}Ra, are presented in Table 8.4. The statistical errors due to the isotope shift are shown in curved brackets. The systematic errors due to the uncertainty on the atomic F and M factors and Δ (for ^{231,233}Ra) are shown in square brackets. The scaling factors, Δ, used to account for nuclear deformation from Ref. [198] are also presented. For the isotopes ^{231,233}Ra, no values for Δ are presented in Ref. [198]. The Δ values of 2.8(1) % have been extrapolated from neighbouring isotopes. The 0.1 % uncertainty on the extrapolation has a small effect (± 0.002 fm^2) on the overall uncertainty of the changes in mean-square charge radii, which is included in the systematic error for ^{231,233}Ra. In all cases, the overall uncertainty is dominated by the systematic uncertainty from the field-shift factor. The much larger statistical error on the isotope shift of ^{233}Ra is a factor of 6 smaller than the systematic error.

Figure 8.9 shows the changes in mean-square charge radii of neutron-rich radium (red circles and squares) and neighbouring francium (green triangles) isotopes, relative to $N = 126$. Literature values of radium isotopes are shown as red circles. The ^{231,233}Ra values from this work shown as red squares. The red-shaded area represents the systematic error resulting from the uncertainties on the atomic F and M factors and the uncertainty of the extrapolated scaling factor, Δ, for ^{231,233}Ra.

The changes in mean-square charge radii of isotopes of elements above $Z = 82$ show remarkable agreement on both sides of the $N = 126$. Below $N = 126$, the bismuth ($Z = 83$), polonium ($Z = 84$) and francium ($Z = 87$) chains agree with that of the proton-magic lead ($Z = 82$) chain. This agreement continues for many isotopes until departures are observed at $N = 116$ in francium [86], $N = 114$ in

TABLE 8.4: Changes in mean-square charge radii of neutron-rich radium isotopes, relative to ^{214}Ra ($N = 126$). Statistical errors from the isotope shifts are given in curved brackets. Systematic errors from uncertainties on the atomic F and M factors and scaling factor, Δ, are given in square brackets.

A	I^π	$\delta\langle r^2\rangle^{214,A}$ (fm^2)		Δ(%)
		This work	Literature	
222	0^+	+1.0449(2)[524]	+1.045(53)	2.8
223	$3/2^+$	+1.1709(2)[587]	+1.170(59)	2.3
224	0^+	+1.2680(2)[636]	+1.268(64)	2.4
225	$1/2^+$	+1.4041(2)[704]	+1.404(71)	2.4
226	0^+	+1.4858(2)[745]	+1.486(75)	2.5
227	$3/2^+$	+1.5871(2)[796]	+1.587(80)	2.5
228	0^+	+1.6980(2)[852]	+1.697(86)	2.6
229	$5/2^+$	+1.8102(2)[908]	+1.810(92)	2.6
230	0^+	+1.9435(2)[975]	+1.943(98)	2.8
231	$(5/2^+)$	+2.0177(2)[1012]	-	2.8(1)
232	0^+	+2.1589(2)[1083]	+2.16(16)	2.8
233	-	+2.225(18)[113]	-	2.8(1)

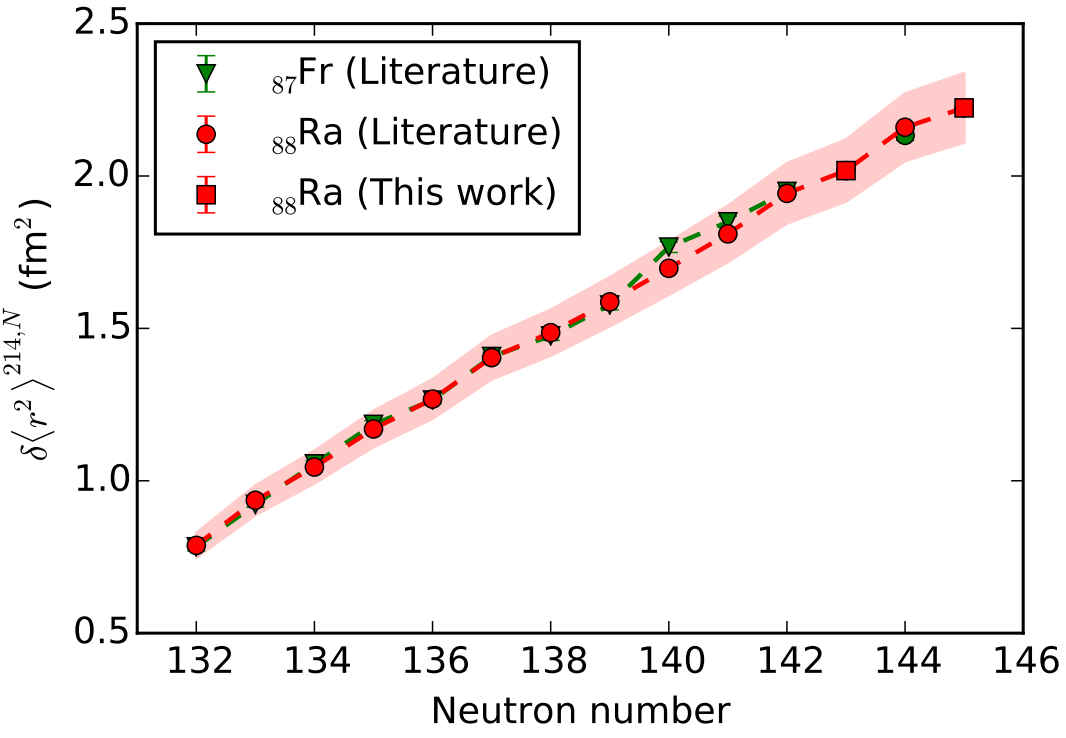

FIGURE 8.9: Changes in mean-square charge radii of neutron-rich radium (red circles and squares) and francium (green triangles) isotopes.

polonium [170] and $N = 110$ in bismuth [149]. The additional protons in the $\pi 1h_{9/2}$ orbital do not significantly affect the total deformation observed in these isotope chains near $N = 126$ and thus act as 'spectator' particles.

Above $N = 126$, the agreement between the changes in mean-square charge radii of francium and radium isotope chains was remarked upon in Ref. [88]. This indicates that the additional $\pi 1h_{9/2}$ proton has little effect on the behaviour of the radium chain when compared to francium. A close agreement between $N = 132 - 139$ can be seen in Figure 8.9. A small departure between the two chains occurs at $N = 140, 141$ due to the change in the odd-even staggering behaviour.

8.4.3 Odd-even staggering

Odd-even staggering is an effect observed throughout the nuclear chart in many observables such as reaction cross sections [218] and binding energies [219]. The odd-even staggering phenomenon is not unique to atomic nuclei. Odd-even staggering behaviour has been observed in the other finite many-fermion systems such as metal clusters [220] and ultra-small superconducting grains [221].

In nuclei, the source is not yet fully understood. The observed odd-even staggering in nuclear masses, where even-particle-number systems exhibit a stronger binding than odd-particle-number systems, suggest that pairing correlations play a crucial role [222]. In light- and medium-mass nuclei, shape effects resulting from a deformed mean field were shown to play an equally important role as pairing correlations in causing odd-even staggering [223]. The interplay between pairing correlations and deformation can cause anomalous odd-even staggering behaviour, often attracting theoretical interest [224]. In some cases, a total inversion of odd-even staggering behaviour is observed.

In the context of changes in the mean-square charge radius, the odd-even staggering phenomenon refers to the smaller radii of odd-N isotopes when compared to the average of their even-N neighbours. This can be parametrized by the

odd-even staggering parameter, $D(N;\delta\langle r^2\rangle^{126,N})$, defined as

$$D(N;\delta\langle r^2\rangle^{126,N}) = (-1)^N(\delta\langle r^2\rangle^{126,N} - \frac{1}{2}(\delta\langle r^2\rangle^{126,N-1} + \delta\langle r^2\rangle^{126,N+1})). \quad (8.5)$$

In this formalism, $D(N;\delta\langle r^2\rangle^{126,N}) > 0$ represents normal odd-even staggering behaviour. $D(N;\delta\langle r^2\rangle^{126,N}) < 0$ represents an inverted odd-even staggering behaviour, where the radius of the odd-N is larger than its even-N neighbours. The systematic uncertainty due to the atomic F and M factors on $\delta\langle r^2\rangle$ cancel out in Equation 8.5. The statistical error on $\delta\langle r^2\rangle$ remains, contributing to the error in calculating $D(N;\delta\langle r^2\rangle^{126,N})$.

Calculations presented in Ref. [225] imply a normal odd-even staggering for even-multipole deformations and an inverted odd-even staggering for odd-multipole deformations. Inverted odd-even staggering was observed in radon, francium and radium isotopes around $N = 136$ [152, 177, 226]. One interpretation of this inversion is that it is indirect evidence for octupole deformation in these isotopes [177]. More recently, inverted odd-even staggering was observed in the astatine isotope ^{218}At with $N = 133$ [150]. The magnitude of the inversion in ^{218}At was found to be larger than in its corresponding francium and radium isotones.

Figure 8.10 shows the odd-even staggering parameter, $D(N;\delta\langle r^2\rangle^{126,N})$, as a function of neutron number for neutron-rich radium (red circles and squares) and francium (green triangles) isotopes. The isotopes $^{221-226}$Ra exhibit an inverted odd-even staggering. ^{227}Ra shows a normal odd-even staggering before a small reinversion at ^{228}Ra. The last isotope for which the odd-even staggering parameter could be previously calculated for is ^{229}Ra where normal odd-even staggering is observed. The new $\delta\langle r^2\rangle$ values for ^{231,233}Ra presented here allow $D(N;\delta\langle r^2\rangle^{126,N})$ to be calculated for ^{230,231,232}Ra. The new data establishes the continuation of normal odd-even staggering towards higher neutron numbers, with a much smoother behaviour than observed in the francium chain [88]. The larger error on $D(N;\delta\langle r^2\rangle^{126,N})$ at $N = 144$ is due to the larger statistical error on the isotope shift of ^{233}Ra. Despite this, the nature of odd-even staggering

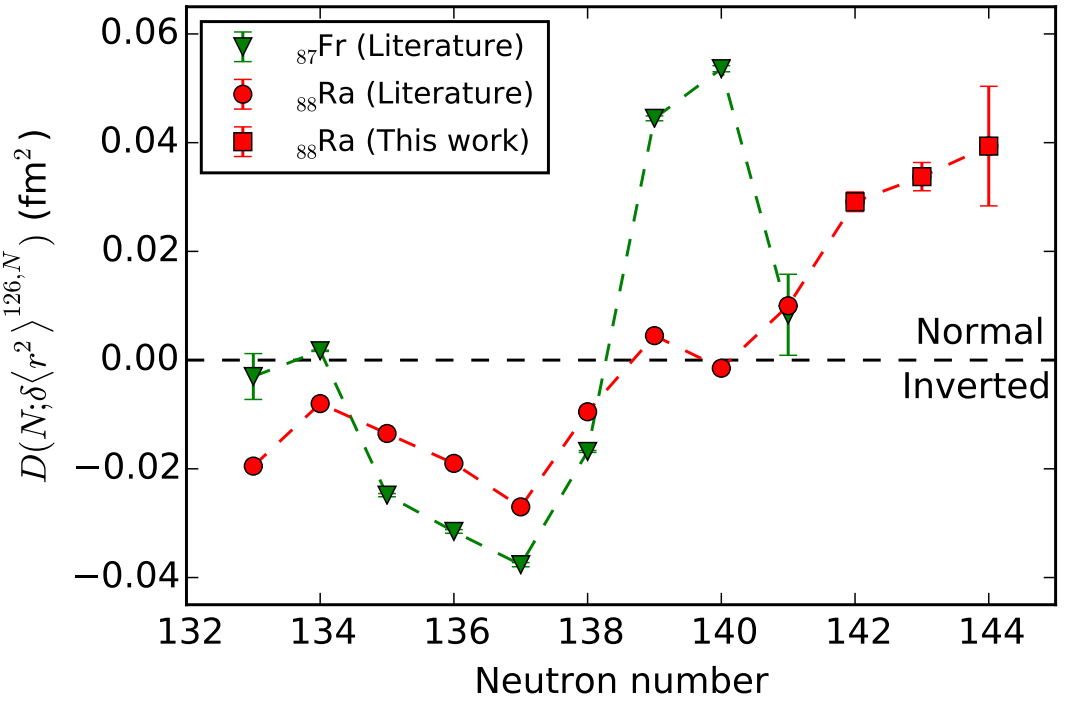

FIGURE 8.10: The odd-even staggering parameter, $D(N;\delta\langle r^2\rangle^{126,N})$, for neutron-rich radium (blue) and francium (red) isotopes.

could still be determined for this nucleus, showing that valuable information may be obtained when using a low-resolution setup.

The magnitude of $D(N;\delta\langle r^2\rangle^{126,N})$ increases with neutron number, agreeing with the observed enhancement of odd-even mass staggering towards $N = 146$ reported in Ref. [227]. In this work, Hartree-Fock and Hartree-Fock-Bogoliubov calculations were performed using the Sly4 interaction [228]. The influence of nuclear deformation on odd-even staggering was illustrated by performing the Hartree-Fock-Bogoliubov calculations with and without quasiparticle blocking present. The enhancement of odd-even staggering towards $N = 146$ was described by both the Hartree-Fock and Hartree-Fock-Bogoliubov calculations, as an effect of quadrupole deformation. The better agreement of the Hartree-Fock-Bogoliubov calculations showed the importance of pairing correlations in the odd-even staggering phenomena. The ^{231}Ra spectroscopic quadrupole measurement presented earlier experimentally verifies the continuation of increasing quadrupole deformation towards higher neutron numbers, lending support to the calculations presented in Ref. [227].

The odd-even staggering parameter value of ^{228}Fr shows a strong, sudden increase for $N = 139, 140$. This then 'dips' towards inverted odd-even staggering behaviour. A measurement of the isotope shift of ^{230}Fr would allow the odd-even staggering parameter to be calculated for ^{229,230}Fr ($N = 142, 143$). This would determine whether a reinversion occurs in contrast to the radium isotopes and what is reported in Ref. [227].

Chapter 9

Conclusions

Collinear resonance ionization spectroscopy was performed on the francium isotopes ^{203,207,219,221}Fr. Hyperfine A and B factors for the $8p^2\ P_{3/2}$ state were measured in ^{203,207}Fr.

The spectroscopic electric quadrupole moment of ^{203}Fr was determined for the first time. The large increase in its magnitude compared to other even-N francium isotopes below $N = 126$ suggest an onset of static deformation. Calculations of the static and total deformation parameters reveal that the increase in quadrupole deformation cannot fully account for the observed departure of its relative charge radius from the lead chain.

Collinear resonance ionization spectroscopy was performed on the radium isotopes $^{214,222-233}$Ra. The hyperfine structure was measured via the $7s^2\ ^1S_0 \rightarrow 7s7p\ ^3P_1$ transition, yielding isotope shifts for $^{227-233}$Ra, hyperfine $A(^3P_1)$ factors in ^{227,229,231}Ra and hyperfine $B(^3P_1)$ factors in ^{227,229,231}Ra for the first time.

The magnetic dipole and spectroscopic electric quadrupole moment of ^{231}Ra were determined to be $\mu = -0.3562(8)\ \mu_N$ and $Q_s = +3.282(1)[170]$ b respectively. A striking linear trend is observed between the intrinsic quadrupole moments with respect to neutron number. The new quadrupole moment for ^{231}Ra establishes the continuation of increasing quadrupole deformation as neutrons are added.

The static deformation parameter, $\langle\beta_2\rangle$, was calculated to be 0.24(1) indicating that the nucleus is strongly deformed.

A King-plot analysis was performed to determine the atomic F and M factors for the $7s^2\ {}^1S_0 \rightarrow 7s7p\ {}^3P_1$ transition, yielding $F_{714} = -28.75(144)$ GHz fm^{-2} and $M_{714} = -305(117)$ GHz amu. The smaller statistical errors on the measured isotope shifts and extended isotope-shift pair data set presented here resulted in slightly smaller uncertainties on the F and M factors determined here, compared to literature [198].

Changes in the mean-square charge radii of ^{231,233}Ra were determined. From this, the odd-even staggering parameter, $D(N; \delta\langle r^2\rangle^{126,N})$, was calculated for ^{230,231,232}Ra. This confirmed the continuation of normal odd-even staggering behaviour in the radium isotope chain towards higher neutron numbers.

The quadrupole moment ^{231}Ra combined with the continuation of normal odd-even staggering behaviour in the very neutron-rich radium isotopes suggest that these isotopes are strongly-quadrupole deformed and can be described by reflection-symmetric shapes.

Appendix A

Appendix

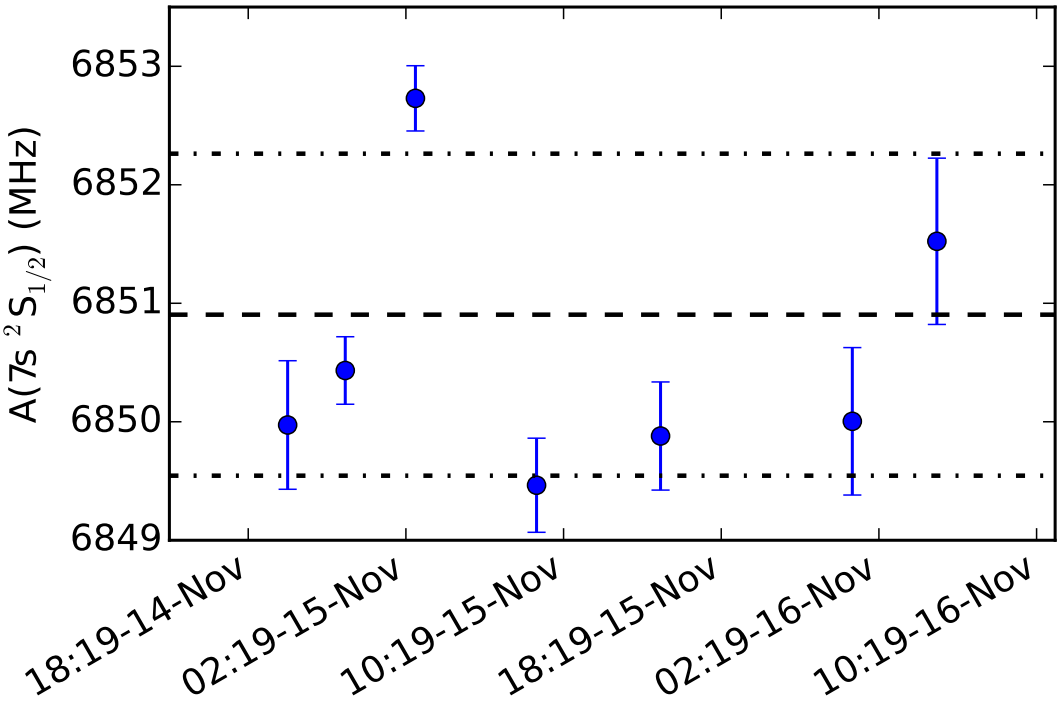

FIGURE A.1: $A(7s\ ^2S_{1/2})$ of ^{219}Fr during the experiment. The black dashed line shows the weighted average of the data. The black dashed and dotted line shows the $\pm 1\sigma$ boundary around the weighted average.

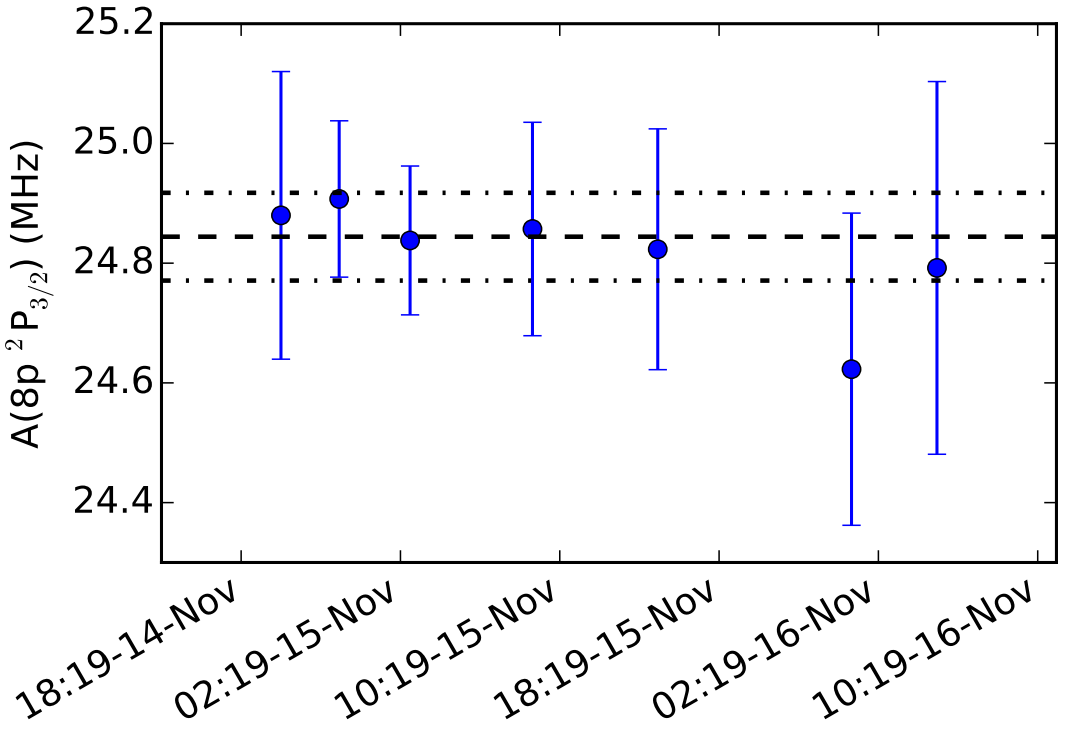

FIGURE A.2: $A(8p\ ^2P_{3/2})$ of ^{219}Fr during the experiment. The black dashed line shows the weighted average of the data. The black dashed and dotted line shows the $\pm 1\sigma$ boundary around the weighted average

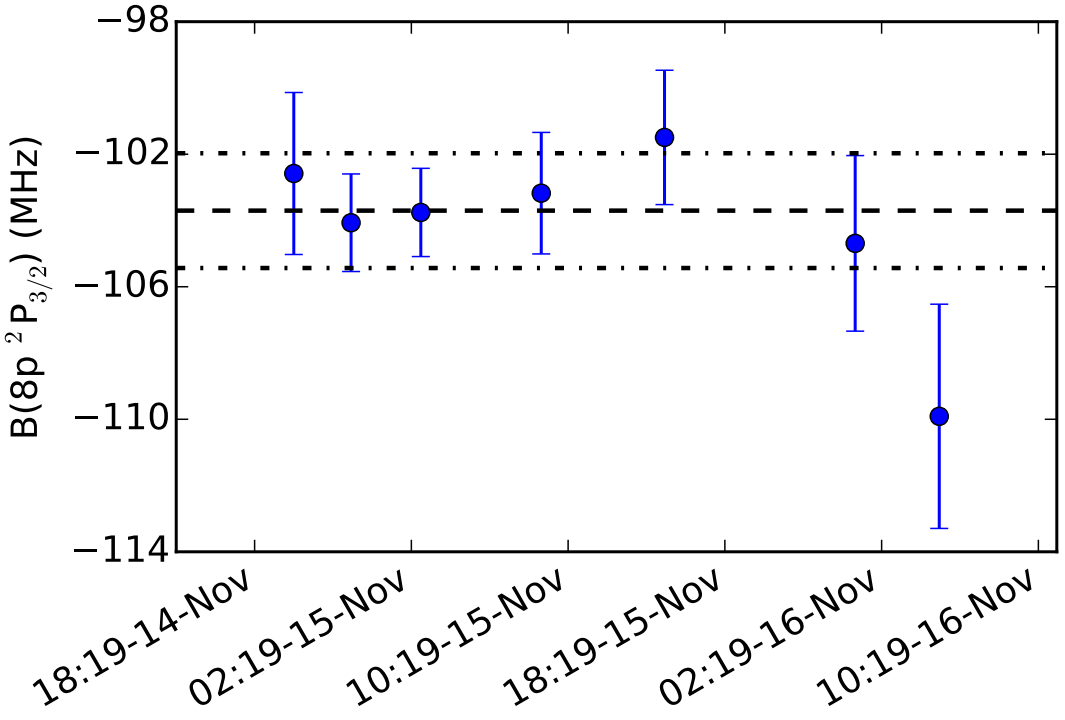

FIGURE A.3: $B(8p\ ^2P_{3/2})$ of ^{219}Fr during the experiment. The black dashed line shows the weighted average of the data. The black dashed and dotted line shows the $\pm 1\sigma$ boundary around the weighted average

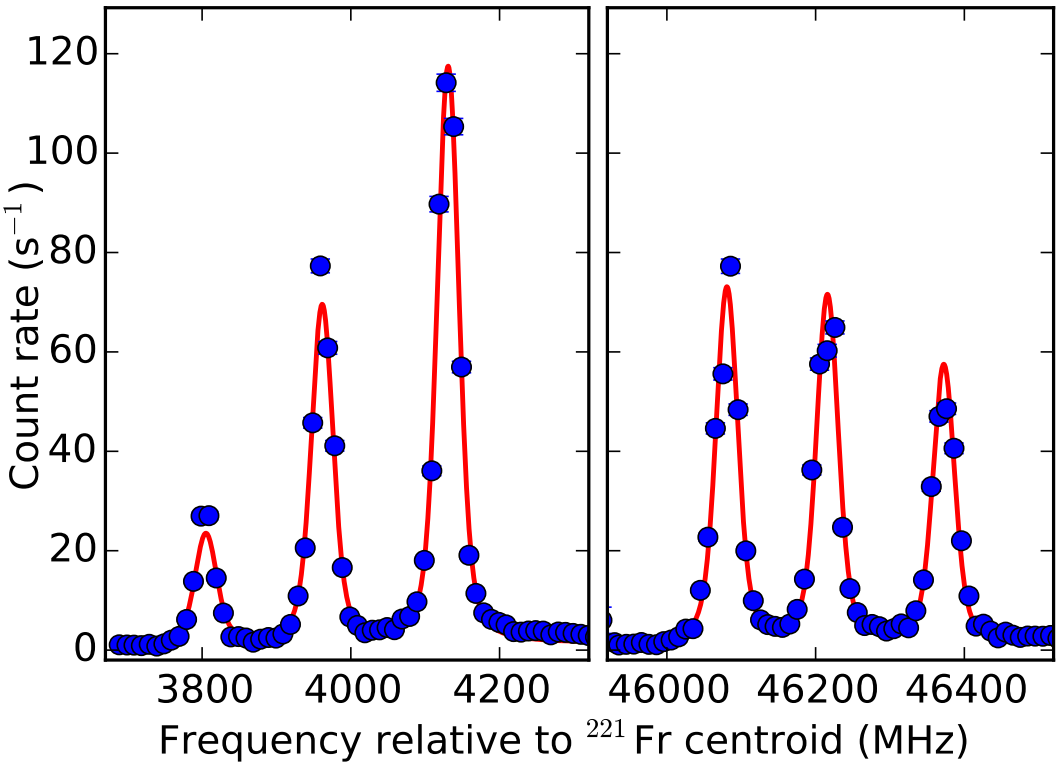

FIGURE A.4: Example spectrum of the $7s\ ^2S_{1/2} \rightarrow 8p\ ^2P_{3/2}$ transition in ^{207}Fr.

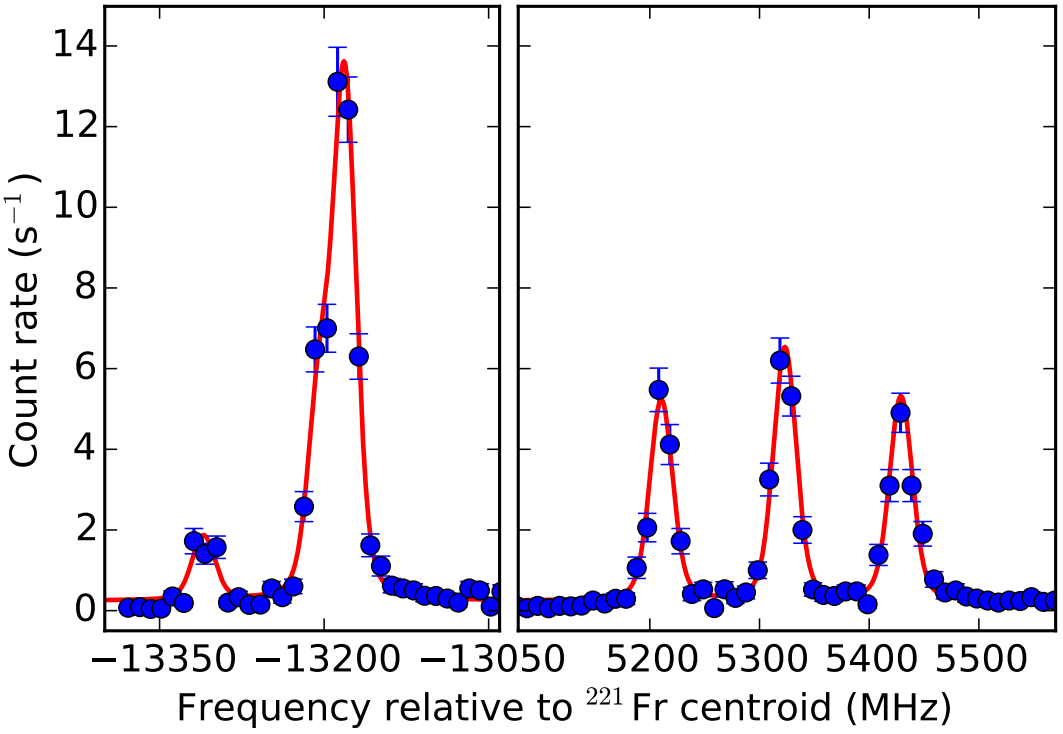

FIGURE A.5: Example spectrum of the $7s\ ^2S_{1/2} \rightarrow 8p\ ^2P_{3/2}$ transition in ^{221}Fr.

Bibliography

[1] J Erler, N Birge, M Kortelainen, W Nazarewicz, E Olsen, A. M. Perhac, and M Stoitsov. The limits of the nuclear landscape. *Nature*, 486(7404): 509–512, 2012.

[2] G. K. Woodgate. *Elementary Atomc Structure*. Oxford University Press, 1999. ISBN 978-0-19-851156-4.

[3] J. D. Jackson. *Classical Electrodynamics*. Wiley, 1999. ISBN 978-0-471-30932-1.

[4] H. B. G. Casimir. *On the Interaction between Atomic Nuclei and Electrons*. Freeman, 1963.

[5] J. E. Rosenthal and G. Breit. The Isotope Shift in Hyperfine Structure. *Physical Review*, 41:459–470, 1932. doi: 10.1103/PhysRev.41.459. URL `https://link.aps.org/doi/10.1103/PhysRev.41.459`.

[6] M. F. Crawford and A. L. Schawlow. Electron-Nuclear Potential Fields from Hyperfine Structure. *Physical Review*, 76:1310–1317, 1949. doi: 10.1103/PhysRev.76.1310. URL `https://link.aps.org/doi/10.1103/PhysRev.76.1310`.

[7] N. J. Ionesco-Pallas. Nuclear Magnetic Moments from Hyperfine Structure Data. *Physical Review*, 117:505–510, 1960. doi: 10.1103/PhysRev.117.505. URL `https://link.aps.org/doi/10.1103/PhysRev.117.505`.

[8] H. J. Rosenberg and H. H. Stroke. Effect of a Diffuse Nuclear Charge Distribution on the Hyperfine-Structure Interaction. *Physical Review A*,

5:1992–2000, 1972. doi: 10.1103/PhysRevA.5.1992. URL https://link.aps.org/doi/10.1103/PhysRevA.5.1992.

[9] A. Bohr and V. F. Weisskopf. The Influence of Nuclear Structure on the Hyperfine Structure of Heavy Elements. *Physical Review*, 77:94–98, 1950. doi: 10.1103/PhysRev.77.94. URL https://link.aps.org/doi/10.1103/PhysRev.77.94.

[10] J. R. Persson. Table of hyperfine anomaly in atomic systems. *Atomic Data and Nuclear Data Tables*, 99(1):62 – 68, 2013. ISSN 0092-640X. doi: https://doi.org/10.1016/j.adt.2012.04.002. URL http://www.sciencedirect.com/science/article/pii/S0092640X1200085X.

[11] M.-A. Bouchiat and C Bouchiat. Parity violation in atoms. *Reports on Progress in Physics*, 60(11):1351, 1997. URL http://stacks.iop.org/0034-4885/60/i=11/a=004.

[12] G. Neyens. Nuclear magnetic and quadrupole moments for nuclear structure research on exotic nuclei. *Reports on Progress in Physics*, 66(4):633, 2003. URL http://stacks.iop.org/0034-4885/66/i=4/a=205.

[13] B. K. Sahoo. Accurate estimate of α variation and isotope shift parameters in Na and Mg^+. *Journal of Physics B: Atomic, Molecular and Optical Physics*, 43(23):231001, 2010. URL http://stacks.iop.org/0953-4075/43/i=23/a=231001.

[14] A. R. Bodmer. Nuclear Scattering of Electrons and Isotope Shift. *Proceedings of the Physical Society. Section A*, 66(11):1041–, 1953. ISSN 0370-1298. URL http://stacks.iop.org/0370-1298/66/i=11/a=308.

[15] W. H. King. Peculiarities of the Isotope Shift in the Samarium Spectrum'. *J. Opt. Soc. Am.*, 53(5):638–639, 1963. doi: 10.1364/JOSA.53.000638. URL http://www.osapublishing.org/abstract.cfm?URI=josa-53-5-638.

[16] A. Bohr. *Kgl. Danske Vid. Selsk. Mat. Fys. Medd.*, 27:14, 1952.

[17] D. L. Hill and J. A. Wheeler. Nuclear Constitution and the Interpretation of Fission Phenomena. *Physical Review*, 89:1102–1145, 1953. doi: 10.1103/PhysRev.89.1102. URL https://link.aps.org/doi/10.1103/PhysRev.89.1102.

[18] R. Casten. *Nuclear Structure from a Simple Perspective*. Oxford science publications. Oxford University Press, 2000. ISBN 9780198507246.

[19] W. D. Myers and K. H. Schmidt. An update on droplet-model charge distributions. *Nuclear Physics A*, 410(1):61 – 73, 1983. ISSN 0375-9474. doi: http://dx.doi.org/10.1016/0375-9474(83)90401-3. URL http://www.sciencedirect.com/science/article/pii/0375947483904013.

[20] D. Berdichevsky and F. Tondeur. Nuclear core densities, isotope shifts, and the parametrization of the droplet model. *Zeitschrift für Physik A Atoms and Nuclei*, 322(1):141–147, 1985. ISSN 0939-7922. doi: 10.1007/BF01412027. URL http://dx.doi.org/10.1007/BF01412027.

[21] W. D. Myers and K. H. Schmidt. An update on droplet-model charge distributions. *Nuclear Physics A*, 410(1):61 – 73, 1983. ISSN 0375-9474. doi: http://dx.doi.org/10.1016/0375-9474(83)90401-3. URL http://www.sciencedirect.com/science/article/pii/0375947483904013.

[22] S. Raman, C. W. Nestor Jr., and P. Tikkanen. Transition probability from the ground to the first-excited 2^+ state of even-even nuclides. *Atomic Data and Nuclear Data Tables*, 78(1):1 – 128, 2001. ISSN 0092-640X. doi: http://dx.doi.org/10.1006/adnd.2001.0858. URL http://www.sciencedirect.com/science/article/pii/S0092640X01908587.

[23] P. Campbell, I. D. Moore, and M. R. Pearson. Laser spectroscopy for nuclear structure physics. *Progress in Particle and Nuclear Physics*, 86:127 – 180, 2016. ISSN 0146-6410. doi: http://dx.doi.org/10.1016/j.ppnp.2015.09.003. URL http://www.sciencedirect.com/science/article/pii/S0146641015000915.

[24] Kluge, H.-J. Atomic physics techniques for studying nuclear ground state properties, fundamental interactions and symmetries: status and perspectives. *Hyperfine Interactions*, 196(1):295–337, 2010. ISSN 1572-9540. doi: 10.1007/s10751-010-0172-9. URL https://doi.org/10.1007/s10751-010-0172-9.

[25] M. J. G. Borge and B. Jonson. ISOLDE past, present and future. *Journal of Physics G: Nuclear and Particle Physics*, 44(4):044011, 2017.

[26] E. Kugler. The ISOLDE facility. *Hyperfine Interactions*, 129(1):23–42, 2000. ISSN 1572-9540. doi: 10.1023/A:1012603025802. URL https://doi.org/10.1023/A:1012603025802.

[27] B. Jonson and A. Richter. More than three decades of ISOLDE physics. *Hyperfine Interact.*, 129(CERN-EP-99-040. 1-4):1–22. 23 p, 1999. URL https://cds.cern.ch/record/384134.

[28] P. G. Hansen, P. Hornshj, H. L. Nielsen, K. Wilsky, H. Kugler, G. Astner, E. Hageb, J. Hudis, A. Kjelberg, F. Mnnich, P. Patzelt, M. Alpsten, G. Andersson, Aa. Appelqvist, B. Bengtsson, R. A. Naumann, O. B. Nielsen, E. Beck, R. Foucher, J. P. Husson, J. Jastrzbski, A. Johnson, J. Alstad, T. Jahnsen, A. C. Pappas, T. Tunaal, R. Henck, P. Siffert, and G. Rudstam. Decay characteristics of short-lived radio-nuclides studied by on-line isotope separator techniques. *Physics Letters B*, 28(6):415 – 419, 1969. ISSN 0370-2693. doi: https://doi.org/10.1016/0370-2693(69)90337-2. URL http://www.sciencedirect.com/science/article/pii/0370269369903372.

[29] M. J. G. Borge. Highlights of the ISOLDE facility and the HIE-ISOLDE project. *Nuclear Instruments and Methods in Physics Research Section B: Beam Interactions with Materials and Atoms*, 376(Supplement C):408 – 412, 2016. ISSN 0168-583X. doi: https://doi.org/10.1016/j.nimb.2015.12.048. URL http://www.sciencedirect.com/science/article/pii/S0168583X16000057. Proceedings of the XVIIth International Conference on Electromagnetic Isotope Separators and Related Topics (EMIS2015), Grand Rapids, MI, U.S.A., 11-15 May 2015.

[30] R. Catherall, W. Andreazza, M. Breitenfeldt, A. Dorsival, G. J. Focker, T. P. Gharsa, T. J. Giles., J. L. Grenard, F. Locci, P. Martins, S. Marzari, J. Schipper, A. Shornikov, and T. Stora. The ISOLDE facility. *Journal of Physics G: Nuclear and Particle Physics*, 44(9):094002, 2017. URL `http://stacks.iop.org/0954-3899/44/i=9/a=094002`.

[31] T. Day Goodacre, J. Billowes, R. Catherall, T. E. Cocolios, B. Crepieux, D. V. Fedorov, V. N. Fedosseev, L. P. Gaffney, T. Giles, A. Gottberg, K. M. Lynch, B. A. Marsh, T. M. Mendona, J. P. Ramos, R. E. Rossel, S. Rothe, S. Sels, C. Sotty, T. Stora, C. Van Beveren, and M. Veinhard. Blurring the boundaries between ion sources: The application of the RILIS inside a FEBIAD type ion source at ISOLDE. *Nuclear Instruments and Methods in Physics Research Section B: Beam Interactions with Materiafls and Atoms*, 376(Supplement C):39 – 45, 2016. ISSN 0168-583X. doi: https://doi.org/10.1016/j.nimb.2016.03.005. URL `http://www.sciencedirect.com/science/article/pii/S0168583X16002111`. Proceedings of the XVIIth International Conference on Electromagnetic Isotope Separators and Related Topics (EMIS2015), Grand Rapids, MI, U.S.A., 11-15 May 2015.

[32] *https://isolde.web.cern.ch/*.

[33] V. N. Fedosseev, K. Chrysalidis, T. Day Goodacre, B. A. Marsh, S. Rothe, C. Seiffert, and K. D. A. Wendt. Ion beam production and study of radioactive isotopes with the laser ion source at ISOLDE. *Journal of Physics G: Nuclear and Particle Physics*, 44(8):084006, 2017. URL `http://stacks.iop.org/0954-3899/44/i=8/a=084006`.

[34] V. N. Fedosseev, L. E. Berg, N. Lebas, O. J. Launila, M. Lindroos, R. Losito, B. A. Marsh, F. K. Österdahl, T. Pauchard, G. Tranströmer, and J. Vannesjö. ISOLDE RILIS: New beams, new facilities. *Nuclear Instruments and Methods in Physics Research Section B: Beam Interactions with Materials and Atoms*, 266(19):4378 – 4382, 2008. ISSN 0168-583X. doi: https://doi.org/10.1016/j.nimb.2008.05.038. URL `http://www.`

sciencedirect.com/science/article/pii/S0168583X08007398. Proceedings of the XVth International Conference on Electromagnetic Isotope Separators and Techniques Related to their Applications.

[35] V. N. Fedosseeev, G. Huber, U. Köster, J. Lettry, V. I. Mishin, H. Ravn, and V. Sebastian. The ISOLDE laser ion source for exotic nuclei. *Hyperfine Interactions*, 127(1):409–416, 2000. ISSN 1572-9540. doi: 10.1023/A:1012609515865. URL https://doi.org/10.1023/A:1012609515865.

[36] F. Schwellnus, K. Blaum, R. Catherall, B. Crepieux, V. Fedosseev, T. Gottwald, H.-J. Kluge, B. Marsh, C. Mattolat, S. Rothe, T. Stora, and K. Wendt. The laser ion source trap for highest isobaric selectivity in online exotic isotope production. *Review of Scientific Instruments*, 81 (2):02A515, 2010. doi: 10.1063/1.3318259. URL http://dx.doi.org/10.1063/1.3318259.

[37] D. A. Fink, T. E. Cocolios, A. N. Andreyev, S. Antalic, A. E. Barzakh, B. Bastin, D. V. Fedorov, V. N. Fedosseev, K. T. Flanagan, L. Ghys, A. Gottberg, M. Huyse, N. Imai, T. Kron, N. Lecesne, K. M. Lynch, B. A. Marsh, D. Pauwels, E. Rapisarda, S. D. Richter, R. E. Rossel, S. Rothe, M. D. Seliverstov, A. M. Sjödin, C. Van Beveren, P. Van Duppen, and K. D. A. Wendt. In-Source Laser Spectroscopy with the Laser Ion Source and Trap: First Direct Study of the Ground-State Properties of ^{217,219}Po. *Physical Review X*, 5:011018, 2015. doi: 10.1103/PhysRevX.5.011018. URL https://link.aps.org/doi/10.1103/PhysRevX.5.011018.

[38] T. Day Goodacre. Developments of the ISOLDE RILIS for radioactive ion beam production and the results of their application in the study of exotic mercury isotopes, 2016. URL http://cds.cern.ch/record/2254839.

[39] E. Mané, J. Billowes, K. Blaum, P. Campbell, B. Cheal, P. Delahaye, K. T. Flanagan, D. H. Forest, H. Franberg, C. Geppert, T. Giles, A. Jokinen, M. Kowalska, R. Neugart, G. Neyens, W. Nörtershuser, I. Podadera, G. Tungate, P. Vingerhoets, and D.T. Yordanov. An ion cooler-buncher for

high-sensitivity collinear laser spectroscopy at ISOLDE. *European Physical Journal A*, 42(3):503–507, 2009. doi: 10.1140/epja/i2009-10828-0. URL https://www.scopus.com/inward/record.uri?eid=2-s2.0-73949150069&doi=10.1140%2fepja%2fi2009-10828-0&partnerID=40&md5=1e99008db57bb03a893665a7f0573c9c.

[40] G. C. Ball, G. Hackman, and R. Krücken. The TRIUMF-ISAC facility: two decades of discovery with rare isotope beams. *Physica Scripta*, 91 (9):093002, 2016. URL http://stacks.iop.org/1402-4896/91/i=9/a=093002.

[41] J. Dilling, R. Krücken, and G. Ball. ISAC overview. *Hyperfine Interactions*, 225(1):1–8, 2014. ISSN 1572-9540. doi: 10.1007/s10751-013-0877-7. URL https://doi.org/10.1007/s10751-013-0877-7.

[42] A. C. C Villari. First results at SPIRAL-GANIL. *Nuclear Instruments and Methods in Physics Research Section B: Beam Interactions with Materials and Atoms*, 204(Supplement C):31 – 41, 2003. ISSN 0168-583X. doi: https://doi.org/10.1016/S0168-583X(02)01887-6. URL http://www.sciencedirect.com/science/article/pii/S0168583X02018876. 14th International Conference on Electromagnetic Isotope Separators and Techniques Related to their Applications.

[43] A.C.C. Villari. GANIL, present and future. *Brazilian Journal of Physics*, 34(3 A):1008–1011, 2004. URL https://www.scopus.com/inward/record.uri?eid=2-s2.0-7644240064&partnerID=40&md5=124a597615bcb02b70add0855f4ca487.

[44] G. de Angelis, G. Prete, A. Andrighetto, M. Manzolaro, S. Corradetti, D. Scarpa, M. Rossignoli, A. Monetti, M. Lollo, M. Calderolla, J. Vasquez, D. Zafiropoulos, L. Sarchiapone, D. Benini, P. Favaron, M. Rigato, R. Pegoraro, D. Maniero, L. Calabretta, M. Comunian, M. Maggiore, A. Lombardi, L. Piazza, A. M. Porcellato, C. Roncolato, G. Bisoffi, A Pisent, A. Galata, M. Giacchini, G. Bassato, S. Canella, F. Gramegna, J. Valiente, J. Bermudez, P. F. Mastinu, J. Esposito, J. Wyss, A. Russo, and

S. Zanella. The SPES Radioactive Ion Beam facility of INFN. *Journal of Physics: Conference Series*, 580(1):012014, 2015. URL http://stacks.iop.org/1742-6596/580/i=1/a=012014.

[45] J. C. Cornell. *Final report of the EURISOL design study (2005-2009): a design study for a european isotope-separation-on-line radioactive ion beam facility*. GANIL, Caen, 2009. URL http://cds.cern.ch/record/1248417.

[46] I. D. Moore, P. Dendooven, and J. Ärje. *The IGISOL technique—three decades of developments*, pages 15–60. Springer Netherlands, Dordrecht, 2014. ISBN 978-94-007-5555-0. doi: 10.1007/978-94-007-5555-0_2. URL https://doi.org/10.1007/978-94-007-5555-0_2.

[47] M. Block, D. Ackermann, D. Beck, K. Blaum, M. Breitenfeldt, A. Chauduri, A. Doemer, S. Eliseev, D. Habs, S. Heinz, F. Herfurth, F. P. Heßberger, S. Hofmann, H. Geissel, H. J. Kluge, V. Kolhinen, G. Marx, J. B. Neumayr, M. Mukherjee, M. Petrick, W. Plass, W. Quint, S. Rahaman, C. Rauth, D. Rodríguez, C. Scheidenberger, L. Schweikhard, M. Suhonen, P. G. Thirolf, Z. Wang, and C. Weber. *The ion-trap facility SHIPTRAP*, pages 49–50. Springer Berlin Heidelberg, 2005. ISBN 978-3-540-37642-2. doi: 10.1007/3-540-37642-9_12. URL https://doi.org/10.1007/3-540-37642-9_12.

[48] S. Rahaman, M. Block, D. Ackermann, D. Beck, A. Chaudhuri, S. Eliseev, H. Geissel, D. Habs, F. Herfurth, F. P. Heberger, S. Hofmann, G. Marx, M. Mukherjee, J. B. Neumayr, M. Petrick, W. R. Pla, W. Quint, C. Rauth, D. Rodrguez, C. Scheidenberger, L. Schweikhard, P. G. Thirolf, and C. Weber. On-line commissioning of SHIPTRAP. *International Journal of Mass Spectrometry*, 251(2):146 – 151, 2006. ISSN 1387-3806. doi: https://doi.org/10.1016/j.ijms.2006.01.049. URL http://www.sciencedirect.com/science/article/pii/S1387380606000807.

[49] K. Minamisono, B. R. Barquest, G. Bollen, K. Cooper, K. Hammerton, M. Hughes, P. F. Mantica, D. J. Morrissey, R. Ringle, J. A. Rodriguez,

C. A. Ryder, D. M. Rossi, S. Schwarz, R. Strum, C. Sumithrarachchi, and D. Tarazona. Commissioning of the collinear laser spectroscopy facility BECOLA at NSCL/MSU. *Hyperfine Interactions*, 230(1):57–63, 2015. ISSN 1572-9540. doi: 10.1007/s10751-014-1089-5. URL `https://doi.org/10.1007/s10751-014-1089-5`.

[50] K. Minamisono, P. F. Mantica, A. Klose, S. Vinnikova, A. Schneider, B. Johnson, and B. R. Barquest. Commissioning of the collinear laser spectroscopy system in the BECOLA facility at NSCL. *Nuclear Instruments and Methods in Physics Research Section A: Accelerators, Spectrometers, Detectors and Associated Equipment*, 709(Supplement C):85 – 94, 2013. ISSN 0168-9002. doi: https://doi.org/10.1016/j.nima.2013.01.038. URL `http://www.sciencedirect.com/science/article/pii/S0168900213001034`.

[51] Y. Yano. The RIKEN RI Beam Factory Project: A status report. *Nuclear Instruments and Methods in Physics Research Section B: Beam Interactions with Materials and Atoms*, 261(1):1009 – 1013, 2007. ISSN 0168-583X. doi: https://doi.org/10.1016/j.nimb.2007.04.174. URL `http://www.sciencedirect.com/science/article/pii/S0168583X07009792`.

[52] H. Geissel, H. Weick, M. Winkler, G. Münzenberg, V. Chichkine, M. Yavor, T. Aumann, K. H. Behr, M. Böhmer, A. Brünle, K. Burkard, J. Benlliure, D. Cortina-Gil, L. Chulkov, A. Dael, J.-E. Ducret, H. Emling, B. Franczak, J. Friese, B. Gastineau, J. Gerl, R. Gernhäuser, M. Hellström, B. Jonson, J. Kojouharova, R. Kulessa, B. Kindler, N. Kurz, B. Lommel, W. Mittig, G. Moritz, C. Mühle, J. A. Nolen, G. Nyman, P. Roussell-Chomaz, C. Scheidenberger, K.-H. Schmidt, G. Schrieder, B. M. Sherrill, H. Simon, K. Sümmerer, N. A. Tahir, V. Vysotsky, H. Wollnik, and A. F. Zeller. The Super-FRS project at GSI. *Nuclear Instruments and Methods in Physics Research Section B: Beam Interactions with Materials and Atoms*, 204 (Supplement C):71 – 85, 2003. ISSN 0168-583X. doi: https://doi.org/10.1016/S0168-583X(02)01893-1. URL `http://www.sciencedirect.com/`

science/article/pii/S0168583X02018931. 14th International Conference on Electromagnetic Isotope Separators and Techniques Related to their Applications.

[53] D. J. Morrissey, B. M. Sherrill, M. Steiner, A. Stolz, and I. Wiedenhoever. Commissioning the A1900 projectile fragment separator. *Nuclear Instruments and Methods in Physics Research Section B: Beam Interactions with Materials and Atoms*, 204(Supplement C):90 – 96, 2003. ISSN 0168-583X. doi: https://doi.org/10.1016/S0168-583X(02)01895-5. URL http://www.sciencedirect.com/science/article/pii/S0168583X02018955. 14th International Conference on Electromagnetic Isotope Separators and Techniques Related to their Applications.

[54] D. J. Morrissey. status of the frib project with a new fragment separator.

[55] G. D. Alkhazov, L. K. Batist, A. A. Bykov, V. D. Vitman, V. S. Letokhov, V. I. Mishin, V. N. Panteleyev, S. K. Sekatsky, and V. N. Fedoseyev. Application of a high efficiency selective laser ion source at the IRIS facility. *Nuclear Instruments and Methods in Physics Research Section A: Accelerators, Spectrometers, Detectors and Associated Equipment*, 306(1):400 – 402, 1991. ISSN 0168-9002. doi: http://dx.doi.org/10.1016/0168-9002(91)90348-T. URL http://www.sciencedirect.com/science/article/pii/016890029190348T.

[56] V. I. Mishin, V. N. Fedoseyev, H. J. Kluge, V. S. Letokhov, H. L. Ravn, F. Scheerer, Y. Shirakabe, S. Sundell, and O. Tengblad. Chemically selective laser ion-source for the CERN-ISOLDE on-line mass separator facility. *Nuclear Instruments and Methods in Physics Research Section B: Beam Interactions with Materials and Atoms*, 73(4):550 – 560, 1993. ISSN 0168-583X. doi: https://doi.org/10.1016/0168-583X(93)95839-W. URL http://www.sciencedirect.com/science/article/pii/0168583X9395839W.

[57] S. Rothe, T. Day Goodacre, D. V. Fedorov, V. N. Fedosseev, B. A. Marsh, P. L. Molkanov, R. E. Rossel, M. D. Seliverstov, M. Veinhard, and K. D. A.

Wendt. Laser ion beam production at CERN-ISOLDE: New features - More possibilities. *Nuclear Instruments and Methods in Physics Research Section B: Beam Interactions with Materials and Atoms*, 376(Supplement C):91 – 96, 2016. ISSN 0168-583X. doi: https://doi.org/10.1016/j.nimb.2016.02.024. URL `http://www.sciencedirect.com/science/article/pii/S0168583X1600152X`. Proceedings of the XVIIth International Conference on Electromagnetic Isotope Separators and Related Topics (EMIS2015), Grand Rapids, MI, U.S.A., 11-15 May 2015.

[58] B. A. Marsh, V. N. Fedosseev, D. A. Fink, T. Day Goodacre, R. E. Rossel, S. Rothe, D. V. Fedorov, N. Imai, M. D. Seliverstov, and P. Molkanov. RILIS applications at CERN/ISOLDE. *Hyperfine Interactions*, 227(1):101–111, 2014. ISSN 1572-9540. doi: 10.1007/s10751-014-1051-6. URL `https://doi.org/10.1007/s10751-014-1051-6`.

[59] S. Rothe, B. A. Marsh, C. Mattolat, V. N. Fedosseev, and K. D. A. Wendt. A complementary laser system for ISOLDE RILIS. *Journal of Physics: Conference Series*, 312(5):052020, 2011. URL `http://stacks.iop.org/1742-6596/312/i=5/a=052020`.

[60] V. N. Fedosseev, Y. Kudryavtsev, and V. I. Mishin. Resonance laser ionization of atoms for nuclear physics. *Physica Scripta*, 85(5):058104, 2012. URL `http://stacks.iop.org/1402-4896/85/i=5/a=058104`.

[61] M.D. Seliverstov, T.E. Cocolios, W. Dexters, A.N. Andreyev, S. Antalic, A.E. Barzakh, B. Bastin, J. Bscher, I.G. Darby, D.V. Fedorov, V.N. Fedoseyev, K.T. Flanagan, S. Franchoo, S. Fritzsche, G. Huber, M. Huyse, M. Keupers, U. Kster, Yu. Kudryavtsev, B.A. Marsh, P.L. Molkanov, R.D. Page, A.M. Sjdin, I. Stefan, J. Van de Walle, P. Van Duppen, M. Venhart, and S.G. Zemlyanoy. Charge radii of odd-A ^{191211}Po isotopes. *Physics Letters B*, 719(4):362 – 366, 2013. ISSN 0370-2693. doi: https://doi.org/10.1016/j.physletb.2013.01.043. URL `http://www.sciencedirect.com/science/article/pii/S0370269313000841`.

[62] R. F. Garcia Ruiz, M. L. Bissell, K. Blaum, A. Ekström, N. Frömmgen, G. Hagen, M. Hammen, K. Hebeler, J. D. Holt, G. R. Jansen, M. Kowalska, K. Kreim, W. Nazarewicz, R. Neugart, G. Neyens, W. Nörtershäuser, T. Papenbrock, J. Papuga, A. Schwenk, J. Simonis, K. D. A. Wendt, and D. T. Yordanov. Unexpectedly large charge radii of neutron-rich calcium isotopes. *Nature Physics*, 12(6):594–598, 2016. doi: doi:10.1038/nphys3645. URL `http://www.nature.com/nphys/journal/v12/n6/full/nphys3645.html`.

[63] W. Borchers, E. Arnold, W. Neu, R. Neugart, K. Wendt, and G. Ulm. Xenon isotopes far from stability studied by collisional ionization laser spectroscopy. *Physics Letters B*, 216(1):7 – 10, 1989. ISSN 0370-2693. doi: https://doi.org/10.1016/0370-2693(89)91359-2. URL `http://www.sciencedirect.com/science/article/pii/0370269389913592`.

[64] R. Neugart, W. Klempt, and K. Wendt. Collisional ionization as a sensitive detection scheme in collinear laser-fast-beam spectroscopy. *Nuclear Instruments and Methods in Physics Research Section B: Beam Interactions with Materials and Atoms*, 17(4):354 – 359, 1986. ISSN 0168-583X. doi: https://doi.org/10.1016/0168-583X(86)90125-4. URL `http://www.sciencedirect.com/science/article/pii/0168583X86901254`.

[65] A. Klein, B. A. Brown, U. Georg, M. Keim, P. Lievens, R. Neugart, M. Neuroth, R. E. Silverans, L. Vermeeren, and ISOLDE Collaboration. Moments and mean square charge radii of short-lived argon isotopes. *Nuclear Physics A*, 607(1):1 – 22, 1996. ISSN 0375-9474. doi: https://doi.org/10.1016/0375-9474(96)00192-3. URL `http://www.sciencedirect.com/science/article/pii/0375947496001923`.

[66] W. Geithner, B. A. Brown, K. M. Hilligsøe, S. Kappertz, M. Keim, G. Kotrotsios, P. Lievens, K. Marinova, R. Neugart, H. Simon, and S. Wilbert. Nuclear moments of neon isotopes in the range from ^{17}Ne at the proton drip line to neutron-rich ^{25}Ne. *Physical Review C*, 71:064319,

2005. doi: 10.1103/PhysRevC.71.064319. URL https://link.aps.org/doi/10.1103/PhysRevC.71.064319.

[67] K. Blaum, W. Geithner, J. Lassen, P. Lievens, K. Marinova, and R. Neugart. Nuclear moments and charge radii of argon isotopes between the neutron-shell closures $N = 20$ and $N = 28$. *Nuclear Physics A*, 799(1): 30 – 45, 2008. ISSN 0375-9474. doi: https://doi.org/10.1016/j.nuclphysa.2007.11.004. URL http://www.sciencedirect.com/science/article/pii/S0375947407007841.

[68] W. Geithner, K.M. Hilligsoe, S. Kappertz, G. Katko, M. Keim, S. Kloos, G. Kotrotsios, P. Lievens, K. Marinova, R. Neugart, L. Vermeeren, S. Wilbert, and the ISOLDE Collaboration. Accurate isotope shift measurements on short lived neon isotopes. *Hyperfine Interactions*, 127(1): 117–120, 2000. ISSN 1572-9540. doi: 10.1023/A:1012614827735. URL https://doi.org/10.1023/A:1012614827735.

[69] R. E. Silverans, P. Lievens, and L. Vermeeren. A sensitive measuring scheme in collinear fast-ion-beam laser spectroscopy: The optical pumping, state-selective neutralization and particle detection sequence. *Nuclear Instruments and Methods in Physics Research Section B: Beam Interactions with Materials and Atoms*, 26(4):591 – 597, 1987. ISSN 0168-583X. doi: https://doi.org/10.1016/0168-583X(87)90548-9. URL http://www.sciencedirect.com/science/article/pii/0168583X87905489.

[70] L. Vermeeren, R. E. Silverans, P. Lievens, A. Klein, R. Neugart, Ch. Schulz, and F. Buchinger. Ultrasensitive radioactive detection of collinear-laser optical pumping: Measurement of the nuclear charge radius of ^{2}Ca. *Physical Review Letters*, 68:1679–1682, 1992. doi: 10.1103/PhysRevLett.68.1679. URL https://link.aps.org/doi/10.1103/PhysRevLett.68.1679.

[71] R. F. Garcia Ruiz, C. Gorges, M. L. Bissell, K. Blaum, W. Gins, H. Heylen, K. Koenig, S. Kaufmann, M. Kowalska, J. Krmer, P. Lievens, S. Malbrunot-Ettenauer, R. Neugart, G. Neyens, W. Nörtershuser, D. T. Yordanov, and

X. F. Yang. Development of a sensitive setup for laser spectroscopy studies of very exotic calcium isotopes. *Journal of Physics G: Nuclear and Particle Physics*, 44(4):044003, 2017. URL http://stacks.iop.org/0954-3899/44/i=4/a=044003.

[72] K. Blaum, J. Dilling, and W. Nörtershuser. Precision atomic physics techniques for nuclear physics with radioactive beams. *Physica Scripta*, 2013 (T152):014017, 2013. URL http://stacks.iop.org/1402-4896/2013/i=T152/a=014017.

[73] T. Eronen, A. Kankainen, and J. Äystö. Ion traps in nuclear physicsRecent results and achievements. *Progress in Particle and Nuclear Physics*, 91(Supplement C):259 – 293, 2016. ISSN 0146-6410. doi: https://doi.org/10.1016/j.ppnp.2016.08.001. URL http://www.sciencedirect.com/science/article/pii/S0146641016300436.

[74] A. Nieminen, J. Huikari, A. Jokinen, and J. Äystö. *Time Characteristics of the Ion Beam Cooler-Buncher at JYFL*, pages 527–530. Springer Netherlands, Dordrecht, 2001. ISBN 978-94-015-1270-1. doi: 10.1007/978-94-015-1270-1_62. URL https://doi.org/10.1007/978-94-015-1270-1_62.

[75] T. Sun, S. Schwarz, G. Bollen, D. Lawton, R. Ringle, and P. Schury. Commissioning of the ion beam buncher and cooler for LEBIT. *The European Physical Journal A - Hadrons and Nuclei*, 25(1):61–62, 2005. ISSN 1434-601X. doi: 10.1140/epjad/i2005-06-126-9. URL https://doi.org/10.1140/epjad/i2005-06-126-9.

[76] F. Herfurth, J. Dilling, A. Kellerbauer, G. Bollen, S. Henry, H. J. Kluge, E. Lamour, D. Lunney, R. B. Moore, C. Scheidenberger, S. Schwarz, G. Sikler, and J. Szerypo. A linear radiofrequency ion trap for accumulation, bunching, and emittance improvement of radioactive ion beams. *Nuclear Instruments and Methods in Physics Research Section A: Accelerators, Spectrometers, Detectors and Associated Equipment*, 469(2):254 –

275, 2001. ISSN 0168-9002. doi: https://doi.org/10.1016/S0168-9002(01)00168-1. URL http://www.sciencedirect.com/science/article/pii/S0168900201001681.

[77] G. Savard, S. Baker, C. Davids, A. F. Levand, E. F. Moore, R. C. Pardo, R. Vondrasek, B. J. Zabransky, and G. Zinkann. Radioactive beams from gas catchers: The CARIBU facility. *Nuclear Instruments and Methods in Physics Research Section B: Beam Interactions with Materials and Atoms*, 266(19):4086 – 4091, 2008. ISSN 0168-583X. doi: https://doi.org/10.1016/j.nimb.2008.05.091. URL http://www.sciencedirect.com/science/article/pii/S0168583X08006848. Proceedings of the XVth International Conference on Electromagnetic Isotope Separators and Techniques Related to their Applications.

[78] R. Boussaid, G. Ban, J. F. Cam, and C. Vandamme. Simulations of high intensity ion beam RFQ cooler for DESIR/SPIRAL 2: SHIRaC. *Journal of Instrumentation*, 9(07):P07009, 2014. URL http://stacks.iop.org/1748-0221/9/i=07/a=P07009.

[79] T. Brunner, M. J. Smith, M. Brodeur, S. Ettenauer, A .T. Gallant, V. V. Simon, A. Chaudhuri, A. Lapierre, E. Mané, R. Ringle, M. C. Simon, J. A. Vaz, P. Delheij, M. Good, M. R. Pearson, and J. Dilling. TITAN's digital RFQ ion beam cooler and buncher, operation and performance. *Nuclear Instruments and Methods in Physics Research Section A: Accelerators, Spectrometers, Detectors and Associated Equipment*, 676(Supplement C):32 – 43, 2012. ISSN 0168-9002. doi: https://doi.org/10.1016/j.nima.2012.02.004. URL http://www.sciencedirect.com/science/article/pii/S0168900212001398.

[80] B. Cheal and K. T. Flanagan. Progress in laser spectroscopy at radioactive ion beam facilities. *Journal of Physics G: Nuclear and Particle Physics*, 37 (11):113101–39, 2010.

[81] I. Podadera Aliseda, T. Fritioff, T. Giles, A. Jokinen, M. Lindroos, and F. Wenander. Design of a second generation RFQ Ion Cooler and Buncher

(RFQCB) for ISOLDE. *Nuclear Physics A*, 746(Supplement C):647 – 650, 2004. ISSN 0375-9474. doi: https://doi.org/10.1016/j.nuclphysa.2004.09.043. URL http://www.sciencedirect.com/science/article/pii/S0375947404009868. Proceedings of the Sixth International Conference on Radioactive Nuclear Beams (RNB6).

[82] A. Jokinen, M. Lindroos, E. Molin, and M. Petersson. RFQ-cooler for low-energy radioactive ions at ISOLDE. *Nuclear Instruments and Methods in Physics Research Section B: Beam Interactions with Materials and Atoms*, 204(Supplement C):86 – 89, 2003. ISSN 0168-583X. doi: https://doi.org/10.1016/S0168-583X(02)01894-3. URL http://www.sciencedirect.com/science/article/pii/S0168583X02018943. 14th International Conference on Electromagnetic Isotope Separators and Techniques Related to their Applications.

[83] Yu. A. Kudriavtsev and V. S. Letokhov. Laser method of highly selective detection of rare radioactive isotopes through multistep photoionization of accelerated atoms. *Applied Physics B*, 29(3):219–221, 1982.

[84] C. Schulz, E. Arnold, W. Borchers, W. Neu, R. Neugart, M. Neuroth, E. W. Otten, M. Scherf, K. Wendt, P. Lievens, Y. A. Kudryavtsev, V. S. Letokhov, V. I. Mishin, and V. V. Petrunin. Resonance ionization spectroscopy on a fast atomic ytterbium beam. *Journal of Physics B: Atomic, Molecular and Optical Physics*, 24(22):4831, 1991. URL http://stacks.iop.org/0953-4075/24/i=22/a=020.

[85] Collinear resonant ionization laser spectroscopy of rare francium isotopes. Technical Report CERN-INTC-2008-010. INTC-P-240, CERN, Geneva, 2008. URL http://cds.cern.ch/record/1080361.

[86] K. T. Flanagan, K. M. Lynch, J. Billowes, M. L. Bissell, I. Budinčević, T. E. Cocolios, R. P. de Groote, S. De Schepper, V. N. Fedosseev, S. Franchoo, R. F. Garcia Ruiz, H. Heylen, B. A. Marsh, G. Neyens, T. J. Procter, R. E. Rossel, S. Rothe, I. Strashnov, H. H. Stroke, and

K. D. A. Wendt. Collinear Resonance Ionization Spectroscopy of Neutron-Deficient Francium Isotopes. *Physical Review Letters*, 111:212501, 2013. doi: 10.1103/PhysRevLett.111.212501. URL `http://link.aps.org/doi/10.1103/PhysRevLett.111.212501`.

[87] K. M. Lynch, J. Billowes, M. L. Bissell, I. Budinčević, T. E. Cocolios, R. P. De Groote, S. De Schepper, V. N. Fedosseev, K. T. Flanagan, S. Franchoo, R. F. Garcia Ruiz, H. Heylen, B. A. Marsh, G. Neyens, T. J. Procter, R. E. Rossel, S. Rothe, I. Strashnov, H. H. Stroke, and K. D. A. Wendt. Decay-Assisted Laser Spectroscopy of Neutron-Deficient Francium. *Physical Review X*, 4:011055, 2014. doi: 10.1103/PhysRevX.4.011055. URL `http://link.aps.org/doi/10.1103/PhysRevX.4.011055`.

[88] I. Budinčević, J. Billowes, M. L. Bissell, T. E. Cocolios, R. P. de Groote, S. De Schepper, V. N. Fedosseev, K. T. Flanagan, S. Franchoo, R. F. Garcia Ruiz, H. Heylen, K. M. Lynch, B. A. Marsh, G. Neyens, T. J. Procter, R. E. Rossel, S. Rothe, I. Strashnov, H. H. Stroke, and K. D. A. Wendt. Laser spectroscopy of francium isotopes at the borders of the region of reflection asymmetry. *Physical Review C*, 90:014317, 2014. doi: 10.1103/PhysRevC.90.014317. URL `https://link.aps.org/doi/10.1103/PhysRevC.90.014317`.

[89] R. P. de Groote, I. Budinčević, J. Billowes, M. L. Bissell, T. E. Cocolios, G. J. Farooq-Smith, V. N. Fedosseev, K. T. Flanagan, S. Franchoo, R. F. Garcia Ruiz, H. Heylen, R. Li, K. M. Lynch, B. A. Marsh, G. Neyens, R. E. Rossel, S. Rothe, H. H. Stroke, K. D. A. Wendt, S. G. Wilkins, and X. Yang. Use of a Continuous Wave Laser and Pockels Cell for Sensitive High-Resolution Collinear Resonance Ionization Spectroscopy. *Physical Review Letters*, 115:132501, 2015. doi: 10.1103/PhysRevLett.115.132501. URL `http://link.aps.org/doi/10.1103/PhysRevLett.115.132501`.

[90] K. M. Lynch, T. E. Cocolios, J. Billowes, M. L. Bissell, I. Budinčević, T. Day Goodacre, R. P. de Groote, G. J. Farooq-Smith, V. N. Fedosseev, K. T. Flanagan, S. Franchoo, R. F. Garcia Ruiz, H. Heylen, R. Li,

B. A. Marsh, G. Neyens, R. E. Rossel, S. Rothe, H. H. Stroke, K. D. A. Wendt, S. G. Wilkins, and X. Yang. Combined high-resolution laser spectroscopy and nuclear decay spectroscopy for the study of the low-lying states in ^{206}Fr, ^{202}At, and ^{198}Bi. *Physical Review C*, 93:014319, 2016. doi: 10.1103/PhysRevC.93.014319. URL `http://link.aps.org/doi/10.1103/PhysRevC.93.014319`.

[91] R. P. de Groote, K. M. Lynch, and S. G. Wilkins. Achieving sensitive, high-resolution laser spectroscopy at CRIS. *Hyperfine Interactions*, 238(1): 5, 2016. ISSN 1572-9540. doi: 10.1007/s10751-016-1378-2. URL `http://dx.doi.org/10.1007/s10751-016-1378-2`.

[92] T. E. Cocolios, H. H. Al Suradi, J. Billowes, I. Budinčević, R. P. de Groote, S. De Schepper, V. N. Fedosseev, K. T. Flanagan, S. Franchoo, R. F. Garcia Ruiz, H. Heylen, F. Le Blanc, K. M. Lynch, B. A. Marsh, P. J. R. Mason, G. Neyens, J. Papuga, T. J. Procter, M. M. Rajabali, R. E. Rossel, S. Rothe, G. S. Simpson, A. J. Smith, I. Strashnov, H. H. Stroke, D. Verney, P. M. Walker, K. D. A. Wendt, and R. T. Wood. The Collinear Resonance Ionization Spectroscopy (CRIS) experimental setup at CERN-ISOLDE. *Nuclear Instruments and Methods in Physics Research Section B: Beam Interactions with Materials and Atoms*, 317(Part B):565 – 569, 2013. ISSN 0168-583X. doi: https://doi.org/10.1016/j.nimb.2013.05.088. URL `http://www.sciencedirect.com/science/article/pii/S0168583X13007088`. XVIth International Conference on ElectroMagnetic Isotope Separators and Techniques Related to their Applications, December 27, 2012 at Matsue, Japan.

[93] K. M. Lynch. Laser assisted nuclear decay spectroscopy: A new method for studying neutron-deficient francium, 2015. URL `https://cds.cern.ch/record/1606787`.

[94] T. J. Procter. New techniques of laser spectroscopy on exotic isotopes of gallium and francium, 2013. URL `https://cds.cern.ch/record/1551521`.

[95] K. M. Lynch, T. E. Cocolios, N. Althubiti, G. J. Farooq-Smith, W. Gins, and A. J. Smith. A simple decay-spectroscopy station at CRIS-ISOLDE.

Nuclear Instruments and Methods in Physics Research Section A: Accelerators, Spectrometers, Detectors and Associated Equipment, 844(Supplement C):14 – 18, 2017. ISSN 0168-9002. doi: https://doi.org/10.1016/j.nima.2016.11.024. URL http://www.sciencedirect.com/science/article/pii/S0168900216311317.

[96] A. Kasapi, G. Y. Yin, and M. Jain. Pulsed Ti:sapphire laser seeded off the gain peak. *Appl. Opt.*, 35(12):1999–2004, 1996. doi: 10.1364/AO.35.001999. URL http://ao.osa.org/abstract.cfm?URI=ao-35-12-1999.

[97] R. P. de Groote, M. Verlinde, V. Sonnenschein, K. T. Flanagan, I. Moore, and G. Neyens. Efficient, high-resolution resonance laser ionization spectroscopy using weak transitions to long-lived excited states. *Physical Review A*, 95:032502, 2017. doi: 10.1103/PhysRevA.95.032502. URL https://link.aps.org/doi/10.1103/PhysRevA.95.032502.

[98] R. P. de Groote, G. Neyens, and K. T. Flanagan. Modeling and simulation of two-step resonance ionization processes using CW and pulsed lasers, 2013. URL https://cds.cern.ch/record/1638355.

[99] M. Verlinde. Modelling of laser-atom interactions for improving efficiency in nuclear laser spectroscopy research, 2016. URL https://fys.kuleuven.be/iks/nm/files/thesis/thesis-matthias-verlinde.pdf.

[100] Tobias Kron. *Pushing the limits of resonance ionization mass spectrometry - ionization efciency in palladium and spectral resolution in technetium.* Univ., Mainz, 2017. doi: urn:nbn:de:hebis:77-diss-1000015058.

[101] S. Rothe. An all-solid state laser system for the laser ion source RILIS and in-source laser spectroscopy of astatine at ISOLDE, CERN, 2012. URL https://cds.cern.ch/record/1519189.

[102] S. Rothe, V. N. Fedosseev, T. Kron, B. A. Marsh, R. E. Rossel, and K. D. A. Wendt. Narrow linewidth operation of the RILIS titanium: Sapphire laser at ISOLDE/CERN. *Nuclear Instruments and Methods in Physics Research*

Section B: Beam Interactions with Materials and Atoms, 317(Part B):561 – 564, 2013. ISSN 0168-583X. doi: https://doi.org/10.1016/j.nimb.2013.08.058. URL http://www.sciencedirect.com/science/article/pii/S0168583X1301001X. XVIth International Conference on ElectroMagnetic Isotope Separators and Techniques Related to their Applications, December 27, 2012 at Matsue, Japan.

[103] V. Sonnenschein, I. D. Moore, S. Raeder, M. Reponen, H. Tomita, and K. Wendt. Characterization of a pulsed injection-locked Ti:sapphire laser and its application to high resolution resonance ionization spectroscopy of copper. *Laser Physics*, 27(8):085701, 2017. URL http://stacks.iop.org/1555-6611/27/i=8/a=085701.

[104] Y. K. Park, G. Giuliani, and R. L. Byer. Stable single-axial-mode operation of an unstable-resonator Nd:YAG oscillator by injection locking. *Opt. Lett.*, 5(3):96–98, 1980. doi: 10.1364/OL.5.000096. URL http://ol.osa.org/abstract.cfm?URI=ol-5-3-96.

[105] Y. K. Park. *Frequency and mode control of Q-switched Nd:YAG lasers*. PhD thesis, Stanford Univ.,Stanford, CA, 1981.

[106] Y. Park, G. Giuliani, and R. Byer. Single axial mode operation of aQ-switched Nd:YAG oscillator by injection seeding. *IEEE Journal of Quantum Electronics*, 20(2):117–125, 1984. ISSN 0018-9197. doi: 10.1109/JQE.1984.1072371.

[107] V. Sonnenschein. *Laser developments and high resolution resonance ionization spectroscopy of actinide elements*. PhD thesis, University of Jyväskylä, 2015.

[108] B. E. A. Saleh and M. C. Teich. *Fundamentals of Photonics*. Wiley Series in Pure and Applied Optics. Wiley, 2007. ISBN 9780471358329.

[109] G. D. Boyd and D. A. Kleinman. Parametric Interaction of Focused Gaussian Light Beams. *Journal of Applied Physics*, 39(8):3597–3639, 1968. doi: 10.1063/1.1656831. URL http://dx.doi.org/10.1063/1.1656831.

[110] D. T. Yordanov, D. L. Balabanski, J. Bieroń, M. L. Bissell, K. Blaum, I. Budinčević, S. Fritzsche, N. Frömmgen, G. Georgiev, Ch. Geppert, M. Hammen, M. Kowalska, K. Kreim, A. Krieger, R. Neugart, W. Nörtershäuser, J. Papuga, and S. Schmidt. Spins, Electromagnetic Moments, and Isomers of $^{107-129}$Cd. *Physical Review Letters*, 110:192501, 2013. doi: 10.1103/PhysRevLett.110.192501. URL `https://link.aps.org/doi/10.1103/PhysRevLett.110.192501`.

[111] C. Jung, K. Kim, B. A. Yu, Y. L. Lee, W. Shin, and Y. C. Noh. Improvement of frequency-tripling efficiency through a walk-off compensation. In *2015 11th Conference on Lasers and Electro-Optics Pacific Rim (CLEO-PR)*, volume 1, pages 1–2, 2015. doi: 10.1109/CLEOPR.2015.7375834.

[112] C. Jung, W. Shin, B. A. Yu, Y. L. Lee, and Y. C. Noh. Enhanced 355-nm generation using a simple method to compensate for walk-off loss. *Opt. Express*, 20(2):941–948, 2012. doi: 10.1364/OE.20.000941. URL `http://www.opticsexpress.org/abstract.cfm?URI=oe-20-2-941`.

[113] Demtröder, W. *Laser spectroscopy*, volume 1. Springer, 2008.

[114] Kara Marie Lynch. Collinear resonance ionization spectroscopy of radium ions. Technical Report CERN-INTC-2014-043. INTC-P-413, CERN, Geneva, 2014. URL `https://cds.cern.ch/record/1704513`.

[115] W. Finkelnburg and W. Humbach. Ionisierungsenergien von atomen und atomionen. *Naturwissenschaften*, 42(2):35–37, 1955. ISSN 1432-1904. doi: 10.1007/BF00621525. URL `https://doi.org/10.1007/BF00621525`.

[116] D. Rapp and W. E. Francis. Charge Exchange between Gaseous Ions and Atoms. *The Journal of Chemical Physics*, 37(11):2631–2645, 1962. doi: 10.1063/1.1733066. URL `http://dx.doi.org/10.1063/1.1733066`.

[117] A. R. Vernon. Year 1 progress report, 2016.

[118] A. Kramida, Yu. Ralchenko, J. Reader, and and NIST ASD Team. NIST Atomic Spectra Database (ver. 5.3), [Online]. Available:

http://physics.nist.gov/asd [2017, September 18]. National Institute of Standards and Technology, Gaithersburg, MD., 2015.

[119] U. Dammalapati, K. Jungmann, and L. Willmann. Compilation of Spectroscopic Data of Radium (Ra I and Ra II). *Journal of Physical and Chemical Reference Data*, 45(1):013101, 2016. doi: 10.1063/1.4940416. URL http://dx.doi.org/10.1063/1.4940416.

[120] T. Day Goodacre. *To be submitted*, 2017.

[121] N. D. Scielzo, J. R. Guest, E. C. Schulte, I. Ahmad, K. Bailey, D. L. Bowers, R. J. Holt, Z.-T. Lu, T. P. O'Connor, and D. H. Potterveld. Measurement of the lifetimes of the lowest $^3P_1$ state of neutral Ba and Ra. *Physical Review A*, 73:010501, Jan 2006. doi: 10.1103/PhysRevA.73.010501. URL https://link.aps.org/doi/10.1103/PhysRevA.73.010501.

[122] K. Heyde and J. L. Wood. Shape coexistence in atomic nuclei. *Reviews of Modern Physics*, 83:1467–1521, 2011. doi: 10.1103/RevModPhys.83.1467. URL https://link.aps.org/doi/10.1103/RevModPhys.83.1467.

[123] J. L. Wood, K. Heyde, W. Nazarewicz, M. Huyse, and P. van Duppen. Coexistence in even-mass nuclei. *Physics Reports*, 215:101–201, 1992. doi: 10.1016/0370-1573(92)90095-H.

[124] K. Heyde, P. Van Isacker, M. Waroquier, J. L. Wood, and R. A. Meyer. Coexistence in odd-mass nuclei. *Physics Reports*, 102(5):291 – 393, 1983. ISSN 0370-1573. doi: https://doi.org/10.1016/0370-1573(83)90085-6. URL http://www.sciencedirect.com/science/article/pii/0370157383900856.

[125] N. Bijnens, P. Decrock, S. Franchoo, M. Gaelens, M. Huyse, H. Y. Hwang, I. Reusen, J. Szerypo, J. Von Schwarzenberg, J. Wauters, et al. Intruder states and the onset of deformation in the neutron-deficient even-even polonium isotopes. *Physical Review Letters*, 75(25):4571, 1995.

[126] G. Ulm, S. K. Bhattacherjee, P. Dabkiewicz, G. Huber, H. J. Kluge, T. Kühl, H. Lochmann, E. W. Otten, K. Wendt, S. A. Ahmad, W. Klempt, and R. Neugart. Isotope shift of ^{182}Hg and an update of nuclear moments and charge radii in the isotope range ^{181}Hg-^{206}Hg. *Zeitschrift für Physik A Atomic Nuclei*, 325(3):247–259, 1986. ISSN 0939-7922. doi: 10.1007/BF01294605. URL `http://dx.doi.org/10.1007/BF01294605`.

[127] M. Huyse, A. N. Andreyev, P. Van Duppen, L. Weissman, D. Ackermann, J. Gerl, F. P. Heßberger, S. Hofmann, A. Kleinbohl, G. Munzenberg, S. Reshitko, C. Schlegel, H. Schaffner, P. Cagarda, M. Matos, Š Šáro, A. Keenan, C. Moore, C. D. O'Leary, R. D. Page, M. Taylor, H. Kettunen, M. Leino, A. Lavrentiev, R. Wyss, and K. Heyde. A triplet of differently shaped spin- zero states in the atomic nucleus ^{186}Pb . *Nature*, 405(6785): 430–433, 2000.

[128] G. L. Poli, C. N. Davids, P. J. Woods, D. Seweryniak, M. P. Carpenter, J. A. Cizewski, T. Davinson, A. Heinz, R. V. F. Janssens, C. J. Lister, J. J. Ressler, A. A. Sonzogni, J. Uusitalo, and W. B. Walters. Proton and α radioactivity of ^{185}Bi. *Physical Review C*, 63:044304, 2001. doi: 10.1103/PhysRevC.63.044304. URL `https://link.aps.org/doi/10.1103/PhysRevC.63.044304`.

[129] C. N. Davids, P. J. Woods, H. T. Penttilä, J. C. Batchelder, C. R. Bingham, D. J. Blumenthal, L. T. Brown, B. C. Busse, L. F. Conticchio, T. Davinson, D. J. Henderson, R. J. Irvine, D. Seweryniak, K. S. Toth, W. B. Walters, and B. E. Zimmerman. Proton Decay of an Intruder State in ^{185}Bi. *Physical Review Letters*, 76:592–595, 1996. doi: 10.1103/PhysRevLett.76.592. URL `http://link.aps.org/doi/10.1103/PhysRevLett.76.592`.

[130] H. Kettunen, T. Enqvist, K. Eskola, T. Grahn, P. T. Greenlees, K. Helariutta, P. Jones, R. Julin, S. Juutinen, H. Kankaanpää, A. Keenan, H. Koivisto, P. Kuusiniemi, M. Leino, A. P. Leppänen, M. Miukku, P. Nieminen, J. Pakarinen, P. Rahkila, and J. Uusitalo. Decay studies of neutron-deficient odd-mass At and Bi isotopes. *The European Physical Journal*

A - Hadrons and Nuclei, 25(1):181–182, 2005. ISSN 1434-601X. doi: 10.1140/epjad/i2005-06-114-1. URL https://doi.org/10.1140/epjad/i2005-06-114-1.

[131] P. Nieminen, S. Juutinen, A. N. Andreyev, J. F. C. Cocks, O. Dorvaux, K. Eskola, P. T. Greenlees, K. Hauschild, K. Helariutta, M. Huyse, P. M. Jones, R. Julin, H. Kankaanpää, H. Kettunen, P. Kuusiniemi, Y. Le Coz, M. Leino, T. Lönnroth, M. Muikku, P. Rahkila, A. Savelius, J. Uusitalo, N. Amzal, N. J. Hammond, C. Scholey, and R. Wyss. γ-ray spectroscopy of ^{191,193}Bi. *Physical Review C*, 69:064326, 2004. doi: 10.1103/PhysRevC.69.064326. URL https://link.aps.org/doi/10.1103/PhysRevC.69.064326.

[132] J. C. Batchelder, E. F. Zganjar, K. S. Toth, C. R. Bingham, J. Wauters, C. N. Davids, D. S. Seweryniak, R. J. Irvine, W. B. Walters, L. F. Conticchio, and L. T. Brown. Behavior of intruder based states in light Bi and Tl isotopes: The study of ^{187}Bi α decay. *AIP Conference Proceedings*, 392(1): 353–356, 1997. doi: 10.1063/1.52709. URL http://aip.scitation.org/doi/abs/10.1063/1.52709.

[133] A. N. Andreyev, D. Ackermann, F. P. Hebberger, K. Heyde, S. Hofmann, M. Huyse, D. Karlgren, I. Kojouharov, B. Kindler, B. Lommel, G. Munzenberg, R D. Page, K. Van de Vel, P. Van Duppen, W. B. Walters, and R. Wyss. Shape-changing particle decays of ^{185}Bi and structure of the lightest odd-mass Bi isotopes. *Physical Review C*, 69:054308, 2004. doi: 10.1103/PhysRevC.69.054308. URL https://link.aps.org/doi/10.1103/PhysRevC.69.054308.

[134] K. Auranen, J. Uusitalo, S. Juutinen, H. Badran, F. Defranchi Bisso, D. Cox, T. Grahn, P. T. Greenlees, A. Herzáň, U. Jakobsson, R. Julin, J. Konki, M. Leino, A. Lightfoot, M. Mallaburn, O. Neuvonen, J. Pakarinen, P. Papadakis, J. Partanen, P. Rahkila, M. Sandzelius, J. Sarén, C. Scholey, J. Sorri, and S. Stolze. Experimental study of isomeric intruder $\frac{1}{2}^+$ states in ^{197,203}At. *Physical Review C*, 95:044311, 2017.

doi: 10.1103/PhysRevC.95.044311. URL https://link.aps.org/doi/10.1103/PhysRevC.95.044311.

[135] K. Auranen, J. Uusitalo, S. Juutinen, U. Jakobsson, T. Grahn, P. T. Greenlees, K. Hauschild, A. Herzáň, R. Julin, J. Konki, M. Leino, J. Pakarinen, J. Partanen, P. Peura, P. Rahkila, P. Ruotsalainen, M. Sandzelius, J. Sarén, C. Scholey, J. Sorri, and S. Stolze. Experimental study of $\frac{1}{2}^+$ isomers in ^{199,201}At. *Physical Review C*, 90:024310, 2014. doi: 10.1103/PhysRevC.90.024310. URL https://link.aps.org/doi/10.1103/PhysRevC.90.024310.

[136] H. Kettunen, T. Enqvist, T. Grahn, P. T. Greenlees, P. Jones, R. Julin, S. Juutinen, A. Keenan, P. Kuusiniemi, M. Leino, A. P. Leppänen, P. Nieminen, J. Pakarinen, P. Rahkila, and J. Uusitalo. Alpha-decay studies of the new isotopes ^{191}At and ^{193}At. *The European Physical Journal A - Hadrons and Nuclei*, 17(4):537–558, 2003. ISSN 1434-601X. doi: 10.1140/epja/i2002-10162-1. URL https://doi.org/10.1140/epja/i2002-10162-1.

[137] M. Nyman, S. Juutinen, I. Darby, S. Eeckhaudt, T. Grahn, P. T. Greenlees, U. Jakobsson, P. Jones, R. Julin, S. Ketelhut, H. Kettunen, M. Leino, P. Nieminen, P. Peura, P. Rahkila, J. Sarén, C. Scholey, J. Sorri, J. Uusitalo, and T. Enqvist. γ-ray and decay spectroscopy of ^{194,195,196}At. *Physical Review C*, 88:054320, 2013. doi: 10.1103/PhysRevC.88.054320. URL https://link.aps.org/doi/10.1103/PhysRevC.88.054320.

[138] K. Andgren, U. Jakobsson, B. Cederwall, J. Uusitalo, T. Bäck, S. J. Freeman, P. T. Greenlees, B. Hadinia, A. Hugues, A. Johnson, P. M. Jones, D. T. Joss, S. Juutinen, R. Julin, S. Ketelhut, A. Khaplanov, M. Leino, M. Nyman, R. D. Page, P. Rahkila, M. Sandzelius, P. Sapple, J. Sarén, C. Scholey, J. Simpson, J. Sorri, J. Thomson, and R. Wyss. γ-ray spectroscopy of ^{197}At. *Physical Review C*, 78:044328, 2008. doi: 10.1103/PhysRevC.78.044328. URL https://link.aps.org/doi/10.1103/PhysRevC.78.044328.

[139] H. Kettunen, T. Enqvist, M. Leino, K. Eskola, P. T. Greenlees, K. Helariutta, P. Jones, R. Julin, S. Juutinen, H. Kankaanpää, H. Koivisto, P. Kuusiniemi, M. Muikku, P. Nieminen, P. Rahkila, and J. Uusitalo. Investigations into the alpha-decay of ^{195}At. *The European Physical Journal A - Hadrons and Nuclei*, 16(4):457–467, 2003. ISSN 1434-601X. doi: 10.1140/epja/i2002-10130-9. URL https://doi.org/10.1140/epja/i2002-10130-9.

[140] U. Jakobsson, S. Juutinen, J. Uusitalo, M. Leino, K. Auranen, T. Enqvist, P. T. Greenlees, K. Hauschild, P. Jones, R. Julin, S. Ketelhut, P. Kuusiniemi, M. Nyman, P. Peura, P. Rahkila, P. Ruotsalainen, J. Sarén, C. Scholey, and J. Sorri. Spectroscopy of the proton drip-line nucleus ^{203}Fr. *Physical Review C*, 87:054320, 2013. doi: 10.1103/PhysRevC.87.054320. URL http://link.aps.org/doi/10.1103/PhysRevC.87.054320.

[141] U. Jakobsson, J. Uusitalo, S. Juutinen, M. Leino, T. Enqvist, P. T. Greenlees, K. Hauschild, P. Jones, R. Julin, S. Ketelhut, P. Kuusiniemi, M. Nyman, P. Peura, P. Rahkila, P. Ruotsalainen, J. Sarén, C. Scholey, and J. Sorri. Recoil-decay tagging study of ^{205}Fr. *Physical Review C*, 85:014309, 2012. doi: 10.1103/PhysRevC.85.014309. URL http://link.aps.org/doi/10.1103/PhysRevC.85.014309.

[142] J. Uusitalo, M. Leino, T. Enqvist, K. Eskola, T. Grahn, P. T. Greenlees, P. Jones, R. Julin, S. Juutinen, A. Keenan, H. Kettunen, H. Koivisto, P. Kuusiniemi, A.-P. Leppänen, P. Nieminen, J. Pakarinen, P. Rahkila, and C. Scholey. α decay studies of very neutron-deficient francium and radium isotopes. *Physical Review C*, 71:024306, 2005. doi: 10.1103/PhysRevC.71.024306. URL https://link.aps.org/doi/10.1103/PhysRevC.71.024306.

[143] J. Uusitalo, J. Sarén, S. Juutinen, M. Leino, S. Eeckhaudt, T. Grahn, P. T. Greenlees, U. Jakobsson, P. Jones, R. Julin, S. Ketelhut, A.-P. Leppänen, M. Nyman, J. Pakarinen, P. Rahkila, C. Scholey, A. Semchenkov, J. Sorri, A. Steer, and M. Venhart. α-decay studies of the

francium isotopes ^{198}Fr and ^{199}Fr. *Physical Review C*, 87:064304, 2013. doi: 10.1103/PhysRevC.87.064304. URL https://link.aps.org/doi/10.1103/PhysRevC.87.064304.

[144] Z. Kalaninová, A. N. Andreyev, S. Antalic, F. P. Hebberger, D. Ackermann, B. Andel, M. C. Drummond, S. Hofmann, M. Huyse, B. Kindler, J. F. W. Lane, V. Liberati, B. Lommel, R. D. Page, E. Rapisarda, K. Sandhu, Š. Šáro, A. Thornthwaite, and P. Van Duppen. α decay of the very neutron-deficient isotopes $^{197-199}$Fr. *Physical Review C*, 87:044335, 2013. doi: 10.1103/PhysRevC.87.044335. URL https://link.aps.org/doi/10.1103/PhysRevC.87.044335.

[145] Z. Kalaninová, S. Antalic, A. N. Andreyev, F. P. Heßberger, D. Ackermann, B. Andel, L. Bianco, S. Hofmann, M. Huyse, B. Kindler, B. Lommel, R. Mann, R. D. Page, P. J. Sapple, J. Thomson, P. Van Duppen, and M. Venhart. Decay of ^{201,203}Ra and ^{200,202}Fr. *Physical Review C*, 89:054312, 2014. doi: 10.1103/PhysRevC.89.054312. URL https://link.aps.org/doi/10.1103/PhysRevC.89.054312.

[146] A. E. Barzakh, D. V. Fedorov, V. S. Ivanov, P. L. Molkanov, F. V. Moroz, S. Yu. Orlov, V. N. Panteleev, M. D. Seliverstov, and Yu. M. Volkov. Laser spectroscopy studies of intruder states in ^{193,195,197}Bi. *Physical Review C*, 94:024334, 2016. doi: 10.1103/PhysRevC.94.024334. URL https://link.aps.org/doi/10.1103/PhysRevC.94.024334.

[147] M. Wang, G. Audi, A. H. Wapstra, F. G. Kondev, M. MacCormick, X. Xu, and B. Pfeiffer. The AME2012 atomic mass evaluation (II). Tables, graphs and references. *Chinese Physics C*, 36:1603, 2012.

[148] A. E. Barzakh, L. Kh. Batist, D. V. Fedorov, V. S. Ivanov, K. A. Mezilev, P. L. Molkanov, F. V. Moroz, S. Yu. Orlov, V. N. Panteleev, and Yu. M. Volkov. Changes in the mean-square charge radii and magnetic moments of neutron-deficient Tl isotopes. *Physical Review C*, 88:024315, 2013. doi: 10.1103/PhysRevC.88.024315. URL https://link.aps.org/doi/10.1103/PhysRevC.88.024315.

[149] A. E. Barzakh, A. N. Andreyev, T. E. Cocolios, R. P. de Groote, D. V. Fedorov, V. N. Fedosseev, R. Ferrer, D. A. Fink, L. Ghys, M. Huyse, U. Köster, J. Lane, V. Liberati, K. M. Lynch, B. A. Marsh, P. L. Molkanov, T. J. Procter, E. Rapisarda, S. Rothe, K. Sandhu, M. D. Seliverstov, A. M. Sjödin, C. Van Beveren, P. Van Duppen, M. Venhart, and M. Veselský. Changes in mean-squared charge radii and magnetic moments of $^{179-184}$Tl measured by in-source laser spectroscopy. *Physical Review C*, 95(1):014324, 2017.

[150] J. Cubiss. In-source laser spectroscopy of At isotopes and decay studies of ^{178}Au, 2017.

[151] G. J. Farooq-Smith, T. E. Cocolios, J. Billowes, M. L. Bissell, I. Budinčević, T. Day Goodacre, R. P. de Groote, V. N. Fedosseev, K. T. Flanagan, S. Franchoo, R. F. Garcia Ruiz, H. Heylen, R. Li, K. M. Lynch, B. A. Marsh, G. Neyens, R. E. Rossel, S. Rothe, H. H. Stroke, K. D. A. Wendt, S. G. Wilkins, and X. F. Yang. Laser and decay spectroscopy of the short-lived isotope ^{214}Fr in the vicinity of the N = 126 shell closure. *Physical Review C*, 94:054305, 2016. doi: 10.1103/PhysRevC.94.054305. URL `http://link.aps.org/doi/10.1103/PhysRevC.94.054305`.

[152] A. Coc, C. Thibault, F. Touchard, H. T. Duong, P. Juncar, S. Liberman, J. Pinard, J. Lermé, J. L. Vialle, S. Büttgenbach, A. C. Mueller, and A. Pesnelle. Hyperfine structures and isotope shifts of $^{207-213,220-228}$Fr; Possible evidence of octupolar deformation. *Physics Letters B*, 163(1):66 – 70, 1985. ISSN 0370-2693. doi: http://dx.doi.org/10.1016/0370-2693(85)90193-5. URL `http://www.sciencedirect.com/science/article/pii/0370269385901935`.

[153] H. T. Duong, P. Juncar, S. Liberman, A. C. Mueller, R. Neugart, E. W. Otten, B. Peuse, J. Pinard, H. H. Stroke, C. Thibault, F. Touchard, J. L. Vialle, K. Wendt, and ISOLDE Collaboration. First Observation of the Blue Optical Lines of Francium. *EPL (Europhysics Letters)*, 3(2):175, 1987. URL `http://stacks.iop.org/0295-5075/3/i=2/a=008`.

[154] E. Gomez, S. Aubin, L. A. Orozco, G. D. Sprouse, E. Iskrenova-Tchoukova, and M. S. Safronova. Nuclear Magnetic Moment of ^{210}Fr: A Combined Theoretical and Experimental Approach. *Physical Review Letters*, 100: 172502, 2008. doi: 10.1103/PhysRevLett.100.172502. URL `http://link.aps.org/doi/10.1103/PhysRevLett.100.172502`.

[155] B. K. Sahoo, D. K. Nandy, B. P. Das, and Y. Sakemi. Correlation trends in the hyperfine structures of ^{210,212}Fr. *Physical Review A*, 91:042507, 2015. doi: 10.1103/PhysRevA.91.042507. URL `http://link.aps.org/doi/10.1103/PhysRevA.91.042507`.

[156] V. A. Dzuba, W. R. Johnson, and M. S. Safronova. Calculation of isotope shifts for cesium and francium. *Physical Review A*, 72:022503, 2005. doi: 10.1103/PhysRevA.72.022503. URL `http://link.aps.org/doi/10.1103/PhysRevA.72.022503`.

[157] A. Voss, F. Buchinger, B. Cheal, J. E. Crawford, J. Dilling, M. Kortelainen, A. A. Kwiatkowski, A. Leary, C. D. P. Levy, F. Mooshammer, M. L. Ojeda, M. R. Pearson, T. J. Procter, and W. Al Tamimi. Nuclear moments and charge radii of neutron-deficient francium isotopes and isomers. *Physical Review C*, 91:044307, 2015. doi: 10.1103/PhysRevC.91.044307. URL `http://link.aps.org/doi/10.1103/PhysRevC.91.044307`.

[158] R. P. de Groote, J. Billowes, C. L. Binnersley, M. L. Bissell, T. E. Cocolios, T. Day Goodacre, G. J. Farooq-Smith, D. V. Fedorov, K. T. Flanagan, S. Franchoo, R. F. Garcia Ruiz, Á. Koszorús, K. M. Lynch, G. Neyens, F. Nowacki, T. Otsuka, S. Rothe, H. H. Stroke, Y. Tsunoda, A. R. Vernon, K. D. A. Wendt, S. G. Wilkins, Z. Y. Xu, and X. F. Yang. Dipole and quadrupole moments of $^{73\text{-}78}$Cu as a test of the robustness of the $Z = 28$ shell closure near ^{78}Ni. *Physical Review C*, 96:041302, Oct 2017. doi: 10.1103/PhysRevC.96.041302. URL `https://link.aps.org/doi/10.1103/PhysRevC.96.041302`.

[159] H. H. Stroke, R. J. Blin-Stoyle, and V. Jaccarino. Configuration Mixing and the Effects of Distributed Nuclear Magnetization on Hyperfine Structure

in Odd-A Nuclei. *Physical Review*, 123:1326–1348, 1961. doi: 10.1103/PhysRev.123.1326. URL https://link.aps.org/doi/10.1103/PhysRev.123.1326.

[160] J. Zhang, M. Tandecki, R. Collister, S. Aubin, J. A. Behr, E. Gomez, G. Gwinner, L. A. Orozco, M. R. Pearson, and G. D. Sprouse. Hyperfine Anomalies in Fr: Boundaries of the Spherical Single Particle Model. *Physical Review Letters*, 115:042501, 2015. doi: 10.1103/PhysRevLett.115.042501. URL https://link.aps.org/doi/10.1103/PhysRevLett.115.042501.

[161] J. S. Grossman, L. A. Orozco, M. R. Pearson, J. E. Simsarian, G. D. Sprouse, and W. Z. Zhao. Hyperfine Anomaly Measurements in Francium Isotopes and the Radial Distribution of Neutrons. *Physical Review Letters*, 83:935–938, 1999. doi: 10.1103/PhysRevLett.83.935. URL https://link.aps.org/doi/10.1103/PhysRevLett.83.935.

[162] M. R. Pearson, P. Campbell, K. Leerungnavarat, J. Billowes, I. S. Grant, M. Keim, J. Kilgallon, I. D. Moore, R. Neugart, M. Neuroth, S. Wilbert, and the ISOLDE Collaboration. Nuclear moments and charge radii of bismuth isotopes. *Journal of Physics G: Nuclear and Particle Physics*, 26(12): 1829, 2000. URL http://stacks.iop.org/0954-3899/26/i=12/a=307.

[163] G. Neyens, S. Ternier, N. Coulier, K. Vyvey, R. Coussement, and D. L. Balabanski. Influence of particle-core coupling on the quadrupole moment of 8^+ isomers in even-even Po isotopes. *Nuclear Physics A*, 625(3):668 – 674, 1997. ISSN 0375-9474. doi: http://dx.doi.org/10.1016/S0375-9474(97)00415-6. URL http://www.sciencedirect.com/science/article/pii/S0375947497004156.

[164] G. Neyens, R. Nouwen, G. S'heeren, M. Van Den Bergh, and R. Coussement. Quadrupole moments of isomeric states in ^{212}Ra, ^{213}Ra and ^{214}Ra. *Nuclear Physics A*, 555(3):629 – 642, 1993. ISSN 0375-9474. doi: https://doi.org/10.1016/0375-9474(93)90492-G. URL http://www.sciencedirect.com/science/article/pii/037594749390492G.

[165] L. Grodzins. The uniform behaviour of electric quadrupole transition probabilities from first 2^+ states in even-even nuclei. *Physics Letters*, 2(2):88 – 91, 1962. ISSN 0031-9163. doi: https://doi.org/10.1016/0031-9163(62)90162-2. URL http://www.sciencedirect.com/science/article/pii/0031916362901622.

[166] H. De Witte, A. N. Andreyev, N. Barré, M. Bender, T. E. Cocolios, S. Dean, D. Fedorov, V. N. Fedoseyev, L. M. Fraile, S. Franchoo, V. Hellemans, P. H. Heenen, K. Heyde, G. Huber, M. Huyse, H. Jeppessen, U. Köster, P. Kunz, S. R. Lesher, B. A. Marsh, I. Mukha, B. Roussière, J. Sauvage, M. Seliverstov, I. Stefanescu, E. Tengborn, K. Van de Vel, J. Van de Walle, P. Van Duppen, and Yu. Volkov. Nuclear Charge Radii of Neutron-Deficient Lead Isotopes Beyond $N = 104$ Midshell Investigated by In-Source Laser Spectroscopy. *Physical Review Letters*, 98: 112502, Mar 2007. doi: 10.1103/PhysRevLett.98.112502. URL https://link.aps.org/doi/10.1103/PhysRevLett.98.112502.

[167] M. D. Seliverstov, A. N. Andreyev, N. Barré, A. E. Barzakh, S. Dean, H. De Witte, D. V. Fedorov, V. N. Fedoseyev, L. M. Fraile, S. Franchoo, J. Genevey, G. Huber, M. Huyse, U. Köster, P. Kunz, S. R. Lesher, B. A. Marsh, I. Mukha, B. Roussière, J. Sauvage, I. Stefanescu, K. Van de Vel, P. Van Duppen, and Yu. M. Volkov. Charge radii and magnetic moments of odd- A 183-189Pb isotopes. *The European Physical Journal A*, 41(3): 315–321, 2009. ISSN 1434-601X. doi: 10.1140/epja/i2009-10817-3. URL https://doi.org/10.1140/epja/i2009-10817-3.

[168] U. Dinger, J. Eberz, G. Huber, R. Menges, S. Schröder, R. Kirchner, O. Klepper, T. Kühl, D. Marx, and G. D. Sprouse. Nuclear moments and change in the charge-radii of neutron deficient lead isotopes. *Zeitschrift für Physik A Atomic Nuclei*, 328(2):253–254, 1987. ISSN 0939-7922. doi: 10.1007/BF01290669. URL https://doi.org/10.1007/BF01290669.

[169] M. Anselment and W. Faubel and S. Göring and A. Hanser and G. Meisel and H. Rebel and G. Schatz. The odd-even staggering of the nuclear charge

radii of Pb isotopes. *Nuclear Physics A*, 451(3):471 – 480, 1986. ISSN 0375-9474. doi: https://doi.org/10.1016/0375-9474(86)90071-0. URL http://www.sciencedirect.com/science/article/pii/0375947486900710.

[170] T. E. Cocolios, W. Dexters, M. D. Seliverstov, A. N. Andreyev, S. Antalic, A. E. Barzakh, B. Bastin, J. Büscher, I. G. Darby, D. V. Fedorov, V. N. Fedosseyev, K. T. Flanagan, S. Franchoo, S. Fritzsche, G. Huber, M. Huyse, M. Keupers, U. Köster, Yu. Kudryavtsev, E. Mané, B. A. Marsh, P. L. Molkanov, R. D. Page, A. M. Sjoedin, I. Stefan, J. Van de Walle, P. Van Duppen, M. Venhart, S. G. Zemlyanoy, M. Bender, and P.-H. Heenen. Early Onset of Ground State Deformation in Neutron Deficient Polonium Isotopes. *Physical Review Letters*, 106:052503, 2011. doi: 10.1103/PhysRevLett.106.052503. URL http://link.aps.org/doi/10.1103/PhysRevLett.106.052503.

[171] T. E. Cocolios. *Private communication.*

[172] J. A. Bounds, C. R. Bingham, H. K. Carter, G. A. Leander, R. L. Mlekodaj, E. H. Spejewski, and W. M. Fairbank. Nuclear structure of light thallium isotopes as deduced from laser spectroscopy on a fast atom beam. *Physical Review C*, 36:2560–2568. doi: 10.1103/PhysRevC.36.2560. URL https://link.aps.org/doi/10.1103/PhysRevC.36.2560.

[173] P. A. Butler. Octupole collectivity in nuclei. *Journal of Physics G: Nuclear and Particle Physics*, 43(7):073002, 2016. URL http://stacks.iop.org/0954-3899/43/i=7/a=073002.

[174] P. A. Butler and W. Nazarewicz. Intrinsic reflection asymmetry in atomic nuclei. *Reviews of Modern Physics*, 68:349–421, 1996. doi: 10.1103/RevModPhys.68.349. URL https://link.aps.org/doi/10.1103/RevModPhys.68.349.

[175] F. Stephens, F. Asaro, and I. Perlman. Low-Lying 1^+ States in Even-Even Nuclei. *Physical Review*, 96:1568–1572, 1954. doi: 10.1103/PhysRev.96.1568. URL https://link.aps.org/doi/10.1103/PhysRev.96.1568.

[176] F. S. Stephens, Frank Asaro, and I. Perlman. Radiations from 1^+ States in Even-Even Nuclei. *Physical Review*, 100:1543–1545, 1955. doi: 10.1103/PhysRev.100.1543. URL https://link.aps.org/doi/10.1103/PhysRev.100.1543.

[177] S. A. Ahmad, W. Klempt, R. Neugart, E. W. Otten, P. G. Reinhard, G. Ulm, and K. Wendt. Mean square charge radii of radium isotopes and octupole deformation in the $^{220-228}$Ra region. *Nuclear Physics A*, 483(2):244 – 268, 1988. ISSN 0375-9474. doi: http://dx.doi.org/10.1016/0375-9474(88)90534-9. URL http://www.sciencedirect.com/science/article/pii/0375947488905349.

[178] L. P. Gaffney, P. A. Butler, M. Scheck, A. B. Hayes, F. Wenander, M. Albers, B. Bastin, C. Bauer, A. Blazhev, S. Bonig, N. Bree, J. Cederkall, T. Chupp, D. Cline, T. E. Cocolios, T. Davinson, H. De Witte, J. Diriken, T. Grahn, A. Herzan, M. Huyse, D. G. Jenkins, D. T. Joss, N. Kesteloot, J. Konki, M. Kowalczyk, T. Kroll, E. Kwan, R. Lutter, K. Moschner, P. Napiorkowski, J. Pakarinen, M. Pfeiffer, D. Radeck, P. Reiter, K. Reynders, S. V. Rigby, L. M. Robledo, M. Rudigier, S. Sambi, M. Seidlitz, B. Siebeck, T. Stora, P. Thoele, P. Van Duppen, M. J. Vermeulen, M. von Schmid, D. Voulot, N. Warr, K. Wimmer, K. Wrzosek-Lipska, C. Y. Wu, and M. Zielinska. Studies of pear-shaped nuclei using accelerated radioactive beams. *Nature*, 497(7448):199–204, 2013. doi: http://dx.doi.org/10.1038/nature12073. URL https://www.nature.com/nature/journal/v497/n7448/full/nature12073.html.

[179] B. Bucher, S. Zhu, C. Y. Wu, R. V. F. Janssens, D. Cline, A. B. Hayes, M. Albers, A. D. Ayangeakaa, P. A. Butler, C. M. Campbell, M. P. Carpenter, C. J. Chiara, J. A. Clark, H. L. Crawford, M. Cromaz, H. M. David, C. Dickerson, E. T. Gregor, J. Harker, C. R. Hoffman, B. P. Kay, F. G. Kondev, A. Korichi, T. Lauritsen, A. O. Macchiavelli, R. C. Pardo, A. Richard, M. A. Riley, G. Savard, M. Scheck,

D. Seweryniak, M. K. Smith, R. Vondrasek, and A. Wiens. Direct Evidence of Octupole Deformation in Neutron-Rich ^{144}Ba. *Physical Review Letters*, 116:112503, 2016. doi: 10.1103/PhysRevLett.116.112503. URL `https://link.aps.org/doi/10.1103/PhysRevLett.116.112503`.

[180] J. Engel, J. L. Friar, and A. C. Hayes. Nuclear octupole correlations and the enhancement of atomic time-reversal violation. *Physical Review C*, 61: 035502, 2000. doi: 10.1103/PhysRevC.61.035502. URL `https://link.aps.org/doi/10.1103/PhysRevC.61.035502`.

[181] B. Graner, Y. Chen, E. G. Lindahl, and B. R. Heckel. Reduced Limit on the Permanent Electric Dipole Moment of ^{199}Hg. *Physical Review Letters*, 116:161601, 2016. doi: 10.1103/PhysRevLett.116.161601. URL `https://link.aps.org/doi/10.1103/PhysRevLett.116.161601`.

[182] R. H. Parker, M. R. Dietrich, M. R. Kalita, N. D. Lemke, K. G. Bailey, M. Bishof, J. P. Greene, R. J. Holt, W. Korsch, Z.-T. Lu, P. Mueller, T. P. O'Connor, and J. T. Singh. First Measurement of the Atomic Electric Dipole Moment of ^{225}Ra. *Physical Review Letters*, 114:233002, 2015. doi: 10.1103/PhysRevLett.114.233002. URL `https://link.aps.org/doi/10.1103/PhysRevLett.114.233002`.

[183] M. Bishof, R. H. Parker, K. G. Bailey, J. P. Greene, R. J. Holt, M. R. Kalita, W. Korsch, N. D. Lemke, Z. T. Lu, P. Mueller, T. P. O'Connor, J. T. Singh, and M. R. Dietrich. Improved limit on the ^{225}Ra electric dipole moment. *Physical Review C*, 94:025501, 2016. doi: 10.1103/PhysRevC.94.025501. URL `https://link.aps.org/doi/10.1103/PhysRevC.94.025501`.

[184] A. J. Aas, H. Mach, M. J. G. Borge, B. Fogelberg, I. S. Grant, K. Gulda, E. Hagebo, W. Kurcewicz, J. Kvasil, A. Lindroth, T. Martinez, D. Nosek, B. Rubio, J. F. Smith, K. Steffensen, J. L. Tain, O. Tengblad, and T. F. Thorsteinsen. Enhanced and quenched B(E1) transition rates between parity doublet bands in ^{227}Ra. *Nuclear Physics A*, 611(2):281 – 314, 1996. ISSN 0375-9474. doi: https://doi.org/10.1016/S0375-9474(96)

00312-0. URL http://www.sciencedirect.com/science/article/pii/S0375947496003120.

[185] L. M. Fraile, A. J. Aas, M. J. G. Borge, B. Fogelberg, L. M. Garca-Raffi, I. S. Grant, K. Gulda, E. Hageb, W. Kurcewicz, J. Kvasil, G. Lvhiden, H. Mach, A. Mackova, T. Martnez, B. Rubio, J. L. Tan, A. G. Teijeiro, O. Tengblad, and T. F. Thorsteinsen. Octupole correlations in ^{229}Ra. *Nuclear Physics A*, 657(4):355 – 390, 1999. ISSN 0375-9474. doi: https://doi.org/10.1016/S0375-9474(99)00330-9. URL http://www.sciencedirect.com/science/article/pii/S0375947499003309.

[186] L. M. Fraile, M. J. G. Borge, H. Mach, R. Boutami, A. J. Aas, B. Fogelberg, L. M. Garca-Raffi, I. S. Grant, K. Gulda, E. Hageb, W. Kurcewicz, J. Kvasil, M. J. Lpez, G. Lvhiden, T. Martnez, B. Rubio, J. L. Tan, and O. Tengblad. Persistence of octupole correlations in ^{231}Ra. *Nuclear Physics A*, 686(1):71 – 108, 2001. ISSN 0375-9474. doi: http://dx.doi.org/10.1016/S0375-9474(00)00572-8. URL http://www.sciencedirect.com/science/article/pii/S0375947400005728.

[187] M. J. G. Borge, R. Boutami, L. M. Fraile, K. Gulda, W. Kurcewicz, H. Mach, T. Martnez, B. Rubio, and O. Tengblad. Beta decay half-life of ^{231}Ra. *Physica Scripta*, 2006(T125):180, 2006. URL http://stacks.iop.org/1402-4896/2006/i=T125/a=040.

[188] W. J. Marciano and J. L. Rosner. Atomic parity violation as a probe of new physics. *Physical Review Letters*, 65:2963–2966, 1990. doi: 10.1103/PhysRevLett.65.2963. URL https://link.aps.org/doi/10.1103/PhysRevLett.65.2963.

[189] C. S. Wood, S. C. Bennett, D. Cho, B. P. Masterson, J. L. Roberts, C. E. Tanner, and C. E. Wieman. Measurement of Parity Nonconservation and an Anapole Moment in Cesium. *Science*, 275(5307):1759–1763, 1997. ISSN 0036-8075. doi: 10.1126/science.275.5307.1759. URL http://science.sciencemag.org/content/275/5307/1759.

[190] S. C. Bennett and C. E. Wieman. Measurement of the $6S \rightarrow 7S$ Transition Polarizability in Atomic Cesium and an Improved Test of the Standard Model. *Physical Review Letters*, 82:2484–2487, 1999. doi: 10.1103/PhysRevLett.82.2484. URL https://link.aps.org/doi/10.1103/PhysRevLett.82.2484.

[191] S. G. Porsev, K. Beloy, and A. Derevianko. Precision determination of weak charge of ^{133}Cs from atomic parity violation. *Physical Review D*, 82:036008, 2010. doi: 10.1103/PhysRevD.82.036008. URL https://link.aps.org/doi/10.1103/PhysRevD.82.036008.

[192] S. G. Porsev, K. Beloy, and A. Derevianko. Precision Determination of Electroweak Coupling from Atomic Parity Violation and Implications for Particle Physics. *Physical Review Letters*, 102:181601, 2009. doi: 10.1103/PhysRevLett.102.181601. URL https://link.aps.org/doi/10.1103/PhysRevLett.102.181601.

[193] C. Bouchiat and P. Fayet. Constraints on the parity-violating couplings of a new gauge boson. *Physics Letters B*, 608(1):87 – 94, 2005. ISSN 0370-2693. doi: https://doi.org/10.1016/j.physletb.2004.12.065. URL http://www.sciencedirect.com/science/article/pii/S0370269304017368.

[194] J. Guéna, M. Lintz, and M. A. Bouchiat. Atomic parity violation: Principles, recent results, present motivations. *Modern Physics Letters A*, 20(06):375–389, 2005. doi: 10.1142/S0217732305016853. URL http://www.worldscientific.com/doi/abs/10.1142/S0217732305016853.

[195] M. A. Bouchiat and C. C. Bouchiat. Weak neutral currents in atomic physics. *Physics Letters B*, 48(2):111 – 114, 1974. ISSN 0370-2693. doi: https://doi.org/10.1016/0370-2693(74)90656-X. URL http://www.sciencedirect.com/science/article/pii/037026937490656X.

[196] N. Fortson. Possibility of measuring parity nonconservation with a single trapped atomic ion. *Physical Review Letters*, 70:2383–2386, 1993. doi: 10.

1103/PhysRevLett.70.2383. URL https://link.aps.org/doi/10.1103/PhysRevLett.70.2383.

[197] L. W. Wansbeek, B. K. Sahoo, R. G. E. Timmermans, K. Jungmann, B. P. Das, and D. Mukherjee. Atomic parity nonconservation in Ra^+. *Physical Review A*, 78:050501, 2008. doi: 10.1103/PhysRevA.78.050501. URL https://link.aps.org/doi/10.1103/PhysRevA.78.050501.

[198] L. W. Wansbeek, S. Schlesser, B. K. Sahoo, A. E. L. Dieperink, C. J. G. Onderwater, and R. G. E. Timmermans. Charge radii of radium isotopes. *Physical Review C*, 86(1):015503–9, 2012.

[199] O. O. Versolato, G. S. Giri, L. W. Wansbeek, J. E. van den Berg, D. J. van der Hoek, K. Jungmann, W. L. Kruithof, C. J. G. Onderwater, B. K. Sahoo, B. Santra, P. D. Shidling, R. G. E. Timmermans, L. Willmann, and H. W. Wilschut. Laser spectroscopy of trapped short-lived Ra^+ ions. *Physical Review A*, 82:010501, 2010. doi: 10.1103/PhysRevA.82.010501. URL https://link.aps.org/doi/10.1103/PhysRevA.82.010501.

[200] O. O. Versolato, G. S. Giri, J. E. van den Berg, O. Bll, U. Dammalapati, D. J. van der Hoek, S. Hoekstra, K. Jungmann, W. L. Kruithof, S. Mller, M. Nuez Portela, C. J. G. Onderwater, B. Santra, R. G. E. Timmermans, L. W. Wansbeek, L. Willmann, and H. W. Wilschut. Hyperfine structure of the $6d^2D3/2$ level in trapped short-lived $^{211,209}Ra^+$ ions. *Physics Letters A*, 375(35):3130 – 3133, 2011. ISSN 0375-9601. doi: https://doi.org/10.1016/j.physleta.2011.07.002. URL http://www.sciencedirect.com/science/article/pii/S0375960111008310.

[201] G. S. Giri, O. O. Versolato, J. E. van den Berg, O. Böll, U. Dammalapati, D. J. van der Hoek, K. Jungmann, W. L. Kruithof, S. Müller, M. Nuñez Portela, C. J. G. Onderwater, B. Santra, R. G. E. Timmermans, L. W. Wansbeek, L. Willmann, and H. W. Wilschut. Isotope shifts of the $6d^2D_{3/2} \rightarrow 7p^2P_{1/2}$ transition in short-lived $^{209-214}Ra^+$. *Physical Review A*, 84:020503, 2011. doi: 10.1103/PhysRevA.84.020503. URL https://link.aps.org/doi/10.1103/PhysRevA.84.020503.

[202] R. Pal, D. Jiang, M. S. Safronova, and U. I. Safronova. Calculation of parity-nonconserving amplitude and other properties of Ra^+. *Physical Review A*, 79:062505, 2009. doi: 10.1103/PhysRevA.79.062505. URL `https://link.aps.org/doi/10.1103/PhysRevA.79.062505`.

[203] V. A. Dzuba, V. V. Flambaum, and J. S. M. Ginges. Calculations of parity-nonconserving $s - d$ amplitudes in Cs, Fr, Ba^+, and Ra^+. *Physical Review A*, 63:062101, 2001. doi: 10.1103/PhysRevA.63.062101. URL `https://link.aps.org/doi/10.1103/PhysRevA.63.062101`.

[204] V. A. Dzuba and V. V. Flambaum. Calculation of nuclear-spin-dependent parity nonconservation in $s^{\smile}d$ transitions of Ba^+, Yb^+, and Ra^+ ions. *Physical Review A*, 83:052513, 2011. doi: 10.1103/PhysRevA.83.052513. URL `https://link.aps.org/doi/10.1103/PhysRevA.83.052513`.

[205] V. A. Dzuba, V. V. Flambaum, and I. B. Khriplovich. Enhancement of P- and T-nonconserving effects in rare-earth atoms. *Zeitschrift für Physik D Atoms, Molecules and Clusters*, 1(3):243–245, 1986. ISSN 1431-5866. doi: 10.1007/BF01436678. URL `https://doi.org/10.1007/BF01436678`.

[206] V. A. Bolshakov, A. G. Dernyatin, K. A. Mezilev, Yu. N. Novikov, A. G. Polyakov, A. V. Popov, Yu. Ya. Sergeev, and V. I. Tikhonov. The production of neutron-rich heavy nuclei of astrophysical interest at the IRIS facility. *Nuclear Instruments and Methods in Physics Research Section B: Beam Interactions with Materials and Atoms*, 70(1):69 – 74, 1992. ISSN 0168-583X. doi: http://dx.doi.org/10.1016/0168-583X(92)95911-A. URL `http://www.sciencedirect.com/science/article/pii/0168583X9295911A`.

[207] G. Audi, O. Bersillon, J. Blachot, and A. H. Wapstra. The Nubase evaluation of nuclear and decay properties. *Nuclear Physics A*, 729(1):3 – 128, 2003. ISSN 0375-9474. doi: http://dx.doi.org/10.1016/j.nuclphysa.2003.11.001. URL `http://www.sciencedirect.com/science/article/pii/S0375947403018074`.

[208] P. Möller, J. R. Nix, and K. L. Kratz. Nuclear properties for astrophysical and radioactive-ion-beam applications. *Atomic Data and Nuclear Data Tables*, 66(2):131 – 343, 1997. ISSN 0092-640X. doi: http://dx.doi.org/10.1006/adnd.1997.0746. URL `http://www.sciencedirect.com/science/article/pii/S0092640X97907464`.

[209] K. Wendt, S. A. Ahmad, W. Klempt, R. Neugart, E. W. Otten, and H. H. Stroke. On the hyperfine structure and isotope shift of radium. *Zeitschrift für Physik D Atoms, Molecules and Clusters*, 4(3):227–241, 1987.

[210] W. Neu, R. Neugart, E. W. Otten, G. Passler, K. Wendt, B. Fricke, E. Arnold, H. J. Kluge, and G. Ulm. Quadrupole moments of radium isotopes from the $7p\ ^3P_{3/2}$ hyperfine structure in Ra II. *Zeitschrift für Physik D Atoms, Molecules and Clusters*, 11(2):105–111, 1988.

[211] E. Arnold, W. Borchers, M. Carre, H. T. Duong, P. Juncar, J. Lermé, S. Liberman, W. Neu, R. Neugart, E. W. Otten, M. Pellarin, J. Pinard, G. Ulm, J. L. Vialle, and K. Wendt. Direct measurement of nuclear magnetic moments of radium isotopes. *Physical Review Letters*, 59(7):771–774, 1987.

[212] S. A. Ahmad, W. Klempt, R. Neugart, E. W. Otten, K. Wendt, and C. Ekstrm. Determination of nuclear spins and moments in a series of radium isotopes. *Physics Letters B*, 133(1):47 – 52, 1983. ISSN 0370-2693. doi: http://dx.doi.org/10.1016/0370-2693(83)90103-X. URL `http://www.sciencedirect.com/science/article/pii/037026938390103X`.

[213] B. A. Brown, A. Derevianko, and V. V. Flambaum. Calculations of the neutron skin and its effect in atomic parity violation. *Physical Review C*, 79:035501, 2009. doi: 10.1103/PhysRevC.79.035501. URL `https://link.aps.org/doi/10.1103/PhysRevC.79.035501`.

[214] M. Bender, G. F. Bertsch, and P.-H. Heenen. Global study of quadrupole correlation effects. *Physical Review C*, 73:034322, 2006. doi: 10.

1103/PhysRevC.73.034322. URL https://link.aps.org/doi/10.1103/PhysRevC.73.034322.

[215] Dieperink, A. E. L. and Van Isacker, P. Shell corrections to a liquid-drop description of nuclear masses and radii. *European Physical Journal A*, 42 (2):269–279, 2009. doi: 10.1140/epja/i2009-10869-3. URL https://doi.org/10.1140/epja/i2009-10869-3.

[216] P. Möller, W. D. Myers, H. Sagawa, and S. Yoshida. New Finite-Range Droplet Mass Model and Equation-of-State Parameters. *Physical Review Letters*, 108:052501, 2012. doi: 10.1103/PhysRevLett.108.052501. URL https://link.aps.org/doi/10.1103/PhysRevLett.108.052501.

[217] P. Möller, A.J. Sierk, T. Ichikawa, and H. Sagawa. Nuclear ground-state masses and deformations: FRDM(2012). *Atomic Data and Nuclear Data Tables*, 109110:1 – 204, 2016. ISSN 0092-640X. doi: https://doi.org/10.1016/j.adt.2015.10.002. URL http://www.sciencedirect.com/science/article/pii/S0092640X1600005X.

[218] K. Hagino and H. Sagawa. Odd-even staggering of reaction cross sections for ^{22,23,24}O isotopes. *Physical Review C*, 85:037604, 2012. doi: 10.1103/PhysRevC.85.037604. URL https://link.aps.org/doi/10.1103/PhysRevC.85.037604.

[219] B. Jurado, H. Savajols, W. Mittig, N. A. Orr, P. Roussel-Chomaz, D. Baiborodin, W. N. Catford, M. Chartier, C. E. Demonchy, Z. Dlouh, A. Gillibert, L. Giot, A. Khouaja, A. Lpine-Szily, S. Lukyanov, J. Mrazek, Y. E. Penionzhkevich, S. Pita, M. Rousseau, and A. C. Villari. Mass measurements of neutron-rich nuclei near the $N = 20$ and 28 shell closures. *Physics Letters B*, 649(1):43 – 48, 2007. ISSN 0370-2693. doi: http://dx.doi.org/10.1016/j.physletb.2007.04.006. URL http://www.sciencedirect.com/science/article/pii/S0370269307004339.

[220] W. A. de Heer. The physics of simple metal clusters: experimental aspects and simple models. *Reviews of Modern Physics*, 65:611–676, 1993. doi: 10.

1103/RevModPhys.65.611. URL https://link.aps.org/doi/10.1103/RevModPhys.65.611.

[221] C. T. Black, D. C. Ralph, and M. Tinkham. Spectroscopy of the Superconducting Gap in Individual Nanometer-Scale Aluminum Particles. *Physical Review Letters*, 76:688–691, 1996. doi: 10.1103/PhysRevLett.76.688. URL https://link.aps.org/doi/10.1103/PhysRevLett.76.688.

[222] A. Bohr, B. R. Mottelson, and D. Pines. Possible Analogy between the Excitation Spectra of Nuclei and Those of the Superconducting Metallic State. *Physical Review*, 110:936–938, 1958. doi: 10.1103/PhysRev.110.936. URL https://link.aps.org/doi/10.1103/PhysRev.110.936.

[223] W. Satuła, J. Dobaczewski, and W. Nazarewicz. Odd-Even Staggering of Nuclear Masses: Pairing or Shape Effect? *Physical Review Letters*, 81: 3599–3602, 1998. doi: 10.1103/PhysRevLett.81.3599. URL https://link.aps.org/doi/10.1103/PhysRevLett.81.3599.

[224] J. Hakala, J. Dobaczewski, D. Gorelov, T. Eronen, A. Jokinen, A. Kankainen, V. S. Kolhinen, M. Kortelainen, I. D. Moore, H. Penttilä, S. Rinta-Antila, J. Rissanen, A. Saastamoinen, V. Sonnenschein, and J. Äystö. Precision Mass Measurements beyond ^{132}Sn: Anomalous Behavior of Odd-Even Staggering of Binding Energies. *Physical Review Letters*, 109:032501, 2012. doi: 10.1103/PhysRevLett.109.032501. URL https://link.aps.org/doi/10.1103/PhysRevLett.109.032501.

[225] Igal Talmi. On the odd-even effect in the charge radii of isotopes. *Nuclear Physics A*, 423(2):189 – 196, 1984. ISSN 0375-9474. doi: http://dx.doi.org/10.1016/0375-9474(84)90587-6. URL http://www.sciencedirect.com/science/article/pii/0375947484905876.

[226] W. Borchers, R. Neugart, E. W. Otten, H. T. Duong, G. Ulm, and K. Wendt. Hyperfine structure and isotope shift investigations in $^{202--222}$Rn

for the study of nuclear structure beyond $Z = 82$. *Hyperfine Interactions*, 34(1):25–29, 1987. ISSN 1572-9540. doi: 10.1007/BF02072676. URL https://doi.org/10.1007/BF02072676.

[227] S. Kreim, D. Beck, K. Blaum, Ch. Borgmann, M. Breitenfeldt, T. E. Cocolios, A. Gottberg, F. Herfurth, M. Kowalska, Yu. A. Litvinov, D. Lunney, V. Manea, T. M. Mendonca, S. Naimi, D. Neidherr, M. Rosenbusch, L. Schweikhard, T. Stora, F. Wienholtz, R. N. Wolf, and K. Zuber. Competition between pairing correlations and deformation from the odd-even mass staggering of francium and radium isotopes. *Physical Review C*, 90:024301, 2014. doi: 10.1103/PhysRevC.90.024301. URL https://link.aps.org/doi/10.1103/PhysRevC.90.024301.

[228] E. Chabanat, P. Bonche, P. Haensel, J. Meyer, and R. Schaeffer. A Skyrme parametrization from subnuclear to neutron star densities Part II. Nuclei far from stabilities. *Nuclear Physics A*, 635(1):231 – 256, 1998. ISSN 0375-9474. doi: https://doi.org/10.1016/S0375-9474(98)00180-8. URL http://www.sciencedirect.com/science/article/pii/S0375947498001808.